



PACIFIC EARTHQUAKE ENGINEERING RESEARCH CENTER

Damage Accumulation in Lightly Confined Reinforced Concrete Bridge Columns

**R. Tyler Ranf
Jared M. Nelson
Zach Price
Marc O. Eberhard
John F. Stanton**

Department of Civil and Environmental Engineering
University of Washington

Damage Accumulation in Lightly Confined Reinforced Concrete Bridge Columns

R. Tyler Ranf

Jared M. Nelson

Zach Price

Marc O. Eberhard

John F. Stanton

Department of Civil and Environmental Engineering
University of Washington

PEER Report 2005/08
Pacific Earthquake Engineering Research Center
College of Engineering
University of California, Berkeley

April 2006

ABSTRACT

Six reinforced concrete columns were tested at the University of Washington to evaluate the effects of cyclic loading on damage progression in lightly confined reinforced concrete circular bridge columns. The six columns, which were nominally identical, were typical of those built by the Washington State Department of Transportation until the mid-1970s.

The columns were subjected to a variety of lateral-deformation histories. These tests showed that increasing the number of cycles from 1 to 15 at each deformation level resulted in an approximately 30% reduction in the maximum column deformation at the three final damage states: 20% and 50% loss of lateral load, and the loss of axial load.

Three damage models (Park-Ang, modified Park-Ang, and cumulative plastic deformation) were used to evaluate the effect of cycling on damage accumulation. There was no clear correlation between the effect of cycling and damage accumulation for the six columns using the Park-Ang damage model because of the model's sensitivity to the yield displacement. Better correlations were obtained when using the cumulative plastic deformation damage model because it is relatively insensitive to small changes in the yield displacement. This model is also convenient because it does not require estimates of the column's force-displacement relationship.

ACKNOWLEDGMENTS

This work was supported in part by the Earthquake Engineering Research Centers Program of the National Science Foundation under award number EEC-9701568 through the Pacific Earthquake Engineering Research Center (PEER).

Any opinions, findings, and conclusions or recommendations expressed in this material are those of the author(s) and do not necessarily reflect those of the National Science Foundation.

Additional support was provided by the Washington State Department of Transportation. The authors would also like to acknowledge the many people who helped in the testing and analyses of the test specimens, including: Paul Barr, Mike Berry, Kylee Zimmer, Greg Banks, Eric Huang, Zak Griffith, Jubum Kim, Myles Parrish, and Jim Pedersen. WSDOT engineers C. Ruth and H. Zhang provided valuable assistance in developing the column prototype.

CONTENTS

ABSTRACT	iii
ACKNOWLEDGMENTS	iv
CONTENTS	v
LIST OF FIGURES	ix
LIST OF TABLES	xiii
1 INTRODUCTION	1
1.1 Previous Studies of Damage Accumulation.....	1
1.2 Objectives.....	2
1.3 Report Organization.....	2
2 EXPERIMENTAL PROGRAM	5
2.1 Development of 1960s' Column Prototype.....	5
2.2 Description of Test Columns.....	8
2.3 Material Properties.....	10
2.4 Testing Procedure.....	12
2.5 Instrumentation.....	17
3 MEASURED FORCE-DISPLACEMENT RESPONSE	21
3.1 Lateral-Load Response.....	21
3.2 Axial Load.....	25
3.3 Yield Displacement.....	27
3.4 Strain Penetration.....	28
4 CALCULATED FORCE-DISPLACEMENT ENVELOPES	31
4.1 Overview of Modeling Methodology.....	31
4.2 Contribution of Flexural Deformations.....	32
4.3 Contribution of Shear Deformations.....	33
4.4 Contribution of Anchorage-Slip Deformations.....	33
4.5 Yield Displacement.....	35
4.6 Elastic Modulus.....	36
4.7 Stiffness Calculations.....	37
4.8 Strength Calculations.....	39
4.9 Strength Degradation.....	40

4.10	Discussion	43
5	OBSERVED DAMAGE.....	45
5.1	First Yield of Longitudinal Reinforcement.....	46
5.2	Significant Flexural Cracking	47
5.3	Residual Cracking	48
5.4	Significant Spalling.....	49
5.5	Longitudinal Bar Buckling.....	50
5.6	Hoop Fracture.....	51
5.7	20% Loss of Lateral Load	52
5.8	50% Loss of Lateral Load	52
5.9	Loss of Axial-Load Capacity	53
6	EFFECT OF CYCLING ON COLUMN DAMAGE	55
6.1	Park-Ang Damage Model	55
6.2	Cumulative Plastic Deformation Damage Model	56
6.3	Model Calibration	58
6.3.1	Least-Squares Approximation.....	58
6.3.2	Maximum Likelihood Approximation	59
6.3.3	Exterior Penalty Function Approximation.....	62
6.3.4	Illustrative Example	64
6.4	Reported Parameters	66
6.5	First Yield of Longitudinal Reinforcement.....	68
6.6	Significant Flexural Cracking	71
6.7	Residual Cracking	73
6.8	Significant Spalling.....	75
6.9	Onset of Bar Buckling.....	77
6.10	Hoop Fracture.....	79
6.11	20% Loss of Lateral Load	81
6.12	50% Loss of Lateral Load	83
6.13	Loss of Axial Load.....	85
6.14	Discussion	89
6.14.1	Comparison of Damage Models	89
6.14.2	Calibration Method Comparison.....	90

6.14.3	Calibration Results Comparison	91
7	CONCLUSIONS AND RECOMMENDATIONS	93
7.1	Measured Force-Displacement Response	93
7.2	Force-Displacement Modeling.....	94
7.3	Evaluation of Damage Models.....	95
7.4	Suggestions for Further Research	95
	REFERENCES.....	97
	APPENDIX A EXPERIMENTAL PROGRAM	101
A.1	Description of Test Columns	101
A.1.1	Prototype	101
A.1.2	Column Geometry and Reinforcement	102
A.1.3	Footing Geometry and Reinforcement.....	103
A.1.4	Hammerhead Geometry and Reinforcement.....	105
A.2	Materials.....	106
A.2.1	Concrete	106
A.2.2	Longitudinal Steel	108
A.2.3	Hoop Steel.....	110
A.3	Testing Procedure.....	111
A.3.1	Loading Setup	111
A.3.2	Components	111
A.3.3	Axial Load.....	113
A.3.4	Lateral Load	113
A.3.5	Internal Instrumentation.....	114
A.3.6	External Instrumentation.....	116
A.3.7	Displacement Histories	120
A.3.8	Data Acquisition	124
	APPENDIX B INSTRUMENT HISTORIES (COLUMNS S3, C2, C4, AND C3R)	127
B.1	Column S3.....	133
B.2	Column C2	144
B.3	Column C4.....	155
B.4	Column C3R	166
	APPENDIX C INSTRUMENT HISTORIES (COLUMNS S1 AND S15)	177

C.1	Column S1.....	178
C.2	Column S15.....	180
APPENDIX D MATERIAL MODELS		183
D.1	Modified Burns-Seiss Steel Model	183
D.2	Mander, Priestley, and Park (1988) Concrete Model.....	184
D.3	Razvi and Saatcioglu (1999) Concrete Model	185
D.4	Lehman Two-Component Bond Stress Model Calibration.....	188
APPENDIX E CALIBRATED PARK-ANG DAMAGE MODEL		195

LIST OF FIGURES

Fig. 2.1	Test column geometry and reinforcement.....	9
Fig. 2.2	Test setup	12
Fig. 2.3	Displacement histories	15
Fig. 2.4	Rotational and shear deformation potentiometers (Columns S3, C2, C4, and C3R)....	18
Fig. 2.5	Translational displacement potentiometers (all columns).....	19
Fig. 2.6	Layout of strain gages (Columns S3, C2, C4 and C3R)	20
Fig. 3.1	Column force-deformation responses (Columns S1, S3, S15, C2, C4, C3R).....	22
Fig. 3.2	Column force-deformation envelopes (to 4%-drift ratio)	25
Fig. 3.3	Axial load versus horizontal displacement histories	26
Fig. 3.4	Column C2 strain penetration at increments of initial yield displacement	29
Fig. 4.1	Bond stress model and stress-strain relationship	33
Fig. 4.2	Measured and calculated force-displacement envelopes for measured amount of transverse reinforcement	38
Fig. 4.3	Measured and calculated force-displacement envelopes for three times the measured transverse reinforcement.....	42
Fig. 5.1	First yield of longitudinal reinforcement (Column C2)	46
Fig. 5.2	Significant flexural cracking (Column S15)	47
Fig. 5.3	Residual cracking (Column S15)	48
Fig. 5.4	Significant spalling (Column S1).....	49
Fig. 5.5	Onset of longitudinal bar buckling (vertical cracking) (from Column C3R).....	50
Fig. 5.6	Observed bar buckling (from Column C3R).....	51
Fig. 5.7	Loss of axial-load capacity; (a) flexure-shear failure (from Column C2); (b) flexure failure (from Column C4)	53
Fig. 6.1	Schematic for maximum likelihood method.....	60
Fig. 6.2	Schematic for penalty function method	62
Fig. 6.3	Illustration of weighted exterior penalty function.....	64
Fig. 6.4	Example showing differences in calibration methods ($\gamma = 20$).....	65
Fig. 6.5	Illustration of reported parameters for each damage state	67
Fig. 6.6	First yield for (a) Park-Ang and (b) modified Park-Ang damage models	70

Fig. 6.7	Significant flexural cracking for (a) modified Park-Ang and (b) cumulative plastic deformation	72
Fig. 6.8	Residual cracking for the (a) modified Park-Ang and (b) cumulative plastic deformation	74
Fig. 6.9	Significant spalling for (a) modified Park-Ang and (b) cumulative plastic deformation	76
Fig. 6.10	Bar buckling for the (a) modified Park-Ang and (b) cumulative plastic deformation	78
Fig. 6.11	Hoop fracture for the (a) modified Park-Ang and (b) cumulative plastic deformation	80
Fig. 6.12	20% loss of lateral load for the (a) modified Park-Ang and (b) cumulative plastic deformation	82
Fig. 6.13	50% loss of lateral load for the (a) modified Park-Ang and (b) cumulative plastic deformation	84
Fig. 6.14	Loss of axial load for the (a) modified Park-Ang and (b) cumulative plastic deformation (all columns)	86
Fig. 6.15	Loss of axial load for the (a) modified Park-Ang and (b) cumulative plastic deformation (excluding Column C4)	88
Fig. A.1	Test column geometry and reinforcement.....	103
Fig. A.2	Plan view of footing geometry and reinforcement.....	104
Fig. A.3	Side view of footing geometry and reinforcement.....	104
Fig. A.4	Plan view of hammerhead geometry and reinforcement.....	105
Fig. A.5	Elevation view of hammerhead geometry and reinforcement	105
Fig. A.6	Stress-strain response of longitudinal steel for (a) Columns S3, C2, C4 and C3R, and (b) Columns S1 and S15.....	109
Fig. A.7	Stress-strain response of hoop reinforcing steel.....	110
Fig. A.8	Test setup	112
Fig. A.9	Strain gage layout (Columns S3, C2, C4, and C3R).....	115
Fig. A.10	Rotational and shear potentiometers (Columns S3, C2, C4, and C3R)	116
Fig. A.11	Details of external instrumentation rods (Columns S3, C2, C4, and C3R)	117
Fig. A.12	Potentiometer-bracket assembly	118
Fig. A.13	Translational displacement potentiometers (all columns).....	119

Fig. A.14	Displacement histories (Column S1, S3, S15, C2, C4, and C3R)	122
Fig. B.1	Bar identification letters	132
Fig. B.2	Displacement history for Column S3	133
Fig. B.3	Column S3 data	134
Fig. B.4	Displacement history for Column C2	144
Fig. B.5	Column C2 data	145
Fig. B.6	Displacement history for Column C4	155
Fig. B.7	Column C4 data	156
Fig. B.8	Displacement history for Column C3R	166
Fig. B.9	Column C3R data	167
Fig. C.1	Displacement history for Column S1	178
Fig. C.2	Column S1 data	179
Fig. C.3	Displacement history for Column S15	180
Fig. C.4	Column S15 data	181
Fig. D.1	Burns-Seiss constitutive model for (a) Columns S3, C2, C4 and C3R and (b) Columns S1 and S15	184
Fig. D.2	Lehman two-component bond stress model	188
Fig. D.3	Stress-strain relationship for (a) bilinear model and (b) Burns-Seiss model	190
Fig. D.4	Optimal bond stress coefficient for each level of displacement	192
Fig. D.5	Error as a function of bond stress coefficient, b , for three ratios of b/a	193
Fig. E.1	Park-Ang damage model for first yield of longitudinal reinforcement	195
Fig. E.2	Park-Ang damage model for significant flexural cracking	196
Fig. E.3	Park-Ang damage model for first significant spalling	196
Fig. E.4	Park-Ang damage model for residual cracking	197
Fig. E.5	Park-Ang damage model for bar buckling	197
Fig. E.6	Park-Ang damage model for hoop fracture	198
Fig. E.7	Park-Ang damage model for 20% loss of lateral load	198
Fig. E.8	Park-Ang damage model for 50% loss of lateral load	199
Fig. E.9	Park-Ang damage model for loss of axial load	199

LIST OF TABLES

Table 2.1	WSDOT material specifications for bridge columns (Ruth and Zhang 1999).....	5
Table 2.2	Diameter and tie spacing for typical bridge columns (Ruth and Zhang 1999)	7
Table 2.3	Details of prototype and test columns	8
Table 2.4	Test column names and descriptions.....	10
Table 2.5	Concrete properties at time of testing	11
Table 2.6	Imposed displacement levels.....	13
Table 2.7	Cycle designations.....	13
Table 3.1	Maximum recorded base slip for each column	21
Table 3.2	Key response parameters for each column.....	27
Table 3.3	Measurements from strain gage data and force-displacement curve	28
Table 4.1	Measured and calculated yield displacement.	35
Table 4.2	Elastic moduli.....	36
Table 4.3	Ratios of measured to calculated effective stiffness (K_m/K_c).....	37
Table 4.4	Ratio of measured to calculated effective strengths (F_m/F_c).....	39
Table 4.5	Ratio of measured to calculated effective strength (F_m/F_c) for various longitudinal steel yield stresses	40
Table 4.6	Measured to calculated strength ratios (F_m/F_c) at a drift ratio of 2% for different amounts of transverse reinforcement.....	41
Table 4.7	Mean strength and stiffness ratios.....	43
Table 5.1	Column displacements at first yield of longitudinal reinforcement	46
Table 5.2	Column characteristics at significant flexural cracking	47
Table 5.3	Column characteristics at residual cracking.....	48
Table 5.4	Column characteristics at significant spalling.....	49
Table 5.5	Column characteristics at onset of longitudinal bar buckling	50
Table 5.6	Column characteristics at hoop fracture.....	51
Table 5.7	Column characteristics at 20% loss of lateral-load capacity.....	52
Table 5.8	Column characteristics at 50% loss of lateral-load capacity	52
Table 5.9	Column characteristics at loss of axial-load capacity	53
Table 6.1	Normalization data for Park-Ang damage model.....	56
Table 6.2	Data at first yield of longitudinal reinforcement.....	68

Table 6.3	Model parameters at first yield of longitudinal reinforcement.....	68
Table 6.4	Data at significant flexural cracking	71
Table 6.5	Model parameters at significant flexural cracking	71
Table 6.6	Data at residual cracking	73
Table 6.7	Model parameters at residual cracking.....	73
Table 6.8	Data at significant spalling.....	75
Table 6.9	Model parameters at significant spalling	75
Table 6.10	Data at onset of bar buckling.....	77
Table 6.11	Model parameters at onset of bar buckling	77
Table 6.12	Data at hoop fracture.....	79
Table 6.13	Model parameters at hoop fracture.....	79
Table 6.14	Data at 20% loss of lateral load.....	81
Table 6.15	Model parameters at 20% loss of lateral load	81
Table 6.16	Data at 50% loss of lateral load.....	83
Table 6.17	Model parameters at 50% loss of lateral load	83
Table 6.18	Data at loss of axial load (all columns).....	85
Table 6.19	Model parameters at loss of axial load (all columns).....	85
Table 6.20	Model parameters at loss of axial load (excluding Column C4).....	87
Table 6.21	Effect of cycling on each damage state.....	92
Table A.1	Details of prototype and test columns	102
Table A.2	Concrete mix	106
Table A.3	Development of concrete strength.....	107
Table A.4	Concrete material properties at time of testing	108
Table A.5	Stress-strain data for longitudinal reinforcement.....	110
Table A.6	Displacement levels.....	124
Table A.7	Cycle nomenclature and displacement levels for each column.....	124
Table B.1	Translational potentiometers nomenclature	128
Table B.2	Rotational and shear potentiometer nomenclature	129
Table B.3	Longitudinal reinforcement strain gage nomenclature.....	130
Table B.4	Hoop reinforcement strain gage nomenclature	131
Table B.5	Load cell nomenclature	131
Table C.1	Load cell nomenclature	177

Table C.2	Translational potentiometer nomenclature.....	178
Table D.1	Properties of longitudinal steel.....	184
Table E.1	Effect of cycling on the maximum displacement at each damage state using the Park-Ang damage model.....	200

1 Introduction

The San Andreas fault and the Cascadia subduction zones have the potential to generate large-magnitude earthquakes with long durations. For example, Heaton and Kanamori (1984), and Kramer et al. (1998) estimated that the Cascadia subduction zone could produce earthquakes with durations of several minutes. Such long earthquakes would subject structural components to numerous displacement reversals (Marsh 1994). The impact that a large number of displacement cycles would have on the function and safety of structures is uncertain but might result in extensive damage.

To account for the effects of long-duration earthquakes, engineers need tools to evaluate the effects of repeated cycling on the function and safety of structures. These tools need to be developed not only for the design of new structures but also to evaluate the vulnerability of existing structures that do not meet current seismic requirements. Many bridge columns were built prior to the mid-1970s before codes were modified following the 1971 San Fernando earthquake (Moehle and Eberhard 1999).

This report investigates the impact of displacement history on the progression of damage in circular reinforced concrete columns with low axial loads and low amounts of transverse reinforcement. Such components are among the most vulnerable and critical components of older bridges.

1.1 PREVIOUS STUDIES OF DAMAGE ACCUMULATION

Williams and Sexsmith (1995) provide an overview of indices that have been proposed to quantify the accumulation of structural damage. The various methods all rely on empirical coefficients, the magnitudes of which vary according to the component type. In general, these models have not been calibrated extensively, and in particular, they do not account for the effects of shear.

One of the most commonly used damage indices is the Park-Ang damage index (Park and Ang 1985), the details of which are provided in Chapter 6. This index is a “combined” damage index that takes into account the effects of both maximum deformation and energy dissipated through cyclic loading. Another combined damage index considered in this research is the cumulative plastic deformation damage index. This index takes into account the effects of both maximum deformation and accumulation of plastic deformation. A modified Park-Ang damage index is also evaluated.

1.2 OBJECTIVES

The first objective of the research described in this report was to perform and document tests of six, poorly confined reinforced concrete bridge columns. The columns were nominally identical, but they were subjected to a variety of displacement histories. In all six tests, the force-displacement histories and progression of damage were recorded. In four of the six tests, the moment-rotation and strain histories were also recorded. Such data are needed to evaluate and calibrate existing models, as well as to develop new ones.

The second objective of this research was to use the force-displacement data to evaluate and calibrate the three damage indices mentioned in Section 1.1 for poorly confined reinforced concrete bridge columns. Such models are needed to investigate the effects of long-duration earthquakes on damage accumulation (Price 2000).

1.3 REPORT ORGANIZATION

The design considerations, column geometry, material properties and testing procedure for the experimental program are summarized in Chapter 2, with details provided in Appendix A. Chapter 3 documents the measured force-displacement response, including: lateral-load response, axial-load response, measured yield displacements, and strain penetration. Additional details of the measured responses of these columns are provided in appendices B and C.

Chapter 4 documents the modeling of the force-displacement envelopes of the six columns, including the contributions of flexure, shear, and bond slip. The accuracy of each model is evaluated by comparing the calculated force-displacement envelope with the measured envelope. Mookerjee (1999) and Parrish (2001) provide the details of the analytical procedure. Material models for the steel, concrete, and bond-slip behavior are provided in Appendix D.

The observed damaged progression is described and documented in Chapter 5, including: the cycle at which each damage state was observed to occur and the maximum previous displacement. Photographs of each damage state are also provided in this chapter.

In Chapter 6, three models of damage accumulation and three methods of calibrating the models are introduced. Using these three calibration methods on the three damage models, the effect of cycling on the maximum displacement at the nine damage states is investigated. The last section of this chapter discusses the results predicted by the calibrated damage models.

The conclusions from the report, including recommendations for further research, are provided in Chapter 7.

2 Experimental Program

Six nominally identical columns with reinforcing details typical of 1960s construction were subjected to a variety of displacement histories. This chapter provides the rationale for selecting the prototype column, the properties of the test columns, the testing procedure, and the instrumentation plan. Appendix A provides further details of the program. All tests were performed in the University of Washington Structural Research Laboratory.

2.1 DEVELOPMENT OF 1960S' COLUMN PROTOTYPE

In support of this study, Washington Department of Transportation (WSDOT) engineers C. Ruth and H. Zhang (1999) identified governing material specifications and key properties for typical bridge columns built before the 1970s. Table 2.1 summarizes the evolution of the WSDOT materials specifications since the 1940s.

Table 2.1 WSDOT material specifications for bridge columns (Ruth and Zhang 1999)

Specifications Year	Concrete		Reinforcing Steel		
	Class	f'_c (psi)	Vert. Bar f_y (ksi)	Tie Bar f_y (ksi)	Comment
1948	A	3600	40	40	ASTM A15, Intermediate Grade
1951 (1948 Amend. 1)	A	3600	40	40	ASTM A15, Intermediate Grade
1953 (1948 Amend. 2)	A	3600	40	40	ASTM A15, Intermediate Grade
1957	A	3600	40	40	ASTM A15, Intermediate Grade
1963	AX	4000	40	40	ASTM A15, Intermediate Grade
1966 (1963 Amend. 1)	AX	4000	40	40	ASTM A15, Intermediate Grade
1968 (1963 Amend. 2)	AX	4000	40	40	ASTM A15, Intermediate Grade
1969	AX	4000	40 ¹	40 ²	¹ ASTM A615, Grade per plans ² ASTM A615, Grade 40
1972	AX	4000	40	40	ASTM A615, Grade 40 except as noted on plans
1974	AX	4000	40	40	ASTM A615, Grade 40 except as noted on plans
1977	AX	4000	60 ¹	60 ²	¹ ASTM A615, Grade 60 except as noted on plans ² Spiral tie. ASTM A615, plain bar Grade per plans
1980	AX	4000	60 ¹	60 ²	¹ ASTM A615, Grade 60 except as noted on plans ² Spiral tie. ASTM A615, plain bar Grade per plans

The required concrete compressive strength listed in the specifications was 3600 psi (24.8 MPa) before 1963, at which time it increased to 4000 psi (27.6 MPa). The specified minimum yield strength of the vertical and lateral reinforcement increased from 40 ksi (276 MPa) to 60 ksi (414 MPa) in 1977, although according to C. Ruth, most bridges were likely constructed with grade 60 reinforcement as early as 1974. The 1977 specifications were the first to require the use of continuous spiral reinforcement in reinforced concrete columns. Before then, transverse reinforcement for circular columns typically consisted of individual hoops with lap splices.

Based on the information summarized in Table 2.1, the yield strength of the transverse and longitudinal reinforcement of the prototype (and test column) was selected as 44 ksi (303 MPa), which includes a 10% increase above the specified minimum yield stress of 40 ksi (276 MPa). Similarly, the probable concrete strength was selected as 6000 psi (41.4 MPa), which includes a 50% increase over the specified concrete strength of 4000 psi (27.6 MPa). This increase reflects the effects of long-term strength gain, and the difference between specified and mean strengths.

In their survey of 33 bridges designed from 1957 to 1969, Ruth and Zhang found that the diameter of 212 out of 216 columns (98%) ranged from 4 feet (1220 mm) to 6 feet (1830 mm). As shown in Table 2.2, nearly half of these columns had a diameter of 5 feet (1520 mm). For all column diameters, the lateral reinforcement was nearly always the same, consisting of individual #4 hoops spaced at 12 inches (305 mm). In contrast, the 1993 WSDOT specifications required that all bridge columns with diameters less than or equal to 8 feet (2440 mm) be confined by continuous spirals with a maximum pitch of 3 inches (76 mm) (WSDOT 1993).

Based on the results of the Ruth and Zhang survey, the diameter of the prototype column was selected as 5 feet (1520 mm), and the lateral reinforcement was taken to consist of #4 hoops spaced at 12 inches (305 mm) with a lap splice of 24 inches (610 mm). The minimum cover to the outside of the spiral was assumed to be 1.5 inches (38 mm). The resulting volumetric ratio for the transverse reinforcement (based on the dimensions of the confined core) was 0.12% for the prototype. This amount of transverse reinforcement is far below current requirements. For a column with these dimensions and specified material properties, the 1994 AASHTO LRFD Bridge Design Specifications (AASHTO 1994) requires a minimum spiral reinforcement ratio of at least 0.76% in non-seismic applications and 1.4% in seismic applications.

On the basis of discussions with WSDOT engineers and the column properties reported by Eberhard and Marsh (1997) for their in-situ tests of a three-span bridge, the longitudinal

reinforcement ratio ($\rho_l = A_s/A_g$) of the prototype column was assumed to be 1.0%, where A_s is the total area of longitudinal steel, and A_g is the area of the column cross section. The target axial-load ratio ($P/A_g f'_c$) based on specified properties was set at 10%, where P is the column axial force and f'_c is the compressive strength of the concrete. Because aging was assumed to increase the concrete strength from 4000 (27.6 MPa) to 6000 psi (41.4 MPa), the target axial-load ratio based on probable concrete strength would be 7%.

Table 2.2 Diameter and tie spacing for typical bridge columns (Ruth and Zhang 1999)

Bridge Location.	Year Designed	Year Spec.	Column Diameter				Tie		
			4'-0"	5'-0"	6'-0"	Others	#4 @ 12"	#5 @ 12"	Others
5/810E	1957	1948			3		3		
5/820E	1957	1948			4		2		2
5/820W	1957	1948			4		2		2
5/807	1960	1957			3		3		
5/564	1961	1957		10			10		
5/515	1962	1957			3		3		
5/545N-E	1962	1957	8				8		
5/545W	1962	1957	10				10		
5/545R	1962	1957	7				7		
5/547E-S	1962	1957	2				2		
5/580N-N	1962	1957		1			1		
5/580RNE	1962	1957		3			3		
5/718E	1962	1957			4		4		
5/718W	1962	1957			4		4		
2/5N	1963	1963		3	9	4	10	6	
5/549	1963	1963	1	2			5		
5/584N-W	1963	1963			3		3		
2/7N	1964	1963		6			6		
90/10E-N	1964	1963			4		4		
5/526.1	1965	1963			6			6	
5/533S-E	1965	1963	2				2		
5/533E-N	1965	1963		3			3		
5/537S	1965	1963		5			5		
5/536N-E	1965	1963		20			20		
5/537N-E	1965	1963		3			3		
5/538E-N	1965	1963	9				9		
5/538S-E	1965	1963		3	4		7		
5/538S-W	1965	1963		11			11		
5/538W-N	1965	1963	9				9		
5/539.5	1965	1963	2	5	1		8		
6/624	1965	1963			1		1		
90/43S-C	1969	1968	7	8			15		
90/43S-E	1969	1968	3	16			19		
Totals	--	--	60	99	53	4	202	12	4

The lengths of many bridge columns fall in the range of 20 to 25 feet (6100 to 7620 mm). Based on the assumption that the distance from the footing to the inflection point slightly exceeds half the column length (corresponding to a fully fixed base and an almost fixed top), an

equivalent cantilever length of 15 feet (4570 mm) was selected for the prototype. The resulting aspect ratio for the 5-ft-diameter column was 3.0. Key properties of the prototype and test columns are listed in Table 2.3.

Table 2.3 Details of prototype and test columns

Item	Prototype	Test Column	Remarks
Column Length	15 feet	5 feet	1:3 Scale
Column Diameter	60 in.	20 in.	1:3 Scale
Longitudinal Steel Ratio	$\rho_l = 1.0\%$	$\rho_l = 0.99\%$	Conserved during scaling
Transverse Hoops	No. 4 Grade 40 @ 12-in. spacing	W2.5 wire @ 4-in. spacing	1:3 scale on spacing
Transverse Reinforcement Ratio	$\rho_t = 0.12\%$	$\rho_t = 0.15\%$	Reinf. far below current requirements
Cover to Hoop	1.5 in.	0.57 in.	1:2.6 Scale
Axial Load	$0.07 f'_c A_g$	$0.1 f'_c A_g$	$f'_c =$ actual concrete strength
Maximum Aggregate Size	1 inch ¹	3/8 in.	1:2.7 Scale

2.2 DESCRIPTION OF TEST COLUMNS

The test column geometry and reinforcement, which were nominally identical for all six columns, are shown in Figure 2.1. Each test specimen consisted of a footing, column, and hammerhead (Appendix A). The hammerhead and footing existed solely to assist in performing the test; the hammerhead was designed to transfer loads from the hydraulic actuator to the column, and the footing was designed to anchor the specimen to the laboratory floor.

The column was designed to be an approximately 1/3-scale model of the prototype, so the height of the test column was 5 feet (1524 mm) from the top of the footing to the loading point, and the diameter of the test column was 20 inches (508 mm). The test columns were longitudinally reinforced by ten D16 grade 420 bars, $A_{\text{bar}} = 0.31 \text{ in.}^2$ (200 mm²), to provide a

¹ Maximum course aggregate size specified by AASHTO (1953, 1961 and 1965)

longitudinal reinforcement ratio, $\rho_l = 0.99\%$. This soft metric rebar satisfied the requirements for No. 5 grade 60 standard rebar. Other key properties of the test columns are listed in Table 2.3.

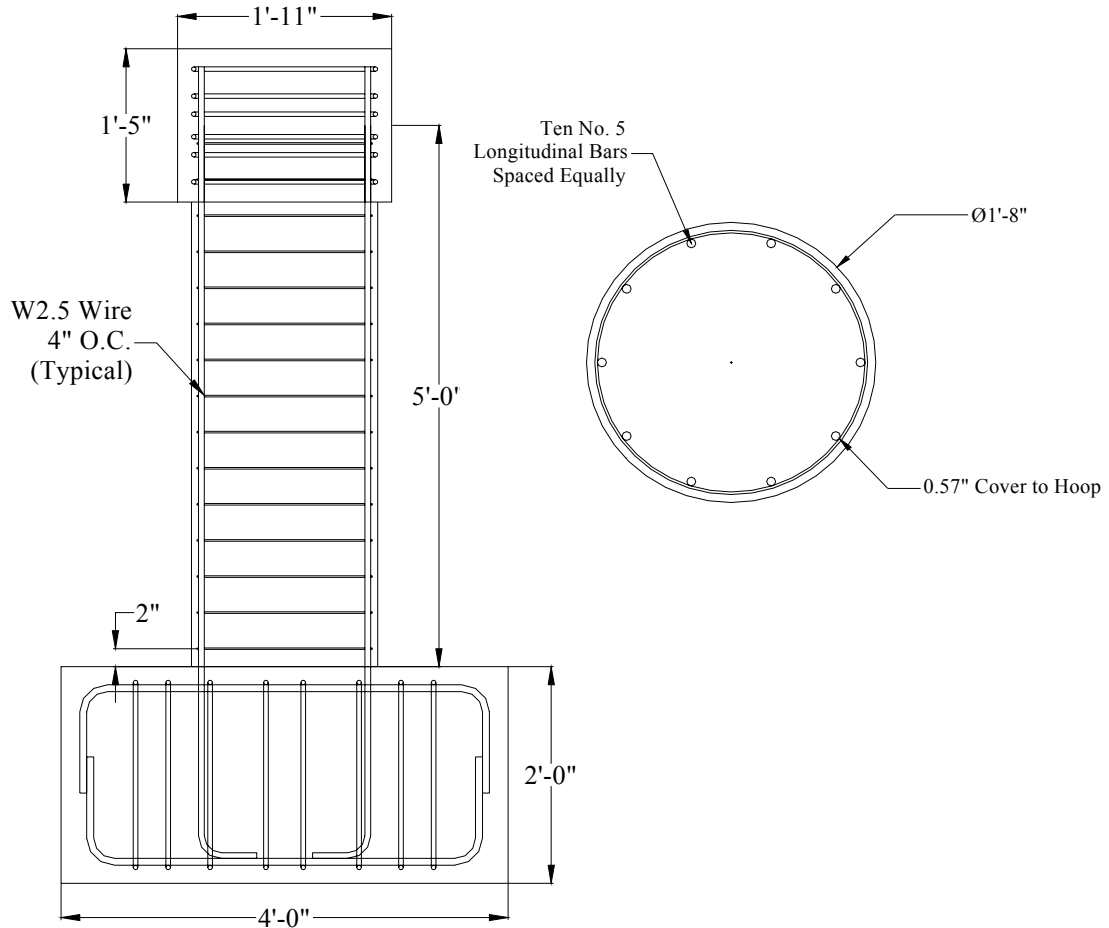


Fig. 2.1 Test column geometry and reinforcement

Some parameters of the prototype column could not be proportioned to satisfy the scaling requirement exactly. For example, the prototype columns were reinforced transversely by #4 bars with $f_y = 64$ ksi (441 MPa). Direct scaling for the test columns would have required a deformed bar diameter of 1/6 in. (4.2 mm) but such material was not available. The closest material that could be found was W2.5 wire with $f_y \leq 80$ ksi (552 MPa) at 4 in. (102 mm) center-to-center. This arrangement preserved the 1:3 scale for the hoop spacing, but the transverse reinforcement ratio of 0.15% exceeded that of the prototype by 25%, and the yield force was 45% too large. Nonetheless, the amount of reinforcement still represented only a fraction of that

required currently (Section 2.1). In addition, W2.5 wire was commercially available only as smooth wire; smooth W2.5 wire undoubtedly had worse bond properties than would be provided by a No. 4 bar. Concrete cover and aggregate diameter were scaled to the nearest readily available dimension.

The name of each test column corresponds to the displacement history to which it was subjected. The column designations and an explanation for how each column was named are presented in Table 2.4. A more detailed description of the displacement history of each column is provided in Section 2.4.

Table 2.4 Test column names and descriptions

Column Name	Description
S1	1 standard cycle between each displacement level, with the displacement incremented each half cycle, until failure
S3	3 standard cycles at each displacement level until failure
S15	15 standard cycles between each displacement level, with the displacement incremented each half cycle, until failure
C2	Constant amplitude cycling at a drift ratio of 2%
C4	Constant amplitude cycling at a drift ratio of 4%
C3R	Constant amplitude cycling at a drift ratio of 3%, followed by a decrease in the amplitude of cycling.

2.3 MATERIAL PROPERTIES

The concrete mix was designed to approximate the current strength of the prototype columns. Appendix A provides details of the concrete mix. The maximum aggregate size in the concrete was 3/8 inch (9.53 mm), the water/total cementitious material ratio was 0.34, and the target slump was 8 inches (203 mm).

The six specimens were cast in four pours (two for footings, and two for the columns and hammerheads, as documented in Table A.3) inside the Structures Laboratory at the University of Washington. Concrete cylinders were stored in the laboratory fog room until they were to be tested. Compressive strength values (f'_c), split tensile strength values (f'_{ct}), and modulus of elasticity values (E_c) of each specimen are listed in Table 2.5.

Nearly all material property tests were conducted within two days of column testing. There were three exceptions; the tensile strength of the concrete used in the footing of Column S1 was not tested, the elastic moduli for Columns S1 and S15 were both determined from tests

conducted on the day of testing of Column S15, and compression tests for Column C3R were conducted approximately three weeks after testing.

Table 2.5 Concrete properties at time of testing

Column Designation	Footing			Age at Test (days)	Column		
	f'_c (psi)	f_{ct} (psi)	E_c (ksi)		f'_c (psi)	f_{ct} (psi)	E_c (ksi)
S1	6320	NA	5480	16	5270	520	4720
S3	4910	470	3260	159	8150	630	4090
S15	6390	580	5480	26	5870	550	4720
C2	4920	370	3610	199	8260	620	4270
C4	5010	430	3280	188	8170	540	4040
C3R	5080	430	3530	220	7640	600	4930

The average compressive strength of the concrete used in the first four columns (S3, C2, C4, and C3R) at the time of testing was 8050 psi (55.5 MPa), which exceeded the target strength of 6,000 psi (41.4 MPa). Part of this difference may have been attributable to the approximately six-month period of strength gain between casting and testing. The last two columns (S1 and S15) were tested within 28 days of casting, which resulted in strengths that were nearer the target values.

The No. 16 grade 420 longitudinal steel for the first four columns was selected from a single batch of steel. Tensile tests of the longitudinal steel indicated that the average yield strength was 66 ksi (455 MPa) and the ultimate strength was approximately 105 ksi (724 MPa). Testing of W2.5 smooth wire used for the hoop reinforcing steel gave a yield stress of approximately 60 ksi (414 MPa) and an ultimate strength of approximately 66 ksi (455 MPa). These values are more representative of grade 60 steel than grade 40 steel, although the yield stress for grade 40 steel often greatly exceeds its minimum. For example, Eberhard and Marsh (1997) found that the mean yield strength for 40 grade longitudinal reinforcement in their test bridge was closer to 60 ksi (414 MPa).

2.4 TESTING PROCEDURE

The test setup (Fig. 2.2) was designed to impose transverse cyclic displacements to a column, while the axial load was held approximately constant. Each test had a unique displacement history.

The column bases were anchored to the floor using two high-strength rods stressed to approximately 125 kips (556 kN) each (the force in the rods was measured for all columns except S3). Axial loads of approximately 256 kips (1140 kN) for the first four columns tested (S3, C2, C4, and C3R) and 180 kips (801 kN) for the last two columns tested (S1 and S15) were applied to each column through a welded steel cross-head placed on top of a spherical bearing; the cross-head was stressed toward the floor by two high-strength rods. Lateral loads were applied to the column hammerhead by a servo-controlled hydraulic actuator spanning between the reaction wall and the column hammerhead.

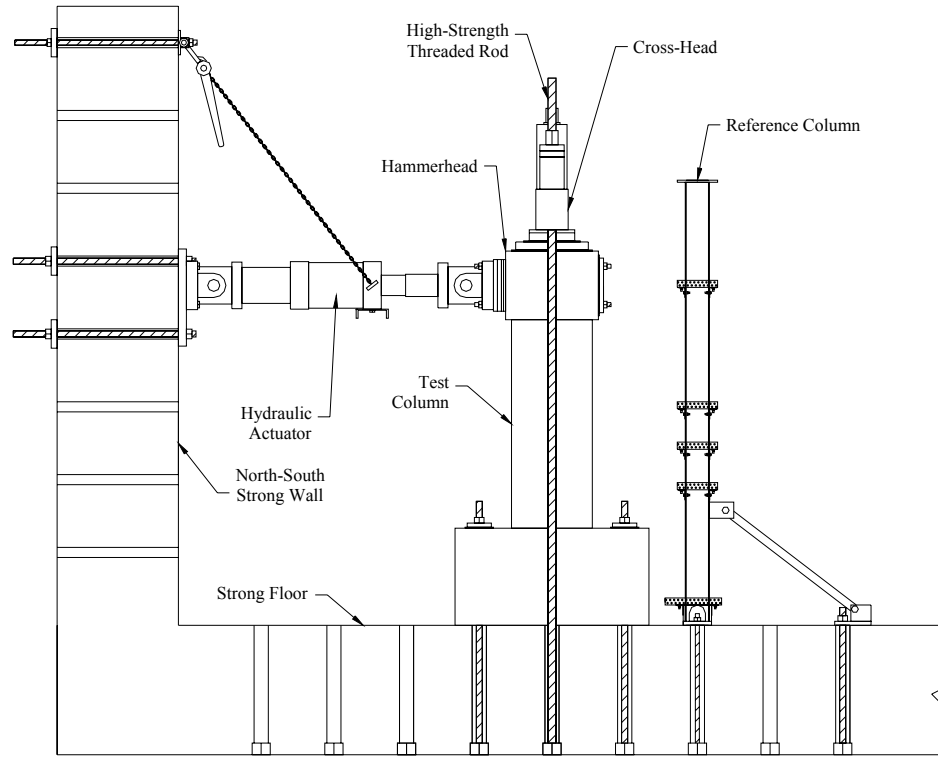


Fig. 2.2 Test setup

Each column was subjected to a unique loading history based on preliminary estimates of the yield displacement (Table 2.6). The loading histories for the six columns are outlined in Table 2.7.

Table 2.6 Imposed displacement levels

Multiple of Estimated Yield Displacement	Displacement (in.)	Drift Ratio (%)
$0.1\Delta_y$	0.02	0.04
$0.2\Delta_y$	0.04	0.07
$0.7\Delta_y$	0.16	0.27
$1.25\Delta_y$	0.29	0.48
$2\Delta_y$	0.46	0.77
$3\Delta_y$	0.69	1.15
$5\Delta_y$	1.14	1.90
$8\Delta_y$	1.83	3.05
$10\Delta_y$	2.29	3.82
$12\Delta_y$	2.74	4.57
$15\Delta_y$	3.43	5.72

Note: Estimated yield displacement = 0.23 in. Actual yield displacements varied from the estimated due to variations in anchorage slip.

Table 2.7 Cycle designations

Drift Ratio (%)	Cycle Numbers at Each Drift Level					
	Column S1	Column S3	Column S15	Column C2	Column C4	Column C3R
0.04		1				
0.07		2-4		1	1	1
0.27	1	5-7	1-15			
0.48	2	8-10	16-30			
0.77	3	11-13	31-45	2	2	2
1.15	4	14-16	46-60			
1.90	5	17-19	61-75	3-14		13-17
3.05	6	20-22		15-17		3-12
3.82				18	3-12	
4.57		23				
5.72					13	

Columns S3, C2, C4, and C3R were displaced at the cycle designations listed in Table 2.7. Columns S1 and S15 were displaced between the cycle designations in Table 2.7. For example, the first cycle of Column C2 was at a drift ratio of 0.07%. By contrast, the first fifteen cycles of Column S15 were between a drift ratio of 0.07% and 0.27%. The cycling history and naming convention of each of the columns are briefly explained in the following list.

- Column S3 was subjected to a displacement history similar to that used by many other investigations, consisting of sets of three cycles of increasing displacement (S3 stands for standard history, three cycles per set). After Column S3 was subjected to a single cycle at

0.02 inches (0.51 mm) to verify the functioning of the instrumentation, the column was subjected to sets of three cycles at displacement levels corresponding to 0.1 times the estimated displacement at first yield ($0.1\Delta_y$), $0.2\Delta_y$, $0.7\Delta_y$, $1.25\Delta_y$, $2.0\Delta_y$, $3.0\Delta_y$, $5.0\Delta_y$, and $8.0\Delta_y$. The test concluded with a single cycle at $12.0\Delta_y$.

- Column S1 (standard history, one cycle per set) was subjected to one cycle at each of the increments described for Column S3. In addition to the standard cycle, the displacement magnitude was incremented every half cycle at equal logarithmic increments. For example, the ratio between the displacement $2.0\Delta_y$ and $3.0\Delta_y$ is 1.5. Therefore, the half cycle between these levels was increased in amplitude by a factor of $(1.5)^{1/2}$.
- Column S15 (standard history, 15 cycles per set) was subjected to fifteen cycles at each of the increments described for Column S3. Like Column S1, the displacement was incremented every half cycle at equal logarithmic increments. In transitioning from a displacement of $2.0\Delta_y$ to a displacement of $3.0\Delta_y$, every half cycle increased in amplitude by a factor of $(1.5)^{1/30}$.
- Column C2 (constant amplitude cycling at a drift of 1.9%) was subjected to single cycles at drift ratios of 0.27% and 0.77%, followed by 12 cycles at 1.9%, 3 cycles at 3.1%, and finally 1 cycle at 3.8%. This history was chosen to investigate the effect of a large number of cycles at a low-deformation amplitude on the maximum column deformation at failure.
- Column C4 (constant amplitude cycling at a drift of 3.8%) was subjected to single cycles at drift ratios of 0.27% and 0.77% before being subjected to 10 cycles at 3.8%, followed by one cycle at 5.7%. This made it possible to observe large-displacement behavior without subjecting the column to a large number of intermediate cycles.
- Column C3R (constant amplitude cycling at a drift of 3.1%, followed by cycles at reduced amplitude) was subjected to the preliminary cycles at drift ratios of 0.27% and 0.77%, followed by 10 cycles at 3.1%, and 5 cycles at 1.9%. This history demonstrated the effect of imposing cycles of moderate displacement after having imposed larger ones. This history was chosen to investigate the effect of reverse loading of the column on the maximum column deformation at failure.

The imposed displacement histories for each column, corresponding to the descriptions in the above list and outlined in Table 2.7, are shown in Figure 2.3.

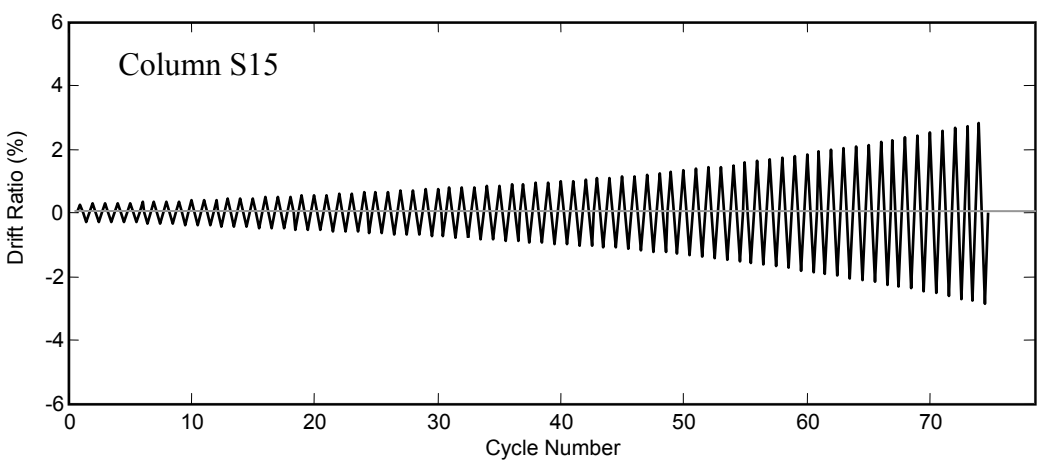
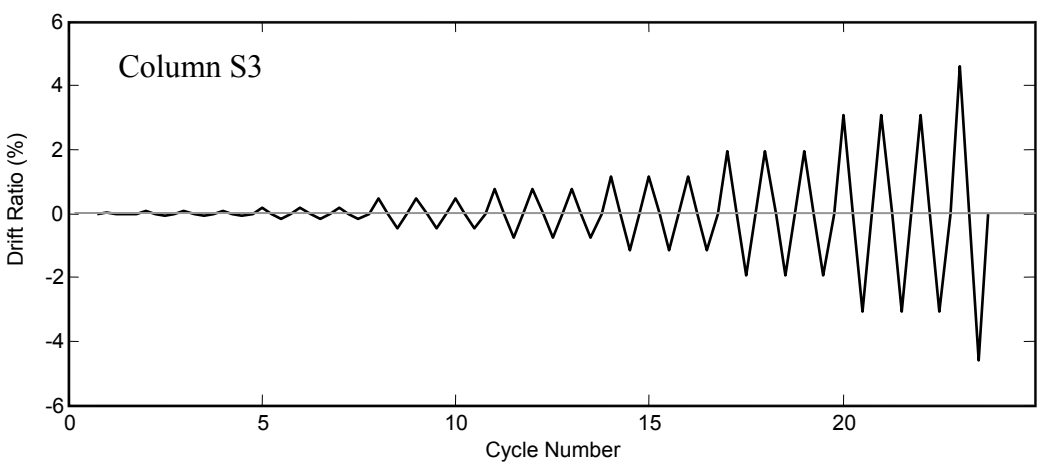
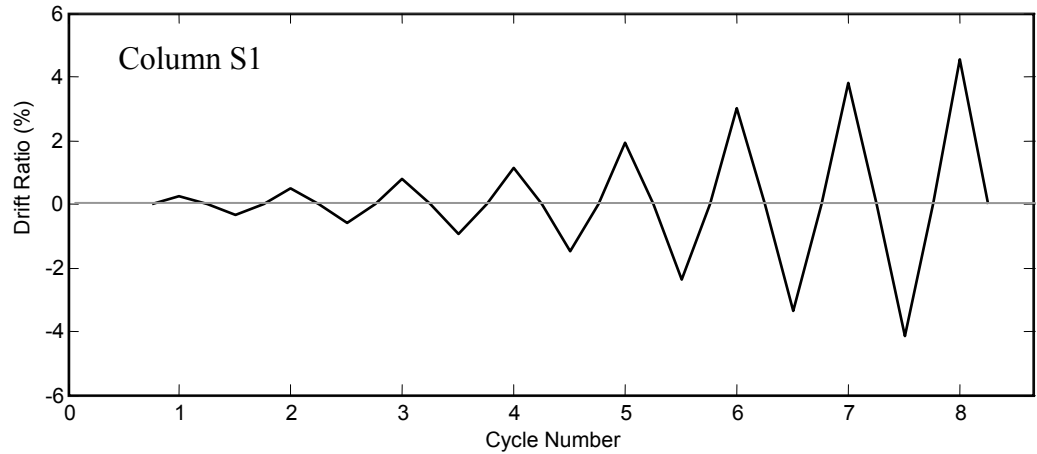


Fig. 2.3 Displacement histories

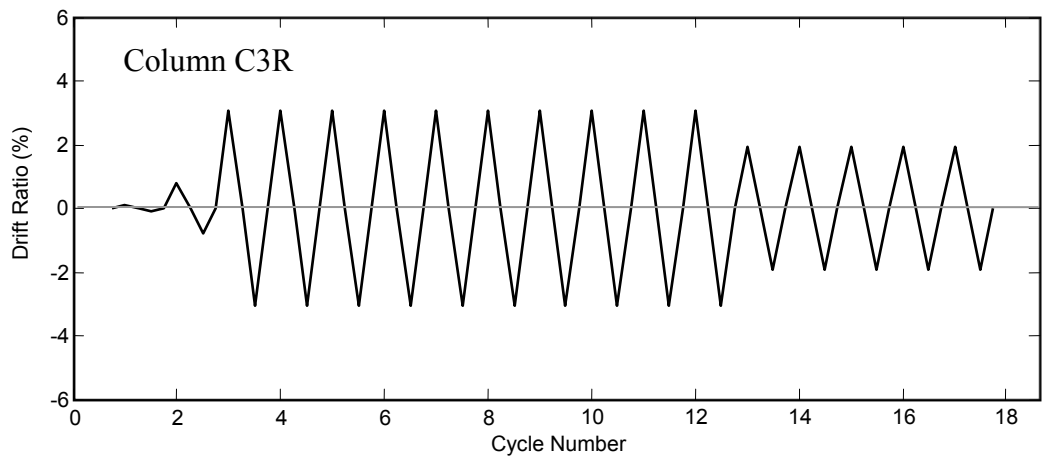
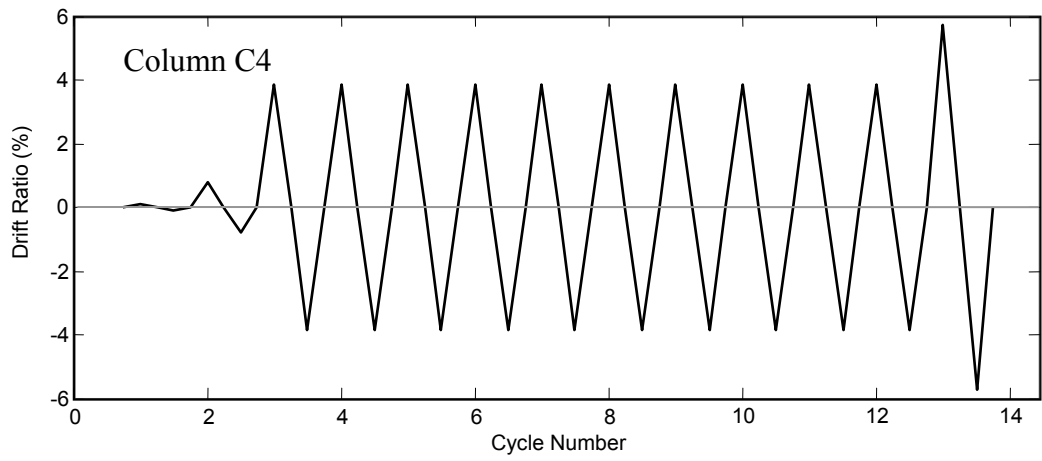
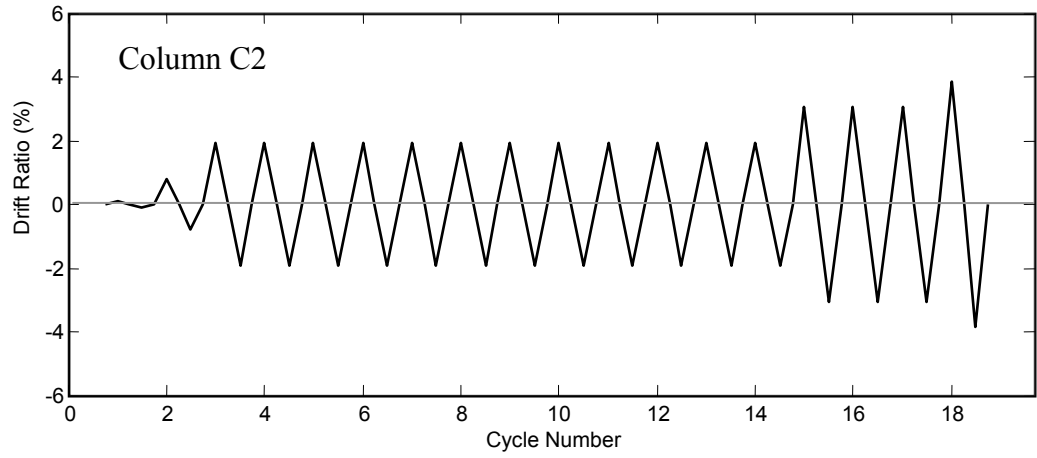


Fig. 2.3 (cont.) Displacement histories

2.5 INSTRUMENTATION

Applied forces, displacements, cross-sectional rotations and reinforcement strains were monitored during the experiments for Columns S3, C2, C4, and C3R. Only applied forces and transverse displacements were monitored for Columns S1 and S15.

Potentiometers were classified into three categories: rotational, shear, and translational displacement potentiometers. The locations of the rotational and shear potentiometers (Columns S3, C2, C4, and C3R) are shown in Figure 2.4. The rotational potentiometers were attached to threaded rods placed through the columns at elevations of 0, 5, 10, 20, and 30 inches (0, 127, 254, 508, and 762 mm), respectively above the top of the footings. These bars were debonded for most of their length to minimize the amount of confinement they provided. The shear potentiometers were attached to smooth rods, attached perpendicular to the instrumentation rods using 90-degree rod connectors, at heights of 0 and 20 inches (0 and 508 mm) from the top of the footing.

The locations of the translational displacement potentiometers (all columns) are shown in Figure 2.5. Displacements were monitored at heights of 10, 20, 30, and 60 inches (254, 508, 762 and 1520 mm) relative to the top of the footing for each test specimen. Additional potentiometers monitored the slip of the base in all but Column S3.

The strain gage layout, which was nominally identical for Columns S3, C2, C4, and C3R, is shown in Figure 2.6. Eight strain gages were placed on each of the two longitudinal bars nearest the front and back faces of the column (bars A and C). In addition, one strain gage was placed on two of the six longitudinal bars that were nearest to the side faces (bars B and D). The hoop steel was instrumented with strain gages at 2, 6, 10, and 18 inches (51, 152, 254, and 457 mm) from the footing-column interface. The strain gage pattern on the hoop steel is also shown in Figure 2.6.

Voltage outputs were processed by a National Instruments data-acquisition system running on a PC-compatible desktop computer. This computer was equipped with LabView software, which read the initial voltage in each channel at the start of the test and converted the voltage changes (relative to these initial voltages) into mechanical units. LabView created separate files for the mechanical output, voltage output, and initial voltages so that mechanical data could be reproduced and verified based on the raw data.

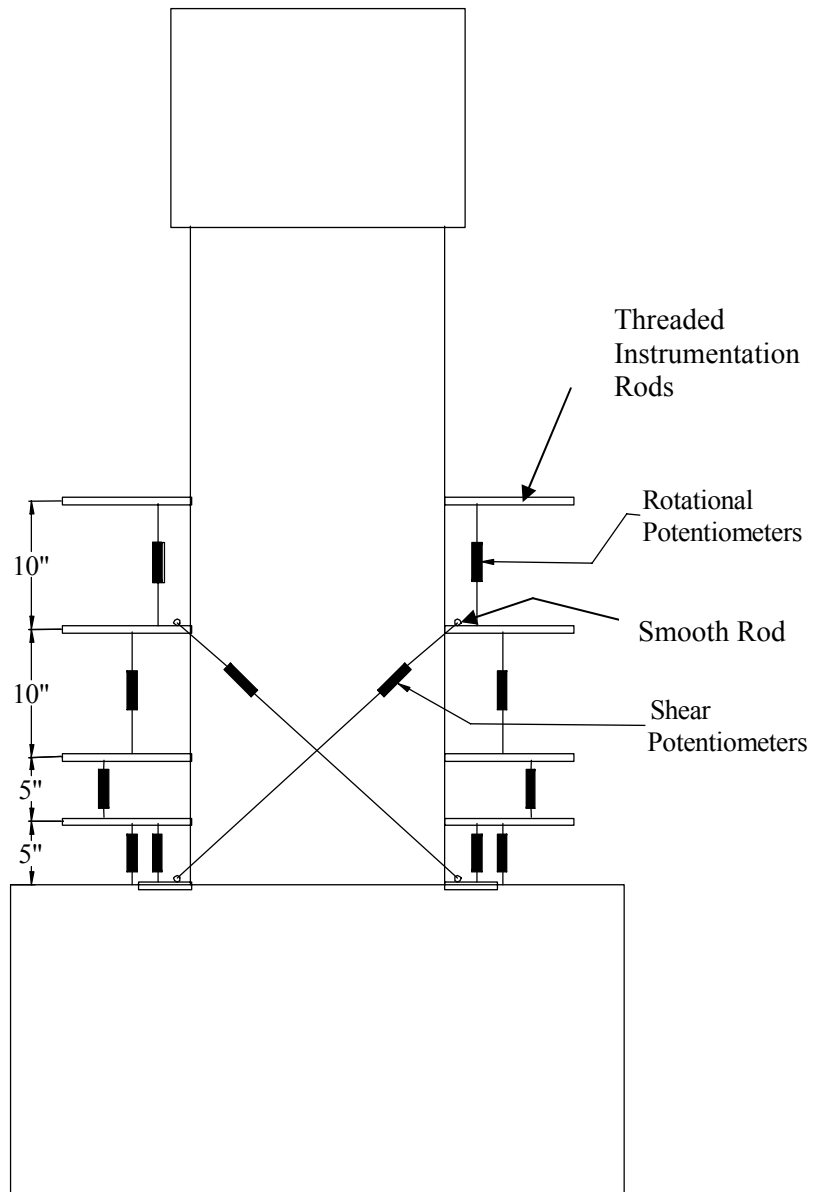


Fig. 2.4 Rotational and shear deformation potentiometers (Columns S3, C2, C4, and C3R)

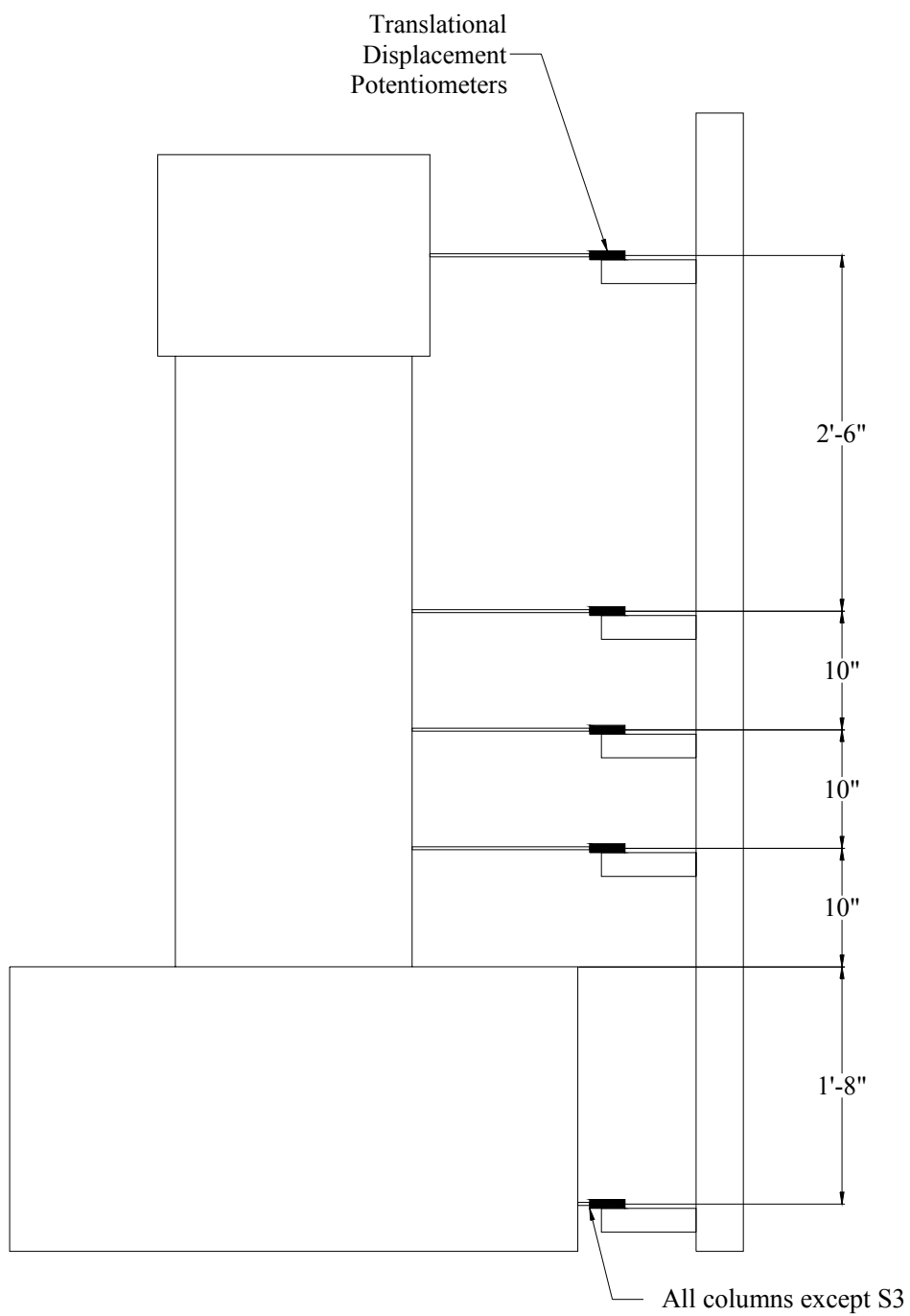


Fig. 2.5 Translational displacement potentiometers (all columns)

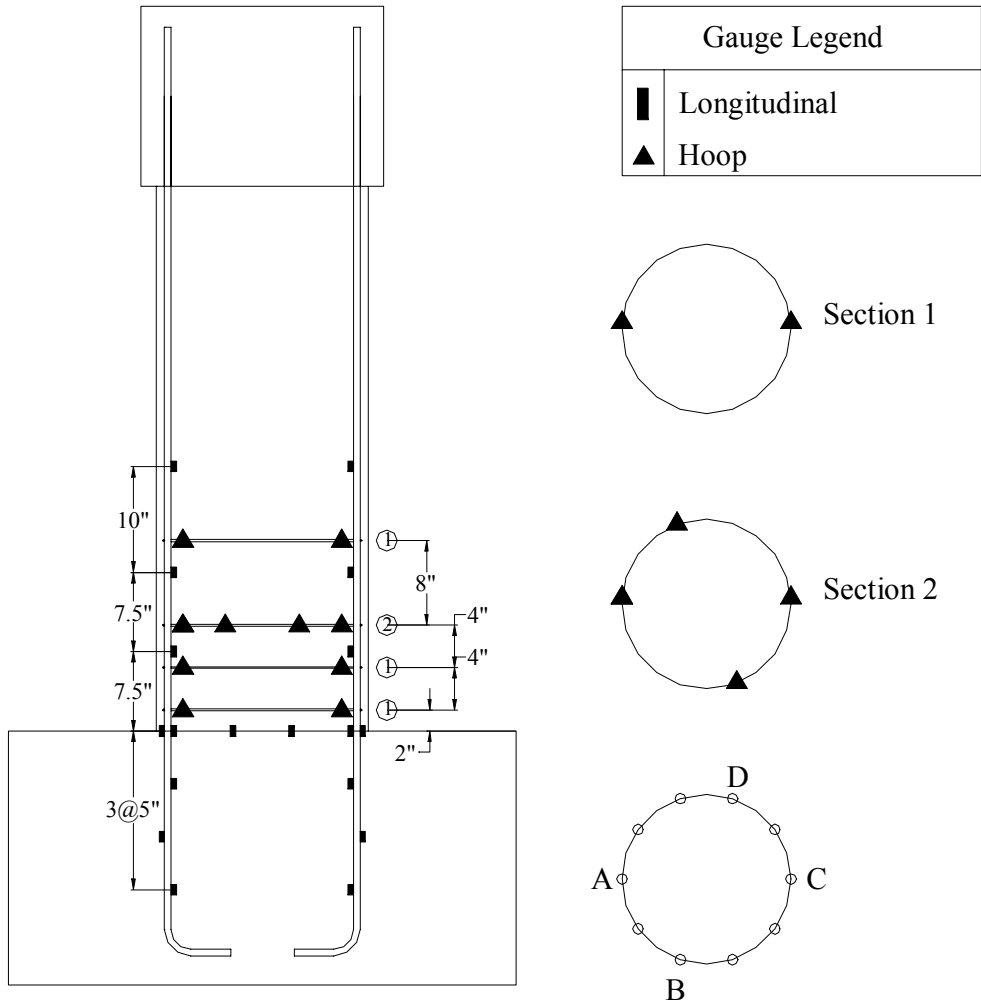


Fig. 2.6 Layout of strain gauges (Columns S3, C2, C4, and C3R)

3 Measured Force-Displacement Response

This chapter documents the lateral and axial force-displacement responses of six circular columns with light transverse reinforcement. For each of these tests, horizontal and vertical loads were measured with load cells at the top of the column. Column displacements were recorded at the base of the column, and at 10, 20, 30, and 60 inches (254, 508, 762, and 1520 mm) above the column base (Fig. 2.5).

3.1 LATERAL-LOAD RESPONSE

The applied lateral loads were measured with a load cell connected to the piston of the 110-kip (489-kN) actuator (Fig. A.8). Column deformations were computed by averaging the top displacements and subtracting the average base slip as follows:

$$Deformation = (Disp60A + Disp60B) / 2 - (DispBaseA + DispBaseB) / 2 \quad (3.1)$$

where $Disp60A$ and $Disp60B$ are the displacements measured by the two reference column potentiometers at the 60-inch (1520-mm) elevation, and $DispBaseA$ and $DispBaseB$ are the displacements measured by the two potentiometers monitoring base slip. The maximum observed values of base slip are listed in Table 3.1. The resulting top effective force-deformation histories for the columns are plotted in Figure 3.1. The effective force corresponds to the base moment divided by the cantilever length (60 in.). The base moment consists of the applied lateral load multiplied by the column height plus the vertical load multiplied by its lever arm (approximately equal to the lateral displacement).

Table 3.1 Maximum recorded base slip for each column

Column	S1	S3	S15	C2	C4	C3R
Maximum Base Slip (in.)	0.005	Not Monitored	0.006	0.006	0.11	0.007

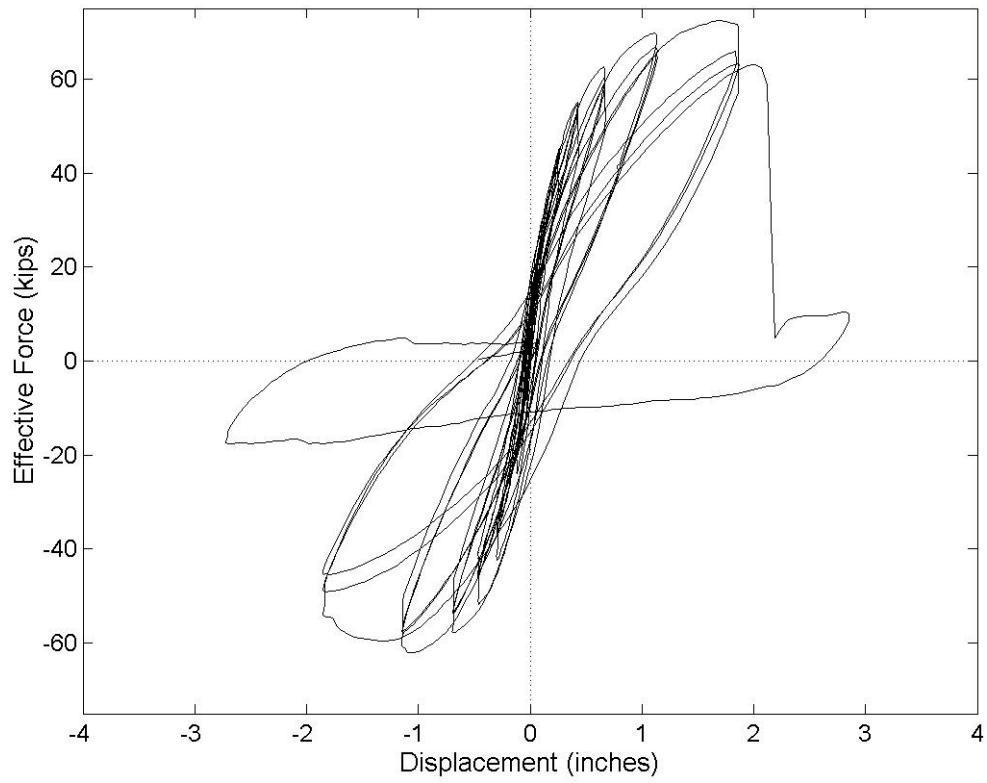
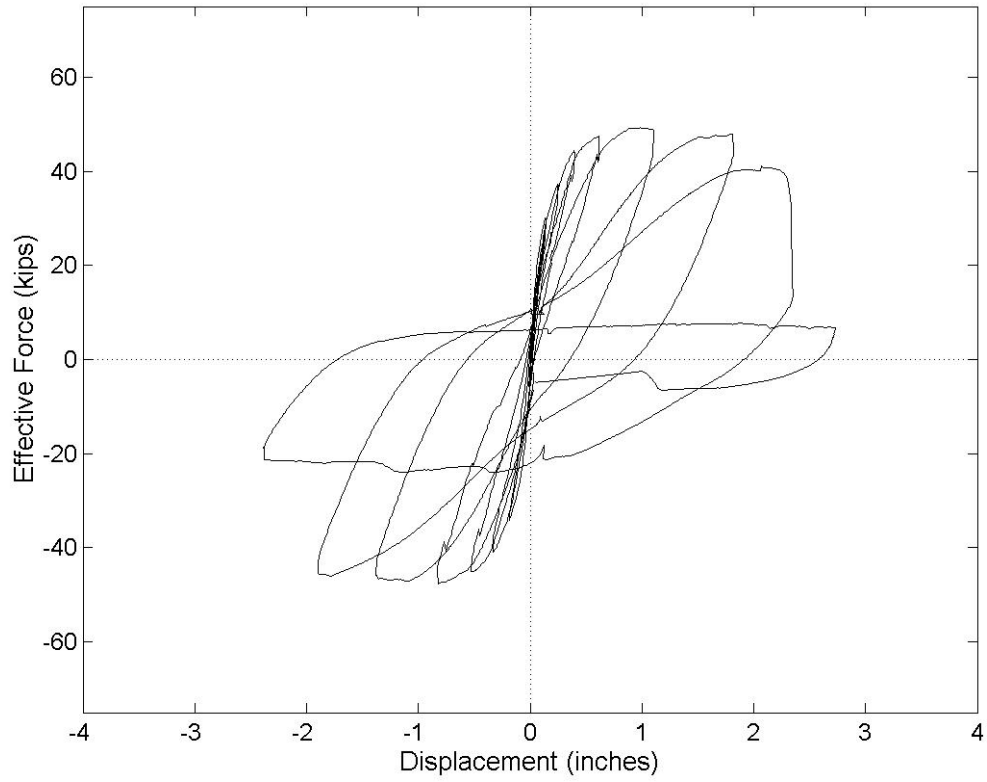


Fig. 3.1 Column force-deformation responses for (a) Column S1 and (b) Column S3

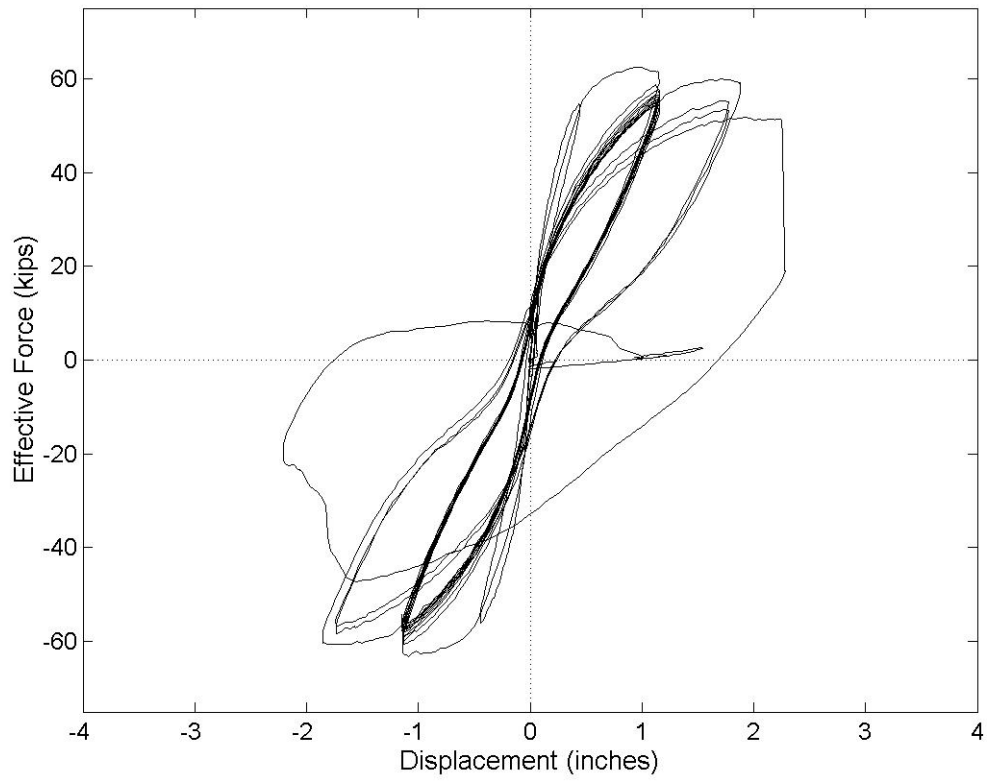
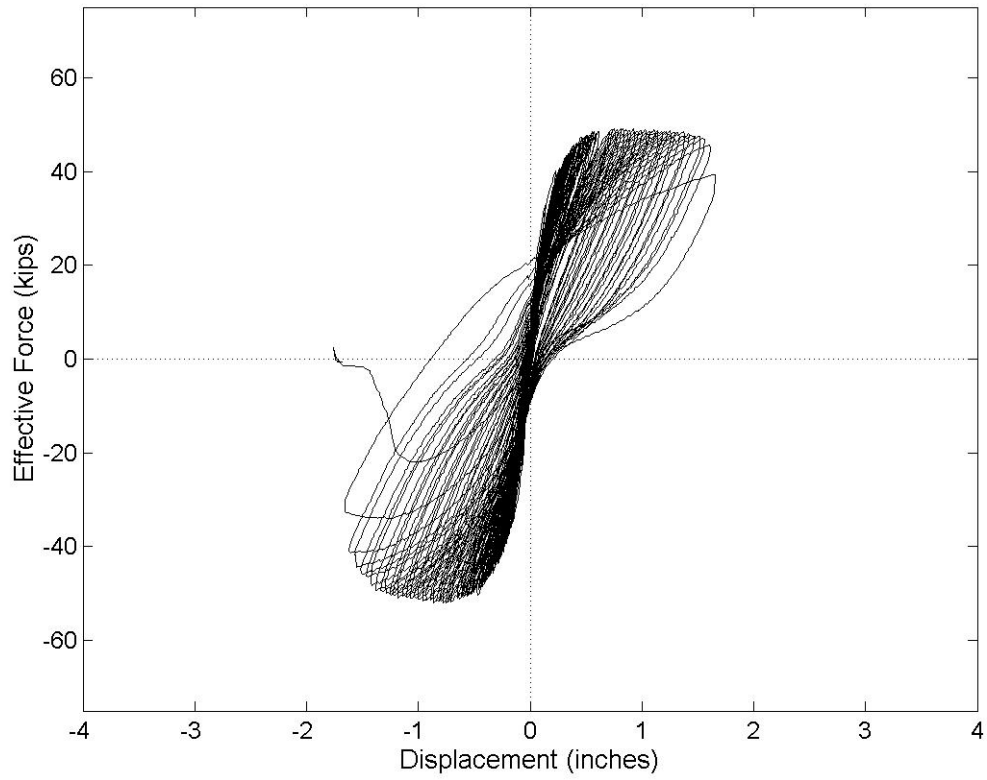


Fig. 3.1 (cont.) Column force-deformation response for (a) Column S15 and (b) Column C2

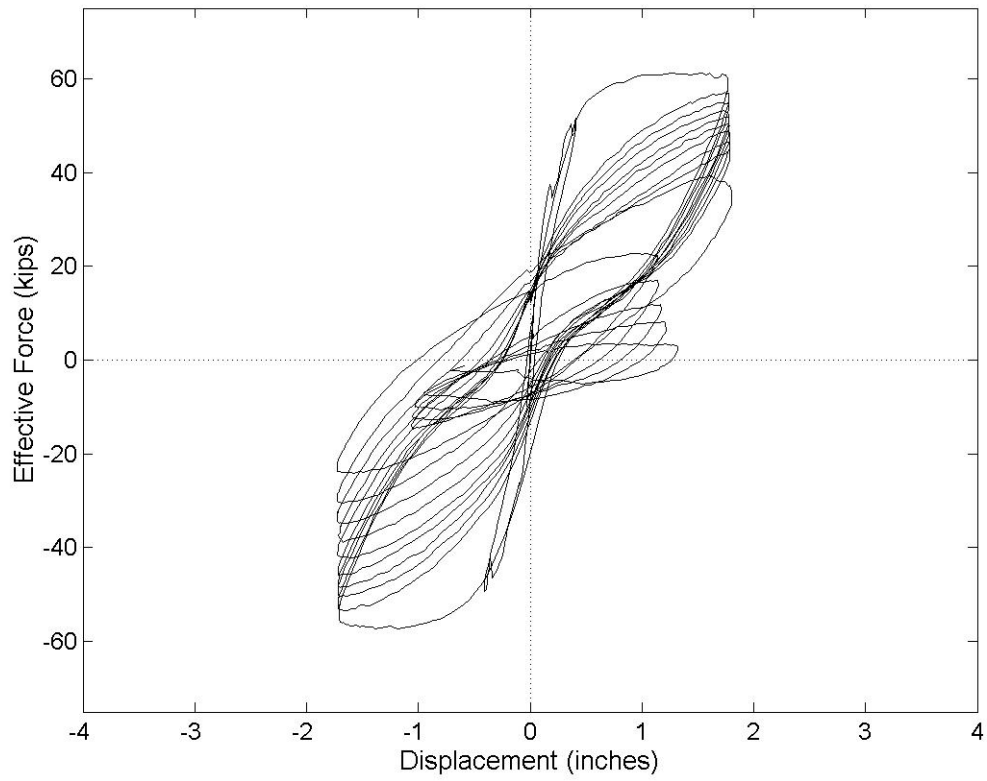
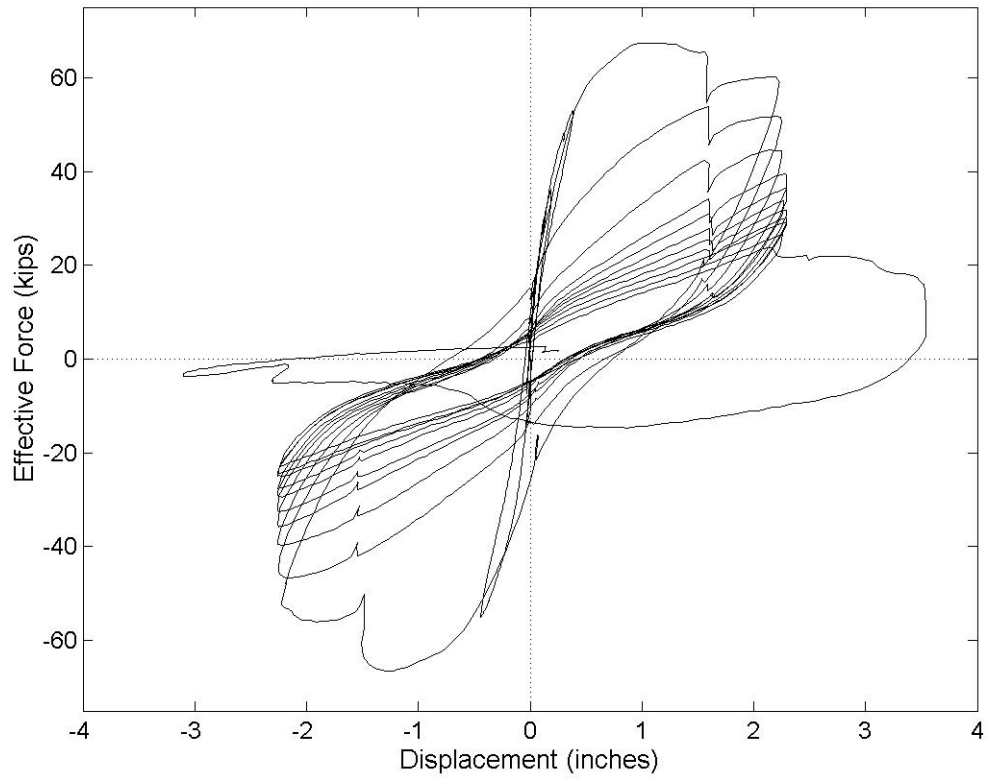


Fig. 3.1 (cont.) Column force-deformation response for (a) Column C4 and (b) Column C3R

The force-deformation envelopes (up to a drift of 4%) for the six columns are shown in Figure 3.2. These envelopes were computed from the histories following an iterative approach developed by Mookerjee (1999). The variations among the envelopes can be attributed in part to differences in load histories and material properties. In addition, the peak lateral forces for Column S3 and Column C4 were higher than for the other columns because at large displacements these columns were subjected to higher axial loads than the other columns. Similarly, Columns S1 and S15, which had lower concrete strengths and axial loads, had lower peak lateral forces.

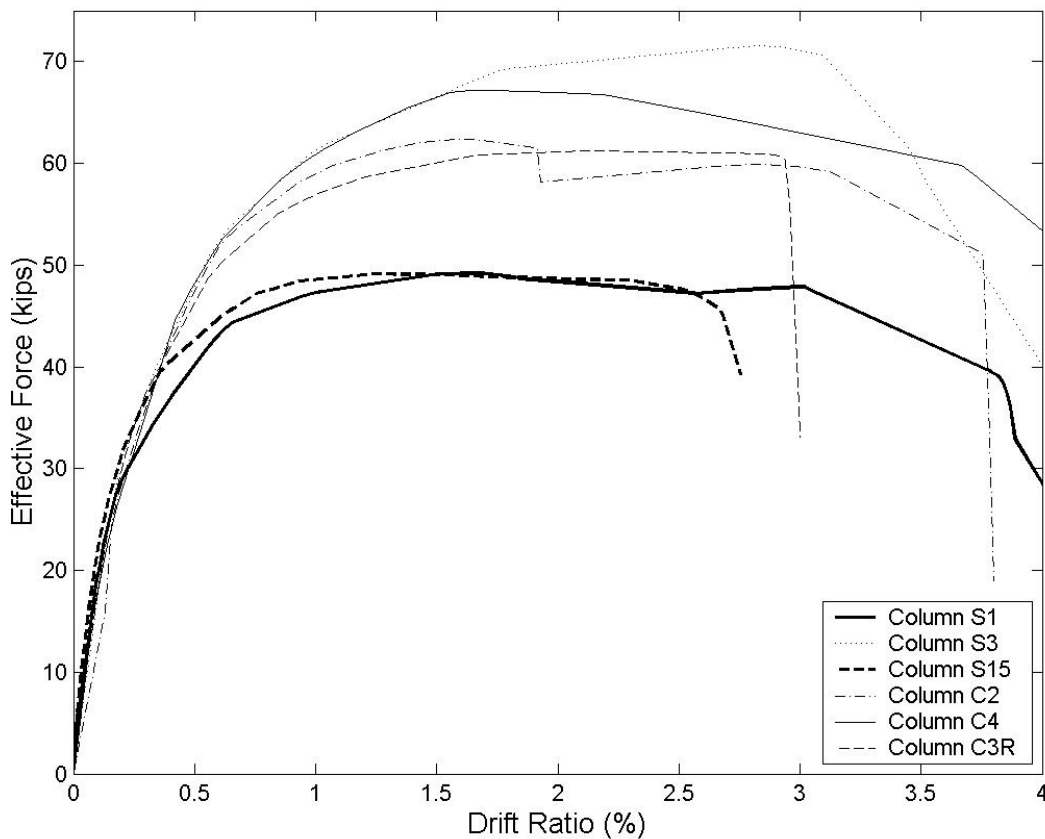


Fig. 3.2 Column force-deformation envelopes (to 4%-drift ratio)

3.2 AXIAL LOAD

The axial load versus horizontal displacement history is shown in Figure 3.3 for each column. When Column S3 was tested, the axial-load cell (Fig. A.8) had been improperly calibrated, causing it to give values slightly lower than the actual axial load. As a result, the initial axial

load was 7.4% higher than the target axial load of 256 kips (1140 kN). In addition, the axial load varied significantly with horizontal displacement during the testing of Column S3. This variation was caused by horizontal displacement of the column, which elongated the rods attached to the axial-load cross-head.

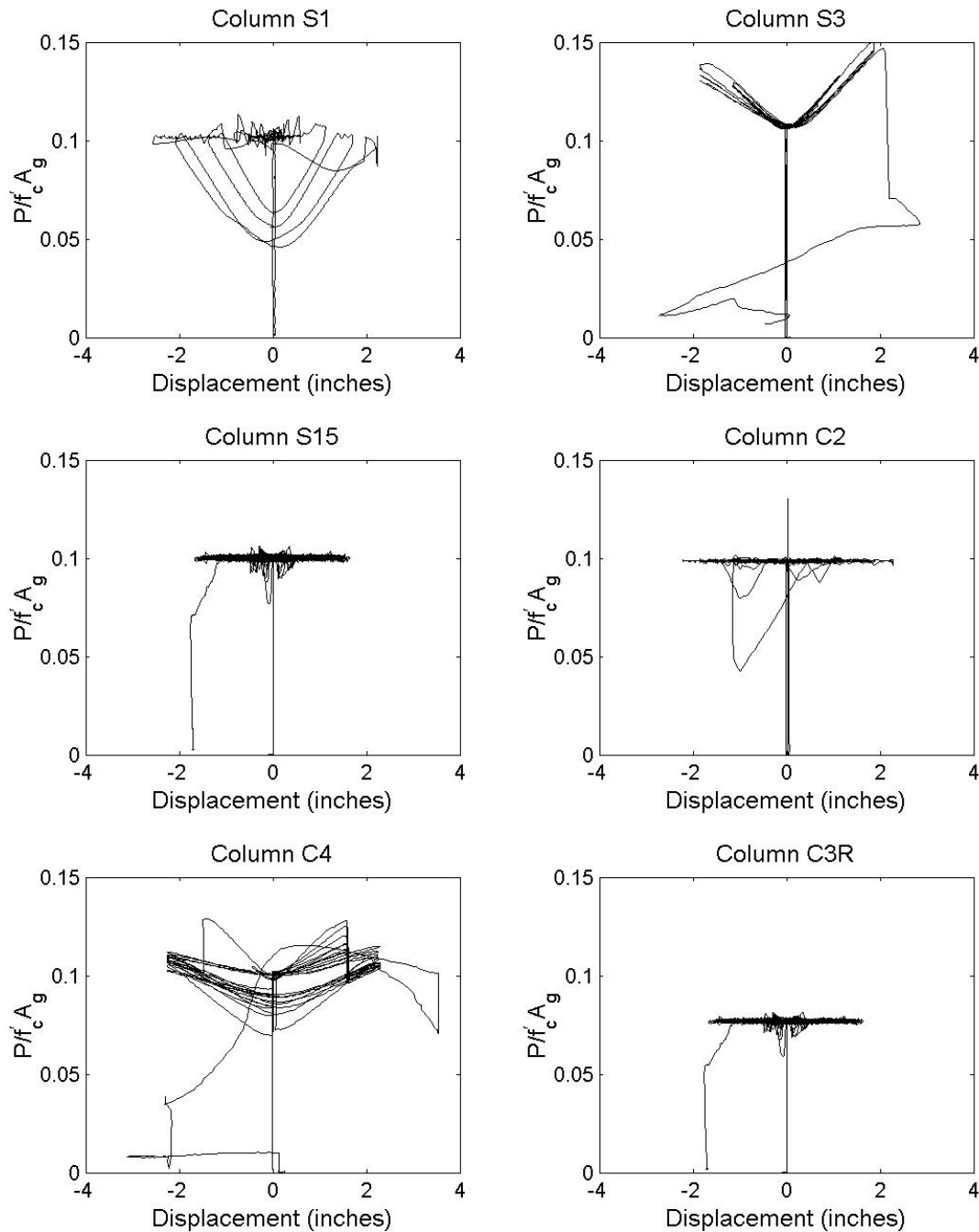


Fig. 3.3 Axial load versus horizontal displacement histories

Column S1 was tested by keeping the axial load the same at the maximum horizontal displacements. Between the peaks, the axial load was not adjusted, resulting in a lower axial load at displacements closer to the zero displacement. Column C4 was tested in the same manner as Column S1, except that the axial load was returned to its initial value halfway between zero and the peak displacement for each phase of the cycle. Because lateral forces decrease with decreased axial load, this approach resulted in simultaneous drops in lateral force as well (Fig. 3.1). For Columns S15, C2, and C3R, the axial load was adjusted continuously.

Table 3.2 shows the initial axial load, initial axial-load ratio, peak lateral force, the data point, and axial load at the peak lateral force, and the axial-load ratio at the peak lateral force. The maximum load applied to the columns never exceeded 15% of $A_g f'_c$, where A_g is the column area and f'_c is the concrete compressive strength on the day of testing.

Table 3.2 Key response parameters for each column

Column	Initial Axial Load, P_i (kips)	$P_i/f'_c A_g$	Peak Lateral Force (kips)	Data Point at Peak Lateral Force	Axial Load at Peak Lateral Force, P_m (kips)	$P_m/f'_c A_g$
S1	168	0.10	48	1088	180	0.11
S3	275	0.11	69	2436	377	0.15
S15	184	0.10	51	8863	188	0.10
C2	256	0.10	62	1458	256	0.10
C4	256	0.10	66	4137	303	0.12
C3R	256	0.11	60	335	260	0.11

3.3 YIELD DISPLACEMENT

The displacement at initial yielding of the longitudinal reinforcement, Δ'_y , is presented in Table 3.3. The initial yield displacement was determined experimentally using two methods:

1. The column displacement at initial yield was determined from the point at which the strain gage at the base of the column reached the yield strain. Such strain measurements were available for Columns S3, C2, C4, and C3R.
2. The initial yield displacement, Δ'_y , was obtained from the measured force-displacement envelope (all columns) based on the calculated moment at initial yield, M'_y (Ch. 4).

Table 3.3 Measurements from strain gage data and force-displacement curve

Column				Based on $\varepsilon = \varepsilon_y$		Based on $M_{base} = M'_y$	
	M'_y Calc. (k-in.)	$M_{0.004}$ Calc. (k-in.)	M'_y (k-in.)	Δ'_y (in.)	Δ_y (in.)	Δ'_y (in.)	Δ_y (in.)
S1	2141	2661	NA	NA	NA	0.22	0.26
S3	2988	3526	3055	0.33	0.39	0.32	0.38
S15	2259	2793	NA	NA	NA	0.19	0.23
C2	2878	3433	2867	0.29	0.35	0.30	0.36
C4	2877	3429	3163	0.37	0.44	0.29	0.35
C3R	2857	3407	2945	0.37	0.44	0.31	0.37

Note: Strain gages were not installed in Columns S1 and S15

As shown in Table 3.3, the initial yield displacements obtained by both methods were similar for each column. The ratio of the two estimates of the initial yield displacement had a mean of 0.91 and a coefficient of variation of 12.8%. Table 3.3 also shows that the measured initial yield displacements were similar for Columns S1 and S15 (~ 0.21 in.) and also for Columns S3, C2, C4, and C3R (~ 0.31 in.). The values observed for these two groups of columns differed significantly. The differences are attributed to strain penetration along the longitudinal reinforcement into the foundation, caused by the presence of the strain gages. The issue is discussed in Section 4.4.

3.4 STRAIN PENETRATION

The installation of strain gages in Columns S3, C2, C4, and C3R made it possible to evaluate the extent of strain penetration into the bases of the columns. For example, Figure 3.4 shows typical strain distributions in the longitudinal reinforcement at various displacement levels. Strain distributions are provided for Column C2 for the range $0.5\Delta'_y$ to $4.0\Delta'_y$ in increments of $0.5\Delta'_y$.

As seen in Figure 3.4, the strain at each gage location increased as the column displacement increased. There is a large jump in the strain measured by the gage at the base of the column between $1.0\Delta'_y$ and $1.5\Delta'_y$.

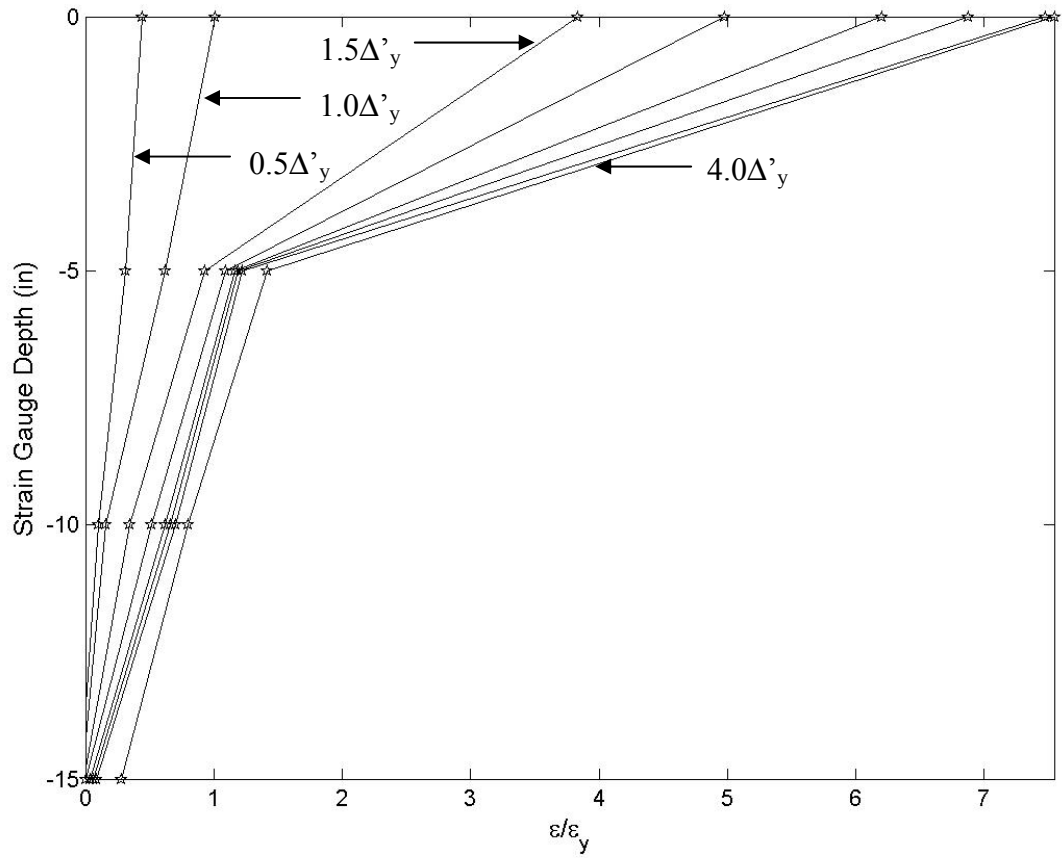


Fig. 3.4 Column C2 strain penetration at increments of initial yield displacement

4 Calculated Force-Displacement Envelopes

Force-displacement envelopes were computed for each of the six test columns using the analytical approach summarized in this chapter. The details of the concrete, steel and bond constitutive models are included in Appendix D. The bond model was developed based on strain measurements in the foundations. The computed envelopes were then compared with the measured envelopes using strength and stiffness ratios.

4.1 OVERVIEW OF MODELING METHODOLOGY

The force-displacement envelopes observed in the laboratory (Fig. 3.2) were compared with the envelopes computed using an approach developed by Mookerjee (1999). The computed envelopes took into account the lateral force and the axial force at each level of column deformation. To account for variations in axial load, a moment-curvature plot was developed at each level of column deformation, using the corresponding axial load.

The ability of each of the force-displacement models to match the measured data was judged quantitatively by the values of two ratios. The first ratio was the maximum measured effective force divided by the maximum force on the calculated force-displacement response (F_m/F_c). The second ratio was the measured effective stiffness divided by the effective stiffness of the calculated force-displacement response (K_m/K_c). The effective stiffness was computed for the force at which the longitudinal steel was predicted to yield by the analysis. The calculated deflections include the contributions of flexural deformations, shear deformations, and anchorage-slip deformations. Mookerjee (1999) provides further details of the analysis methodology.

4.2 CONTRIBUTION OF FLEXURAL DEFORMATIONS

Up to the column's calculated lateral-load capacity, bending moments were calculated at points along the column through statics including P- Δ effects. Curvatures were calculated at each of these points using the moment-curvature relationship for the column cross section. The column deformation was then calculated by integrating these curvatures along the column length.

Beyond the peak lateral load, lateral forces were calculated from the deflections using plastic-hinge and moment-curvature analysis as follows. The plastic-hinge length was calculated using the recommendations of Priestley et al. (1996). Then, for a given deflection, the rotation and curvature within the hinge region were computed. The moment corresponding to this curvature was determined from the moment-curvature analysis, and the effective force was then computed by dividing this moment by the column length.

In performing the moment-curvature analyses, the reinforcing steel stress, f_s , was modeled using the modified Burns and Seiss (1962) constitutive model (Appendix D).

Two constitutive relationships were used to model the concrete behavior: the Mander, Priestley, and Park model (1988) and the Razvi and Saatcioglu model (1999). Both models provide relationships for both confined and unconfined concrete. The details of these models for confined and unconfined concrete are provided in Appendix D. The calculations were repeated for three values of the concrete elastic modulus E_c .

The Mander, Priestley, and Park concrete model (Appendix D), based on an equation previously developed by Popovics (1973), was developed for normal-strength concrete, and recommends the use of Equation 4.4 to compute the elastic modulus, E_c . However, as this equation tends to overestimate the elastic modulus for high-strength concrete, analyses were also performed using E_c values from Equation 4.5 and the measured values from laboratory tests.

In response to evidence that existing concrete models had shortcomings in predicting the behavior of high-strength concrete, Razvi and Saatcioglu (1999) proposed a method to model both high-strength and normal-strength concrete. As with the Mander, Priestley, and Park model, the basic equation is based on the Popovics (1973) equation. This model recommends the use of Equation 4.5 to compute E_c , and therefore, the analysis was not performed with Equation 4.4.

To determine the performance of the models in matching the measured force-displacement envelopes, the ratios of the measured stiffness to the calculated stiffness (Section

4.7), and the ratios of the measured strength to the calculated strength (Section 4.8), were compared for both concrete models, using all values of the elastic modulus. In addition, the measured and calculated strength degradation are compared in Section 4.9.

4.3 CONTRIBUTION OF SHEAR DEFORMATIONS

The column shear deformation, Δ_{shear} , was calculated using the elastic equation:

$$\Delta_{shear} = \frac{kFl}{GA_g} \quad (4.1)$$

where $k = 4/3$ for circular columns, F = the applied lateral force, l = the column length, A_g = the gross cross-sectional area, and G = the shear modulus of concrete.

4.4 CONTRIBUTION OF ANCHORAGE-SLIP DEFORMATIONS

Anchorage-slip deformations were calculated using a two-component bond stress model proposed by Lehman (1998). The magnitude of the bond stress differs for elastic and inelastic behavior of the longitudinal reinforcement, as shown in Figure 4.1. In this figure L_{di} , L_{de} , and L_{dt} refer to the inelastic, elastic, and total development lengths, respectively. The terms τ_{bi} and τ_{be} are the inelastic and elastic bond stresses, and σ_b and ϵ_b are the stress and strain at the footing-column interface.

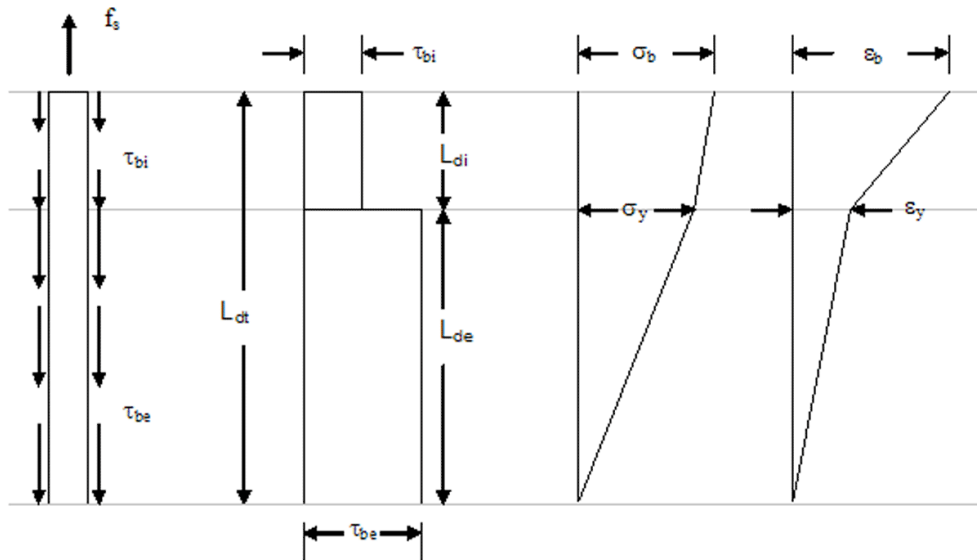


Fig. 4.1 Bond stress model and stress-strain relationship

The inelastic bond stress was assumed to be half of the elastic bond stress. Both the elastic and inelastic bond stress was assumed to be directly proportional to the concrete compressive strength in the footing, which often differed significantly from the column concrete strengths, as shown in Table 2.5.

A modified Burns and Seiss model, adjusted for the measured stresses and strains at the yield and ultimate points of the bar tension tests, was used in calculating the strain in the steel at a given stress. The steel deformations in the extreme tension steel, u_{st} , and the extreme compression steel, u_{sc} , were calculated by integrating the corresponding bar strains. The methodology for determining the bar deformation is outlined in Appendix D. The bond stress model was calibrated using two methods. One calibration was performed by minimizing the difference between the measured strain of each gage and the calculated strain using the model. The other calibration was performed by minimizing the difference between the calculated deformation in the extreme tension steel using the strain gage measurements and using the bond stress model. These two calibrations were then compared to determine the best methodology. It was determined that the differences were smaller when calibrating the bond stress model based on the bar deformation rather than calibrating based on the measured and calculated strains at the gage locations. This led to using the optimization based on the differences between the measured and calculated slip displacements. Through the model calibration, the elastic bond stress, τ_{be} , was determined to be $7\sqrt{f'_c}$ for columns with strain gages (S3, C2, C4, and C3R). For the columns without strain gages, τ_{be} was taken as $12\sqrt{f'_c}$, as recommended by Lehman (1998). The smaller bond stress for the columns with the strain gages was attributed to the waterproofing applied to the reinforcement to protect the gages.

The base rotation at the footing-column interface, θ_{slip} , was calculated from the tensile and compressive steel deformations with the equation

$$\theta_{slip} = \frac{u_{st} - u_{sc}}{D'} \quad (4.2)$$

where u_{st} and u_{sc} are the steel deformations in the extreme tension and compression steel, respectively, as defined in the preceding paragraph. D' = the diameter of the concrete core. The resulting displacement at the top of the column, Δ_{slip} , is defined as

$$\Delta_{slip} = \theta_{slip} l \quad (4.3)$$

where l is the column height.

4.5 YIELD DISPLACEMENT

The initial yield displacement was calculated as the sum of the contributions of flexure, shear, and slip displacements at first yield of the longitudinal reinforcement. Each of the components of the initial yield displacement was calculated the same way for each column, except for the slip component. As discussed in Section 4.4, because of the presence of strain gages in Columns S3, C2, C4, and C3R, the bond stress in these columns ($7\sqrt{f'_c}$) was less than the bond stress in Columns S1 and S15 ($12\sqrt{f'_c}$).

Using the appropriate bond stresses for each column, the measured and calculated yield displacements are tabulated in Table 4.1.

Table 4.1 Measured and calculated yield displacement

Column	Measured		Calculated						
	Δ'_y (in.)	Δ_y (in.)	b (in.)	Δ'_y (in.)	$\Delta'_{y,slip}$ (in.)	$\Delta'_{y,noslip}$ (in.)	Δ_y (in.)	$\Delta_{y,slip}$ (in.)	$\Delta_{y,noslip}$ (in.)
S1	0.22	0.26	12	0.21	0.05	0.16	0.26	0.07	0.19
S3	0.32	0.38	7	0.30	0.11	0.19	0.35	0.13	0.22
S15	0.19	0.23	12	0.21	0.05	0.16	0.25	0.07	0.18
C2	0.30	0.36	7	0.30	0.11	0.19	0.35	0.13	0.22
C4	0.29	0.35	7	0.31	0.11	0.20	0.37	0.13	0.24
C3R	0.31	0.37	7	0.29	0.11	0.18	0.35	0.13	0.22
μ	0.27	0.33	8.67	0.27	0.09	0.18	0.32	0.11	0.21
σ	0.05	0.06	2.36	0.04	0.03	0.02	0.05	0.03	0.02
COV	17.96	17.83	27.20	15.86	31.43	8.49	14.85	25.71	9.61

In Table 4.1, the term b is the elastic bond stress coefficient used for calculating the slip displacement. Shown in the table are the initial yield displacements, Δ'_y , the slip displacement at initial yield, $\Delta'_{y,slip}$, and the portion of the initial yield displacement not attributed to slip, $\Delta'_{y,noslip}$. The same procedure has been used for the yield displacement. The measured values of the yield displacement, presented in Section 3.3, are also shown as a comparison with the calculated values.

As seen in Table 4.1, when using the optimal value of the bond stress coefficient, b, that was generated by minimizing the differences in the measured and calculated slip displacements, the initial yield displacements are approximately the same between the measured and calculated

values. Furthermore, by subtracting out the calculated slip displacement from the total displacement at initial yielding, the resultant displacement that is due to all components besides slip is approximately the same for all six columns.

4.6 ELASTIC MODULUS

The value assumed for the elastic modulus affects the force-displacement envelope. The equation presented in Section 8.5.1 of ACI 318-02 (ACI 2002) is often used to compute E_c :

$$E_c = 57,000\sqrt{f'_c} \text{ (psi)} \quad (4.4)$$

$$E_c = 4730\sqrt{f'_c} \text{ (MPa)} \quad (4.4m)$$

where f'_c is the concrete strength. However, Carrasquillo et al. (1981) suggested that this equation is inaccurate for high-strength concrete, and proposed the following equation for concrete with strengths between 3000–12,000 psi (21–83 MPa):

$$E_c = 40,000\sqrt{f'_c} + 1.0 \times 10^6 \text{ (psi)} \quad (4.5)$$

$$E_c = 3320\sqrt{f'_c} + 6900 \text{ (MPa)} \quad (4.5m)$$

Table 4.2 shows the measured column concrete strength for each test, the elastic modulus, E_c , computed using Equations 4.4 and 4.5, and the measured values of E_c from laboratory tests.

Table 4.2 Elastic moduli

Column	f'_c (psi)	E_c (ksi) Eq. 4.4	E_c (ksi) Eq. 4.5	E_c (ksi) Measured
S1	5271	4138	3904	4797 ¹
S3	8150	5150	4610	4090
S15	5870	4367	4065	4797 ¹
C2	8260	5180	4640	4270
C4	8170	5150	4620	4040
C3R	7640	4980	4500	4930

¹ The elastic modulus for Columns S1 and S15 were determined at the conclusion of test S15.

The measured material properties for Column C3R were unexpected. Columns C2, C3R, and C4 were all cast from the same batch and the columns were all tested when the concrete was quite old (159 – 220 days as shown in Table 2.5). They were thus expected to have similar

properties. Yet, on test day, the measured concrete strength of Column C3R was lower than those of the other three specimens, and the elastic modulus was much higher. Both properties are inconsistent with the relative ages of the four specimens.

4.7 STIFFNESS CALCULATIONS

The ratios of the measured effective stiffness to the calculated effective stiffness for both the Mander, Priestley, and Park concrete model and the Razvi and Saatcioglu concrete model are reported in Table 4.3. Each of these models were compared using calculated and measured values of the elastic modulus.

Table 4.3 Ratios of measured to calculated effective stiffness (K_m/K_c)

Column	Mander, Priestley, and Park Model			Razvi and Saatcioglu Model	
	$E_{c,calc}$ (Eq. 4.4)	$E_{c,calc}$ (Eq. 4.5)	$E_{c,meas}$	$E_{c,calc}$ (Eq. 4.5)	$E_{c,meas}$
S1	1.01	1.03	0.99	1.07	1.04
S3	0.92	0.98	1.04	1.00	1.04
S15	1.16	1.19	1.13	1.22	1.19
C2	0.96	1.02	1.07	1.05	1.08
C4	1.03	1.08	1.15	1.11	1.15
C3R	0.92	0.97	0.92	1.00	0.97
Mean	1.00	1.04	1.05	1.07	1.08
St. Dev.	0.090	0.082	0.086	0.084	0.080
C.O.V.	9.1%	7.8%	8.2%	7.8%	7.4%

Depending on the modeling assumptions, the mean effective stiffness ratio for the six columns ranged between 1.00–1.08, with a coefficient of variation between 7–9%. This shows that the calculated results are relatively insensitive to the choice of the concrete model or values of the elastic modulus. The measured and calculated force-displacement envelopes using the Mander, Priestley, and Park concrete model are seen in Figure 4.2. As seen in Figure 4.2, the rising portions of the measured and calculated force-displacement curves (where the effective stiffness is calculated) match very well for all columns.

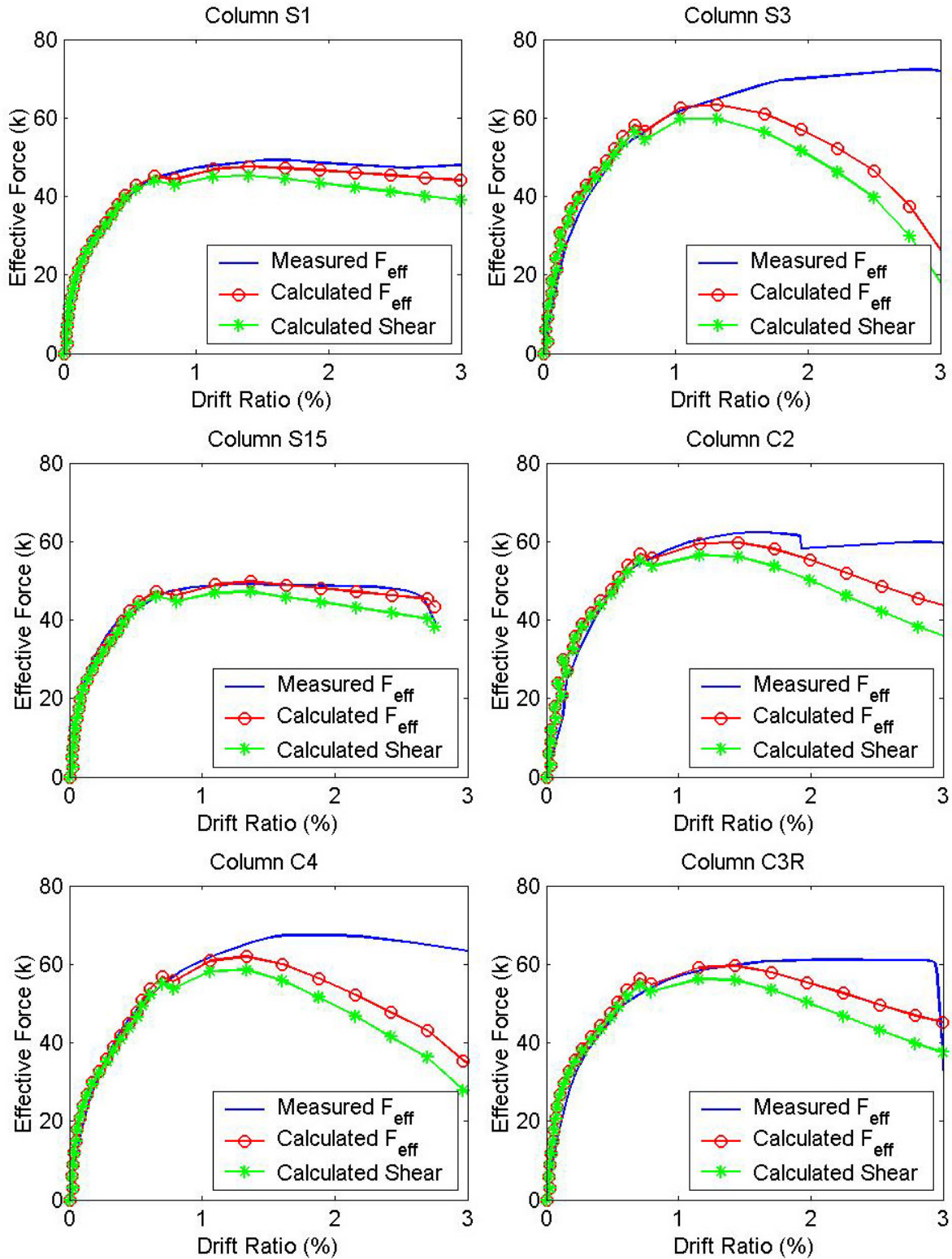


Fig. 4.2 Measured and calculated force-displacement envelopes for measured amount of transverse reinforcement

4.8 STRENGTH CALCULATIONS

The ratios of the measured effective strength to the calculated effective strength (effective strength ratio) were compared using both the Mander, Priestley, and Park, and the Razvi and Saatcioglu concrete models (Table 4.4). Each of these models was analyzed using measured and calculated values for the elastic modulus.

Table 4.4 Ratio of measured to calculated effective strengths (F_m/F_c)

Column	Mander, Priestley, and Park Model			Razvi and Saatcioglu Model	
	$E_{c,calc}$ (Eq. 4.4)	$E_{c,calc}$ (Eq. 4.5)	$E_{c,meas}$	$E_{c,calc}$ (Eq. 4.5)	$E_{c,meas}$
S1	1.07	1.08	1.06	1.07	1.07
S3	1.18	1.21	1.30	1.17	1.17
S15	1.02	1.04	1.01	1.02	1.02
C2	1.09	1.11	1.16	1.07	1.07
C4	1.13	1.17	1.25	1.11	1.12
C3R	1.07	1.08	1.07	1.06	1.06
Mean	1.09	1.12	1.14	1.08	1.09
St. Dev.	0.057	0.065	0.114	0.051	0.054
C.O.V.	5.2%	5.9%	10.0%	4.7%	4.9%

Table 4.4 shows that the effective column strength was slightly underestimated for each concrete model and each value of the elastic modulus. The underestimation of the effective column strengths was similar for all the methods used, with a mean strength ratio ranging from 1.08–1.14. The calculated effective strengths of Columns S3 and C4, which had the highest peak axial-load ratios, were particularly low, as seen in Figure 4.2.

One means of making the calculated strength match with the measured value would be to increase the yield stress of the longitudinal reinforcement. The ratios of the measured to the calculated effective strength (F_m/F_c) are shown for each column at yield stresses from 0%–20% above the measure values are shown in Table 4.5. The ratios reported in Table 4.5 are for the Mander, Priestley, and Park concrete model, and the concrete elastic modulus from Equation 4.4.

Table 4.5 Ratio of measured to calculated effective strengths (F_m/F_c) for various longitudinal steel yield stresses

Column	Ratio of measured to calculated effective strength (F_m/F_c)			
	$F_y = 1.00F_{y,meas}$	$F_y = 1.05F_{y,meas}$	$F_y = 1.10F_{y,meas}$	$F_y = 1.20F_{y,meas}$
S1	1.07	1.01	0.99	0.96
S3	1.18	1.13	1.11	1.09
S15	1.02	0.97	0.95	0.92
C2	1.09	1.03	1.02	1.00
C4	1.13	1.08	1.06	1.04
C3R	1.07	1.01	1.00	0.98
<i>Mean</i>	<i>1.09</i>	<i>1.04</i>	<i>1.02</i>	<i>1.00</i>
<i>St. Dev.</i>	<i>0.06</i>	<i>0.06</i>	<i>0.06</i>	<i>0.06</i>
<i>C.O.V.</i>	<i>5.07</i>	<i>5.38</i>	<i>5.75</i>	<i>5.81</i>

As seen in Table 4.5, as the yield stress of the longitudinal reinforcement is increased by 20% of the measured yield stress, the calculated effective strength increases, reducing the ratio of the measured to the calculated effective strengths to 1.0. Other parameters that could increase the calculated effective strength of the column are the unconfined concrete strength and the confinement ratio of the column. Increasing the confinement ratio would not only increase the strength of the confined concrete, it would also increase the ultimate strain of the concrete, making the column more ductile.

4.9 STRENGTH DEGRADATION

As seen in Figure 4.2, the calculated column strength degraded faster than the measured column strength for each column except Columns S1 and S15. It appears that the columns are more ductile than the modeling methodology predicted. For example, at a drift of 2% the measured and calculated strengths of Column S3 are 70.1 k (312 kN) and 56.1 k (250 kN), respectively, which corresponds to a measured-to-calculated ratio of 1.25. One way of adding ductility into the computational models is to adjust the column confinement ratio by increasing the amount of transverse reinforcement. Table 4.6 shows the measured to calculated strength ratios for each column at a drift of 2% using the Mander, Priestley, and Park model for an amount of transverse reinforcement two, three, and five times the actual column reinforcement. The Mander,

Priestley, and Park model was implemented with an elastic modulus calculated with Equation 4.4.

Table 4.6 Measured to calculated strength ratios (F_m/F_c) at a drift ratio of 2% for different amounts of transverse reinforcement

Column	Measured to calculated strength ratio (F_m/F_c) at 2% drift			
	$A_{s,calc} = 1.0A_{s,act}$	$A_{s,calc} = 2.0A_{s,act}$	$A_{s,calc} = 3.0A_{s,act}$	$A_{s,calc} = 5.0A_{s,act}$
S1	1.04	0.99	0.98	0.95
S3	1.25	1.19	1.07	1.06
S15	1.02	0.97	0.95	0.94
C2	1.06	0.98	0.96	0.94
C4	1.23	1.09	1.05	1.04
C3R	1.11	1.03	1.01	1.00
Mean	1.12	1.04	1.00	0.99
St. Dev.	0.10	0.08	0.05	0.05
C.O.V.	8.99	8.16	4.87	5.37

As seen in Table 4.6, the calculated column strengths at a 2% drift ratio matched much more closely to the measured column strengths when a transverse reinforcement ratio of 3 times the actual transverse reinforcement ratio was used. Adding additional transverse reinforcement to the models did not significantly affect the effective stiffness ratios because the stiffness does not rely heavily on this design parameter. Figure 4.3 shows the measured and calculated force-displacement envelopes for each column using the Mander, Priestley, and Park model with three times the actual reinforcement. As seen in Figure 4.3, the calculated effective force-drift envelopes match much more closely to the measured at large drifts for all columns when the more ductility is added to the columns (compared to Figure 4.2). The same is true when using the Razvi-Saatcioglu model.

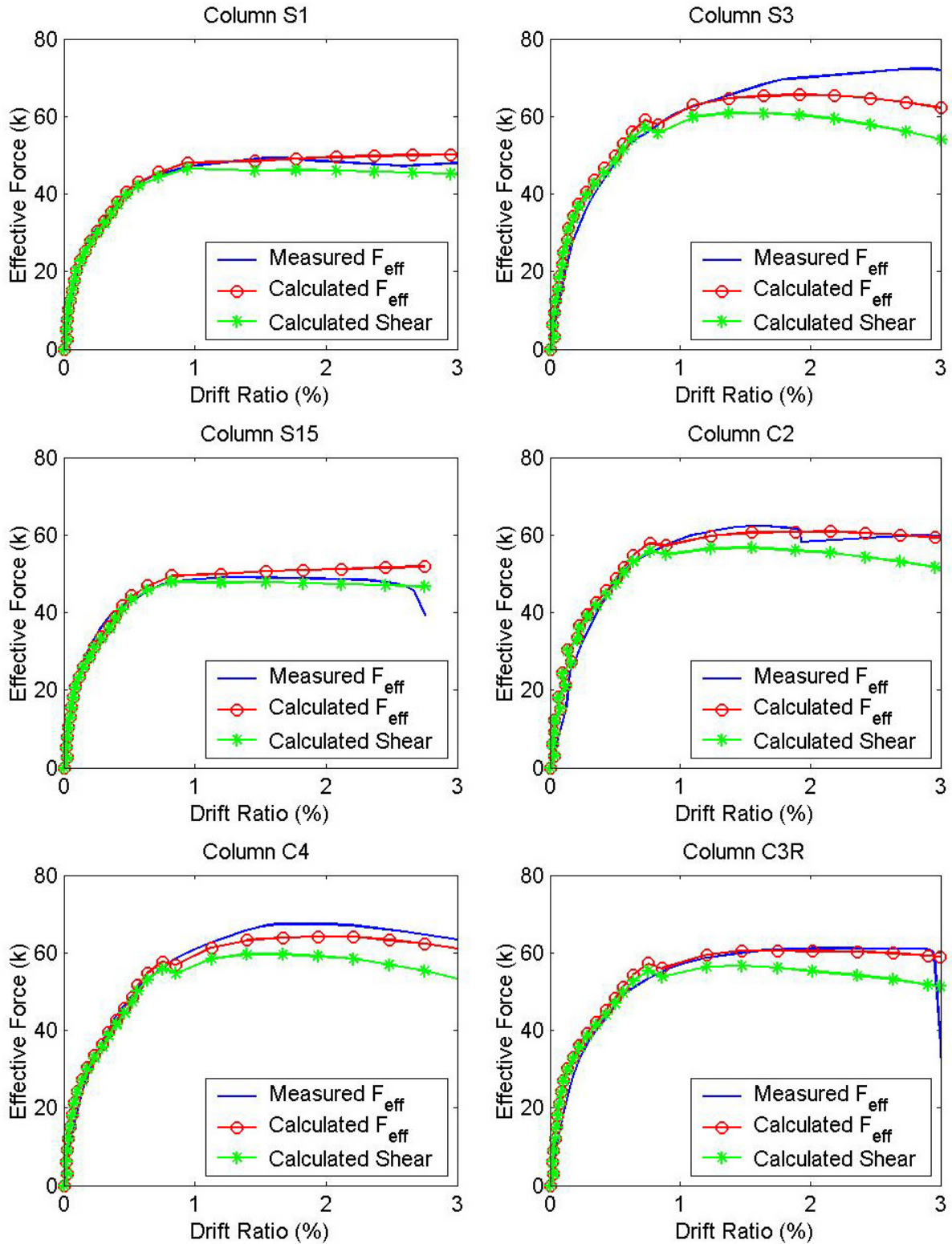


Fig. 4.3 Measured and calculated force-displacement envelopes for three times the measured transverse reinforcement

4.10 DISCUSSION

The force-displacement envelopes were calculated by adding the contributions of three factors: flexural deformations, shear deformations, and anchorage-slip deformations. Although the six columns had nominally the same design and material properties, the anchorage-slip deformations for Columns S3, C2, C4, and C3R were considerably higher than for Columns S1 and S15. This can mostly be attributed to the presence of waterproof-coated strain gages for four of the tests, which caused the bond stress in Columns S3, C2, C4, and C3R to be approximately half of the bond stress in Columns S1 and S15.

Two concrete models and three methods for computing the concrete's elastic modulus were used to develop the force-displacement envelope. Stiffness and strength were not affected significantly by the choice of concrete model or the equation for calculating the concrete elastic modulus. Tables 4.3 and 4.4 show the average ratios computed for each concrete model and method of computing E_c . Both models, regardless of which elastic modulus was used, predicted the effective column stiffness relatively well and slightly underpredicted the peak column strength, summarized in Table 4.7.

Table 4.7 Mean strength and stiffness ratios

Ratio	Mander, Priestley, and Park			Razvi and Saatcioglu	
	$E_{c,calc}$ (Eq. 4.4)	$E_{c,calc}$ (Eq. 4.5)	$E_{c,meas}$	$E_{c,calc}$ (Eq. 4.5)	$E_{c,meas}$
K_m/K_c	1.00	1.04	1.05	1.07	1.08
F_m/F_c	1.09	1.12	1.14	1.08	1.09

The calculated peak column strength better matched the measured if the yield stress of the longitudinal reinforcement was increased by 20%. Other methods of matching the calculated and measured peak column strengths include increasing the peak unconfined concrete stress or increasing the transverse reinforcement ratio. The strength deterioration was characterized by the column strength at 2% drift. The calculated column strength at 2% drift better matched the measured if the transverse reinforcement ratio is increased to three times the actual transverse reinforcement ratio. This adjustment did not significantly affect the effective stiffness calculation because the point at which the effective stiffness is calculated is not heavily influenced by the amount of transverse reinforcement.

5 Observed Damage

Various states of observed column damage were documented during each of the six tests to determine whether the amount of cycling affected the maximum deformation at which each damage state occurred. This trend was investigated for nine damage states:

1. First yield of longitudinal reinforcement (Section 5.1)
2. Significant flexural cracking (Section 5.2)
3. Residual cracking (Section 5.3)
4. Significant spalling (Section 5.4)
5. Longitudinal bar buckling (Section 5.5)
6. Hoop fracture (Section 5.6)
7. 20% loss of lateral load capacity (Section 5.7)
8. 50% loss of lateral-load capacity (Section 5.8)
9. Loss of axial-load capacity (Section 5.9).

For each damage state, the cycle designation and maximum displacement up to the point at which the damage was observed were recorded. The maximum displacement at the previous observation point is also provided for the damage states in which the exact point of damage is unknown. Except for the 20% and 50% loss of lateral-load-capacity damage states, at least one photograph is provided for each damage level.

The nomenclature for the cycle designations is as follows: the number refers to the cycle number (as listed in Table 2.7), and the letter refers to the part of the cycle in which the damage was observed; *P* refers to the positive peak, *N* refers to the negative peak, and *E* refers to the end of a cycle. For example, cycle 2P refers to the positive peak displacement of the second cycle. The upper-bound and lower-bound displacements of the six columns are used in Chapter 6 to evaluate and calibrate the proposed damage models for each damage state.

5.1 FIRST YIELD OF LONGITUDINAL REINFORCEMENT

A yield strain of $\epsilon_y = 0.00235$ for the longitudinal reinforcement was determined from tensile tests. The point at which the reinforcement first yielded in the column was determined from strain gage data for the bars furthest from the column center. Because strain gages were not installed in Columns S1 and S15, the displacement at initial yield was estimated based on when the column base reached the calculated moment at first yield, M'_y (Section 3.3).

A typical column at the point of first yield of the longitudinal reinforcement is shown in Figure 5.1. At this point, no significant damage was visible. Table 5.1 shows the data corresponding to this damage level.



Fig. 5.1 First yield of longitudinal reinforcement (Column C2)

Table 5.1 Column displacements at first yield of longitudinal reinforcement

Column	Cycle Designation	First Yield Disp. (in.)
S1	2N	0.22
S3	11P	0.32
S15	9N	0.19
C2	2P	0.30
C4	2P	0.29
C3R	2P	0.31
<i>Mean</i>		0.27
<i>St. Dev.</i>		0.05
<i>C.O.V. (%)</i>		20

5.2 SIGNIFICANT FLEXURAL CRACKING

The “significant flexural cracking” damage state was defined as the first observation of a crack width greater than or equal to 0.02 inches (0.5 mm). Figure 5.2 shows a typical test column at this state, and Table 5.2 gives the data corresponding to this damage level. The values in columns labeled “Obs.” are the values corresponding to the cycle in which the damage state was observed; the values in the columns labeled “Prev.” are the values from the previous cycle in which the column was checked for this damage level. Therefore, the “Prev.” and “Obs.” values are the lower and upper bounds to this damage level. For example, in Column S1, the crack widths were smaller than 0.02 in. at cycle 2N but exceeded 0.02 in. at cycle 3P.

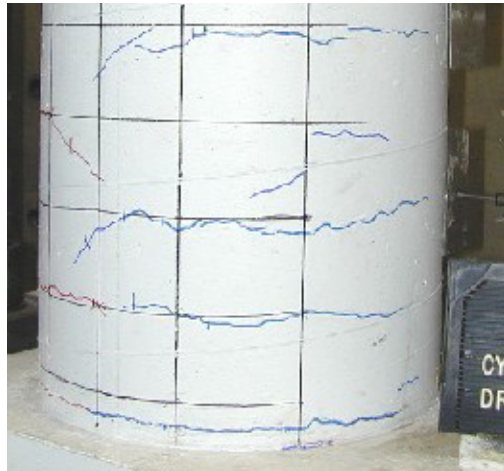


Fig. 5.2 Significant flexural cracking (Column S15)

Table 5.2 Column characteristics at significant flexural cracking

Column	Cycle Designation		Maximum Disp. (in.)	
	Prev.	Obs.	Prev.	Obs.
S1	2N	3P	0.33	0.40
S3	8P	11P	0.26	0.43
S15	24N	30P	0.33	0.39
C2	1P	2P	0.09	0.44
C4	1N	2N	0.18	0.44
C3R	1P	2P	0.03	0.41
<i>Mean</i>			<i>0.20</i>	<i>0.42</i>
<i>Std. Dev.</i>			<i>0.13</i>	<i>0.020</i>
<i>COV</i>			<i>62</i>	<i>5.1</i>

5.3 RESIDUAL CRACKING

The criterion for reaching the residual cracking damage state was the existence of a crack width greater than or equal to 0.01 inches (0.25 mm) upon unloading. An example of this damage level is shown in Figure 5.3. Table 5.3 gives the data for this damage state.

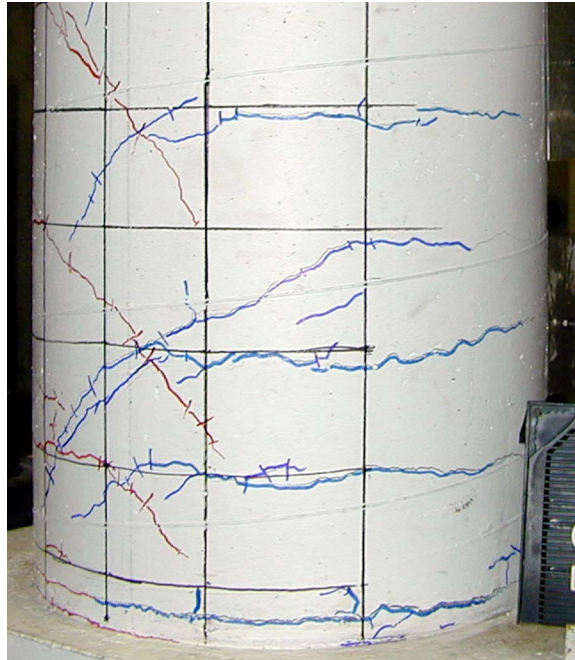


Fig. 5.3 Residual cracking (Column S15)

Table 5.3 Column characteristics at residual cracking

Column	Cycle Designation		Maximum Disp. (in.)	
	Prev.	Obs.	Prev.	Obs.
S1	4N	5P	0.83	1.10
S3	13E	16E	0.47	0.70
S15	54N	57P	0.86	0.94
C2	3E	4E	1.15	1.16
C4	2E	3E	0.44	2.23
C3R	2E	3E	0.41	1.77
<i>Mean</i>			<i>0.69</i>	<i>1.32</i>
<i>Std. Dev.</i>			<i>0.30</i>	<i>0.57</i>
<i>COV</i>			<i>43</i>	<i>43</i>

5.4 SIGNIFICANT SPALLING

The definition of significant spalling was when spalling reached a height of 1/10 of the cross section depth; for these columns, that height was 2 inches (51 mm). Figure 5.4 shows a photograph of Column S1 at this damage level. Table 5.4 provides the data corresponding to this damage state.

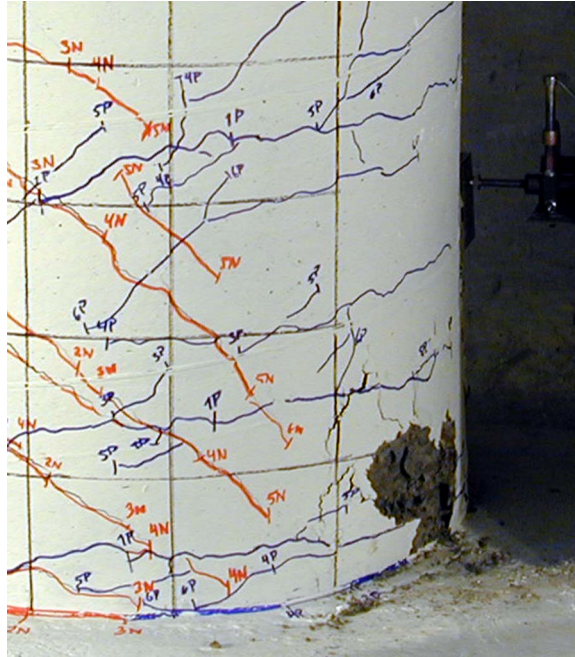


Fig. 5.4 Significant spalling (Column S1)

Table 5.4 Column characteristics at significant spalling

Column	Cycle Designation		Maximum Disp. (in.)	
	Prev.	Obs.	Prev.	Obs.
S1	5N	6P	1.38	1.82
S3	14P	17P	0.67	1.14
S15	63N	66P	1.07	1.14
C2	2N	3N	0.45	1.15
C4	2P	3P	0.38	2.23
C3R	2N	3N	0.41	1.77
Mean			0.73	1.54
Std. Dev.			0.41	0.46
COV			57	30

5.5 LONGITUDINAL BAR BUCKLING

The onset of longitudinal bar buckling was defined as occurring when vertical cracks appeared in the concrete cover directly above a longitudinal bar. This state was quickly followed by concrete bulging and separation of the longitudinal reinforcement from the core concrete. Figure 5.5 shows a typical vertical crack of this type. Table 5.5 gives the data for this state.

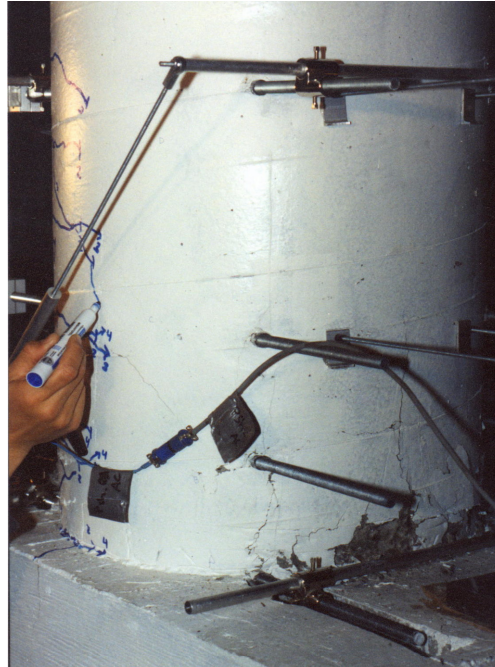


Fig. 5.5 Onset of longitudinal bar buckling (vertical cracking) (Column C3R)

Table 5.5 Column characteristics at onset of longitudinal bar buckling

Column	Cycle Designation		Maximum Disp. (in.)	
	Prev.	Obs.	Prev.	Obs.
S1	4N	5P	1.38	1.82
S3	17N	20N	1.15	1.87
S15	57N	60N	1.14	1.25
C2	14N	15N	1.16	1.88
C4	2P	3P	0.38	2.23
C3R	3P	4P	1.77	1.77
<i>Mean</i>			<i>1.16</i>	<i>1.80</i>
<i>Std. Dev.</i>			<i>0.45</i>	<i>0.32</i>
<i>COV</i>			<i>39</i>	<i>18</i>

5.6 HOOP FRACTURE

Hoop fracture refers to the point at which the exposed transverse reinforcement was observed to fracture. Hoop fracture was not observed in Columns S1 and S15. Figure 5.6 shows the occurrence of hoop fracture for Column C3R. Table 5.6 gives the data for this damage state.



Fig. 5.6 Observed bar buckling (from Column C3R)

Table 5.6 Column characteristics at hoop fracture

Column	Cycle Des.	Maximum Disp. (in.)
S1	NA	NA
S3	20E	1.87
S15	NA	NA
C2	16P	1.88
C4	3P	2.23
C3R	5N	1.77
<i>Mean</i>		<i>1.93</i>
<i>St. Dev.</i>		<i>0.20</i>
<i>C.O.V.</i>		<i>10</i>
Note: Hoop fracture was not observed in Columns S1 and S15		

5.7 20% LOSS OF LATERAL LOAD

The 20% loss of lateral-load capacity was reached when the maximum lateral load of a given displacement cycle was at least 20% less than the maximum lateral load of all previous cycles.

Table 5.7 shows the points at which this damage state occurred.

Table 5.7 Column characteristics at 20% loss of lateral-load capacity

Column	Cycle Des.	Maximum Disp. (in.)
S1	7P	2.27
S3	22N	2.12
S15	74P	1.62
C2	18P	2.25
C4	3N	2.23
C3R	8P	1.78
<i>Mean</i>		2.05
<i>St. Dev.</i>		0.28
<i>C.O.V.</i>		14

5.8 50% LOSS OF LATERAL LOAD

The 50% loss of lateral-load capacity was reached when the maximum lateral load of a given displacement cycle was at least 50% less than the maximum lateral load of all previous cycles.

Table 5.8 shows the points at which this damage state occurred. As seen in Table 5.8, for many of the columns, this damage state quickly followed the previous damage state.

Table 5.8 Column characteristics at the 50% loss of lateral-load capacity

Column	Cycle Des.	Maximum Disp. (in.)
S1	7P	2.34
S3	22N	2.12
S15	75P	1.66
C2	18N	2.28
C4	8P	2.29
C3R	12P	1.80
<i>Mean</i>		2.08
<i>St. Dev.</i>		0.29
<i>C.O.V.</i>		14

5.9 LOSS OF AXIAL-LOAD CAPACITY

Loss of axial-load capacity was reached when the columns experienced a drop in the axial load, and attempts to increase the axial load resulted in column instability. Figure 5.7 shows both flexure-shear and flexure failure mechanisms. Since the axial load was monitored continuously during testing, the exact point where axial capacity was lost could be determined. The data for this damage state is shown in Table 5.9.

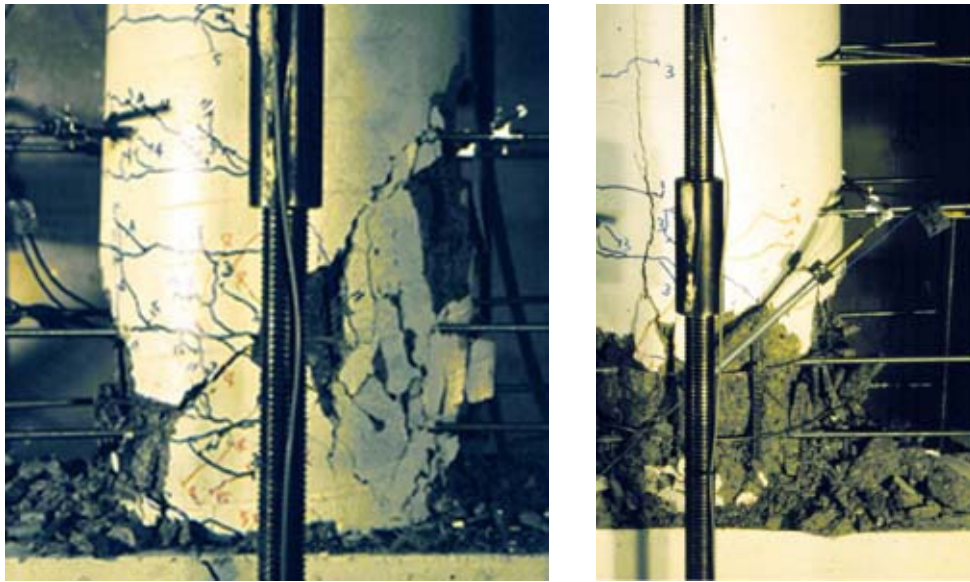


Fig. 5.7 Loss of axial-load capacity; (a) flexure-shear failure (from Column C2); (b) flexure failure (from Column C4)

Table 5.9 Column characteristics at the loss of axial-load capacity

Column	Cycle Des.	Maximum Disp. (in.)
S1	8P	2.73
S3	23P	2.85
S15	75N	1.76
C2	18E	2.28
C4	13N	3.54
C3R	17N	1.80
<i>Mean</i>		2.49
<i>St. Dev.</i>		0.68
<i>C.O.V.</i>		27

6 Effect of Cycling on Column Damage

The importance of accounting for the effects of the amount of cycling on damage progression was investigated using two measures of cycling: energy dissipation and cumulative plastic deformation. Section 6.1 introduces the Park-Ang damage model, which accounts for cycling through energy dissipation, and a modification of the Park-Ang damage model. Section 6.2 introduces the cumulative plastic deformation model, an alternative means of accounting for cycling, which is less sensitive to the estimate of the yield displacement. Section 6.3 presents three methods used to calibrate the three damage models: least-squares approximation, maximizing a likelihood function, and minimizing a penalty function. Section 6.4 introduces parameters that will be reported in subsequent sections (Sections 6.5–6.13) for each of the nine damage states. Section 6.14 discusses the possible causes and the implications of the results.

6.1 PARK-ANG DAMAGE MODEL

The level of damage predicted by the Park-Ang model depends on a combination of the energy dissipated by the structure and its maximum displacement (Williams and Sexsmith 1995). The Park-Ang damage index (Park and Ang 1985) is defined as

$$D = \alpha \frac{\Delta_{\max}}{\Delta_y} + \beta \frac{E_h}{\Delta_y F_y} \quad (6.1)$$

in which D is the damage index, Δ_{\max} is the maximum displacement experienced by the component, Δ_y is the yield displacement, α is a non-negative factor representing the reciprocal of the ductility capacity of the structure at failure in a monotonic load test (μ_u), E_h is the hysteretic energy dissipated during cycling, F_y is the force at yield, and β is a non-negative factor representing the effect of cyclic loading. The effective yield displacement and effective yield force that were used to normalize the data for each column, discussed in Chapter 3, are listed in Table 6.1.

Table 6.1 Normalization data for Park-Ang damage model

Column	Δ_y (in.)	F_y (k)
S1	0.26	44.3
S3	0.38	58.8
S15	0.23	46.5
C2	0.36	57.2
C4	0.35	57.1
C3R	0.37	56.8

Although all six columns were nominally identical, the yield displacements of Columns S1 and S15 were significantly smaller (32%) than the yield displacements of the other columns. Section 4.5 showed that the differences in these displacements are mainly attributable to the larger slip displacements in Columns S3, C2, C4 and C3R. This was most likely due to the placement of strain gages in the footings of these four columns, which decreased the bond stress between the longitudinal reinforcement and the concrete.

The results of the calibrated Park-Ang damage model for the nine damage states are provided in Appendix E. These results show a poor correlation between damage progression in the columns and the level of cycling, which is attributed to the use of the yield displacement as the normalizing factor.

A modified Park-Ang model is proposed, which normalizes the data by the length of the column (L) instead of the yield displacement, given by the equation:

$$D = \alpha_m \frac{\Delta_{\max}}{L} + \beta_m \frac{E_h}{LF_y} \quad (6.2)$$

where α_m is a non-negative factor representing the reciprocal of the ultimate drift ratio under monotonic loading, and β_m is a non-negative factor that represents the effect of cycling on the maximum drift. This model is much less sensitive to the accuracy of the estimated yield displacement.

6.2 CUMULATIVE PLASTIC DEFORMATION DAMAGE MODEL

It is convenient to formulate a damage model based on column plastic deformation because plastic deformation is related to the plastic strain. The total strain in the reinforcement (ϵ) can be separated into the yield strain (ϵ_y) and the plastic strain (ϵ_p), as follows:

$$\varepsilon = \varepsilon_y + \varepsilon_p \quad (6.3)$$

The curvature of the column can be related to the reinforcement strains by relating the yield and plastic curvatures separately. Priestley et al. (1996) found that the yield curvature (ϕ_y) can be approximated based on the column diameter (D) and the yield strain of the longitudinal reinforcement:

$$\phi_y \cong \lambda \frac{\varepsilon_y}{D} \quad (6.4)$$

where $\lambda = 2.45$ is a constant accounting for the neutral axis depth in spiral-reinforced columns. The plastic curvature can also be written as a function of the plastic strain in the extreme longitudinal reinforcement, the distance between the compressive face of the column and the extreme tension steel (d) and the distance from the compressive face of the column and the neutral axis (c):

$$\phi_p = \frac{\varepsilon_p}{d - c} \quad (6.5)$$

According to plastic-hinge analysis, the column drift can be determined from the yield and plastic curvatures through the equation:

$$\Delta = \frac{1}{3} \phi_y L^3 + \phi_p L_p \left(L - \frac{L_p}{2} \right) \quad (6.6)$$

where L and L_p are the column length and the plastic-hinge length, respectively. Substituting Equations 6.4 and 6.5 into Equation 6.6, the total column displacement is

$$\Delta = \frac{1}{3} \lambda \frac{\varepsilon_y}{D} L^3 + \left(\frac{D}{d - c} \right) \frac{\varepsilon_p}{D} L_p \left(L - \frac{L_p}{2} \right) \quad (6.7)$$

The plastic displacement of the column can be expressed as

$$\Delta_p = \left(\frac{D}{d - c} \right) \frac{\varepsilon_p}{D} L_p \left(L - \frac{L_p}{2} \right) \quad (6.8)$$

Solving Equation 6.8 for the plastic strain, the relationship becomes

$$\varepsilon_p = \left(\frac{d - c}{D} \right) \left(\frac{D}{L_p} \right) \frac{\Delta_p / L}{1 - L_p / 2L} \quad (6.9)$$

Berry (2003) found that the location of the neutral axis depends mainly on the axial-load ratio and, to a lesser extent, the longitudinal reinforcement ratio. Therefore, if the axial-load ratio and longitudinal reinforcement ratios are constant, as they were for the six test columns, the neutral axis depth can also be approximated as a constant. Assuming that the ratios D/L_p and L_p/L in Equation 6.9 are also constant, the plastic strain is proportional to Δ_p/L .

$$\varepsilon_p \propto \frac{\Delta_p}{L} \quad (6.10)$$

Therefore, the plastic displacement can be used to indirectly reflect the amount of plastic strain in the longitudinal reinforcement. A new damage index can be defined as

$$D = \alpha_p \frac{\Delta_{\max}}{L} + \beta_p \frac{\Sigma \Delta_p}{L} \quad (6.11)$$

where α_p and β_p are non-negative factors calibrated for each damage state, and D is the fraction of damage for each damage state, ranging from 0 to 1. When $D = 1$, column damage has reached the specified damage state.

6.3 MODEL CALIBRATION

The exact deformation needed to reach most of the damage states is unknown. Instead, for each of the six columns, there is a single observation point preceding the damage observation, and a later point when the damage is observed. For example, bar buckling occurred in Column S1 upon unloading from cycle 5P (Table 5.5). However, bar buckling could also have occurred if the peak displacement of the cycle were between this cycle and the previous one (cycle 4N). Therefore, the peak displacement of the previous cycle (4N) is considered the lower-bound estimate of when bar buckling could have occurred. The values of the model parameters depend on the means by which these 12 observations are combined.

The coefficients for each of the damage models (α and β in Eq. 6.1, α_m and β_m in Eq. 6.2, and α_p and β_p in Eq. 6.11) were calibrated using three methods: a least-squares method, a maximum likelihood method, and an exterior-penalty-function method.

6.3.1 Least-Squares Approximation

The damage model coefficients were first determined using a least-squares approximation, in which the observations were taken as the averages of the lower and upper bounds for each of the six columns. The least-squares approximation determines a best-fit of the observations by minimizing the sum of the squares of the differences between the observed and the approximated maximum displacements, written as

$$diff = \sum_{i=1}^N (y_i' - y_i)^2 \quad (6.12)$$

where N is the number of observations, and y_i and y_i' are the recorded and calculated values, respectively. If a linear fit is assumed, Equation 6.12 can be rewritten as

$$diff = \sum_{i=1}^N (Ax_i + B - y_i)^2 \quad (6.13)$$

where A and B are the slope and y-intercept of the approximating line, respectively, and x_i and y_i are the coordinates of the observation. To find the best-fit line, Equation 6.13 is minimized with respect to both A and B by taking the partial derivatives in A and B and setting them equal to zero.

$$\frac{\partial}{\partial A} diff = \sum_{i=1}^N (Ax_i^2 + Bx_i - y_i x_i) = 0 \quad (6.14a)$$

$$\frac{\partial}{\partial B} diff = \sum_{i=1}^N (Ax_i + B - y_i) = 0 \quad (6.14b)$$

Rewriting Equation 6.14 in matrix form:

$$\begin{bmatrix} \sum x_i^2 & \sum x_i \\ \sum x_i & N \end{bmatrix} \begin{Bmatrix} A \\ B \end{Bmatrix} = \begin{Bmatrix} \sum x_i y_i \\ \sum y_i \end{Bmatrix} \quad (6.15)$$

The parameters of the best-fit line, A and B, can be solved directly from Equation 6.15 through matrix inversion.

6.3.2 Maximum Likelihood Approximation

The maximum likelihood approximation, illustrated in Figure 6.1, finds the damage model coefficients and associated normal density function that maximizes the likelihood that all 12 observations would have been made during testing.

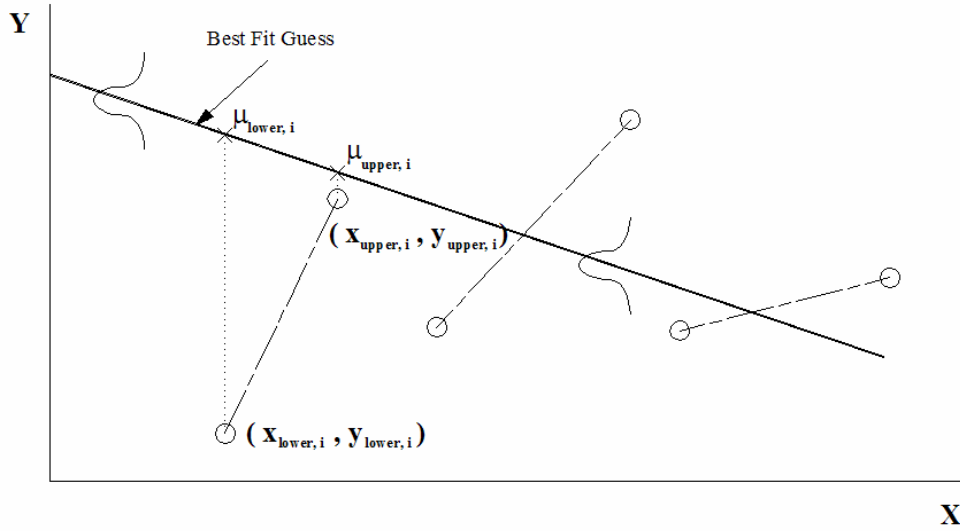


Fig. 6.1 Schematic for maximum likelihood method

In Figure 6.1, the coordinate pairs $(x_{lower,i}, y_{lower,i})$ and $(x_{upper,i}, y_{upper,i})$ are the lower-bound and upper-bound observations for the i^{th} column, respectively, and $\mu_{lower,i}$ and $\mu_{upper,i}$ are the y-components of the best-fit guesses corresponding to the lower- and upper-bound observations, respectively. The procedure for calculating the maximum likelihood best-fit line is outlined in the following steps.

1. For each column, begin with trial values for the slope (A) and y-intercept (B) of the best-fit line (A and B , respectively), as well as a distribution (σ) around that line. In this study, the first trial line was estimated using the least-squares approximation. The initial standard deviation was taken as 5% of the difference between the maximum of the upper-bound observations and the minimum of the lower-bound observations.

$$\sigma_{initial} = 0.05[\max(y_{upper}) - \min(y_{lower})] \quad (6.16)$$

2. For each column, calculate the y-component of the best-fit guess corresponding to the lower-bound and upper-bound observations for each column ($\mu_{lower,i}$ and $\mu_{upper,i}$) using the trial parameters of the fitting line.

$$\mu_{lower,i} = Ax_{lower,i} + B \quad (6.17a)$$

$$\mu_{upper,i} = Ax_{upper,i} + B \quad (6.17b)$$

3. For each column, compute the likelihood that there would have been no damage before the lower-bound observation.

$$L_{lower,i} = \int_{y=y_{lower,i}}^{\infty} \frac{1}{\sqrt{2\pi}\sigma} \text{Exp}\left[-\frac{(y-\mu_{lower,i})^2}{2\sigma^2}\right] dy \quad (6.18)$$

4. For each column, compute the likelihood that there would have been damage before the upper-bound observation.

$$L_{upper,i} = \int_{y=-\infty}^{y_{upper,i}} \frac{1}{\sqrt{2\pi}\sigma} \text{Exp}\left[-\frac{(y-\mu_{upper,i})^2}{2\sigma^2}\right] dy \quad (6.19)$$

5. For each column, determine the likelihood that both the upper- and lower-bound observations would have been made

$$L_i = L_{lower,i} \times L_{upper,i} \quad (6.20)$$

6. Assuming that the individual tests are statistically independent, determine the likelihood that all the lower-bound and upper-bound observations would have been made for N columns:

$$L = \prod_{i=1}^N L_i \quad (6.21)$$

7. Determine the best-fit line by varying the parameters of the fitting line (A, B, and σ) to maximize the likelihood that all of the observations (that damage did not occur before the lower bound and that damage did occur before the upper bound) would have been made during the testing.

In this study, a few restrictions were placed on the value of the standard deviation to enforce convergence on the global maximum, creating the best-fit line. These restrictions include enforcing a lower- and upper-bound value to the standard deviation, and limiting the standard deviation to only integer values. The reasons for these restrictions are explained below.

If it was possible to satisfy all of the lower and upper bounds (as in Fig. 6.1), the maximum likelihood would occur when the standard deviation equaled zero. However, if the standard deviation equaled zero, the total likelihood for the system would be unity as long as the boundaries were met, which would lead to a non-unique solution. To develop a unique solution for these cases, a lower-bound standard deviation of 5% of the difference between the maximum of the upper-bound observations and the minimum of the lower-bound observations was imposed.

If the upper- and lower-bound observations are in the same place for each column (as is the case when the exact location of damage is known, e.g.. loss of axial-load capacity), the maximum likelihood would occur at a standard deviation of $\sigma=+\infty$. However, for efficiency of

the numerical computation, this study assumed an upper bound on the standard deviation of 1000% of the difference between the maximum of the upper-bound observations and the minimum of the lower-bound observations.

6.3.3 Exterior Penalty Function Approximation

The exterior-penalty-function method is similar to the least-squares method but places greater weight on the upper and lower bounds by placing two penalties on the fitting line. The procedure for approximating a best-fit line using the exterior penalty function is illustrated in Figure 6.2 and described below.

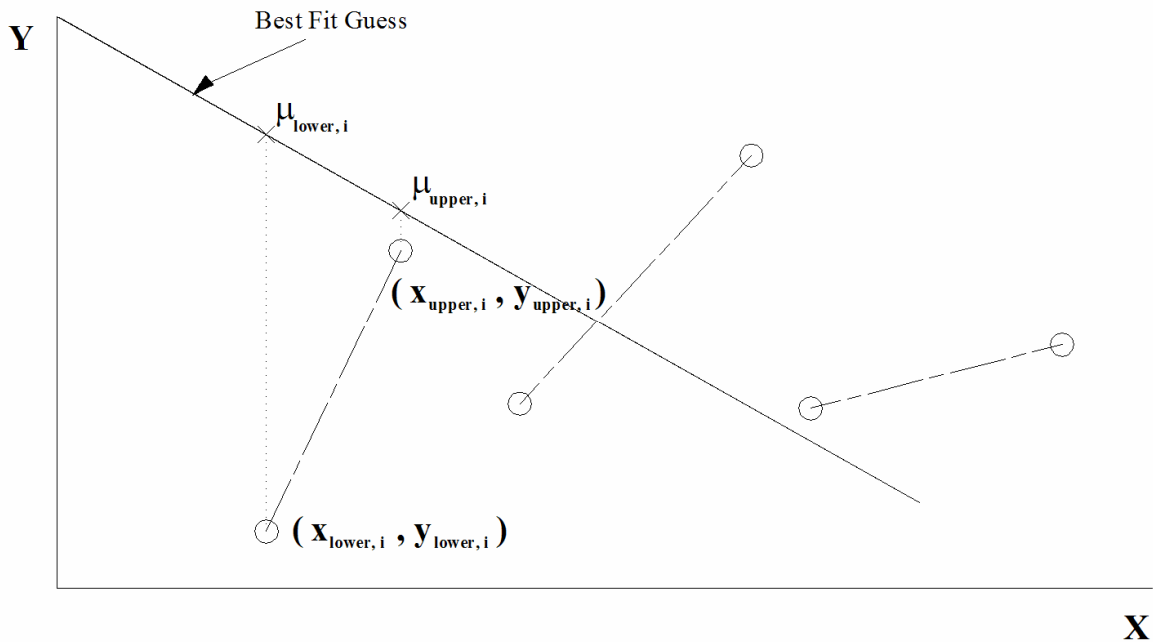


Fig. 6.2 Schematic for penalty function method

1. For each column, begin with trial values for the slope (A) and y-intercept (B) of the best-fit line. In this study, the first trial line was estimated using the least-squares approximation.
2. For each column, calculate the y-component of the best-fit guess corresponding to the lower-bound and upper-bound observations for each column ($\mu_{\text{lower},i}$ and $\mu_{\text{upper},i}$) using the trial parameters of the fitting line:

$$\mu_{lower,i} = Ax_{lower,i} + B \quad (6.22a)$$

$$\mu_{upper,i} = Ax_{upper,i} + B \quad (6.22b)$$

3. For each column, compute the least-squares error for the lower- and upper-bound observations for each column ($LS_{lower,i}$ and $LS_{upper,i}$, respectively):

$$LS_{lower,i} = (\mu_{lower,i} - y_{lower,i})^2 \quad (6.23a)$$

$$LS_{upper,i} = (\mu_{upper,i} - y_{upper,i})^2 \quad (6.23b)$$

4. For each column, if the lower-bound observation ($y_{lower,i}$) is greater than the corresponding point on the fitting line ($\mu_{lower,i}$), apply an exterior penalty function ($EPF_{lower,i}$), defined by

$$EPF_{lower,i} = \begin{cases} 0 & \mu_{lower,i} > y_{lower,i} \\ \gamma \max(y_{upper})^2 \left\{ \text{Exp} \left[\frac{y_{lower,i} - \mu_{lower,i}}{y_{upper,i} - y_{lower,i}} \right] - 1 \right\} & \mu_{lower,i} \leq y_{lower,i} \end{cases} \quad (6.24)$$

The coefficient, γ , represents the severity of the penalty function.

5. For each column, if the upper-bound observation ($y_{upper,i}$) is less than the corresponding point on the fitting line ($\mu_{upper,i}$), apply an exterior penalty function ($EPF_{upper,i}$), defined by

$$EPF_{upper,i} = \begin{cases} 0 & \mu_{upper,i} < y_{upper,i} \\ \gamma \max(y_{upper})^2 \left\{ \text{Exp} \left[\frac{\mu_{upper,i} - y_{upper,i}}{y_{upper,i} - y_{lower,i}} \right] - 1 \right\} & \mu_{upper,i} \geq y_{upper,i} \end{cases} \quad (6.25)$$

The coefficient, γ , represents the severity of the penalty function.

6. For each column, add the four penalties to get the column penalty (P_i).

$$P_i = LS_{lower,i} + LS_{upper,i} + EPF_{lower,i} + EPF_{upper,i} \quad (6.26)$$

7. Add each of the N column penalties to obtain the total penalty for the fitting line (P_{tot}).

$$P_{tot} = \sum_{i=1}^N P_i \quad (6.27)$$

8. Determine the best-fit line by changing the slope (A) and the y-intercept (B) to minimize the total penalty.

Equations 6.24 and 6.25 introduce a weighting factor, γ , which is used to change the severity of the exterior penalty relative to the least-squares penalty. When $\gamma = 0$, there is no exterior penalty, and the best-fit line becomes the least-squares approximation. For this study, γ

= 20 was used to place importance on ensuring that the best-fit line lay within the pair of bounding y-values.

The exterior penalty functions in Equations 6.24 and 6.25 assign a penalty based on the distance between the best-fit guess and the observation, normalized by the y-component of the distance between the upper-bound and lower-bound observations.

To illustrate this point, consider the horizontal line and two data sets defined in Figure 6.3. The first observation set is defined by (1,1) and (1,5), while the second is defined by (3,3) and (3,5). The y-component of the best-fit guess is 1 ordinate above the upper bounds of each of the data sets. However, because the window for observation 1 is larger than the window for observation 2, the error between the best-fit line and data set two is larger than data set 1, relative to the window size. Therefore, the difference between the best-fit guess and data set 2 should be more heavily weighted.

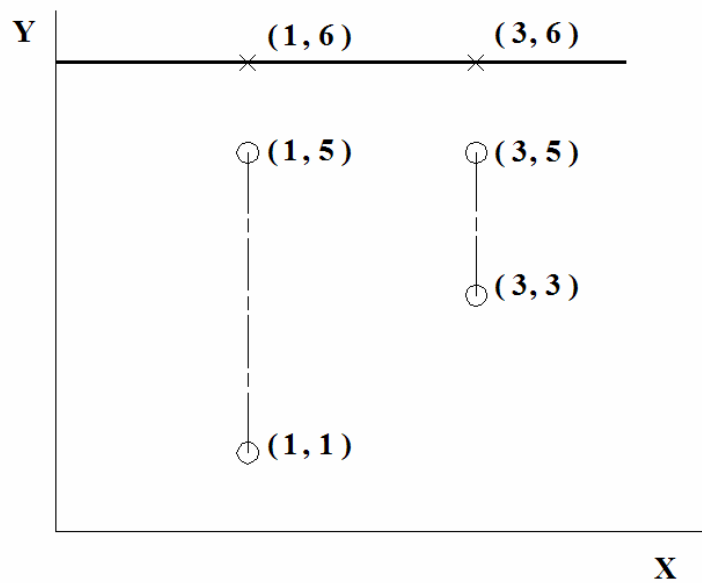


Fig. 6.3 Illustration of weighted exterior penalty function

The exponential functions in Equations 6.24 and 6.25 weigh the penalty independent of the values of the y-axis. Because the least-squares approximation depends on the square of the value of the y-axis, the penalty function was multiplied by the square of the maximum y-component of the observations. This makes the weights of the exterior penalty function and the conventional least squared error have similar dependency on the magnitude of the y-axis.

6.3.4 Illustrative Example

An example illustrating the variation among the least-squares approximation, the maximum likelihood approximation, and the exterior penalty function approximation is shown in Figure 6.4.

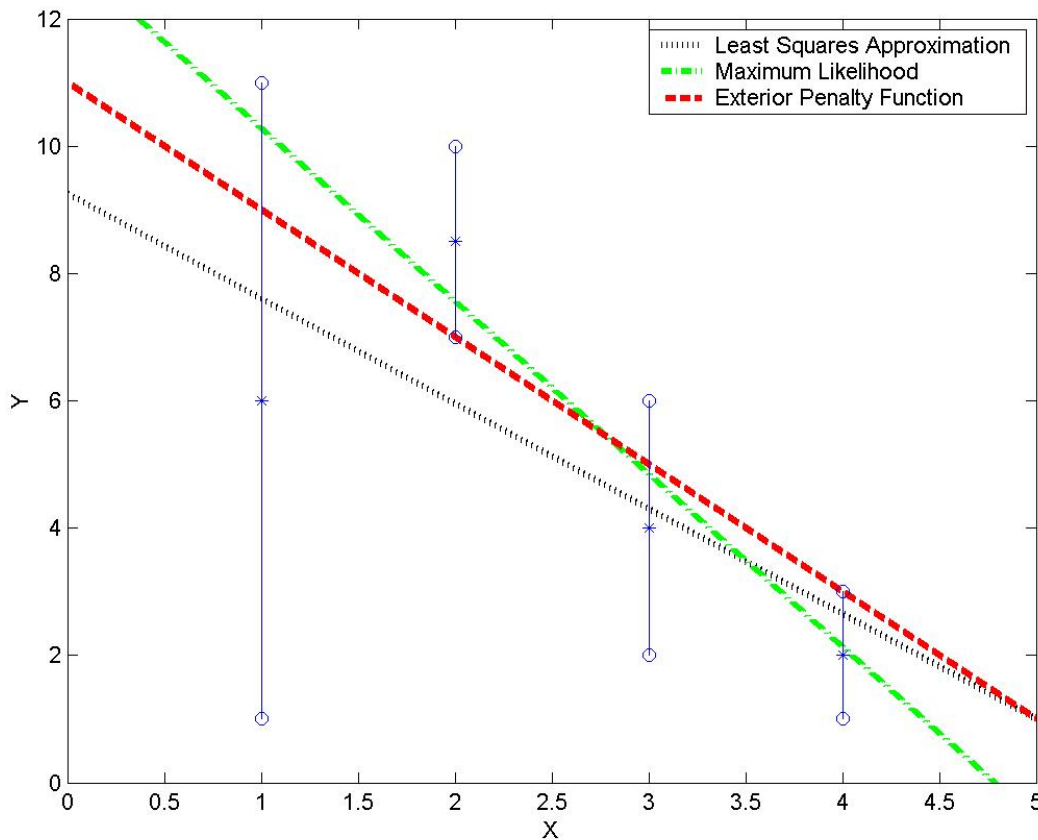


Fig. 6.4 Example showing differences in calibration methods ($\gamma = 20$)

For this example, four lower- and upper-bound sets of data were used, each having a range of values, denoted by two circles. Using the least-squares approximation, the best fit falls outside of the range of one of the data sets. With the exterior penalty function, the best-fit line barely satisfies all of the data ranges. The maximum likelihood approximation shows that the data ranges for all the sets are also satisfied, and the fit within the region is optimized using a standard deviation of 0.5, which corresponds to the minimum standard deviation allowed in this study, as defined in Equation 6.16 ($\sigma = 0.05*(11-1)$).

6.4 REPORTED PARAMETERS

The same parameters are reported for each of the nine damage states. The data needed for the three damage models (Park-Ang, modified Park-Ang, and cumulative plastic deformation) are first tabulated: maximum displacement, hysteretic energy dissipated through cycling of the column, and cumulative plastic deformation experienced by the column. The mean and coefficient of variation for all six columns were reported for each of these quantities to develop a relationship between cycling and damage progression in the columns.

The data are then graphed for the three damage models (the graphs for the Park-Ang damage model are shown in Appendix E). A best-fit line of the data for each damage model was then determined using three methods: the least-squares method, the maximum likelihood method, and the exterior-penalty-function method. After obtaining the upper- and lower-bound observations for the damage state, the parameters that define the best-fit line for each of the calibration methods were computed.

When the exact location of the damage is known (the upper- and lower-bound observations are in the same location), the exterior penalty function defaults to the least-squares approximation. Furthermore, as the standard deviation increases toward infinity, the maximum likelihood method converges to the least-squares approximation. Therefore, the exterior penalty function and maximum likelihood approximation of the best-fit line is not shown in either tabular or graphical form.

The second table of each section provides four parameters for each combination of normalization method and damage model, illustrated in Figure 6.5.

The inverse of the alpha terms (Eqs. 6.1, 6.2 and 6.11) represent the y-intercepts of the best-fit lines. For the Park-Ang damage model, this is the displacement ductility of the column under monotonic loading at each damage state. For the modified Park-Ang and the cumulative plastic deformation damage models, this represents the ultimate drift ratio (%) under monotonic loading for each damage state. The inverse of the beta terms (Eqs. 6.1, 6.2 and 6.11) represent the theoretical maximum amount of cycling needed to reach the damage state. This helps define the best-fit line.

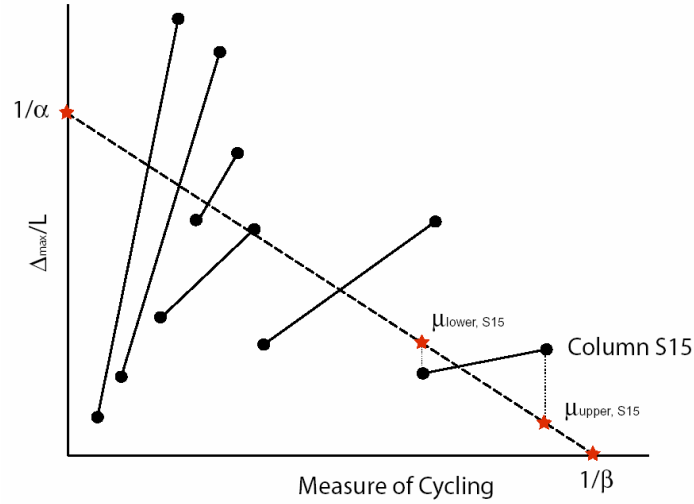


Fig. 6.5 Illustration of reported parameters for each damage state

The slope of the theoretical best-fit line was reported as the ratio of the theoretical maximum displacement at the observation for Column S15 ($\mu_{mean,S15}$) to the theoretical maximum displacement under monotonic loading ($1/\alpha$) shown in Equation 6.28,

$$\frac{\mu_{upper,S15} + \mu_{lower,S15}}{2/\alpha} = \frac{\mu_{mean,S15}}{1/\alpha} = \alpha\mu_{mean,S15} \quad (6.28)$$

where μ_{upper} and μ_{lower} are defined in Sections 6.3.2 and 6.3.3. Because Column S15 underwent much more cycling than the other five columns, this ratio was treated as a proxy for how cycling affected the maximum displacement for each damage state. Based on this ratio, the effect of cycling on the maximum displacement for each damage state was separated into four levels of severity, defined by Equation 6.29:

$$\text{if } \left\{ \begin{array}{l} 1.00 \geq \alpha\mu_{mean,S15} \geq 0.90 \\ 0.90 > \alpha\mu_{mean,S15} \geq 0.75 \\ 0.75 > \alpha\mu_{mean,S15} \geq 0.60 \\ 0.60 > \alpha\mu_{mean,S15} \geq 0.00 \end{array} \right\} \text{ then the effect of cycling is } \left\{ \begin{array}{l} \textit{insignificant} \\ \textit{small} \\ \textit{moderate} \\ \textit{great} \end{array} \right\} \quad (6.29)$$

The final number reported in the second table for each damage state is $\sigma\alpha$, which represents the standard deviation normalized by the y-intercept of the best-fit line. Because the maximum likelihood method assumes that the best-fit line is the mean with a given distribution, this term measures the relative size of that distribution in the same way as a coefficient of variation. When the exact damage state is known, only the least-squares approximation is reported. Therefore, the r^2 value is reported as the measure of goodness of fit.

6.5 FIRST YIELD OF LONGITUDINAL REINFORCEMENT

Table 6.2 and Figure 6.6 show the deformation and energy dissipation for each column at first yield of the longitudinal reinforcement. Because the exact point at which the longitudinal reinforcement first yielded is known, only the best-fit line using the least-squares approximation is reported in Table 6.3.

Table 6.2 Data at first yield of longitudinal reinforcement

Column	Δ_{\max} (in.)	E_h (k-in.)	$\Sigma\Delta_p$ (in.)
S1	0.22	7.16	0.0
S3	0.33	26.9	0.0
S15	0.20	6.20	0.0
C2	0.30	9.40	0.0
C4	0.29	10.1	0.0
C3R	0.32	9.55	0.0
μ	0.28	11.6	0.0
σ	0.05	7.67	0.0
δ (%)	17	66	NA

Defining cumulative plastic deformation as the summation of all deformations beyond the yield displacement means that there will be no plastic deformation for the first yield of longitudinal reinforcement. As a result, a best-fit line of the data for the cumulative plastic deformation damage model could not be generated because by definition the cumulative plastic deformation is 0.0 for all of the columns at this point.

Table 6.3 Model parameters at first yield of longitudinal reinforcement

Damage model		Normalization Method
		Least Squares
Park-Ang	$1/\alpha$	0.84
	$1/\beta$	-36.6
	$\mu_{\text{mean,S15}}/(1/\alpha)$	1.02
	r^2	0.23
Modified Park-Ang	$1/\alpha_m$	0.38
	$1/\beta_m$	-0.016
	$\mu_{\text{mean,S15}}/(1/\alpha)$	1.14
	r^2	0.32

The initial yield displacements fall into two groups (Columns S3, C2, C4, and C3R, and Columns S1 and S15). The initial yield displacements between these two sets differed because of the additional slip displacement in Columns S3, C2, C4, and C3R, discussed in Chapter 3.

Therefore, instead of a trend for this damage state for the six columns, it is expected that two groups of data should be clustered.

Figure 6.6 shows that the Park-Ang damage model predicts that the effect of cycling on the maximum displacement at this damage state is insignificant (the slope of the line in Fig. 6.6a is relatively flat). The modified Park-Ang damage model shows that the two groups of data, defined by the two different yield displacements, are separated.

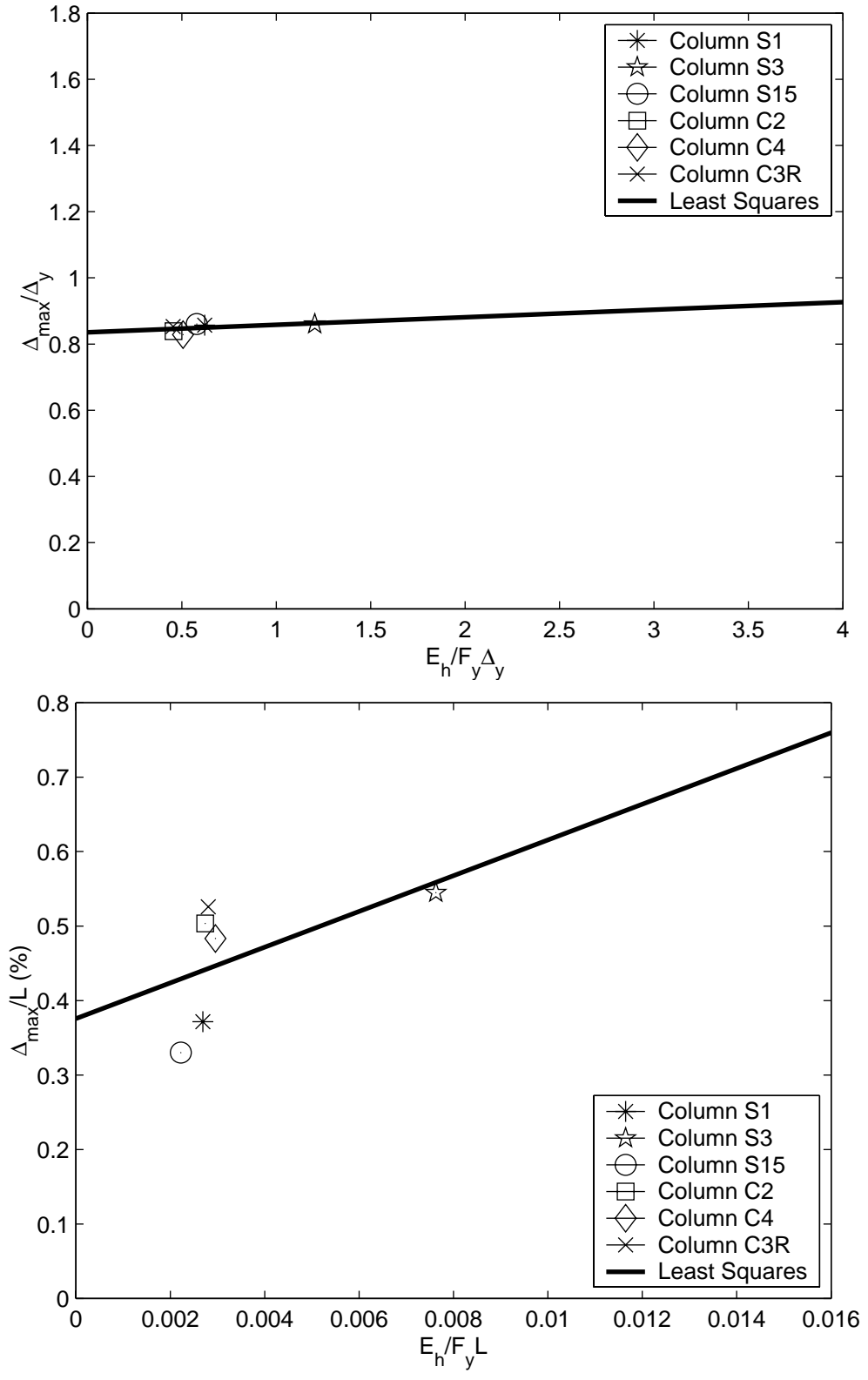


Fig. 6.6 First yield for (a) Park-Ang and (b) modified Park-Ang damage models

6.6 SIGNIFICANT FLEXURAL CRACKING

Table 6.4 and Figure 6.7 show the lower bounds (L.B.) and upper bounds (U.B.) for each column at significant flexural cracking, along with the best-fit lines using each of the calibration methods. The parameters of these lines are tabulated in Table 6.5.

Table 6.4 Data at significant flexural cracking

Column	Δ_{\max} (in.)		E_h (k-in.)		$\Sigma\Delta_p$ (in.)	
	L.B.	U.B.	L.B.	U.B.	L.B.	U.B.
S1	0.33	0.40	13.2	18.1	0.074	0.33
S3	0.26	0.43	10.8	32.5	0.00	0.072
S15	0.33	0.39	28.4	41.6	1.71	4.33
C2	0.09	0.44	0.44	16.6	0.00	0.086
C4	0.18	0.44	4.15	20.9	0.00	0.16
C3R	0.03	0.41	0.16	14.1	0.00	0.039
μ	0.20	0.42	9.53	24.0	0.30	0.84
σ	0.13	0.020	10.7	10.8	0.69	1.72
δ (%)	62	5.4	112	44.9	233	205

Table 6.5 Model parameters at significant flexural cracking

Damage model		Normalization Method		
		Least Squares	Maximum Likelihood	Exterior Penalty
Park-Ang	$1/\alpha$	0.66	0.89	1.13
	$1/\beta$	-2.10	-4.91	-9.45
	$\mu_{\text{mean},S15}/(1/\alpha)$	2.55	1.67	1.35
	$\sigma\alpha$	NA	0.23	NA
Modified Park-Ang	$1/\alpha_m$	0.42	0.63	0.51
	$1/\beta_m$	-0.022	0.21	-0.055
	$\mu_{\text{mean},S15}/(1/\alpha)$	1.57	0.94	1.23
	$\sigma\alpha_m$	NA	0.054	NA
Cumulative Plastic Deformation	$1/\alpha_p$	0.50	0.62	0.56
	$1/\beta_p$	-23.3	120	-42.7
	$\mu_{\text{mean},S15}/(1/\alpha)$	1.22	0.96	1.12
	$\sigma\alpha_p$	NA	0.056	NA

As seen from Table 6.5 and Figure 6.7, both the modified Park-Ang model and the cumulative deformation damage model predict that cycling has an insignificant effect on the maximum drift at the point of significant flexural cracking. Figure 6.7 also shows that Column S15, which had much more cumulative plastic deformation at significant flexural cracking than the other columns, dominates the best-fit line for the cumulative plastic deformation damage model.

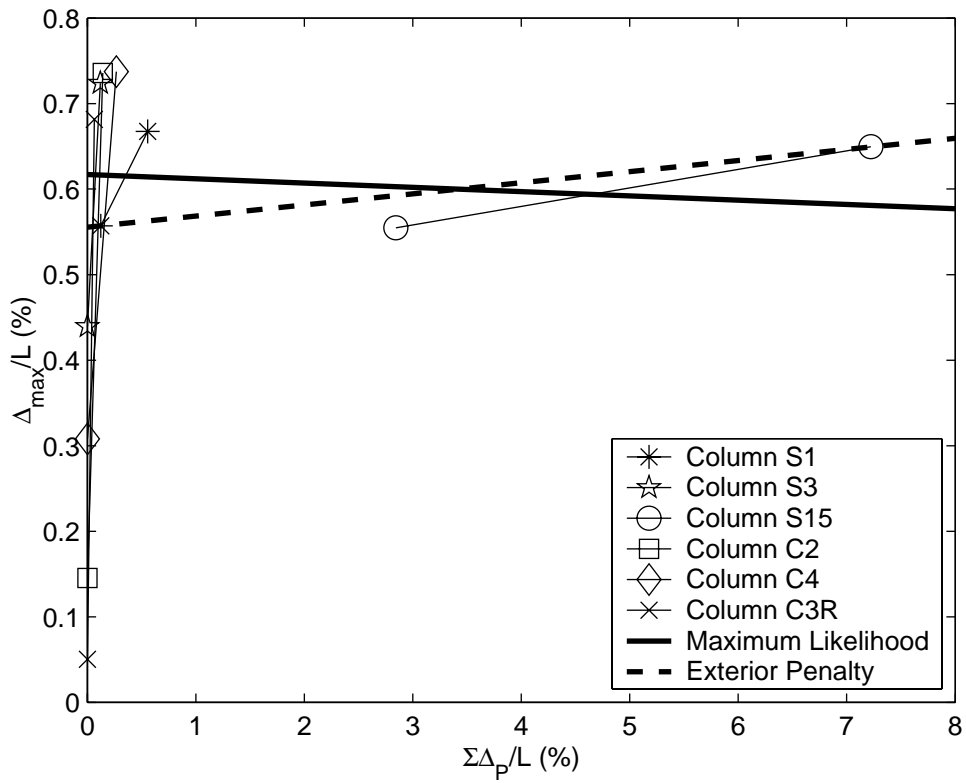
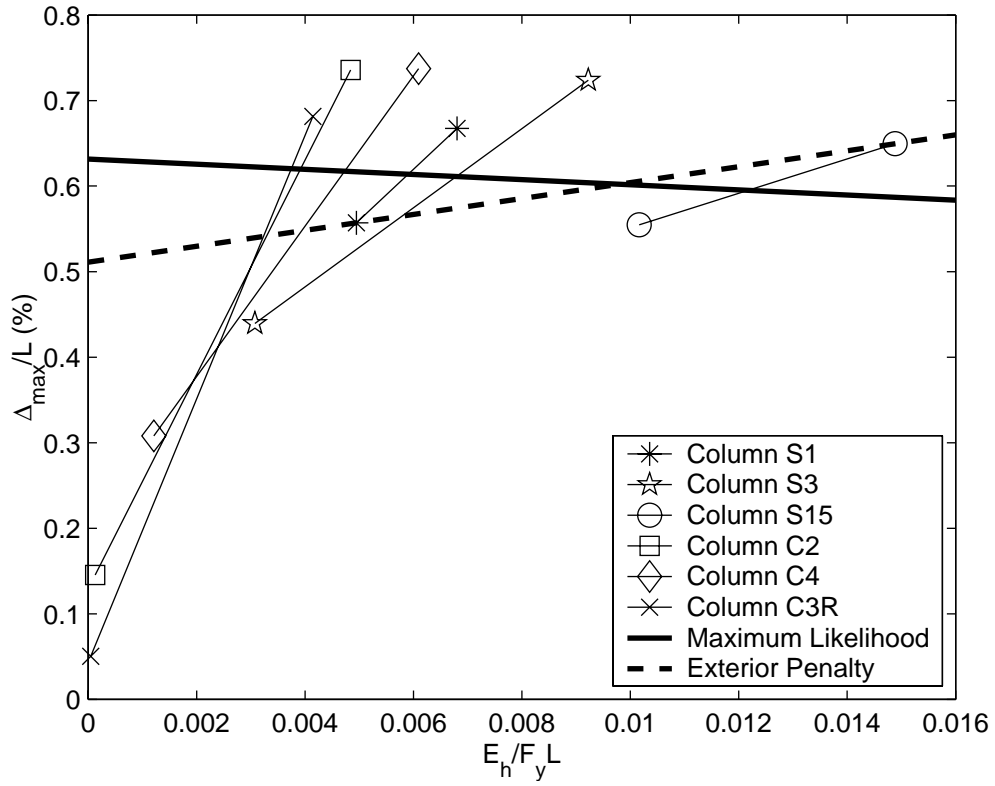


Fig. 6.7 Significant flexural cracking for (a) modified Park-Ang and (b) cumulative plastic deformation

6.7 RESIDUAL CRACKING

Table 6.6 and Figure 6.8 show the lower bounds (L.B.) and upper bounds (U.B.) for each column at residual cracking, along with the best-fit lines using each of the calibration methods. The parameters of these lines are tabulated in Table 6.7.

Table 6.6 Data at residual cracking

Column	Δ_{\max} (in.)		E_h (k-in.)		$\Sigma\Delta_p$ (in.)	
	L.B.	U.B.	L.B.	U.B.	L.B.	U.B.
S1	0.83	1.10	53.0	78.1	2.35	3.79
S3	0.47	0.70	47.4	110	0.87	4.53
S15	0.86	0.94	270	330	38.3	45.0
C2	1.15	1.16	68.8	110	3.50	6.66
C4	0.44	2.23	9.19	210	0.25	7.85
C3R	0.41	1.77	8.32	130	0.15	5.63
μ	0.69	1.32	76.1	161	7.57	12.2
σ	0.30	0.57	98.0	93.8	15.1	16.1
δ (%)	43	43	129	58	200	132

Table 6.7 Model parameters at residual cracking

Damage model		Normalization Method		
		Least Squares	Maximum Likelihood	Exterior Penalty
Park-Ang	$1/\alpha$	2.82	2.98	3.16
	$1/\beta$	-64.7	-183	-315
	$\mu_{\text{mean},S15}/(1/\alpha)$	1.43	1.15	1.09
	$\sigma\alpha$	NA	0.48	NA
Modified Park-Ang	$1/\alpha_m$	1.73	1.79	2.05
	$1/\beta_m$	1.15	0.33	0.33
	$\mu_{\text{mean},S15}/(1/\alpha)$	0.91	0.68	0.67
	$\sigma\alpha_m$	NA	0.36	NA
Cumulative Plastic Deformation	$1/\alpha_p$	1.72	1.64	1.97
	$1/\beta_p$	635	427	237
	$\mu_{\text{mean},S15}/(1/\alpha)$	0.89	0.84	0.71
	$\sigma\alpha_p$	NA	0.37	NA

As seen from Table 6.7 and Figure 6.8, both the modified Park-Ang model and the cumulative deformation damage model predict that cycling has a small effect on the maximum drift at the point of residual cracking. The best-fit lines for both the modified Park-Ang damage model and the cumulative plastic deformation damage model (shown in Fig. 6.8) depend greatly on the data from Column S15, since it had much more cumulative plastic deformation at residual cracking than the other columns.

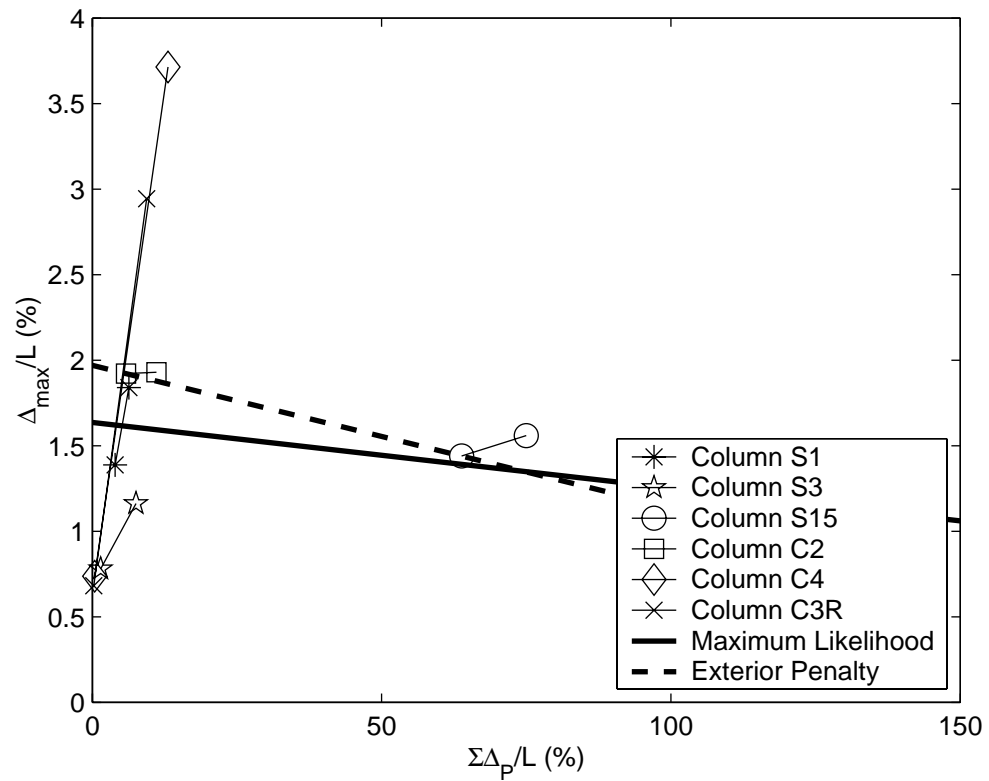
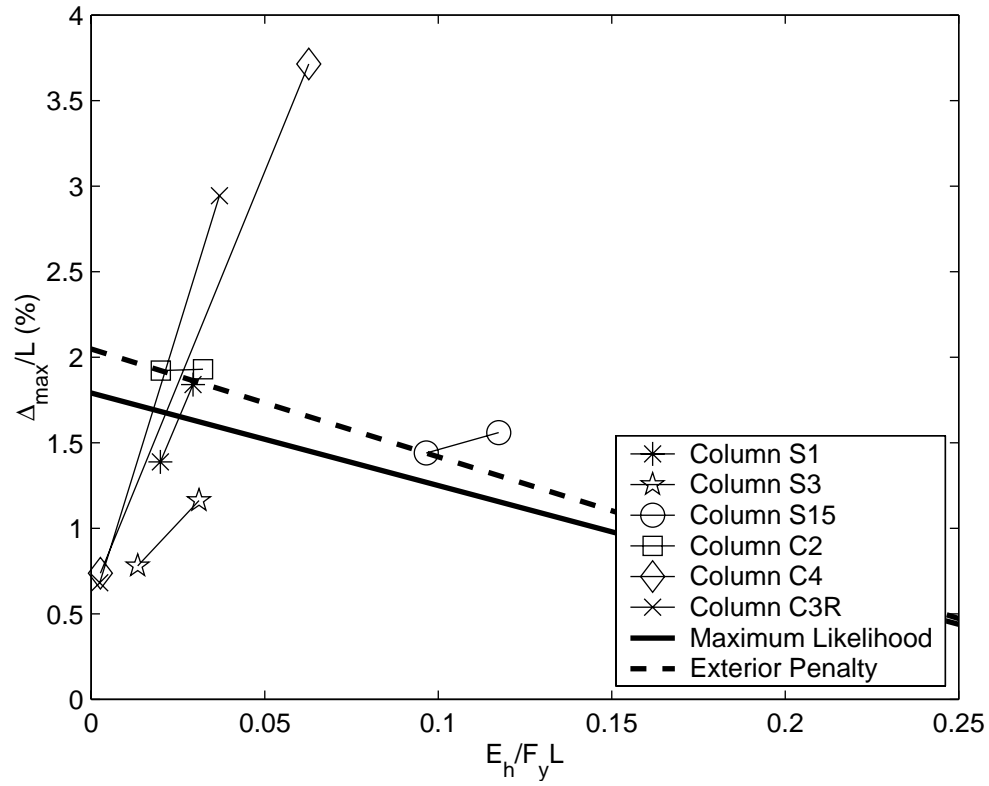


Fig. 6.8 Residual cracking for the (a) modified Park-Ang and (b) cumulative plastic deformation

6.8 SIGNIFICANT SPALLING

Table 6.8 and Figure 6.9 show the lower bounds (L.B.) and upper bounds (U.B.) for each column at significant spalling, along with the best-fit lines using each of the calibration methods. The parameters of these lines are tabulated in Table 6.9.

Table 6.8 Data at significant spalling

Column	Δ_{\max} (in.)		E_h (k-in.)		$\Sigma\Delta_p$ (in.)	
	L.B.	U.B.	L.B.	U.B.	L.B.	U.B.
S1	1.37	1.82	114	162	5.75	8.47
S3	0.67	1.14	76.5	165	1.17	5.29
S15	1.07	1.14	438	548	55.8	66.4
C2	0.45	1.15	22.2	98.0	0.26	2.72
C4	0.38	2.23	14.9	137	0.034	2.15
C3R	0.41	1.77	18.1	155	0.12	4.29
μ	0.73	1.54	114	211	10.5	14.9
σ	0.41	0.46	166	167	22.3	25.3
δ (%)	56	30	144	79	212	170

Table 6.9 Model parameters at significant spalling

Damage model		Normalization Method		
		Least Squares	Maximum Likelihood	Exterior Penalty
Park-Ang	$1/\alpha$	3.13	3.42	3.32
	$1/\beta$	-67.7	-147	-103
	$\mu_{\text{mean},S15}/(1/\alpha)$	1.68	1.31	1.45
	$\sigma\alpha$	NA	0.55	NA
Modified Park-Ang	$1/\alpha_m$	1.85	1.96	1.92
	$1/\beta_m$	-2.57	1.54	19.6
	$\mu_{\text{mean},S15}/(1/\alpha)$	1.07	0.89	0.99
	$\sigma\alpha_m$	NA	0.30	NA
Cumulative Plastic Deformation	$1/\alpha_p$	1.89	1.90	1.92
	$1/\beta_p$	-13300	1690	12400
	$\mu_{\text{mean},S15}/(1/\alpha)$	1.01	0.94	0.99
	$\sigma\alpha_p$	NA	0.29	NA

As seen in Table 6.9 and Figure 6.9, both the modified Park-Ang model and the cumulative deformation damage model predict that cycling had an insignificant effect on the maximum drift at the point of significant spalling. As in the previous damage states, the best-fit lines for the modified Park-Ang damage model and the cumulative plastic deformation damage model depend greatly on the data from Column S15.

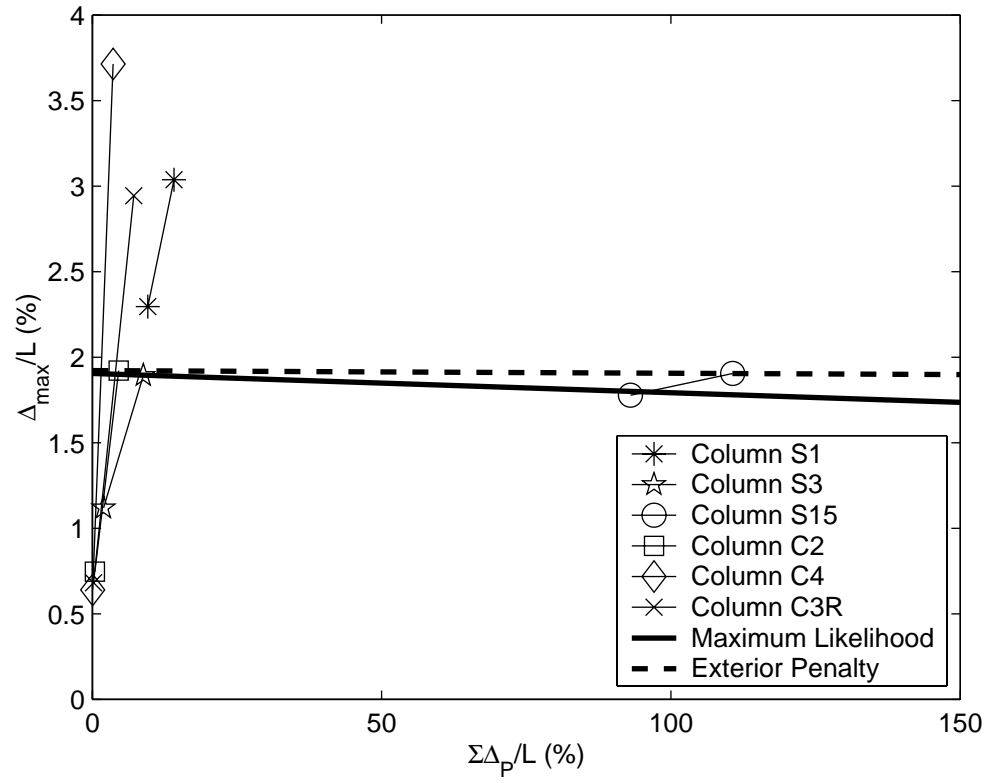
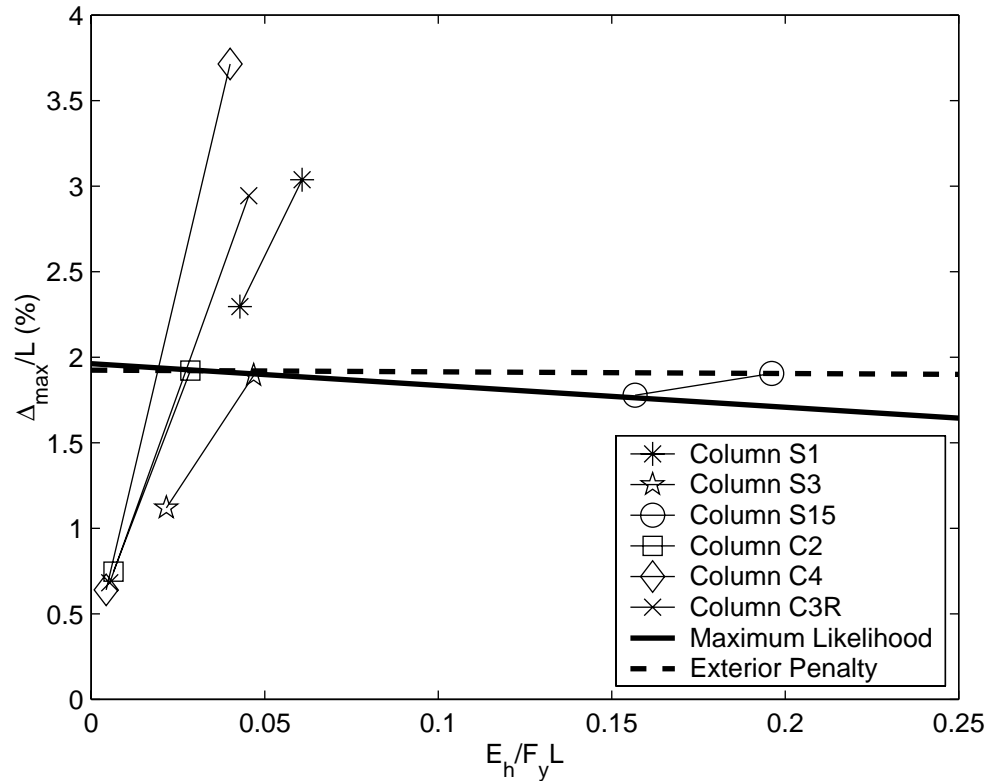


Fig. 6.9 Significant spalling for (a) modified Park-Ang and (b) cumulative plastic deformation

6.9 ONSET OF BAR BUCKLING

Table 6.10 and Figure 6.10 show the lower bounds (L.B.) and upper bounds (U.B.) for each column at the onset of bar buckling, along with the best-fit lines using each of the calibration methods. The parameters of these lines are tabulated in Table 6.11.

Table 6.10 Data at onset of bar buckling

Column	Δ_{\max} (in.)		E_h (k-in.)		$\Sigma\Delta_p$ (in.)	
	L.B.	U.B.	L.B.	U.B.	L.B.	U.B.
S1	1.38	1.82	114	162	5.75	8.47
S3	1.15	1.87	189	404	6.82	18.2
S15	1.14	1.25	547	657	66.4	76.4
C2	1.16	1.88	487	598	37.2	42.6
C4	0.38	2.23	14.9	137	0.034	2.15
C3R	1.77	1.77	102	203	1.55	7.04
μ	1.16	1.82	242	360	19.6	25.8
σ	0.45	0.31	221	228	26.7	28.7
δ (%)	39	17	91	63.4	136	111

Table 6.11 Model parameters at onset of bar buckling

Damage model		Normalization Method		
		Least Squares	Maximum Likelihood	Exterior Penalty
Park-Ang	$1/\alpha$	4.43	4.97	4.75
	$1/\beta$	-359	2320	-1080
	$\mu_{\text{mean},S15}/(1/\alpha)$	1.16	0.98	1.05
	$\sigma\alpha$	NA	0.14	NA
Modified Park-Ang	$1/\alpha_m$	2.69	3.20	3.07
	$1/\beta_m$	1.18	0.56	0.74
	$\mu_{\text{mean},S15}/(1/\alpha)$	0.82	0.61	0.71
	$\sigma\alpha_m$	NA	0.048	NA
Cumulative Plastic Deformation	$1/\alpha_p$	2.64	2.99	2.96
	$1/\beta_p$	603	350	410
	$\mu_{\text{mean},S15}/(1/\alpha)$	0.80	0.66	0.71
	$\sigma\alpha_p$	NA	0.051	NA

As seen from Table 6.11 and Figure 6.10, both the modified Park-Ang model and the cumulative plastic deformation damage model predict that cycling moderately decreased the maximum drift at the point of the onset of bar buckling.

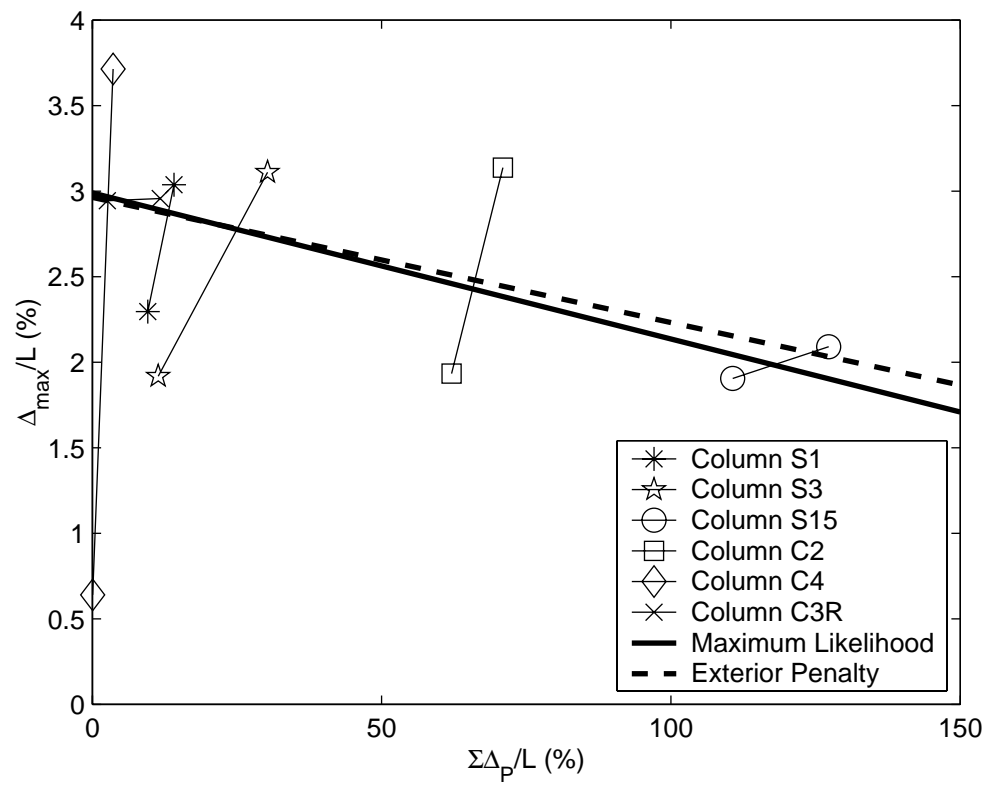
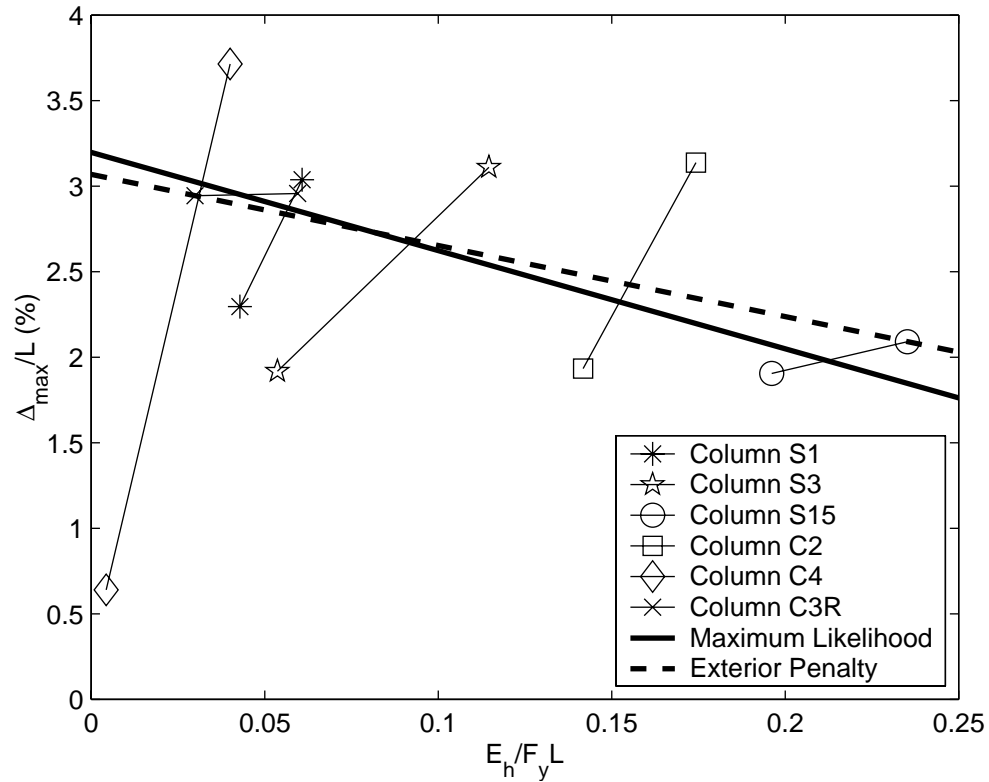


Fig. 6.10 Bar buckling for the (a) modified Park-Ang and (b) cumulative plastic deformation

6.10 HOOP FRACTURE

Table 6.12 and Figure 6.11 show the exact observation for each column at hoop fracture, along with the best-fit line using the least-squares method. The parameters of these lines are tabulated in Table 6.13.

Table 6.12 Data at hoop fracture

Column	Δ_{\max} (in.)	E_h (k-in.)	$\Sigma\Delta_p$ (in.)
S1	NA	NA	NA
S3	1.87	404	18.2
S15	NA	NA	NA
C2	1.88	598	42.6
C4	2.23	137	2.15
C3R	1.77	203	7.03
μ	1.94	336	17.5
σ	0.20	209	18.0
δ (%)	10	62	103

Table 6.13 Model parameters at hoop fracture

Damage model		Normalization Method
		Least Squares
Park-Ang	$1/\alpha$	5.77
	$1/\beta$	208
	$\mu_{\text{mean},S15}/(1/\alpha)$	NA
	r^2	0.13
Modified Park-Ang	$1/\alpha_m$	3.47
	$1/\beta_m$	1.43
	$\mu_{\text{mean},S15}/(1/\alpha)$	NA
	r^2	0.17
Cumulative Plastic Deformation	$1/\alpha_m$	3.35
	$1/\beta_m$	781
	$\mu_{\text{mean},S15}/(1/\alpha)$	NA
	r^2	0.14

Columns S1 and S15 did not experience hoop fracture and are therefore not shown in Table 6.12 or Figure 6.11. As seen from Table 6.13 and Figure 6.11, both the modified Park-Ang model and the cumulative plastic deformation damage model predict that cycling has a small effect on the maximum drift at the point of hoop fracture.

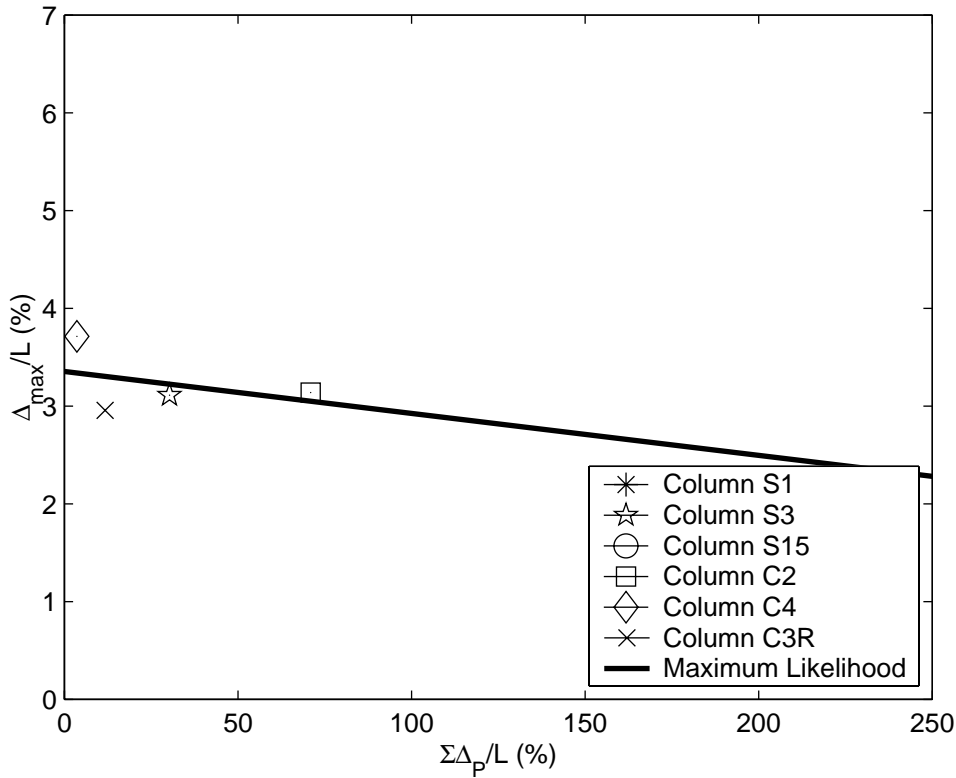
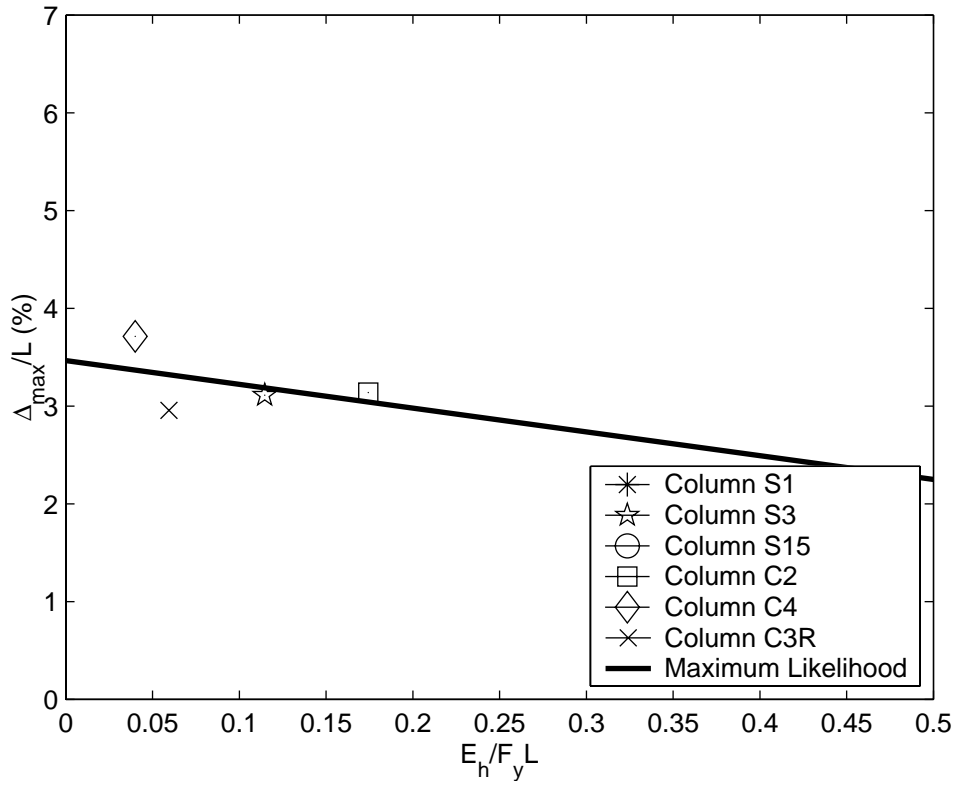


Fig. 6.11 Hoop fracture for the (a) modified Park-Ang and (b) cumulative plastic deformation

6.11 20% LOSS OF LATERAL LOAD

Table 6.14 and Figure 6.12 show the exact observations for each column at 20% loss of lateral load, along with the best-fit line using the least-squares method. The parameters of these lines are tabulated in Table 6.15.

Table 6.14 Data at 20% loss of lateral load

Column	Δ_{\max} (in.)	E_h (k-in.)	$\Sigma\Delta_p$ (in.)
S1	2.27	269	15.3
S3	2.12	640	33.2
S15	1.62	1120	115
C2	2.25	806	57.1
C4	2.23	231	5.88
C3R	1.78	502	29.1
μ	2.05	595	42.6
σ	0.28	338	39.5
δ (%)	14	57	93

Table 6.15 Model parameters at 20% loss of lateral load

Damage model		Normalization Method
		Least Squares
Park-Ang	$1/\alpha$	6.20
	$1/\beta$	-898
	$\mu_{\text{mean},S15}/(1/\alpha)$	1.12
	r^2	0.02
Modified Park-Ang	$1/\alpha_m$	3.91
	$1/\beta_m$	1.48
	$\mu_{\text{mean},S15}/(1/\alpha)$	0.73
	r^2	0.43
Cumulative Plastic Deformation	$1/\alpha_m$	3.75
	$1/\beta_m$	775
	$\mu_{\text{mean},S15}/(1/\alpha)$	0.75
	r^2	0.47

As seen from Table 6.15 and Figure 6.12, both the modified Park-Ang model and the cumulative deformation damage model predict that cycling significantly decreases the maximum drift at the point of 20% loss of lateral load.

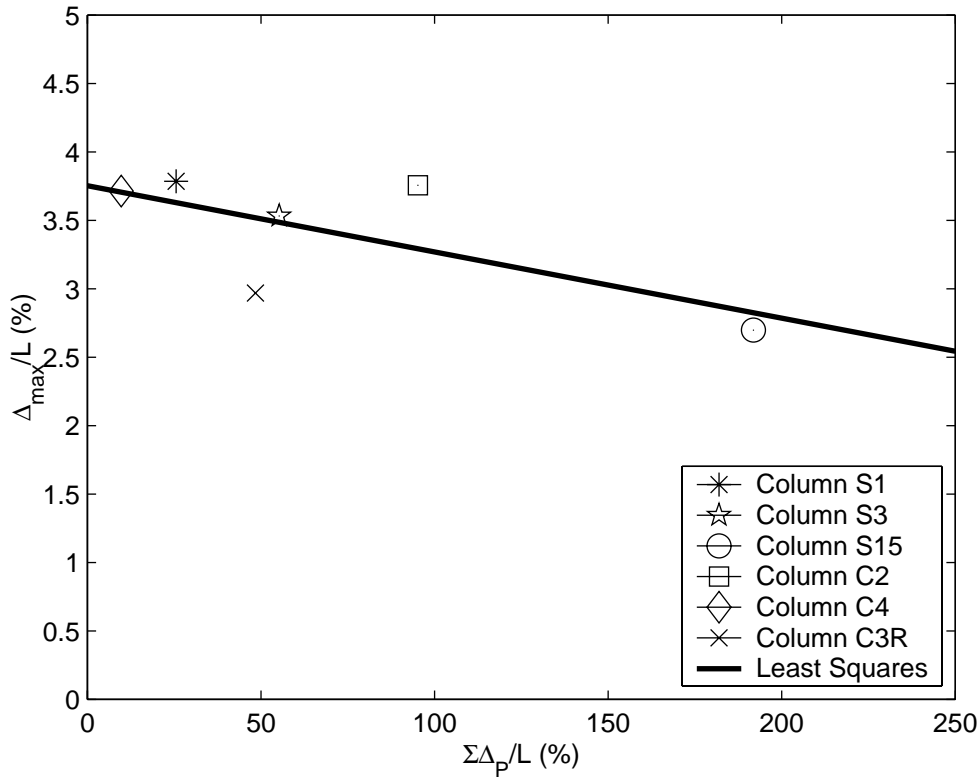
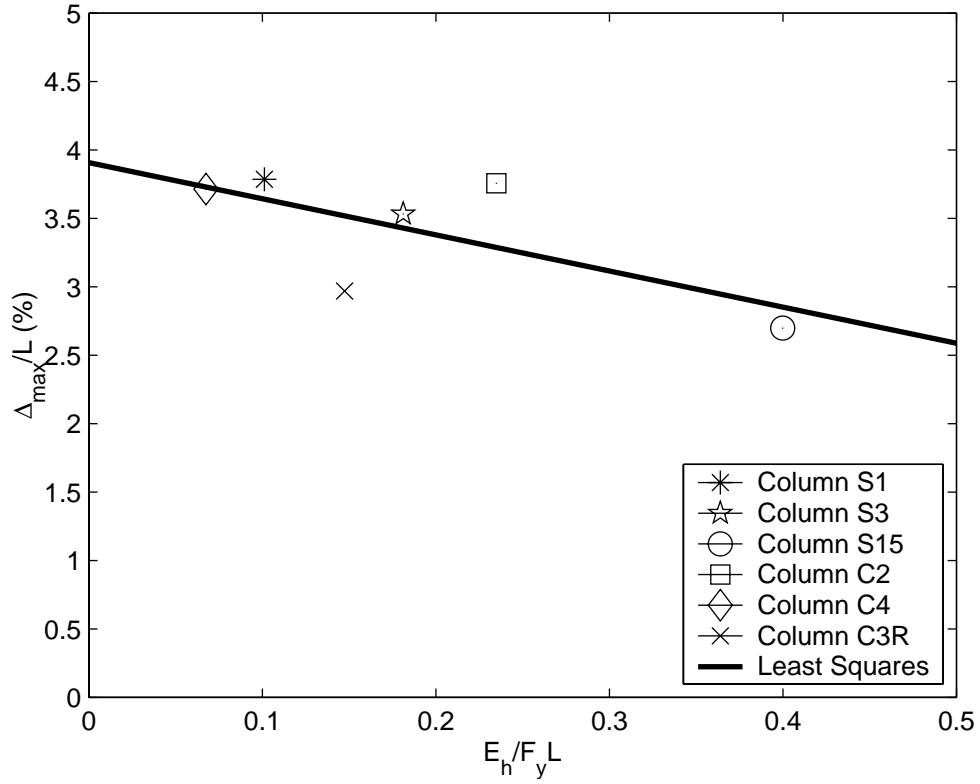


Fig. 6.12 20% loss of lateral load for the (a) modified Park-Ang and (b) cumulative plastic deformation

6.12 50% LOSS OF LATERAL LOAD

Table 6.16 and Figure 6.13 show the exact observations for each column at 50% loss of lateral load, along with the best-fit line using the least-squares method. The parameters of these lines are tabulated in Table 6.17.

Table 6.16 Data at 50% loss of lateral load

Column	Δ_{\max} (in.)	E_h (k-in.)	$\Sigma\Delta_p$ (in.)
S1	2.34	272	15.4
S3	2.12	639	33.2
S15	1.66	1180	121
C2	2.28	907	60.6
C4	2.29	614	40.5
C3R	1.80	745	51.2
μ	2.08	726	53.7
σ	0.29	305	36.5
δ (%)	14	42	68

Table 6.17 Model parameters at 50% loss of lateral load

Damage model		Normalization Method
		Least Squares
Park-Ang	$1/\alpha$	6.39
	$1/\beta$	-1440
	$\mu_{\text{mean},S15}/(1/\alpha)$	1.08
	r^2	0.03
Modified Park-Ang	$1/\alpha_m$	4.21
	$1/\beta_m$	1.30
	$\mu_{\text{mean},S15}/(1/\alpha)$	0.67
	r^2	0.48
Cumulative Plastic Deformation	$1/\alpha_m$	4.00
	$1/\beta_m$	670
	$\mu_{\text{mean},S15}/(1/\alpha)$	0.70
	r^2	0.50

As seen from Table 6.17 and Figure 6.13, both the modified Park-Ang model and the cumulative plastic deformation damage model predict that cycling moderately decreases the maximum drift at the point of 50% loss of lateral load.

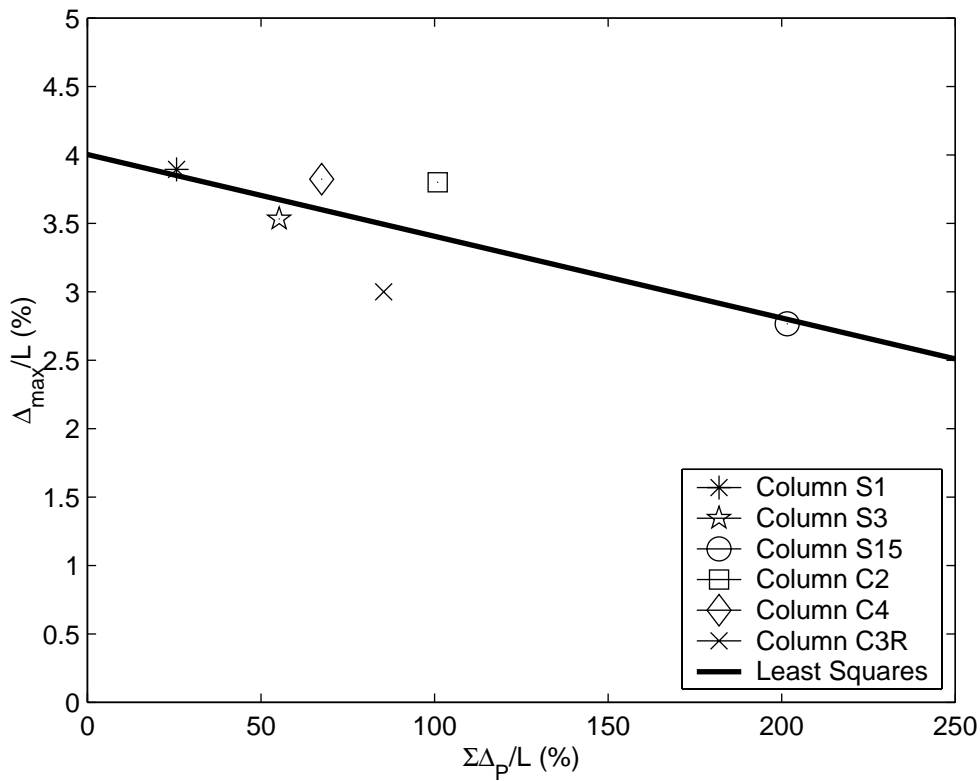
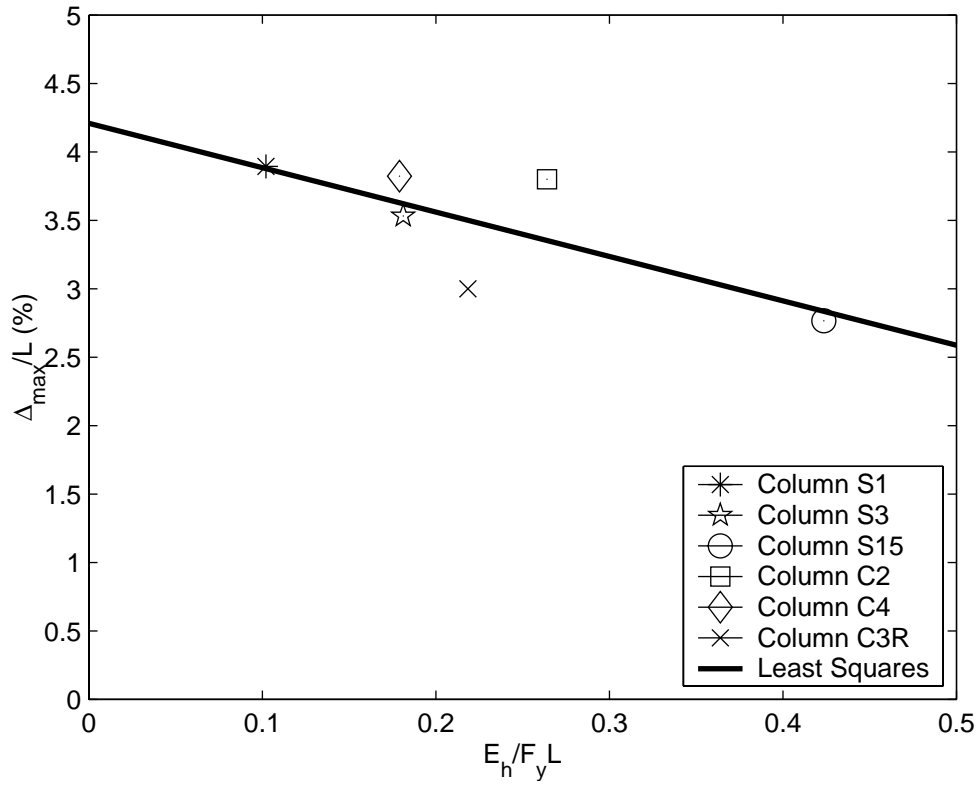


Fig. 6.13 50% loss of lateral load for the (a) modified Park-Ang and (b) cumulative plastic deformation

6.13 LOSS OF AXIAL LOAD

Table 6.18 and Figure 6.14 show the exact observations for each column at the loss of axial load, along with the best-fit line using the least-squares method. The parameters of these lines are tabulated in Table 6.19.

Table 6.18 Data at loss of axial load (all columns)

Column	Δ_{\max} (in.)	E_h (k-in.)	$\Sigma\Delta_p$ (in.)
S1	2.73	381	26.8
S3	2.85	709	41.1
S15	1.76	1190	124
C2	2.25	929	63.2
C4	3.54	852	80.2
C3R	1.80	854	69.2
μ	2.49	819	67.4
σ	0.69	267	33.8
δ (%)	28	33	50

Table 6.19 Model parameters at loss of axial load (all columns)

Damage model		Normalization Method
		Least Squares
Park-Ang	$1/\alpha$	8.19
	$1/\beta$	1140
	$\mu_{\text{mean},S15}/(1/\alpha)$	0.90
	r^2	0.01
Modified Park-Ang	$1/\alpha_m$	5.85
	$1/\beta_m$	0.89
	$\mu_{\text{mean},S15}/(1/\alpha)$	0.52
	r^2	0.30
Cumulative Plastic Deformation	$1/\alpha_m$	5.09
	$1/\beta_m$	612
	$\mu_{\text{mean},S15}/(1/\alpha)$	0.66
	r^2	0.17

As seen from Table 6.19 and Figure 6.14, both the modified Park-Ang model and the cumulative plastic deformation damage model predict that cycling greatly decreases the maximum drift at the point of loss of axial load.

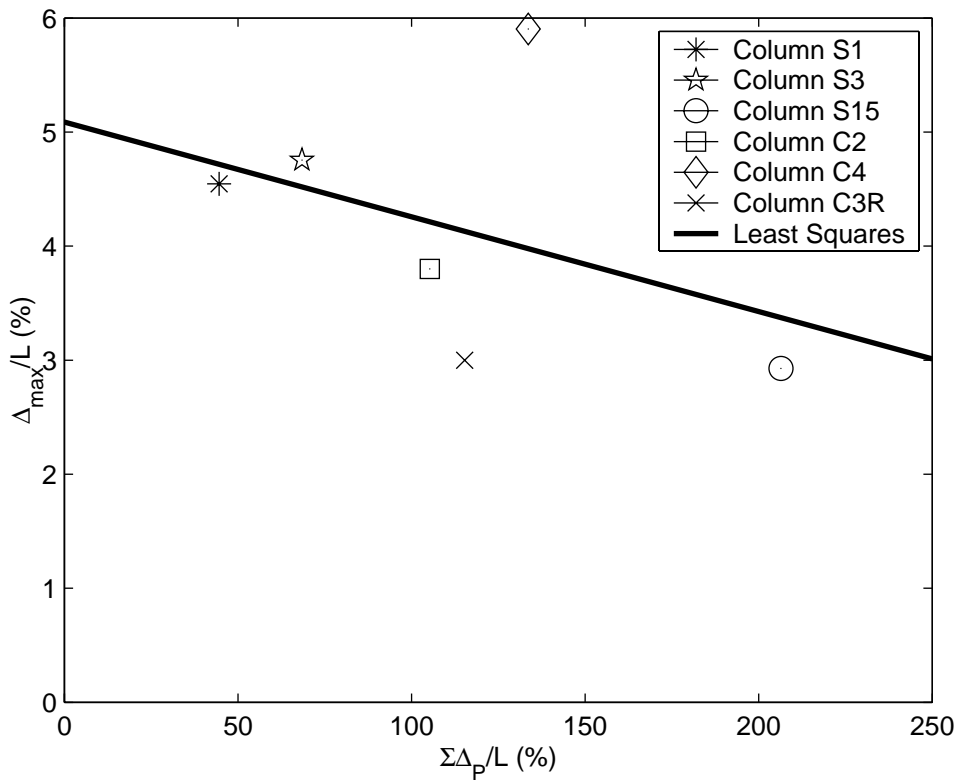
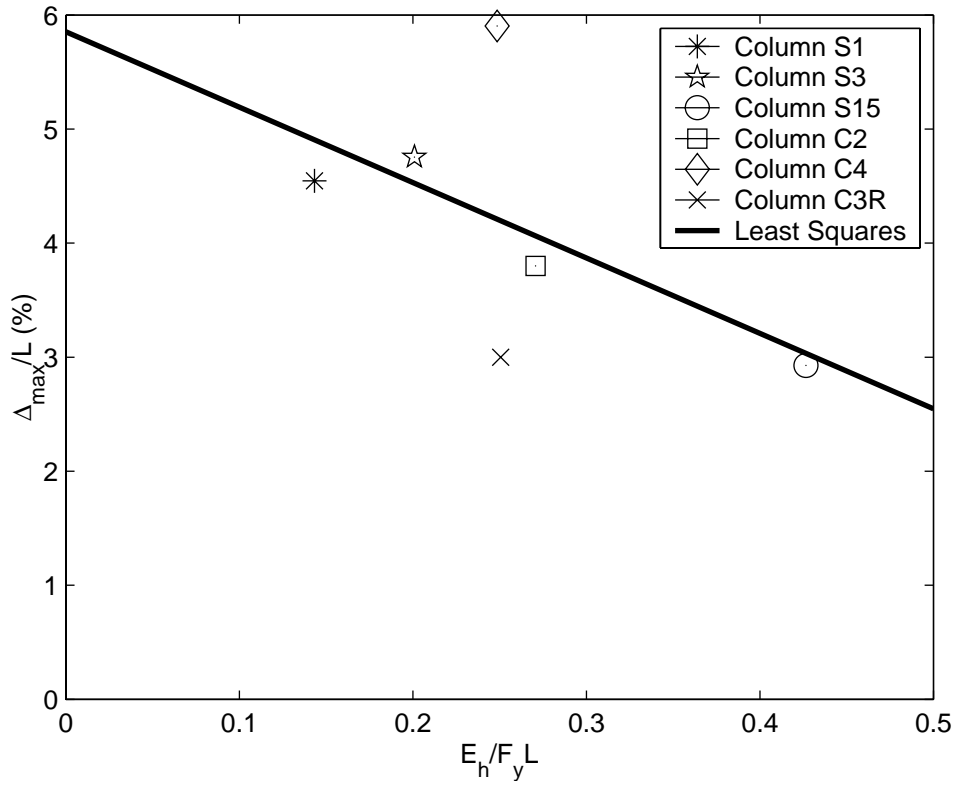


Fig. 6.14 Loss of axial load for the (a) modified Park-Ang and (b) cumulative plastic deformation (all columns)

Because Column C4 experienced a flexural failure, and the other five columns experienced flexure-shear failures, the damage models were also calibrated using the data for only Columns S1, S3, S15, C2 and C3R, as seen in Figure 6.15. The calibration parameters for this case are listed in Table 6.20.

Table 6.20 Model parameters at loss of axial load (excluding Column C4)

Damage model		Normalization Method
		Least Squares
Park-Ang	$1/\alpha$	7.49
	$1/\beta$	3220
	$\mu_{\text{mean},S15}/(1/\alpha)$	0.97
	r^2	0.00
Modified Park-Ang	$1/\alpha_m$	5.42
	$1/\beta_m$	0.87
	$\mu_{\text{mean},S15}/(1/\alpha)$	0.51
	r^2	0.55
Cumulative Plastic Deformation	$1/\alpha_m$	5.05
	$1/\beta_m$	438
	$\mu_{\text{mean},S15}/(1/\alpha)$	0.53
	r^2	0.68

Comparison of Figure 6.14 and Figure 6.15 shows that the damage models predict that cycling had a slightly larger influence on the maximum displacement at the loss of axial-load capacity if Column C4 is excluded from the calibration.

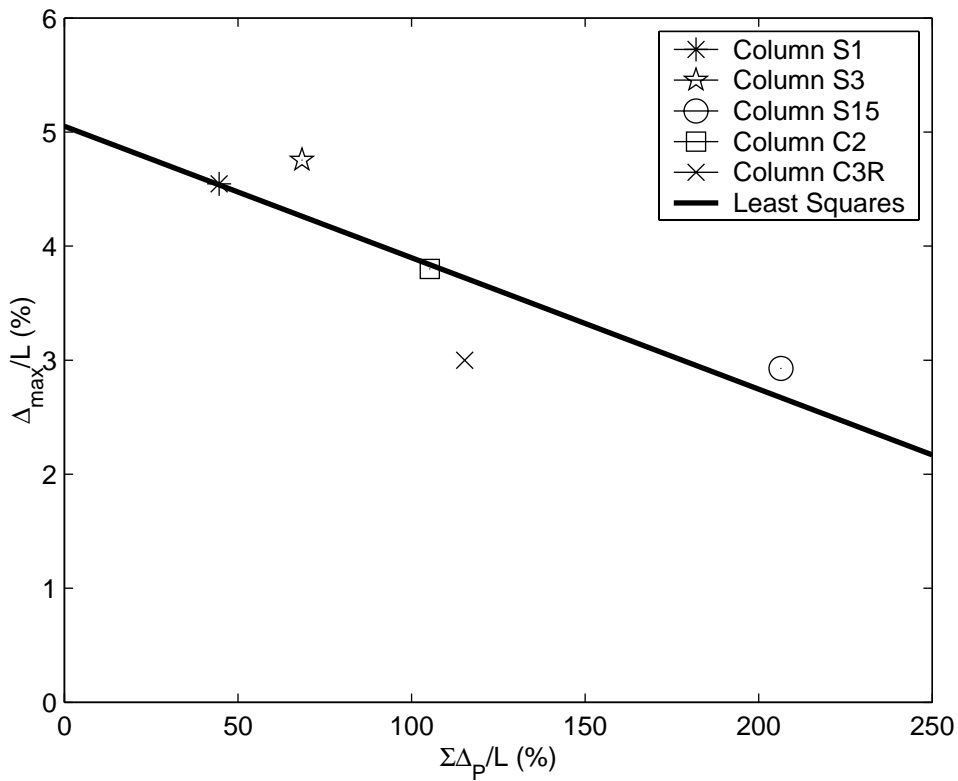
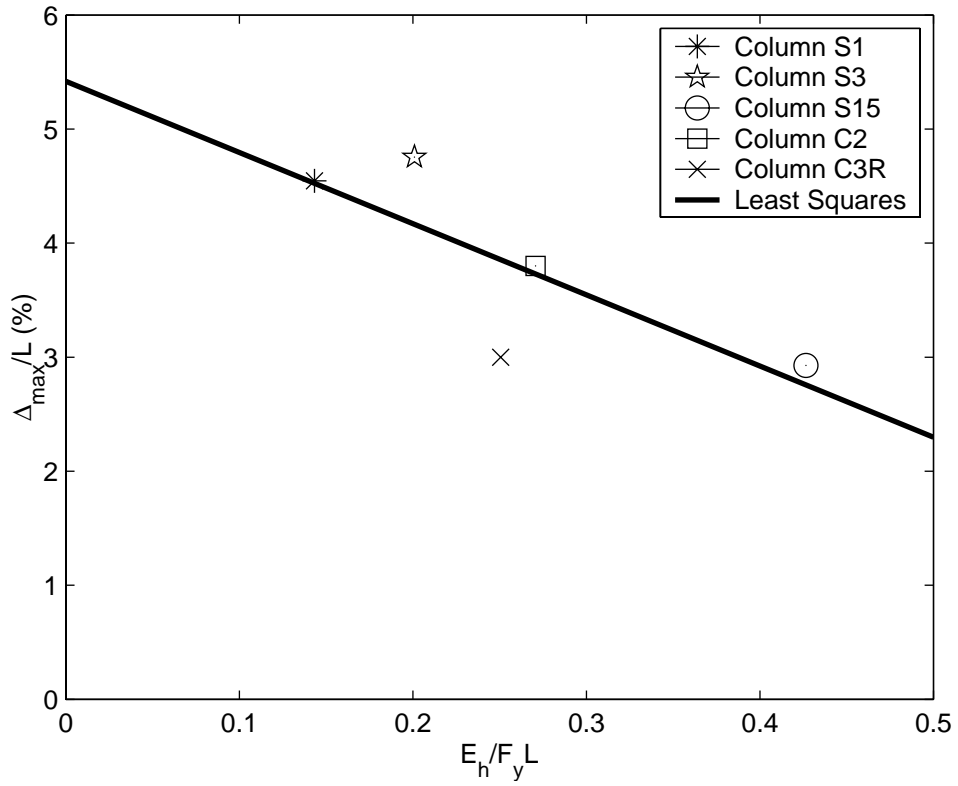


Fig. 6.15 Loss of axial load for the (a) modified Park-Ang and (b) cumulative plastic deformation (excluding Column C4)

6.14 DISCUSSION

The effect of cycling on the maximum column displacement for the nine damage states was investigated using the Park-Ang damage model, the modified Park-Ang damage model, and the cumulative plastic deformation damage model. The Park-Ang damage model measures the effect of cycling by the dissipated hysteretic energy, and normalizes these data by the column's yield force and displacement. The modified Park-Ang model also measures cycling by the dissipated hysteretic energy, but normalizes the data by the column height. The cumulative plastic deformation damage model measures the effect of cycling by the total amount of deformation above the yield displacement that the column experiences, and normalizes the data by the column height. The three damage models were calibrated using three methods: the least-squares approximation, the maximum likelihood approximation, and the external penalty function approximation.

6.14.1 Comparison of Damage Models

Once the data were normalized for each column, the predictions made by the Park-Ang model became inconsistent with the predictions made by the modified Park-Ang and cumulative plastic deformation damage models. Although all six columns were nominally the same, the yield displacement of Columns S1 and S15 were significantly smaller (32%) than the yield displacements of the other columns. Section 4.5 showed that the differences in these displacements are mainly attributed to the larger slip displacements in Columns S3, C2, C4, and C3R. This larger slip deformation was attributed to the presence of strain gages in the footings of these four columns, which decreased the bond stress between the longitudinal reinforcement and the concrete.

The yield displacement was based on a combination of three factors: flexure, shear, and anchorage slip. If the yield displacement had been a function of only the flexure and shear, the yield displacement would have been similar for the six columns, and the results of the analyses in this chapter using the Park-Ang damage model would resemble the results obtained by the modified Park-Ang damage model. However, because the inconsistencies of the Park-Ang damage model are attributed to its sensitivity to the differences in the anchorage slip portion of

the yield displacement, the results from this model are shown in Appendix E but were not used in this evaluation phase of the study.

Both the modified Park-Ang damage model and the cumulative plastic deformation damage model use column length instead of the yield displacement as a normalizing factor. The cumulative plastic deformation damage model includes the yield displacement of each column because it is used in determining the plastic deformation. However, because the column deformations are much larger than the difference in the yield displacements of each column, this inclusion does not significantly affect the data.

Another benefit of using the cumulative plastic deformation damage model is that the measure of cycling is only deformation dependent. This allows the cumulative plastic deformation model to be used as a predictive tool if the applied displacement history is known.

Both the modified Park-Ang damage model and the cumulative plastic deformation damage model were calibrated based on six columns with the same aspect ratio, axial-load ratio, and reinforcing details. To increase the range of application of the results, the calibrations should include data from column tests with other properties.

6.14.2 Calibration Method Comparison

The least-squares approximation was used to fit the data of each damage state. This method does not apply a weight to the lower and upper bounds, and therefore does not do a good job fitting the data when only the bounds are available, and not the exact value. Therefore, if the exact values at each damage state are unknown, the exterior penalty function and maximum likelihood approximations are applied.

The exterior penalty function uses the least-squares approximation and adds a penalty if the bounds are broken. If the weight on the exterior penalty function is large ($\gamma \geq 20$), compared to the least-squares approximation, this method will place a large priority on minimizing the maximum relative boundary break. In this study, this method optimizes the fit by starting at the least-squares approximation and then adjusting the line to minimize the penalty. When there are no bounds, and only a single point is known, the exterior penalty function defaults to the least-squares method.

The maximum likelihood approximation incorporates satisfying the bounds while searching for the best fit by placing a normal distribution on the fitting line. The value of the

standard deviation of this distribution is optimized along with the parameters of the line (y-intercept and slope), to maximize the likelihood that the predicted value lies between the lower- and upper-bound observations. This method is valid for either bounded or exact observations. For bounded observations that can all be satisfied, the optimum distribution of the best-fit line would be $\sigma = 0$, which would give a likelihood of 1. When all of the bounded observations cannot be satisfied with a standard deviation of zero, the standard deviation of the best-fit line is chosen to maximize the likelihood that all the observations are satisfied. If the observations for a particular damage state are exact (the lower-bound and upper-bound observations are in the same location), the optimum distribution would be $\sigma = \infty$, which gives the same answer as the least-squares approximation. Lower-bound and upper-bound limitations were applied to the standard deviation to ensure convergence to a unique solution.

Because of the limitations of the least-squares and exterior-penalty-function methods, and the robustness of the maximum likelihood method, the best-fit line using the maximum likelihood approximation was determined to be the best method.

6.14.3 Calibration Results Comparison

Whereas the modified Park-Ang damage model quantifies cycling by the amount of hysteretic energy dissipated by the column, the cumulative plastic deformation damage model quantifies the amount of cycling by the cumulative column deformation above the yield displacement. Despite this difference, both models predicted a similar effect of cycling for each damage state, summarized in Table 6.21.

The effect of cycling on each damage state was defined in Equation 6.29. The value $\mu_{\text{mean},S15}$, which relates the estimated maximum displacement for Column S15 to the maximum displacement in a monotonic test, was approximated by averaging the ratio from the following combinations: the modified Park-Ang damage model and the cumulative plastic deformation damage model, each calibrated by the exterior-penalty-function method and the maximum likelihood method. This average number, as well as the classification for the effect of cycling for each damage state (defined in Eq. 6.29), are both listed in Table 6.21. This measure was not possible for hoop fracture because Columns S1 and S15 did not experience this damage state.

Using the definition listed in Equation 6.29, Table 6.21 shows that the effect of cycling on the early damage states is insignificant, while its effect on the later damage states becomes

more significant. Specifically, that cycling moderately or greatly decreases the column displacement corresponding to the damage states of bar buckling, the 20% and 50% loss of lateral-load capacity, and the loss of axial load.

Table 6.21 Effect of cycling on each damage state

Damage State	$Y_{\text{mean,S15}}/(1/\alpha)$	Effect of Cycling
First Yield of Longitudinal Reinforcement	1.0	Insignificant
Significant Flexural Cracking	1.2	Insignificant
Residual Cracking	0.83	Small
Significant Spalling	0.98	Insignificant
Bar Buckling	0.72	Moderate
Hoop Fracture	NA	NA
20% Loss of Lateral Load	0.74	Moderate
50% Loss of Lateral Load	0.69	Moderate
Loss of Axial Load (All Columns)	0.59	Great
Loss of Axial Load (Excluding Column C4)	0.52	Great

Defining the effect of cycling as the estimated maximum deformation of Column S15, normalized by the maximum column deformation under a monotonic test, places a lot of emphasis on the results of the Column S15 test. The maximum column deformation vs. cycling figures (sections 6.5–6.13) also show that many times the calibration of the damage models are highly dependent on Column S15. For example, Figure 6.9 shows that only a weak trend could be established without the data for Column S15.

7 Conclusions and Recommendations

The effect of cycling on the behavior of reinforced concrete columns was investigated experimentally by subjecting six nominally identical columns to a variety of load histories. The measured response of the columns provided the opportunity to evaluate the accuracy of force-displacement modeling strategies and damage accumulation models.

7.1 MEASURED FORCE-DISPLACEMENT RESPONSE

The experimental program for the six lightly confined columns is summarized in Chapter 2, with details provided in Appendix A. The measured force-displacement response of the columns are presented in Chapter 3; appendices B and C report the individual response histories.

In all cases, the peak column force was governed by the flexural strength of the columns. The force-displacement envelopes for Columns S3, C2, C4, and C3R were similar, but they differed from the envelopes for Columns S1 and S15. The main cause of the differences among the peak forces between the six columns was the axial load in the two groups of columns. Although the axial-load ratios for all six columns were similar, the concrete strength for Columns S1 and S15 was less than that of the other four columns. As a result, Columns S1 and S15 were subjected to a lower axial load, and they had a lower flexural strength.

All columns besides Column C4 lost their axial capacity as a result of flexure-shear failures at drift ratios in the range of 2.9–4.8%. Column C4 lost its axial capacity due to a pure flexural failure at a drift ratio of 5.9%. The differences in failure mode and displacement suggest that the load history can change the failure mode.

7.2 FORCE-DISPLACEMENT MODELING

The calculated to the measured force-displacement envelopes were compared in Chapter 4. The calculated force-displacement envelopes were composed of a combination of estimates of the flexural, shear, and anchorage-slip deformations.

The analytical results were computed with concrete models proposed by Mander, Priestley, and Park (1988), as well as Razvi and Saatcioglu (1999). Steel behavior was modeled using a modified Burns and Seiss (1962) constitutive model, and bond slip was modeled using a methodology proposed by Lehman (1998). Based on comparisons of measured stiffness to computed stiffness and measured peak force to computed peak force, the following conclusions were made:

- The peak column force was consistently underpredicted (8%–12%) and the effective column stiffness was overpredicted (0%–8%). The accuracy of the estimate depended on the assumptions of the concrete model and the value of the concrete elastic modulus.
- In general, the effective column stiffness was most accurately predicted when the Razvi-Saatcioglu model was used. The Razvi-Saatcioglu model was more successful at predicting post-peak force behavior at large displacements than the Mander-Priestley-Park model, particularly when lower values of E_c were assumed.
- The column ductility was underpredicted in Columns S3, C2, C4, and C3R. At 2% drift ratio the average predicted strength for these four columns was 14% lower than the measured strength. The column ductility was accurately predicted for Columns S1 and S15. At 2% drift, the average predicted drift for these two columns was 3% lower than the measured strength.
- One method of increasing the ductility of the calculated column force-deformation relationship is to increase the confinement ratio. The ductility of all of the columns was accurately predicted when the confinement ratio was tripled (from 0.15%–0.45%).

Although all six columns were nominally identical, Columns S3, C2, C4, and C3R had a yield displacement that was approximately 48% larger than that of Columns S1 and S15 (0.37 in. vs. 0.25 in.). Half of this difference can be explained by the difference in slip displacements of the six columns. From strain gage data in the footings of Columns S3, C2, C4, and C3R, the bond stress was determined to be approximately half the bond stress in Columns S1 and S15

($7\sqrt{f_c'}$ vs. $12\sqrt{f_c'}$). This difference in bond stress accounts for a difference of 0.06 in. in the yield displacement (0.13 in. of slip displacement vs. 0.07 in. of slip displacement).

7.3 EVALUATION OF DAMAGE MODELS

Damage levels were recorded for each column at nine damage states (Chapter 5). The point at which the damage occurred, as well as the cycle number and the maximum deformation, were recorded, and each damage state was documented with a picture.

In Chapter 6, three methods were presented for measuring the effect of cycling on the maximum column displacement before each damage state: the Park-Ang damage model, a modified Park-Ang damage model and a cumulative plastic deformation damage model.

The Park-Ang damage model normalizes the measured effect of cycling by the yield displacement. Therefore, this model is sensitive to small changes in the yield displacement. Although the six columns were nominally identical, the presence of strain gages in the footings of Columns S3, C2, C4, and C3R increased the portion of the yield displacement that is attributable to anchorage slip. Because of this added displacement, the effect of cycling did not correlate well with damage accumulation using the Park-Ang damage model. Although the modified Park-Ang damage model also quantified the effect of cycling by the amount of hysteretic energy dissipated, it normalizes the data by the column height instead of the yield displacement, which makes it relatively insensitive to small changes in the yield displacement.

The cumulative plastic deformation damage model quantifies the effect of cycling by the accumulation of plastic column deformation. Although this calculation requires an estimate of the yield displacement, it is less sensitive to errors in the estimate of the yield displacement because it normalizes these data by the column height.

The three damage models were calibrated using three methods: a least-squares approximation, a maximum likelihood approximation, and an exterior penalty function approximation. The least-squares approach was sufficient when a damage state could be measured exactly and did not have upper-bound and lower-bound observations. When upper- and lower-bound observations were necessary, the least-squares approximation did not account for the bounding values. The maximum likelihood and exterior penalty function approximations were developed to better handle the calibration of the damage states with bounded observations.

A method for quantifying the effect of cycling on each damage state was developed. This method took the ratio of the maximum predicted deformation after the cycling of Column S15 to the predicted deformation under monotonic loading. If this ratio was in the ranges of 1.00– 0.90, 0.89–0.75, 0.74– 0.60, or 0.59–0.00, then the effect of cycling was considered insignificant, small, moderate or large, respectively. Both the modified Park-Ang damage model and the cumulative plastic deformation damage model resulted in the same predictions for how cycling effected each damage state, independent of the measure of cycling.

Both the modified Park-Ang damage model and the cumulative plastic deformation damage model predicted that cycling has insignificant effect on three damage states: first yield of longitudinal reinforcement, significant flexural cracking and significant spalling. The two damage models predicted that there was a small effect of cycling on residual cracking, and moderate effect of cycling on bar buckling, 20% loss of lateral-load capacity, and 50% loss of lateral-load capacity. They predicted that cycling had a large effect on the loss of axial-load capacity.

7.4 SUGGESTIONS FOR FURTHER RESEARCH

The three damage models for the lightly confined columns were calibrated using the results of six column tests. To further refine the calibration parameters, a larger series of tests is needed. For example, the concrete used for the first four column tests (Columns S3, C2, C4, and C3R) was stronger than intended and exceeds the likely present strength of Washington State bridge columns. A series of tests should be performed with a lower concrete strength (as in Columns S1 and S15). To test the validity of using a damage model calibrated for a column of one aspect ratio to predict damage for a similar column of a different aspect ratio, tests of columns with different aspect ratios should be performed. The observed damage could then be compared to the damage predicted by the previously calibrated damage model. Such tests might also lead to alternate expressions for the plastic-hinge length.

Many of the trends found for each damage level depended heavily on the data for Column S15. Therefore, tests with a cycling pattern similar to Column S15 should be conducted to reinforce these trends.

REFERENCES

- AASHO (1953), *Standard Specifications for Highway Bridges (6th Edition)*. The American Association of State Highway Officials (AASHO), Washington, D.C.
- AASHO (1961), *Standard Specifications for Highway Bridges (8th Edition)*. The American Association of State Highway Officials (AASHO), Washington, D.C.
- AASHO (1965), *Standard Specifications for Highway Bridges (9th Edition)*. The American Association of State Highway Officials (AASHO), Washington, D.C.
- AASHTO (1989), *Standard Specifications for Highway Bridges (14th Edition)*. The American Association of State Highway and Transportation Officials (AASHTO), Washington, D.C.
- AASHTO (1994), *LRFD Bridge Design Specifications (1st Edition)*. The American Association of State Highway and Transportation Officials (AASHTO), Washington, D.C.
- ACI (1996), *Building Code Requirements for Structural Concrete (ACI 318-95) and Commentary (ACI 318R-95) (Third Printing)*. American Concrete Institute (ACI), Farmington Hills, Michigan.
- ACI (1999), *Building Code Requirements for Structural Concrete (ACI 318-99) and Commentary (ACI 318R-99) (First Printing)*. American Concrete Institute (ACI), Farmington Hills, Michigan.
- Ang, A.H.-S., Kim, W.J., and Kim, S.B. (1993), "Damage Estimation of Existing Bridge Structures." *Structural Engineering in Natural Hazards Mitigation: Proceedings of the ASCE Structures Congress*, Irvine, California, Volume 2, 1137-1142.
- Atwater, B.F. (1997), *Coastal Evidence for Great Earthquakes in Western Washington*. United States Government Printing Office (reprinted from *U.S. Geological Survey Professional Paper 1560*), Washington, D.C.
- Atwater B.F. (1995), "Summary of Coastal Geologic Evidence for Past Great Earthquakes in the Cascadia Subduction Zone." *Earthquake Spectra*, Earthquake Engineering Research Institute, 11(1), 1-18.
- Berry, M., Eberhard, M. (2003), "Performance Models for Flexural Damage in Reinforced Concrete Columns," *Pacific Earthquake Engineering Research Center Report 2004*, University of California, Berkeley, California.
- Burns, N.H., and Seiss, C.P. (1962), *Load-Deformation Characteristics of Beam-Column Connections in Reinforced Concrete*. Civil Engineering Studies Structural Research Series No. 234, University of Illinois, Urbana, Illinois.
- CALTRANS (1992), *Bridge Design Specifications*. State of California Department of Transportation, Office of Structural Design, Sacramento, California.
- Carrasquillo, R.L., Nilson, A.H., and Slate, F.O. (1981), "Properties of High Strength Concrete Subject to Short-Term Loads." *ACI Journal*, American Concrete Institute (ACI), 78(3), 171-178.

- Chai, Y.H., Priestley, M.J., and Seible, F. (1991), "Seismic Retrofit of Circular Bridge Columns for Enhanced Flexural Performance." *ACI Structural Journal*, American Concrete Institute (ACI), 88(5), 572-584.
- Eberhard, M.O., Marsh, M.L., (1997), "Lateral-Load Response of a Reinforced Concrete Bridge." *Journal of Structural Engineering*, American Society of Civil Engineers (Structural Division), 123(4).
- Heaton, T.H., and Hartzell, S.H. (1987), "Earthquake Hazards on the Cascadia Subduction Zone." *Science*, American Association for the Advancement of Science, 236(4797), 162-236.
- Heaton, T.H., Kanamori, H., (1984), "Seismic Potential Associated with Subduction in the Northwestern United States," *Bulletin of the Seismological Society of America*, 74(3), 933-941.
- Kappos, A.J. (1997), "Seismic Damage Indices for RC Buildings: Evaluation of Concepts and Procedures." *Progress in Structural Engineering and Materials*, Construction Research Communications Limited, 1(1), 78-87.
- Kramer, S. L., Silva, W. J., Baska, D. A., (1998), "Ground Motions Due to Large Magnitude Subduction Zone Earthquakes." *Technical Report WA-RD 450.1*. Washington State Transportation Center.
- Kunnath, S.K., El-Bahy, A., Taylor, A. and Stone, W. (1997), *Cumulative Seismic Damage of Reinforced Concrete Bridge Piers*. Technical Report NCEER-97-0006, National Center for Earthquake Engineering Research, Buffalo, New York.
- Lehman, D.E. (1998), *Performance-Based Seismic Design of Well-Confined Concrete Columns*. Ph.D. Dissertation, Department of Civil and Environmental Engineering, University of California, Berkeley, California.
- MacGregor, J.G. (1997), *Reinforced Concrete: Mechanics and Design (Third Edition)*. Prentice-Hall, Inc., New York.
- Mander, J.B., Priestley, M.J.N., and Park, R. (1988 August), "Theoretical Stress-Strain Model for Confined Concrete." *Journal of Structural Engineering*, American Society of Civil Engineers (Structural Division), 114(8).
- Marsh, M.L. (1994), *Structural Response to Long Duration Earthquakes*. Report number WA-RD 340.2, Washington State Department of Transportation, Olympia, Washington.
- Mehta, P.K., and Monteiro, P.J.M. (1993), *Concrete: Microstructure, Properties, and Materials (Second Edition)*. The McGraw-Hill Companies, Inc., New York.
- Moehle, J.P. and Eberhard, M.O., "Earthquake Damage to Bridges," Chapter 34 in *The Handbook of Bridge Engineering*, Ed. W.F. Chen and L. Duan, CRC Press, 1999, pp. 34.1-34.33.
- Mookerjee, A. (1999), *Reliability of Performance Estimates of Spiral and Hoop Reinforced Concrete Columns*. Master's Thesis, Department of Civil Engineering, University of Washington, Seattle, Washington.
- Natural Resources Canada (1998), "Earthquake Processes: Cascadia Subduction Zone." [<http://www.pgc.nrcan.gc.ca/geodyn/cascadia.htm>], Accessed June 2000.
- Park, R., and Pauley, T. (1975), *Reinforced Concrete Structures*. John Wiley and Sons, Inc., New York.

- Park, Y.-J., and Ang, A.H.-S. (1985), "Mechanistic Seismic Damage Model." *Journal of Structural Engineering*, American Society of Civil Engineers (Structural Division), 111(4), 722-739.
- Parrish, M.M., (2001), *Accuracy of Seismic Performance Methodologies for Rectangular Reinforced Concrete Columns*. Master's Thesis, Department of Civil Engineering, University of Washington, Seattle, Washington.
- Popovics, S. (1973), "A Numerical Approach to the Complete Stress-Strain Curves for Concrete." *Cement and Concrete Research*, Pergamon Press, 3(5), 583-599.
- Price, Z.M. (2000), *Bridge Column Damage Estimates for Cascadia Subduction Zone Earthquakes*. Master's Thesis, Department of Civil and Environmental Engineering, University of Washington, Seattle, Washington.
- Priestley, M.J.N., Seible, F., and Calvi, G.M. (1996), *Seismic Design and Retrofit of Bridges*. John Wiley and Sons, Inc., New York.
- Razvi, S., and Saatcioglu, M. (1999), "Confinement Model for High Strength Concrete." *Journal of Structural Engineering*, American Society of Civil Engineers (Structural Division), 125(3), 281-289.
- Rogers, A.M., Walsh, T.J., Kockelman, W.J., and Priest, G.R. (1991), *Earthquake Hazards in the Pacific Northwest - An Overview*. Open File Report 91-441-0, United States Geological Survey, Denver, Colorado.
- Ruth, C., and Zhang, H. (1999), Personal Correspondence. Washington State Department of Transportation (WSDOT), Olympia, Washington.
- Saatcioglu, M. (2000), Personal Correspondence. University of Ottawa, Ottawa, Ontario, Canada.
- Williams, M.S., and Sexsmith, R.G. (1995), "Seismic Damage Indices for Concrete Structures: A State-of-the-Art Review." *Earthquake Spectra*, Earthquake Engineering Research Institute, 11(2), 319-349.
- WSDOT (September 1993), *Bridge Design Manual (M23-50)*. Washington State Department of Transportation (WSDOT), Olympia, Washington.
- Young, S.C., Meyer, C., and Shinozuka, S. (1989), "Modeling of Concrete Damage." *ACI Structural Journal*, American Concrete Institute (ACI), 86(3), 259-271.

Appendix A: Experimental Program

Appendix A provides a detailed discussion of the experimental program, which consists of a description of the test specimens and the prototype after which they were modeled (Section A.1), material properties of the concrete and steel (Section A.2), and an outline of the column testing procedure (Section A.3).

A.1 DESCRIPTION OF TEST COLUMNS

Test columns were designed to be representative of Washington State Department of Transportation (WSDOT) bridge columns constructed prior to the mid-1970s. This section describes the geometry and reinforcement of the column, footing, and hammerhead.

A.1.1 Prototype

The prototype column, which served as the model for the six test columns, was a WSDOT bridge column from the 1960s or early 1970s. Many bridge columns constructed by WSDOT in this time period were 20 to 25 feet (6.10 to 7.62 m) in length, and 60 inches (1.52 m) in diameter. An equivalent cantilever length of 15 feet (4.57 m) was selected for the prototype, based on the assumption that the distance from the footing to the inflection point is slightly greater than half the column length. Table A.1 summarizes the properties of the prototype and the six test columns.

Table A.1 Details of prototype and test columns

Item	Prototype	Test Column	Remarks
Column Length	15 feet	5 feet	1:3 Scale
Column Diameter	60 inches	20 inches	1:3 Scale
Longitudinal Steel Ratio	$\rho_l = 1.0\%$	$\rho_l = 0.99\%$	Ten No. 16 Grade 420 bars (soft metric)
Hoop Steel	No. 4 Grade 60	W2.5 wire	$\rho_t = 0.14\%$
Hoop Spacing	12 inches	4 inches	1:3 Scale
Cover to Hoop	1.5 inches	0.57 inches	1:2.6 Scale
Axial Load	$0.07f'_cA_g$	$0.1f'_cA_g$	$f'_c =$ actual concrete strength
Maximum Aggregate Size	1 inch ¹	3/8 inches	1:2.7 Scale
¹ Maximum course aggregate size specified by AASHTO (1953, 1961, and 1965)			

A.1.2 Column Geometry and Reinforcement

The test column geometry and reinforcement, nominally identical for all six columns, is shown in Figure A.1. The test columns were designed to be one third the size of the full-scale prototype column. The height of the test column was 5 feet (1.52 m), and the diameter of the test column was 20 inches (508 mm); these dimensions were scaled down from column prototype dimensions of 15 feet (4.57 m) and 60 inches (1.52 m), respectively. The test columns were longitudinally reinforced by ten No. 5 grade 60 bars ($\rho_l = 0.99\%$) and transversely reinforced by W2.5 wire at 4-inch (102 mm) spacing ($\rho_t = 0.14\%$). The longitudinal and transverse reinforcement ratios of the test column were approximately the same as the reinforcement ratios of the prototype column. However, some parameters of the prototype column could not be scaled precisely; therefore, concrete cover, longitudinal bar diameter and hoop diameter were scaled to the nearest readily available dimension. Additionally, W2.5 wire, scaled down from No. 4 reinforcing bar, was only commercially available as smooth wire; the difference in bond between the No. 4 reinforcing bar and the W2.5 wire was not taken into account.

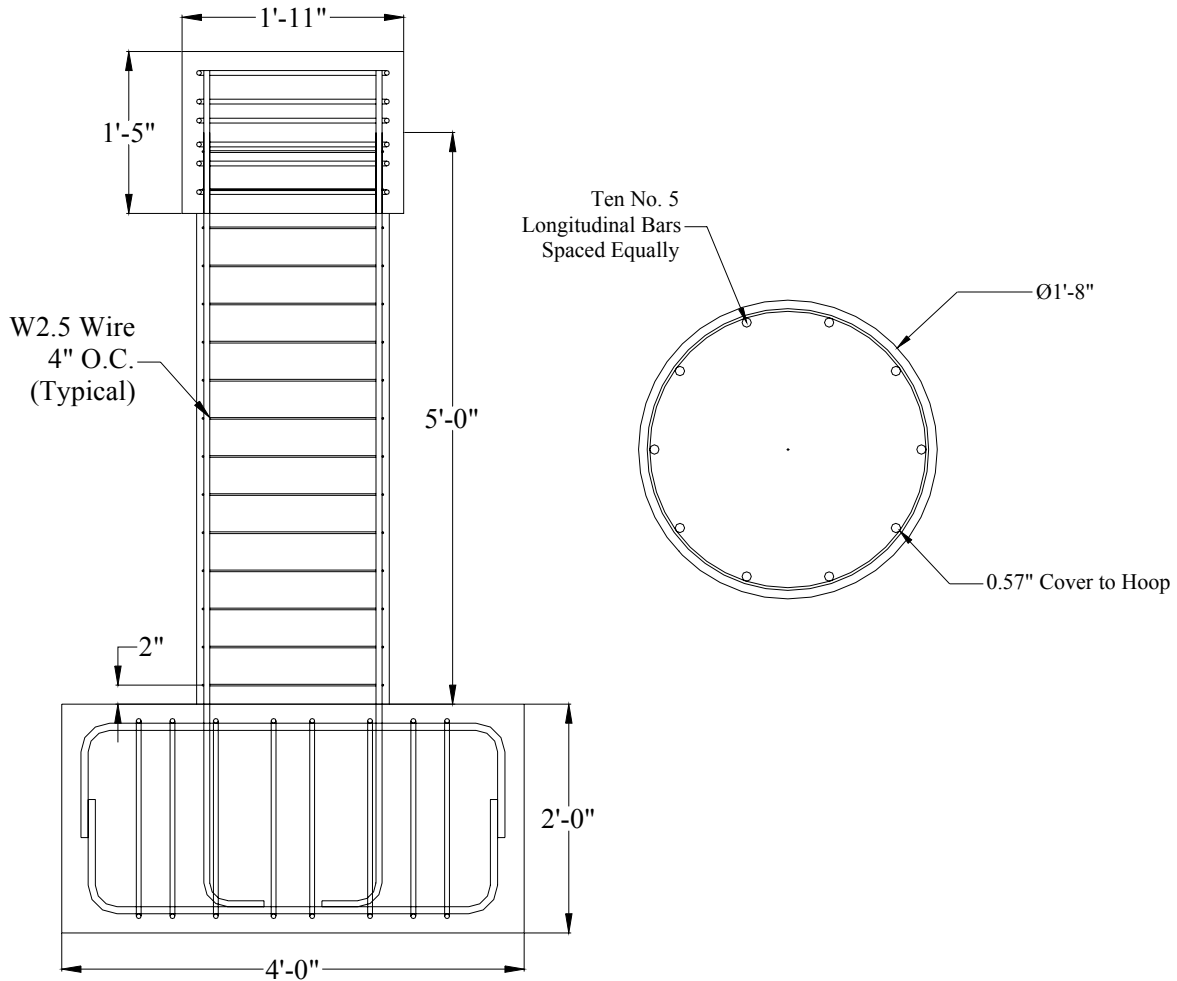


Fig. A.1 Test column geometry and reinforcement

A.1.3 Footing Geometry and Reinforcement

The geometry and reinforcement of the column footings are shown in Figure A.2 and Figure A.3. The footing dimensions were 4 feet by 2 feet by 2 feet (1.22 m by 610 mm by 610 mm). Eight No. 6 bars (four top and bottom) longitudinally reinforced the footing and four No. 8 bars transversely reinforced the footing. Eight No. 4 square hoops and ten No. 4 U-bars provided confinement. Additionally, PVC pipe was placed through the footing in four locations, two vertically and two horizontally. The vertical PVC pipes, 3 inches (76.2 mm) in diameter, were inserted to allow for the footing to be attached to the floor via tie-downs. The horizontal PVC pipes, 2 inches (50.8 mm) in diameter, were inserted to allow for transportation of the column.

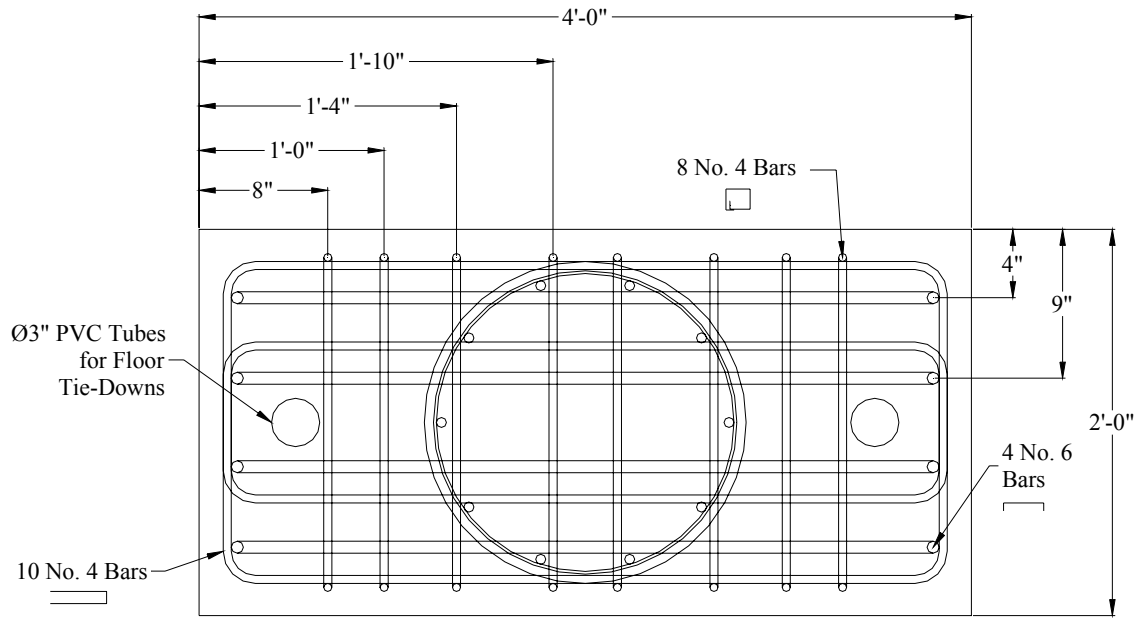


Fig. A.2 Plan view of footing geometry and reinforcement

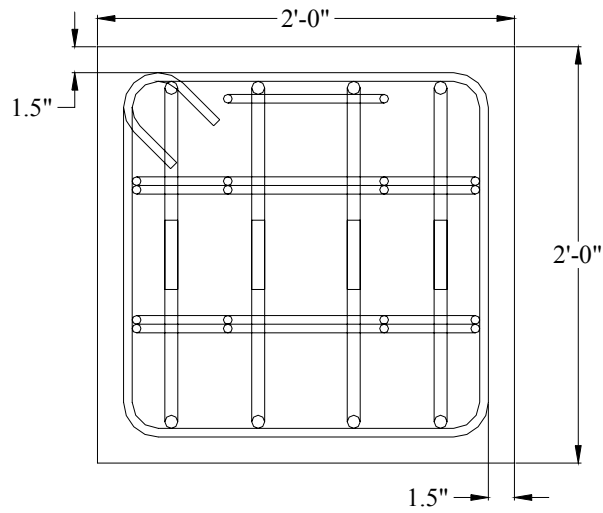


Fig. A.3 Side view of footing geometry and reinforcement

A.1.4 Hammerhead Geometry and Reinforcement

The geometry and reinforcement of the column hammerheads are shown in Figure A.4 and Figure A.5. The hammerhead dimensions were 2 feet by one foot-11 inches by one foot-5 inches (610 mm by 584 mm by 432 mm). Six No. 4 square ties, six No. 4 J-hooks, and six No. 4 straight bars provided the necessary reinforcement in the column hammerheads. Additionally, PVC pipes were inserted through the column hammerhead in four locations. These PVC pipes, 1.5 inches (38 mm) in diameter, were inserted to allow for the attachment of the hydraulic actuator to the column hammerhead.

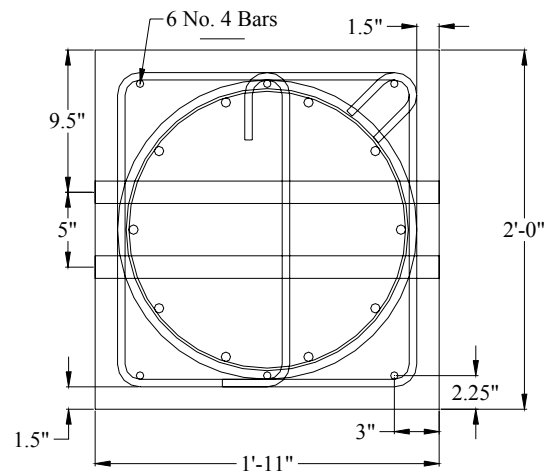


Fig. A.4 Plan view of hammerhead geometry and reinforcement

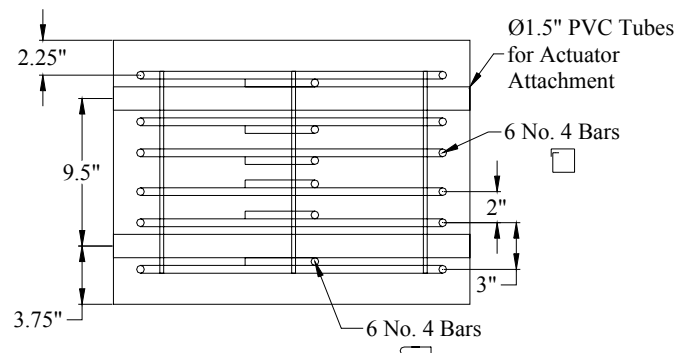


Fig. A.5 Elevation view of hammerhead geometry and reinforcement

A.2 MATERIALS

Concrete cylinders, longitudinal steel samples, and hoop steel samples were tested to determine their material properties. Steel and concrete material properties used in modeling the column were based on the results of material tests.

A.2.1 Concrete

The concrete mix was designed to approximate the present-day strength of the prototype columns. The concrete was provided by Cadman, Inc.; mix number 200004 with 10 pounds per cubic yard (432 kg per cubic meter) of additional water was ordered. Table A.2 provides details of the concrete mix. The nominal 56-day compressive strength of the column was 6,000 psi (41.4 MPa). However, the actual 56-day compressive strength was approximately 33% higher for Columns S3, C2, C4, and C3R. The maximum aggregate size in the concrete was 3/8 inch (9.53 mm), the water/cement ratio was 0.34, and the target slump was 8 inches (203 mm).

Table A.2 Concrete mix

Component	Weight (lb/yd)
Cement	578
Fly Ash	120
Water	250
Coarse Aggregate	2005
Fine Aggregate	1420
MRWA	53 ¹
HRWR	32 ¹
¹ Value listed has units of oz/yd ³	

The six specimens were cast in four pours inside the Civil Engineering Structures Laboratory at the University of Washington. The first four tests were conducted in 2000, while the last two tests were conducted in 2003. For the first four tests (Columns S3, C2, C4, and C3R), the column footings were cast on September 27, 1999, from a single batch of concrete. The columns and the column hammerheads were cast on October 14, 1999, from a second batch of concrete. For the last two tests (Columns S1, and S15), the column footings were cast on July 2, 2003, from the third batch of concrete. The columns and column hammerheads were cast on

July 9, 2003, from the fourth batch of concrete. Prior to each casting, slump tests were performed to verify that the concrete slump was within one inch of the 8-inch target. Thirty-six concrete cylinders, 12 inches (305 mm) in height by 6 inches (152 mm) in diameter, were cast from each of the first two batches of concrete. Sixteen concrete cylinders of the same dimensions were cast from each of the last two batches of concrete. The concrete cylinders were stored in the laboratory fog room until they were to be tested. Compressive strength tests (f'_c) were performed at 3, 7, and 28 days, except when testing was conducted before the 28-day strength, and split tensile strength tests (f'_{ct}) were performed at 28 days, or at the time of testing if testing was conducted before the 28-day mark. Additionally, compression tests, split tensile tests, and modulus of elasticity tests (E_c) were performed at the time of testing of each specimen. These results are summarized in Tables A.3 and A.4.

Table A.3 Development of concrete strength

Cylinder	3-Day	7-Day	28-Day	
	f'_c (psi)	f'_c (psi)	f'_c (psi)	f'_{ct} (psi)
Batch 1 (Footings S3, C2, C4, and C4R)	3080	3370	4010	360
Batch 2 (Columns S3, C2, C4, and C4R)	3970	6270	7250	490
Batch 3 (Footings S1 and S15)	3698	4871	6320	576 ¹
Batch 4 (Columns S1 and S15)	3158	4429	5870	554 ¹
¹ Measured at test of Column S15				

Table A.4 Concrete material properties at time of testing¹

Column Designation	Age of Column at Day of Test (days)	Footing			Column		
		f'_c (psi)	f_{ct} (psi)	E_c (ksi)	f'_c (psi)	f_{ct} (psi)	E_c (ksi)
S1	16	6320	NA ²	5475 ³	5271	520	4724 ³
S3	159	4910	470	3260	8150	630	4090
S15	26	6387	576	5475	5870	554	4724
C2	199	4920	370	3610	8260	620	4270
C4	188	5010	430	3280	8170	540	4040
C3R	220	5080	430	3530	7640 ⁴	600	4930

¹ All tests of material properties were conducted within two days of the testing of the column.
² Footing tensile strength was not determined for Column S1
³ The elastic modulus for Columns S1 and S15 were both determined from a test cylinder broken on the day of testing for Column S15.
⁴ Compression tests for Column C3R were performed on June 13, 2000.

A.2.2 Longitudinal Steel

The Seattle, Washington, Steel Division of Birmingham Steel Corporation produced the longitudinal reinforcement (ASTM Designation A615/A615M-96a GR 420); the rebar was then fabricated by CT Sales, Incorporated, of Woodinville, Washington. Birmingham Steel adopted a “soft metric” manufacturing process several years ago, meaning that their rebar has metric bar size designations but still imperial nominal diameters and areas. The longitudinal steel used was actually No. 16 grade 420 soft metric rebar, which corresponds to No. 5 grade 60 imperial rebar.

To limit the variation in the steel properties, the longitudinal reinforcement used for the construction of the first four test specimens and for material testing was designated to be from a single batch of steel. Likewise, the last two test specimens (Columns S1 and S15), were built from another batch of steel. To determine material properties, reinforcing bars were tested using standard ASTM testing methods. The longitudinal steel for the first four and last two columns was cut into 24-inch (610 mm) and 42-inch (1067 mm) lengths, respectively. The center sections were machined to localize bar yielding and allow for precise measurement of the stress-

strain response. The results of a longitudinal steel material test of each batch are shown in Figure A.6.

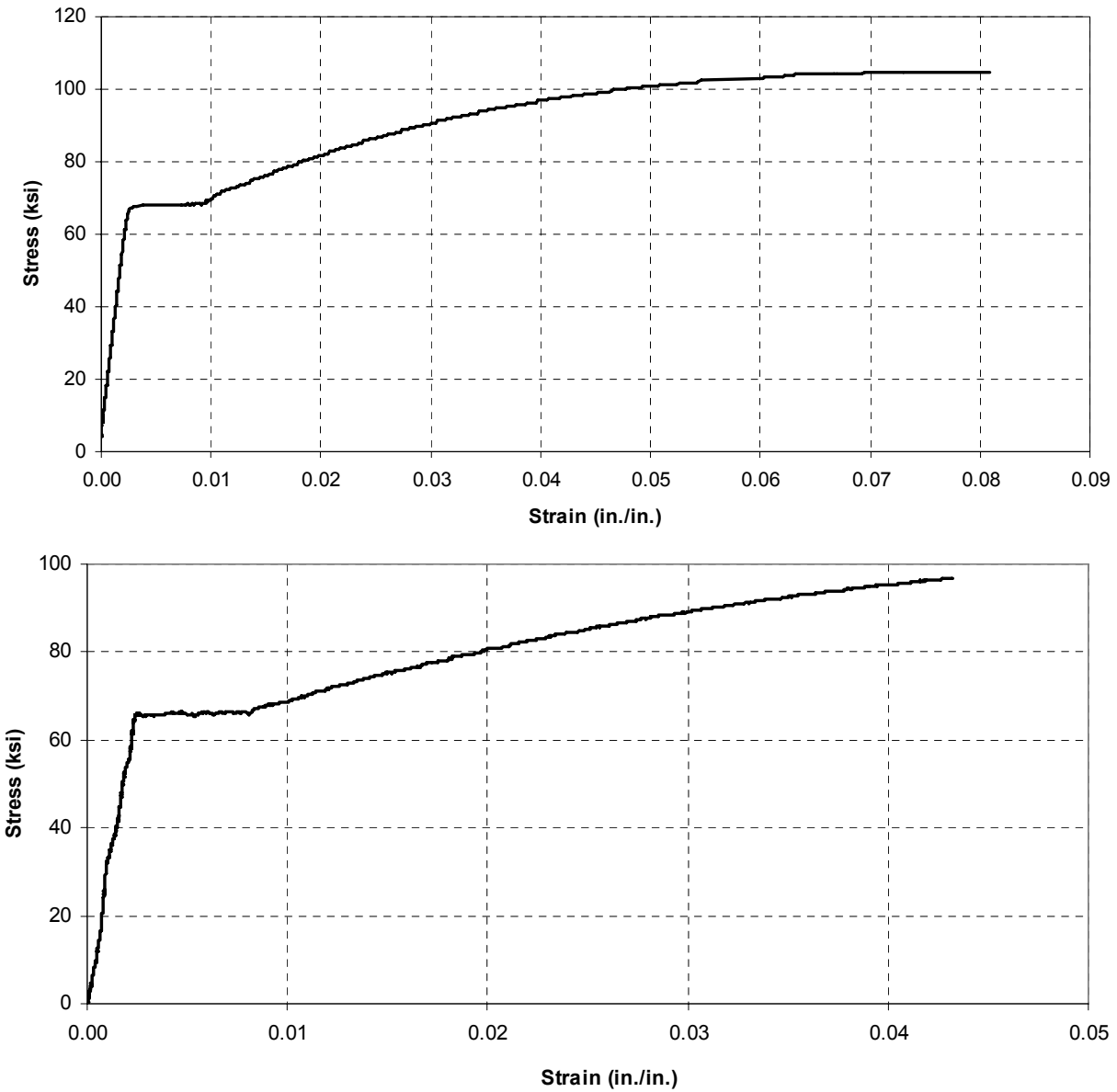


Fig. A.6 Stress-strain response of longitudinal steel for (a) Columns S3, C2, C4, and C3R, and (b) Columns S1 and S15

Both the material test and the mill test results are displayed in Table A.5 for the points at yield and ultimate.

Table A.5 Stress-strain data for longitudinal reinforcement

Batch	Material Test				Mill Test		
	Yield Strength (ksi)	Ultimate Strength (ksi)	Yield Strain	Ultimate Strain	Yield Strength (ksi)	Ultimate Strength (ksi)	Ultimate Strain
Columns S3, C2, C4, and C3R	66	105	NA ¹	NA	67	107	NA
Columns S1 and S15	65	107	0.00235	0.136	64	102	0.156

¹ The strains were not recorded for Columns 1-4.

From the stress-strain response, it can be seen that the yield strength of the longitudinal steel was approximately 66 ksi (455 MPa) and the ultimate strength was approximately 105 ksi (724 MPa). The yield plateau extended from approximately 0.27% strain to approximately 1.0% strain. These results compare favorably with the mill test results shown in Table A.5.

A.2.3 Hoop Steel

The hoop reinforcing steel used was W2.5 smooth wire; smooth wire was used because deformed wire of this size was not commercially available. A straight segment of the wire used for the hoop reinforcing steel was tested in the same manner as the longitudinal steel. The results of the hoop reinforcing steel test are shown in Figure A.7. The hoop steel for all six columns came from the same batch.

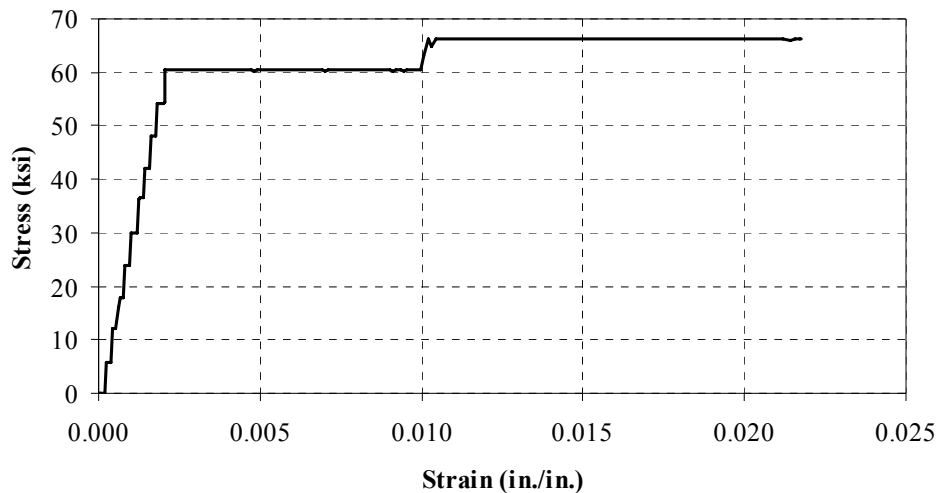


Fig. A.7 Stress-strain response of hoop reinforcing steel

From the stress-strain response, it can be seen that the yield strength of the hoop steel was approximately 60 ksi (414 MPa), and the ultimate strength was approximately 66 ksi (455 MPa).

A.3 TESTING PROCEDURE

Section A.3 details the procedure used to test the columns. The loading setup is first detailed, followed by the instrumentation plan. The displacement histories are then summarized, followed by a summary of the data-acquisition system.

A.3.1 Loading Setup

The test setup (Fig. A.8) was designed to apply transverse cyclic displacements to an axially loaded column. Displacements were applied to the column hammerhead using a servo-controlled hydraulic actuator; a hydraulic center-hole ram applied the axial load through an assembly consisting of a cross-head anchored to the floor using two high-strength rods.

A.3.2 Components

The test columns were anchored to the laboratory strong floor using two 1-1/2-inch- (38 mm) diameter B7 threaded rods extending from the floor sockets through the vertical ducts in the column footing. Each rod extended through a 1-inch- (25 mm) thick A36 steel plate that sat on top of the footing; the tie-down force was held in the rods by nuts bearing against these plates. Each rod was stressed to a force of 125 kips (556 kN) using a 100-ton (890 kN) capacity hand-operated hydraulic center-hole ram. However, the force in the rods for Column S3 was determined only indirectly by measuring the rod elongation; it is likely that these forces were lower than 125 kips (556 kN) for Column S3.

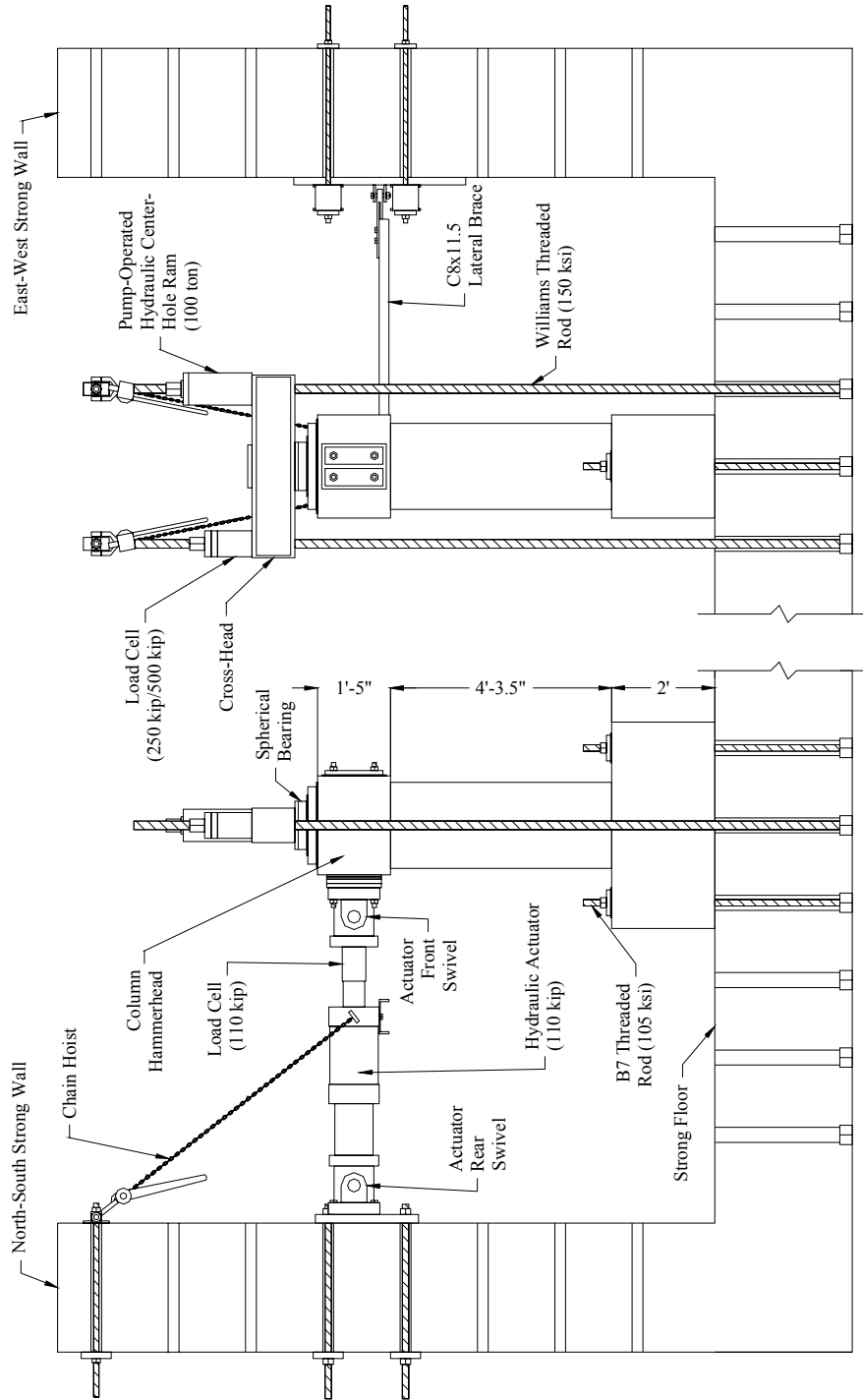


Fig. A.8 Test setup

A.3.3 Axial Load

The axial-load apparatus is also shown in Figure A.8. This load was applied to the column through a welded steel cross-head that was stressed to the floor by two, 1-3/4-inch (44 mm) Williams 150 ksi (1034 MPa) threaded rods. These rods were threaded into the floor sockets on each side of the column. The cross-head was placed on top of a spherical bearing, which ensured that the axial force remained applied in the direction of the column axis (even if the cross-head or hammerhead top surface were not perfectly horizontal). A 2-inch (51 mm) thick A36 steel plate was placed underneath the spherical bearing to distribute the axial force over the hammerhead top surface. To improve the contact surfaces, masonite was placed on both sides of the plate. The Williams rods were stressed using a 100-ton (890 kN) capacity pump-operated hydraulic center-hole ram placed on top of the cross-head; the ram was placed over one rod, and a load cell was placed over the other rod. A 250-kip (1112 kN) capacity load cell was used at the start of the testing program; it was replaced with a 500-kip(2224 kN) capacity load cell early in the second test. Fixed nuts were installed above both the load cell and the center-hole ram; consequently, the actual axial load was twice the load measured by the load cell.

A.3.4 Lateral Load

Lateral loads were applied to the column hammerhead by a 110-kip (489 kN) servo-controlled hydraulic actuator (Fig. A.8) at an elevation of 84 inches (2134 mm) above the laboratory strong floor. The actuator had swivels on both the front and rear ends to allow rotation in the vertical plane as the column displaced. To connect the actuator to the north-south laboratory reaction wall, a 2-inch- (51 mm) thick A36 steel plate was first mounted on the wall using two 1-1/2-inch- (38 mm) B7 threaded rods. The swivels on the rear of the actuator were then attached to this plate using four, 3/4-inch (19 mm) A325 bolts. In addition, 2-1/2-inch-(64 mm) thick A36 steel plates were inserted between the rear swivels and the wall plate (so that the “zero” position of the actuator would be as close to the edge of the hammerhead as possible).

To fill any additional gap between the actuator at zero position and the column hammerhead face, two A36 steel plates of 1-inch (25 mm) thickness were drilled with holes corresponding to the hole locations in the front swivels; these spacer plates were then inserted between the ram swivels and the column hammerhead face. In addition, two sheets of 1/4-inch- (6.4 mm) thick plywood were used to improve the contact surface between the outermost spacer

plate and the column hammerhead. The front swivel was attached to the column using four 1-inch (25 mm) B7 threaded rods, which were inserted through the hammerhead ducts. These rods extended through 1-inch- (25 mm) thick A36 steel plates on the opposite face of the column hammerhead; the actuator connection force was held in these rods by nuts bearing against these plates. In addition, masonite was placed between these plates and the column hammerhead face to improve the contact surface.

The force required to impose the displacement history was monitored using a 110-kip (489 kN) load cell connected between the actuator piston and the front swivels. To provide backup force data, a Delta-P circuit was monitored. This circuit computes forces based on the pressure differential of the hydraulic oil in the actuator; this circuit is accurate only at higher forces (above 20–25 kips, or 89–111 kN).

The actuator was braced laterally by a C8x11.5 steel brace connecting the actuator body to the east-west reaction wall. In addition, two chain-hoists were mounted near the top of the reaction wall to provide vertical support for the actuator during assembly and between tests.

A.3.5 Internal Instrumentation

Internal instrumentation was used for the first four test columns (Columns S3, C2, C4, and C3R). The instrumentation consisted of strain gages placed on the longitudinal and hoop steel, which was nominally identical for all four columns and is shown in Figure A.9. Only the lower half of the column was instrumented with strain gages, since this was the region where inelastic bending was expected to occur.

Eight strain gages were placed on each of the two longitudinal bars nearest the front and back faces of the column (bars A and C). In addition, one strain gage was placed on two of the four longitudinal bars that were nearest to the side faces (bars B and D).

The hoop steel was instrumented with strain gages at four elevations: 2 inches (51 mm), 6 inches (152 mm), 10 inches (254 mm), and 18 inches (457 mm) from the footing-column interface. The strain gage pattern on the hoop steel is also shown in Figure A.9.

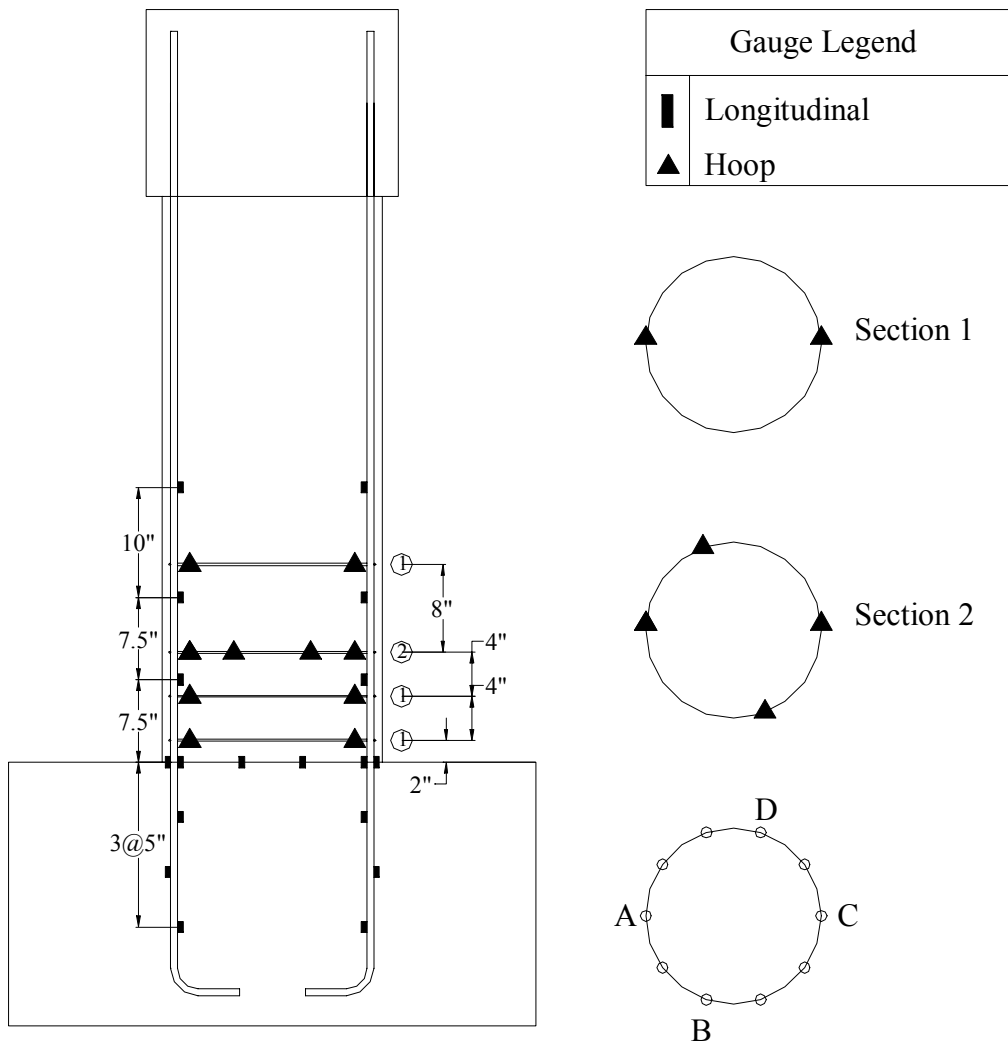


Fig. A.9 Strain gage layout (Columns S3, C2, C4, and C3R)

All strain gages were purchased from Texas Measurements Laboratory (TML). The longitudinal strain gages were designated YFLA-5 High Elongation Strain Gages. Readings from the longitudinal strain gages were reliable up to a strain of 5%. The hoop strain gages were designated YFLA-2 High Elongation Strain Gages, and readings from these gages were also reliable up to a strain of 5%.

A.3.6 External Instrumentation

The external instrumentation consisted of 22 potentiometers in three categories: rotational, shear and translational displacement potentiometers. The first four columns that were tested (Columns S3, C2, C4, and C3R) used all 22 potentiometers. The last two columns tested (Columns S1 and S15) used only six translational displacement potentiometers. The locations of the rotational and shear potentiometers are shown in Figure A.10.

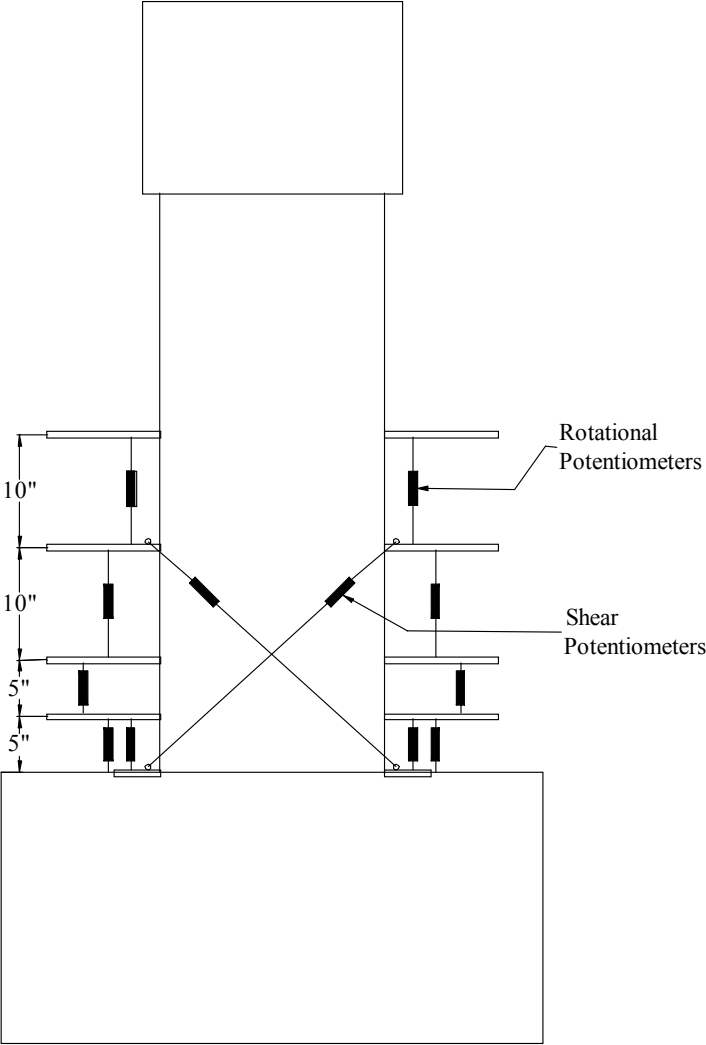


Fig. A.10 Rotational and shear potentiometers (Columns S3, C2, C4, and C3R)

The data acquired with the rotational potentiometers allowed for the calculation of local and global average column curvatures. The rotational potentiometers were attached to threaded rods placed through the column cross section (Fig. A.11) at elevations of 0, 5, 10, 20, and 30 inches (0, 127, 254, 508, and 762 mm) above the footing-column interface. Between the 0 and 5

inch (0 and 127 mm) elevations, potentiometers spanned between the rod at 5 inches (127 mm) and both the rod at 0 inches (0 mm) and the footing surface; the difference in these readings measured bond slip. Each of the instrumentation rods was 3 feet (914 mm) long and had a 1/2-inch (13 mm) diameter. The instrumentation rods were placed in plastic tubing, except for a 3-inch (76 mm) segment in the center of the rod. This configuration allowed for the instrumentation rods to rotate with the column, while minimizing the additional confinement caused by the instrumentation rods.

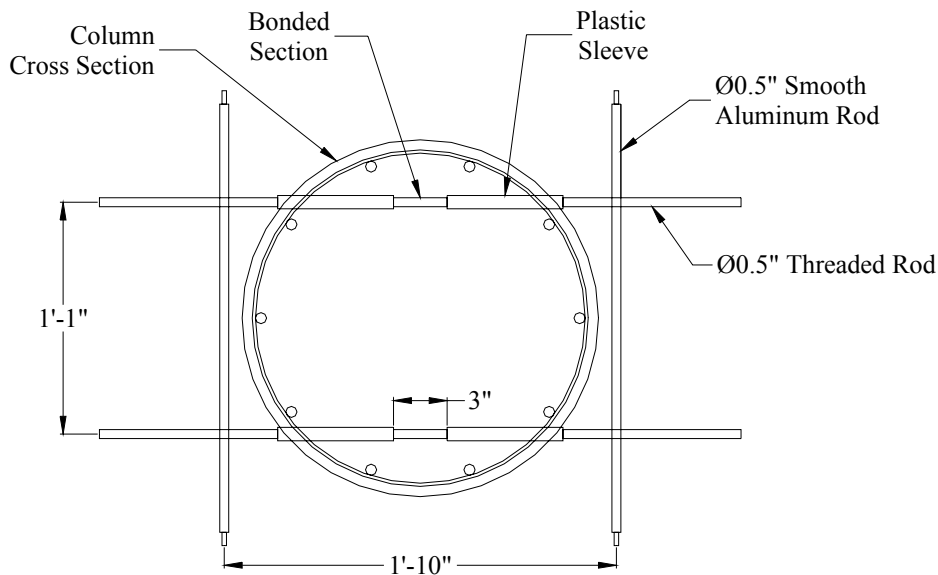


Fig. A.11 Details of external instrumentation rods (Columns S3, C2, C4, and C3R)

The shear potentiometers were attached to smooth rods, attached perpendicular to the instrumentation rods using 90-degree rod connectors, at heights of 0 and 20 inches (0 and 508 mm) from the footing-column interface. Eye-bolts with rotating holes were attached to both ends of the shear pot assembly to connect to the smooth rods (Fig. A12).

The rotational potentiometers were attached to the instrumentation rods using pairs of aluminum brackets. One block held the potentiometer, the other end held the rod, and press-fit bearings allowed free rotation between them. This assembly is shown in Figure A.12.

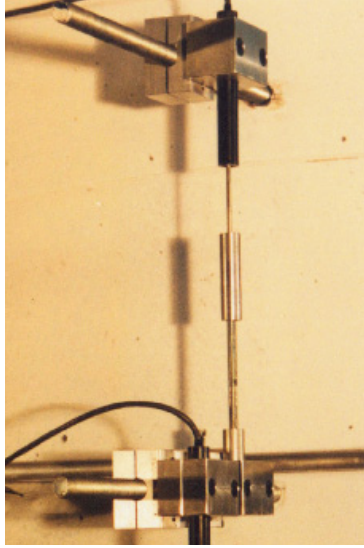


Fig. A.12 Potentiometer-bracket assembly

The locations of the translational displacement potentiometers are shown in Figure A.13. Displacement was monitored at heights of 10, 20, 30, and 60 inches (254, 508, 762, and 1520 mm) relative to the footing-column interface for each test specimen. These displacement potentiometers were attached to an independent reference column and relied on compression springs to maintain contact with each of the specimens.

Additionally, Columns S1, S15, C2, C4, and C3R had two potentiometers attached to the reference column and bearing against the footing to monitor slip of the base.

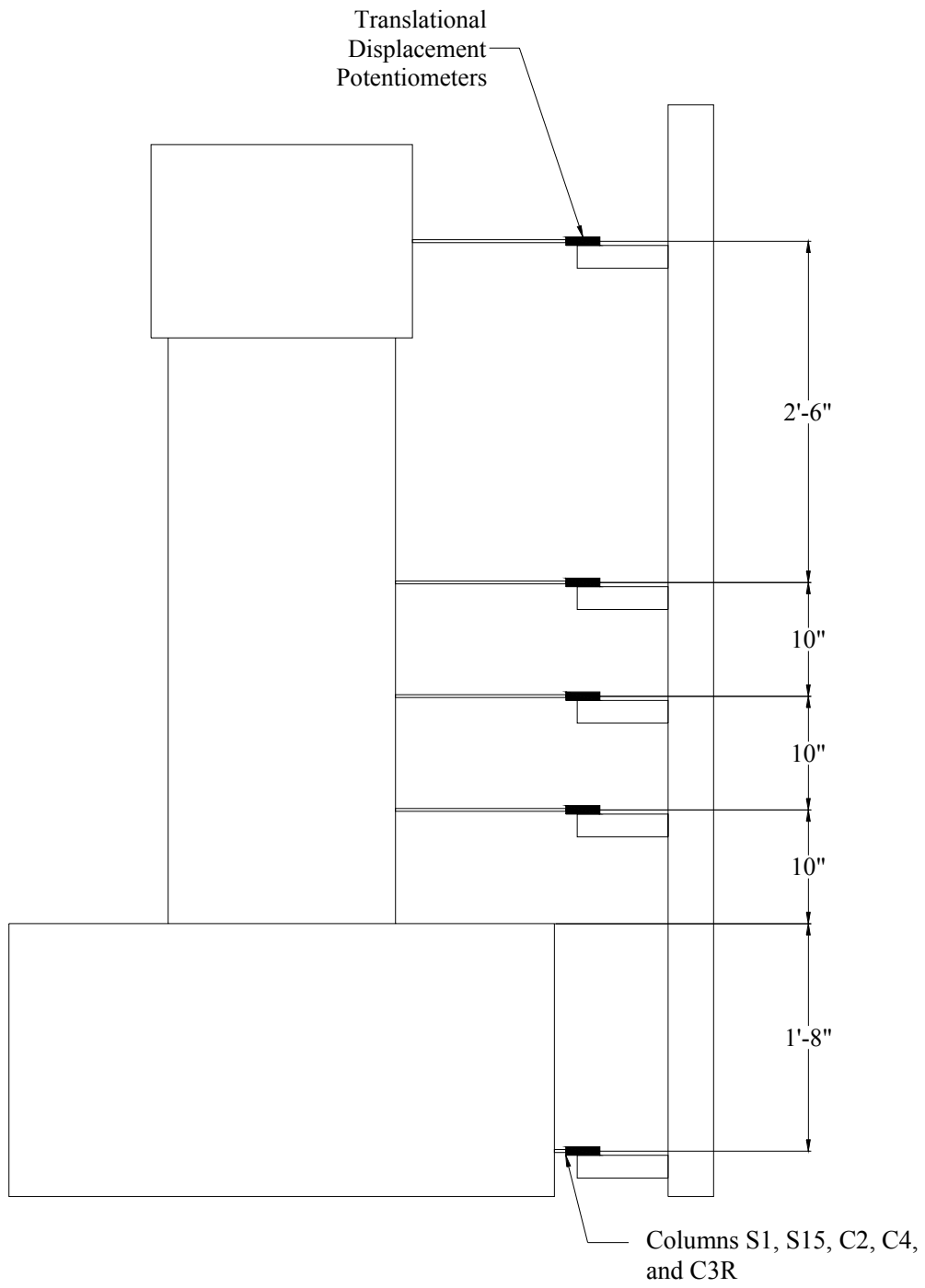


Fig. A.13 Translational displacement potentiometers (all columns)

A.3.7 Displacement Histories

To gain the most information possible from a limited number of tests, each column was subjected to a different loading history.

Column S3 was subjected to a displacement history similar to that used by many other investigations, consisting of sets of three cycles of increasing displacement (S3 stands for Standard history, three cycles per set). After Column S3 was subjected to a single cycle at 0.02 inches (0.51 mm) to verify the functioning of the instrumentation, the column was subjected to sets of three cycles at displacement levels corresponding to 0.1 times the estimated displacement at first yield ($0.1\Delta_y$), $0.2\Delta_y$, $0.7\Delta_y$, $1.25\Delta_y$, $2.0\Delta_y$, $3.0\Delta_y$, $5.0\Delta_y$, and $8.0\Delta_y$. The test concluded with a single cycle at $12.0\Delta_y$.

Column S1 (Standard history, one cycle per set) was subjected to one cycle at each of the increments described for Column S3. In addition to the standard cycle, the displacement was incremented every half cycle at equal logarithmic increments. For example, the ratio between the displacement $2.0\Delta_y$ and $3.0\Delta_y$ is 1.5. Therefore, the half cycle between these levels was increased in amplitude by a factor of $(1.5)^{1/2}$. This history was chosen to maximize the total displacement at failure while minimizing the amount of cycles needed to reach this displacement.

Column S15 (Standard history, 15 cycles per set) was subjected to fifteen cycles at each of the increments described for Column S3. Like Column S1, the displacement was incremented every half cycle at equal logarithmic increments. In transitioning from a displacement of $2.0\Delta_y$ to a displacement of $3.0\Delta_y$, every half cycle increased in amplitude by a factor of $(1.5)^{1/30}$. This history was chosen to maximize the number of cycles before failure.

Column C2 (Constant amplitude cycling at a drift of 1.9%) was subjected to single cycles at drift ratios of 0.27% and 0.77%, followed by 12 cycles at 1.9%, 3 cycles at 3.1%, and finally 1 cycle at 3.8%. This history was chosen to investigate the effect of a large number of cycles at a low-deformation amplitude on the maximum column deformation at failure.

Column C4 (constant amplitude cycling at a drift of 3.8%) was subjected to one single cycle at drift ratios of 0.27% and 0.77% before being subjected to 10 cycles at 3.8%, followed by one cycle at 5.7%. This made it possible to observe large-displacement behavior without subjecting the column to a large number of intermediate cycles. This history was chosen to investigate the effect of a large number of cycles at a large deformation amplitude on the maximum column deformation at failure.

Column C3R (constant amplitude cycling at a drift of 3.1%, followed by cycles at reduced amplitude) was subjected to the preliminary cycles at drift ratios of 0.27% and 0.77%, followed by 10 cycles at 3.1%, and 5 cycles at 1.9%. This history demonstrated the effect of imposing cycles of moderate displacement after having imposed larger ones. This history was chosen to investigate the effect of reverse loading of the column on the maximum column deformation at failure.

The displacement histories for all of the columns are shown in Figure A.14. In addition, Table A.6 shows numerical values for displacements and their significance. Table A.7 provides the cycle name nomenclature.

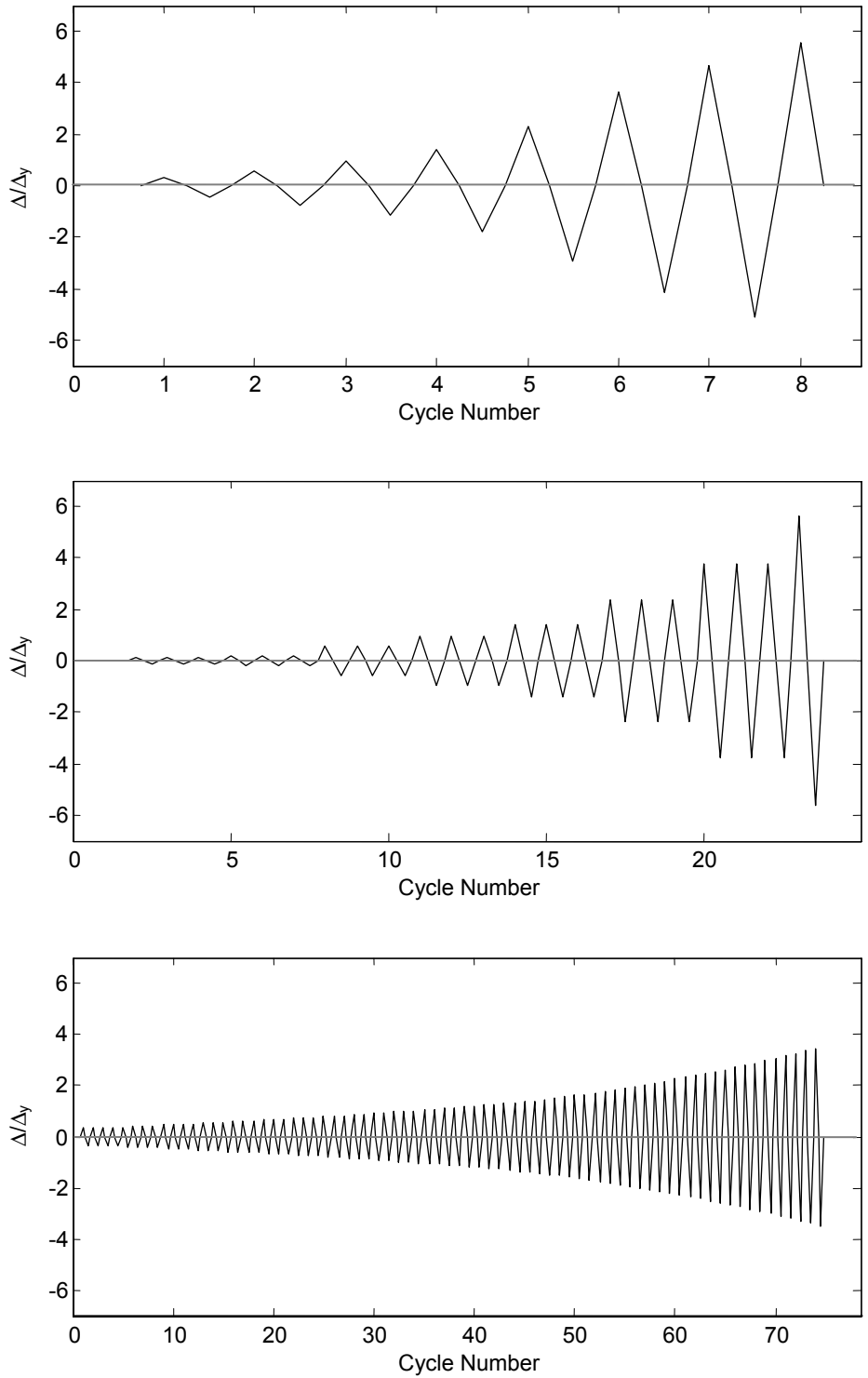


Fig. A.14 Displacement histories for: (a) Column S1, (b) Column S3, and Column (c) S15

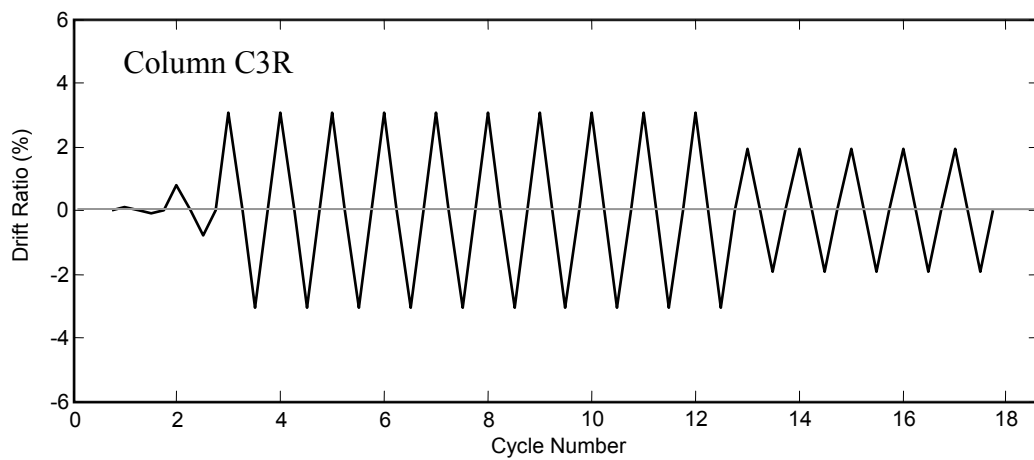
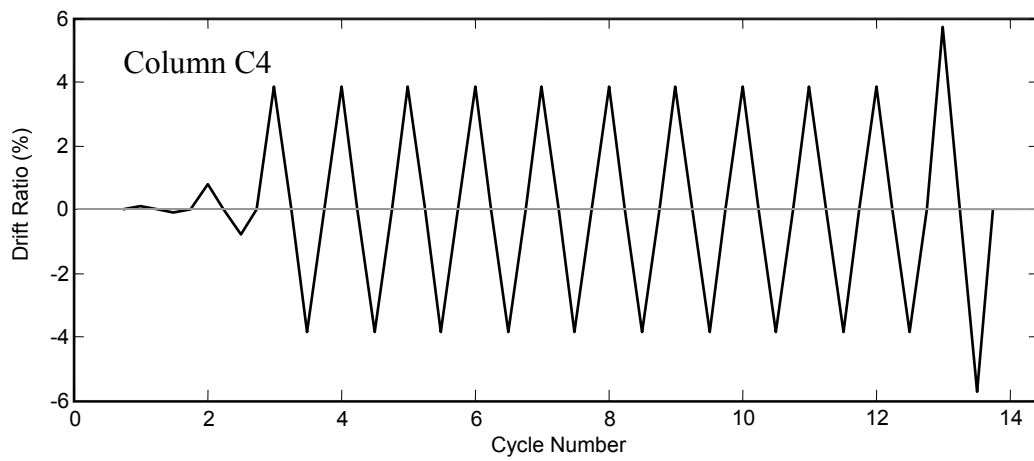
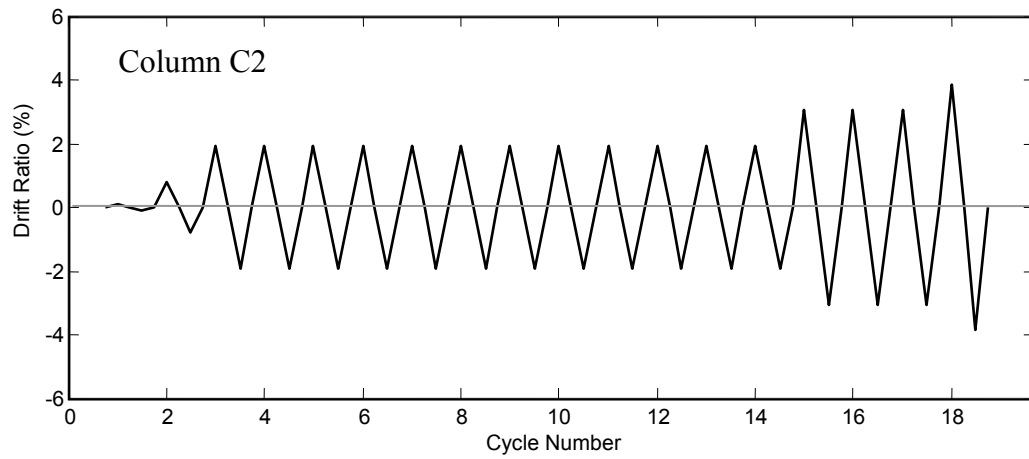


Fig. A.14 (cont.) Displacement histories for: (a) Column C2, (b) Column C4, and (c) Column C3R

Table A.6 Displacement levels

Multiple of Estimated Yield Displacement	Displacement (in.)	Drift Ratio (%)
$0.1\Delta_y$	0.02	0.04
$0.2\Delta_y$	0.04	0.07
$0.7\Delta_y$	0.16	0.27
$1.25\Delta_y$	0.29	0.48
$2\Delta_y$	0.46	0.77
$3\Delta_y$	0.69	1.15
$5\Delta_y$	1.14	1.90
$8\Delta_y$	1.83	3.05
$10\Delta_y$	2.29	3.82
$12\Delta_y$	2.74	4.57
$15\Delta_y$	3.43	5.72

Note: Estimated yield displacement = 0.23 in. Actual yield displacements varied from the estimated due to variations in anchorage slip.

Table A.7 Cycle nomenclature and displacement levels for each column

Drift Ratio (%)	Cycle Numbers at Each Drift Level					
	Column S1	Column S3	Column S15	Column C2	Column C4	Column C3R
0.04		1				
0.07		2-4		1	1	1
0.27	1	5-7	1-15			
0.48	2	8-10	16-30			
0.77	3	11-13	31-45	2	2	2
1.15	4	14-16	46-60			
1.90	5	17-19	61-75	3-14		13-17
3.05	6	20-22		15-17		3-12
3.82				18	3-12	
4.57		23				
5.72					13	

A.3.8 Data Acquisition

Voltage outputs were processed by a National Instruments data-acquisition system running on a PC-compatible desktop computer. This computer was equipped with LabView software, which reads the initial voltage in each channel at the start of the test and converts the voltage changes (relative to these initial voltages) into mechanical units. For potentiometers and load cells, the voltages were converted into mechanical units using the following equations:

$$Displacement = (V - V_i) \times CF \quad (A.1)$$

$$Force = (V - V_i) \times CF \quad (A.2)$$

where V is the output voltage, V_i is the initial voltage, and CF is the calibration factor. For strain gages, the voltages were converted into strains using the following equations:

$$Strain = \frac{-4V_r}{GF(1 + 2V_r)} \quad (A.3)$$

with

$$V_r = \frac{V - V_i}{V_{ex}} \quad (A.4)$$

where GF is the gage factor, V is the output voltage, V_i is the initial voltage, and V_{ex} is the excitation voltage (equal to 3.333 volts for all strain gages).

Each channel was scanned continuously with data recorded at preset changes in displacement and load. LabView also allows data recording to be triggered manually (without interfering with the displacement and load recording controls), which was done at the start, end, and peaks of each cycle.

LabView created separate files for the output. All mechanical output was stored in the file *finalout*. The voltage readings were stored in *finalvolt*. The initial voltages were stored in *strainvolt* (strain gages), *potvolt* (potentiometers), and *lcellvolt* (load cells). In addition, a backup file of the mechanical values called *tmpout* was created in a different file directory in case there was a problem with *finalout*. All mechanical values can be reproduced using the voltage output and initial voltage files.

Appendix B: Instrument Histories (Columns S3, C2, C4, and C3R)

This section contains all of the column data recorded during the testing program of the first four columns (Columns S3, C2, C4, and C3R). The values output from the axial-load cell have been converted into the true axial load (i.e., the load cell reading has been multiplied by two). Data offset by a constant value (such as from re-zeroing the data-acquisition system during testing) have been adjusted to the correct values. In addition, the following data points have been removed:

- Data points resulting from stray voltage spikes or potentiometer slip
- Data recorded after the failure of a given strain gage
- Data points after the loss of axial capacity

All of the channels included in this section are defined in Tables B.1–B.5. Figure B.1 shows schematically how the bar identification letters (A–D) correspond to the test geometry. References are made to “Side A,” “Side B,” “Side C,” and “Side D;” these refer to the side of the column on which the longitudinal rebar of the same letter is located. For further details about instrumentation, refer to Appendix A. Channels not functioning or damaged are noted on the plot.

In plotting the data, certain quantities need to be defined. All reference column and base slip data are plotted on the x-axis versus actuator force, with the channel data plotted on the x-axis and the force data plotted on the y-axis; the force data are simply the data from Ram_LC. All other channels are plotted on the y-axis, with the drift ratio on the x-axis; the drift ratio is determined by the following equation:

$$\text{Drift Ratio} = [(P_{Ref_60A} + P_{Ref_60B})/2 - (P_{Foot_A} + P_{Foot_B})/2]/L \quad (\text{B.1})$$

Physically, this is average displacement recorded by the 60-inch reference column potentiometers minus the average base slip recorded by the base slip potentiometers (if one of the potentiometers in Equation B.1 was either not connected or not functioning, this equation was modified accordingly), with this quantity divided by L (the column height of 60 inches (1520 mm)).

In Chapter 3, the force and displacement values on the hysteresis plots (Fig. 3.1) each had their signs changed so that the force-displacement envelopes (Fig. 3.2) of the forward loading cycles would appear in the first quadrant (positive force and displacement values). The sign of the displacement values are also reversed on the plots of the axial-load variation (Fig. 3.3). All the plots in this section reflect the original sign convention of the recorded data.

Table B.1 Translational potentiometers nomenclature

Channel	Description
PRef_60A	Reference column, 60-inch elevation, on Side B
PRef_60B	Reference column, 60-inch elevation, on Side D
PRef_30A	Reference column, 30-inch elevation, on Side B
PRef_30B	Reference column, 30-inch elevation, on Side D
PRef_20A	Reference column, 20-inch elevation, on Side B
PRef_20B	Reference column, 20-inch elevation, on Side D
PRef_10A	Reference column, 10-inch elevation, on Side B
PRef_10B	Reference column, 10-inch elevation, on Side D
PFoot_A	Base slip, on Side B
PFoot_B	Base slip, on Side A

Table B.2 Rotational and shear potentiometer nomenclature

Channel	Description
PA1	Spans between 30-inch rod and 20-inch rod on Side A; attached to the set of rods on Side B
PA2	Spans between 20-inch rod and 10-inch rod on Side A; attached to the set of rods on Side B
PA3	Spans between 10-inch rod and 5-inch rod on Side A; attached to the set of rods on Side B
PA4	Spans between 5-inch rod and 0-inch rod on Side A; attached to the set of rods on Side B
PA5	Spans between 5-inch rod and footing surface on Side A; attached to the set of rods on Side B
PC1	Spans between 30-inch rod and 20-inch rod on Side C; attached to the set of rods on Side D
PC2	Spans between 20-inch rod and 10-inch rod on Side C; attached to the set of rods on Side D
PC3	Spans between 10-inch rod and 5-inch rod on Side C; attached to the set of rods on Side D
PC4	Spans between 5-inch rod and 0-inch rod on Side C; attached to the set of rods on Side D
PC5	Spans between 5-inch rod and footing surface on Side C; attached to the set of rods on Side D
PSh_AC	Spans from 20-inch rod on Side A to 0-inch rod on Side C; spans the column on Side D
PSh_CA	Spans from 20-inch rod on Side C to 0-inch rod on Side A; spans the column on Side B

Table B.3 Longitudinal reinforcement strain gage nomenclature

Channel	Description
A1	Bar A, 15 inches below footing surface, facing inward
A2	Bar A, 10 inches below footing surface, facing outward
A3	Bar A, 5 inches below footing surface, facing inward
A4I	Bar A, at footing surface, facing inward
A4E	Bar A, at footing surface, facing outward
A5	Bar A, 7.5 inches above footing surface, facing inward
A6	Bar A, 14 inches above footing surface, facing inward
A7	Bar A, 25 inches above footing surface, facing inward
B1	Bar B, at footing surface, facing inward
C1	Bar C, 15 inches below footing surface, facing inward
C2	Bar C, 10 inches below footing surface, facing outward
C3	Bar C, 5 inches below footing surface, facing inward
C4I	Bar C, at footing surface, facing inward
C4E	Bar C, at footing surface, facing outward
C5	Bar C, 7.5 inches above footing surface, facing inward
C6	Bar C, 14 inches above footing surface, facing inward
C7	Bar C, 25 inches above footing surface, facing inward
D1	Bar D, at footing surface, facing inward

Table B.4 Hoop reinforcement strain gage nomenclature

Channel	Description
HA1	Hoop at 2 inches, at position of Bar A
HA2	Hoop at 6 inches, at position of Bar A
HA3	Hoop at 10 inches, at position of Bar A
HA4	Hoop at 18 inches, at position of Bar A
HB1	Hoop at 10 inches, at position of Bar B
HC1	Hoop at 2 inches, at position of Bar C
HC2	Hoop at 6 inches, at position of Bar C
HC3	Hoop at 10 inches, at position of Bar C
HC4	Hoop at 18 inches, at position of Bar C
HD1	Hoop at 10 inches, at position of Bar D

Table B.5 Load cell nomenclature

Channel	Description
Axial_LC	Axial-load cell, placed on one side of axial-load spreader beam
Ram_LC	Actuator load cell, attached between piston and front swivels
Delta_P	Estimate of actuator force based on internal pressure differential

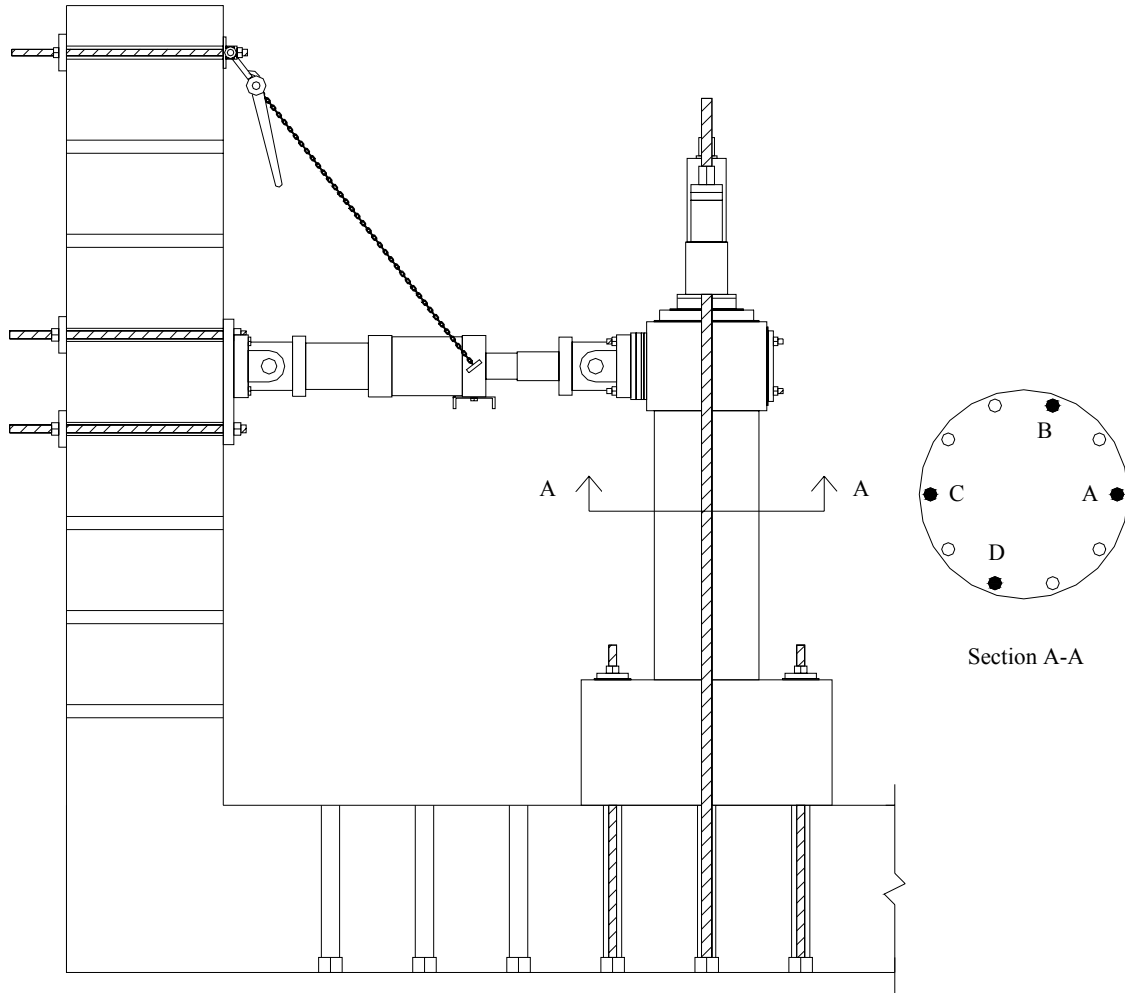


Fig. B.1 Bar identification letters

B.1 COLUMN S3

Column S3 was subjected to one cycle at 0.02 inches (0.51 mm), followed by sets of three cycles at displacement levels corresponding to half the calculated cracking moment, the average of the calculated cracking moment, and the calculated yield moment, $1.25\Delta_y$, $2\Delta_y$, $3\Delta_y$, $5\Delta_y$, and $8\Delta_y$; the test concluded with one cycle at $12\Delta_y$. This displacement history is shown in Figure B.2 below.

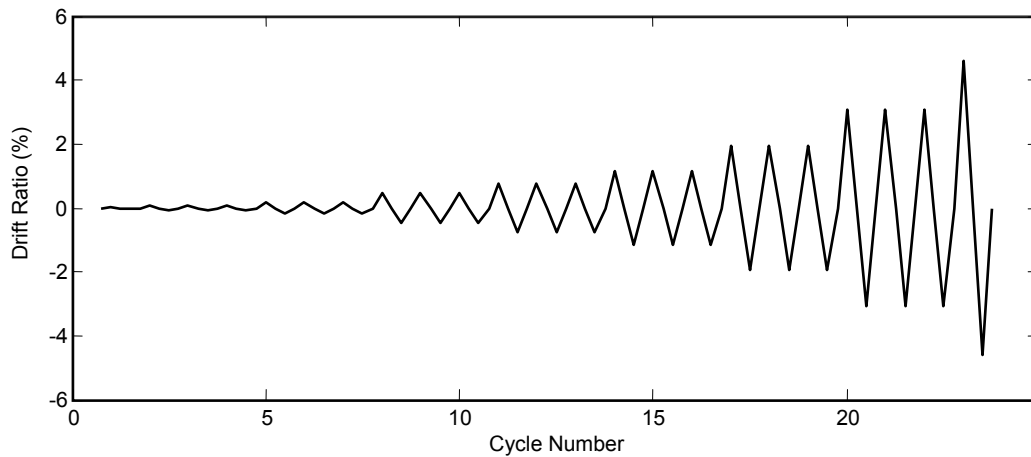


Fig. B.2 Displacement history for Column S3

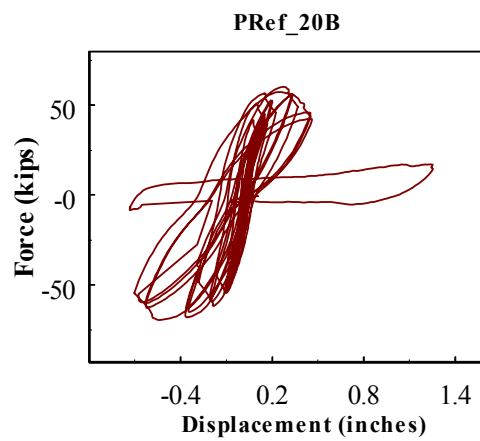
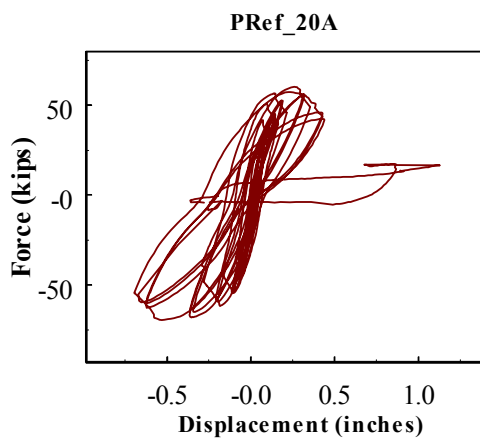
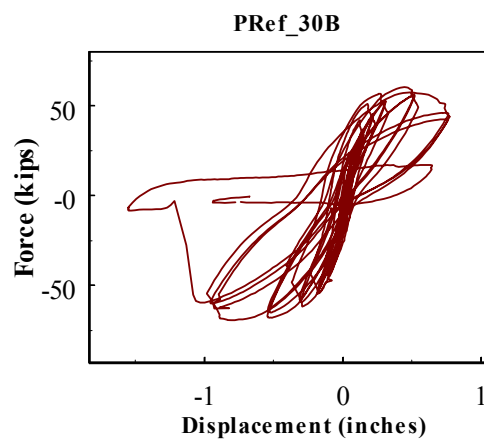
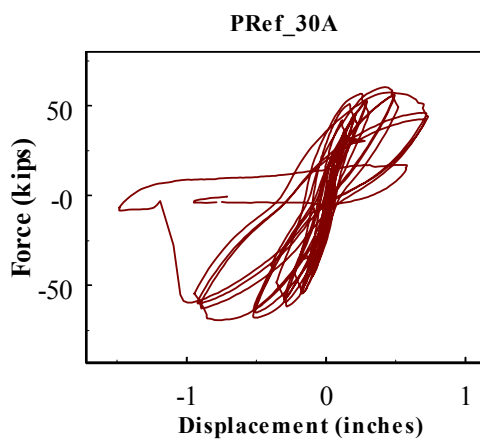
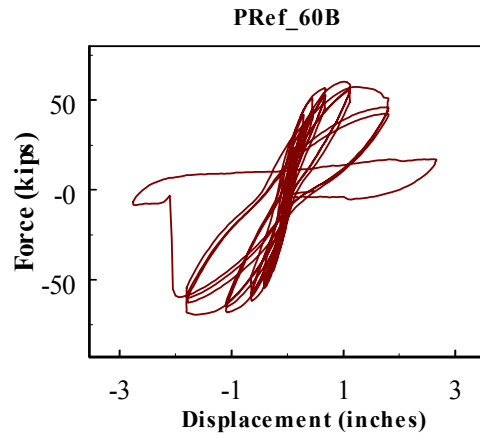
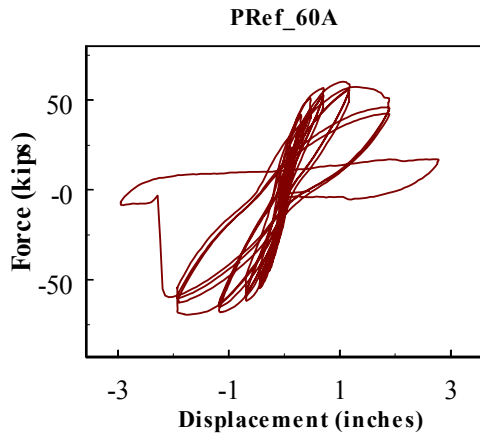


Fig. B.3 Column S3 data

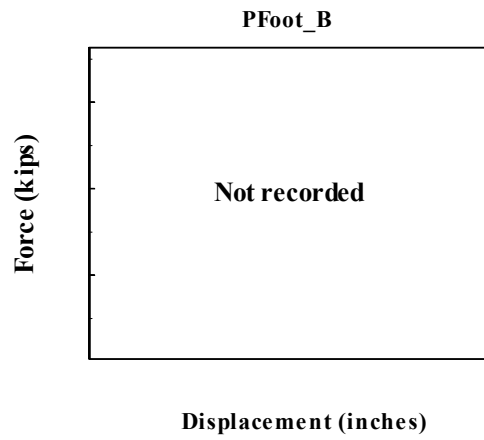
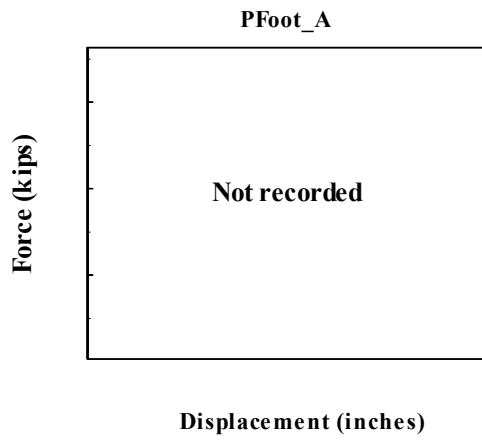
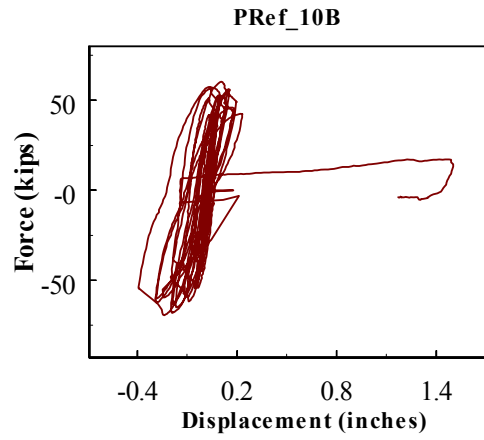
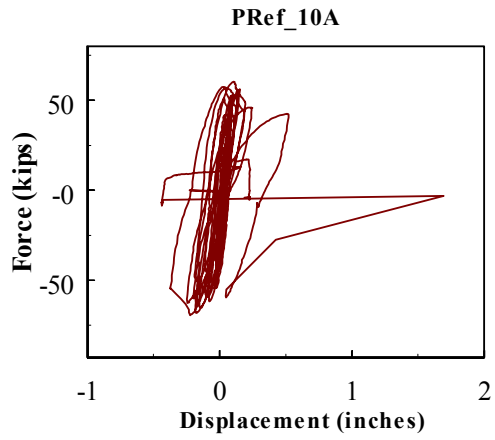


Fig. B.3 (cont.) Column S3 data

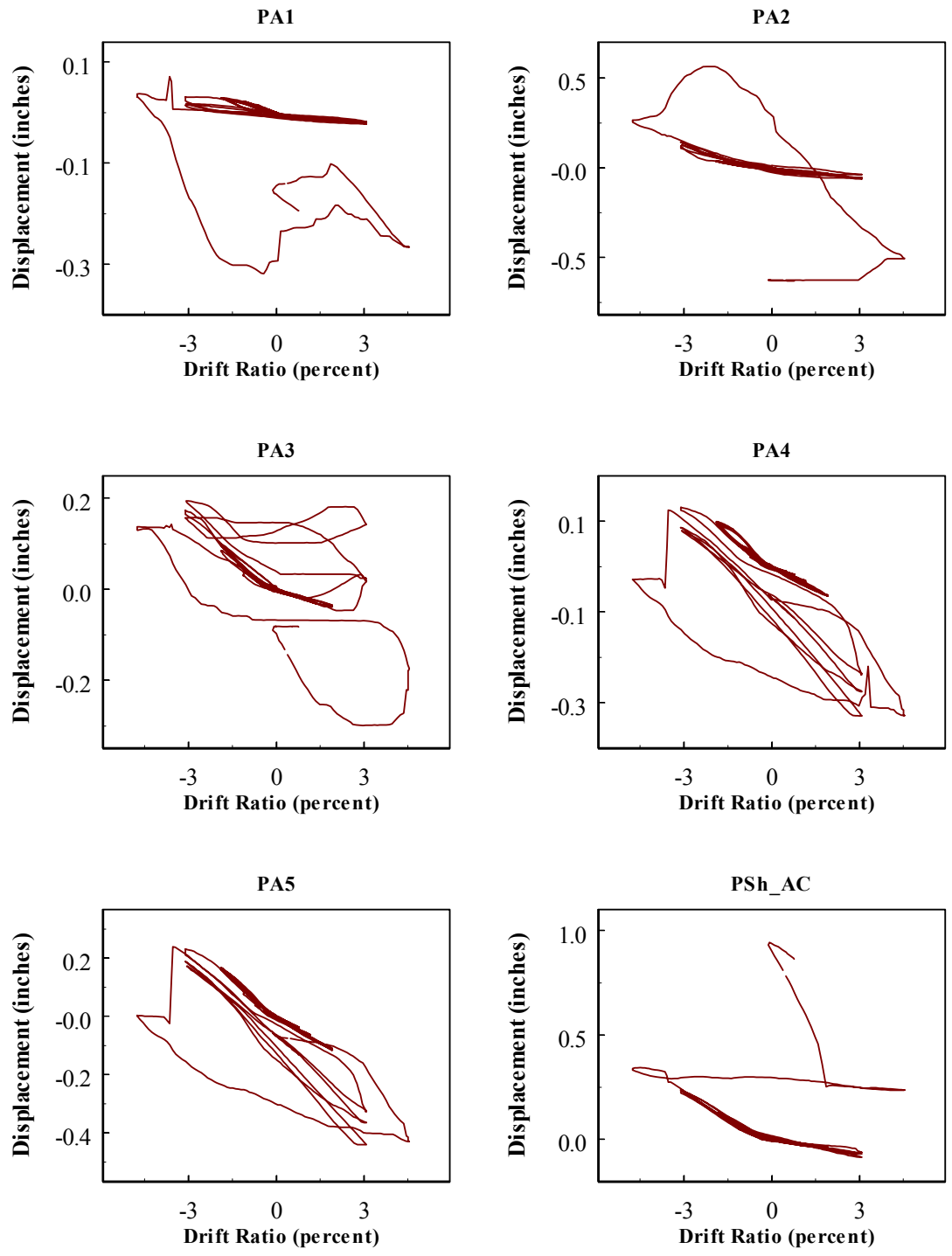


Fig. B.3 (cont.) Column S3 data

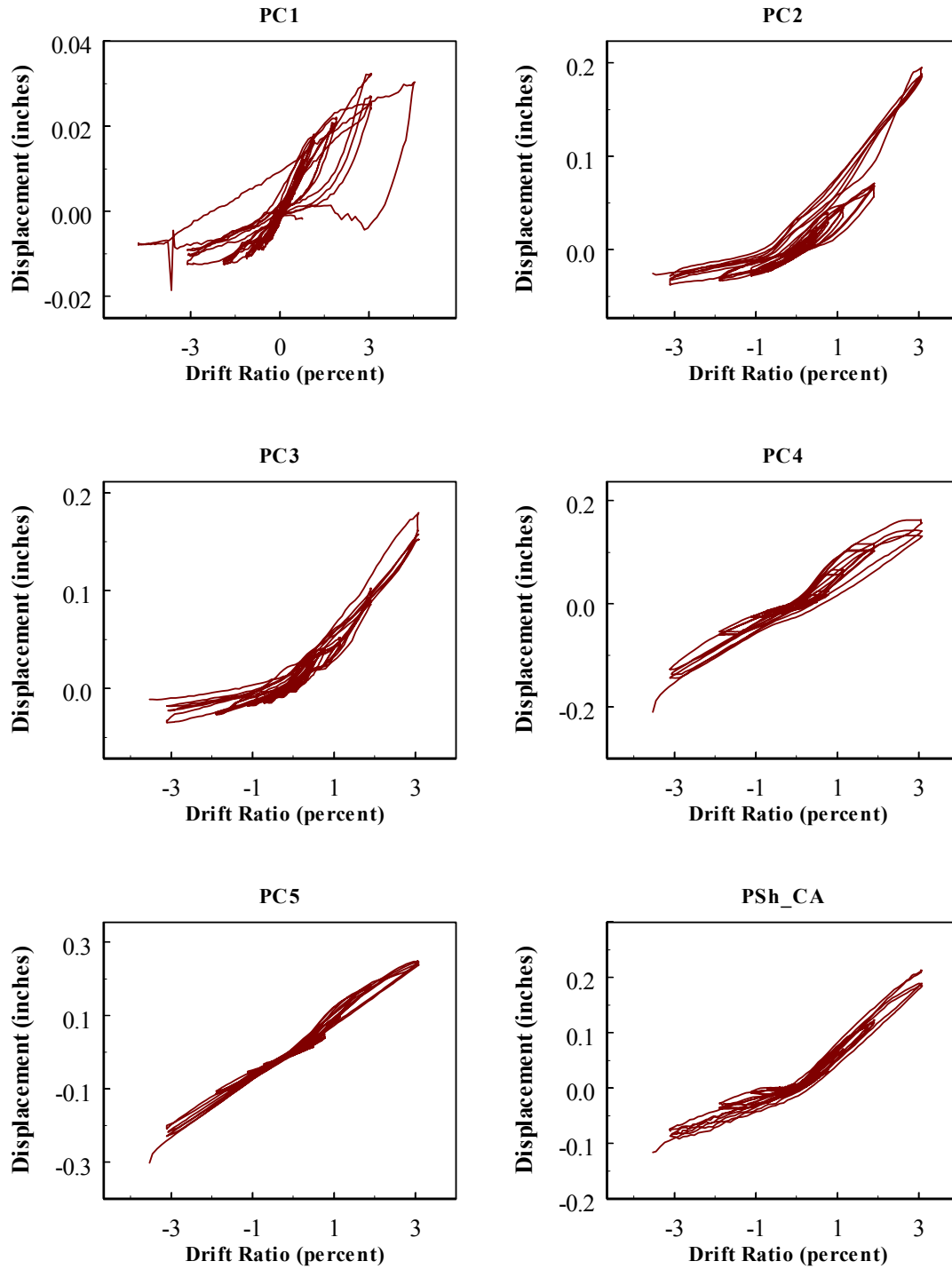


Fig. B.3 (cont.) Column S3 data

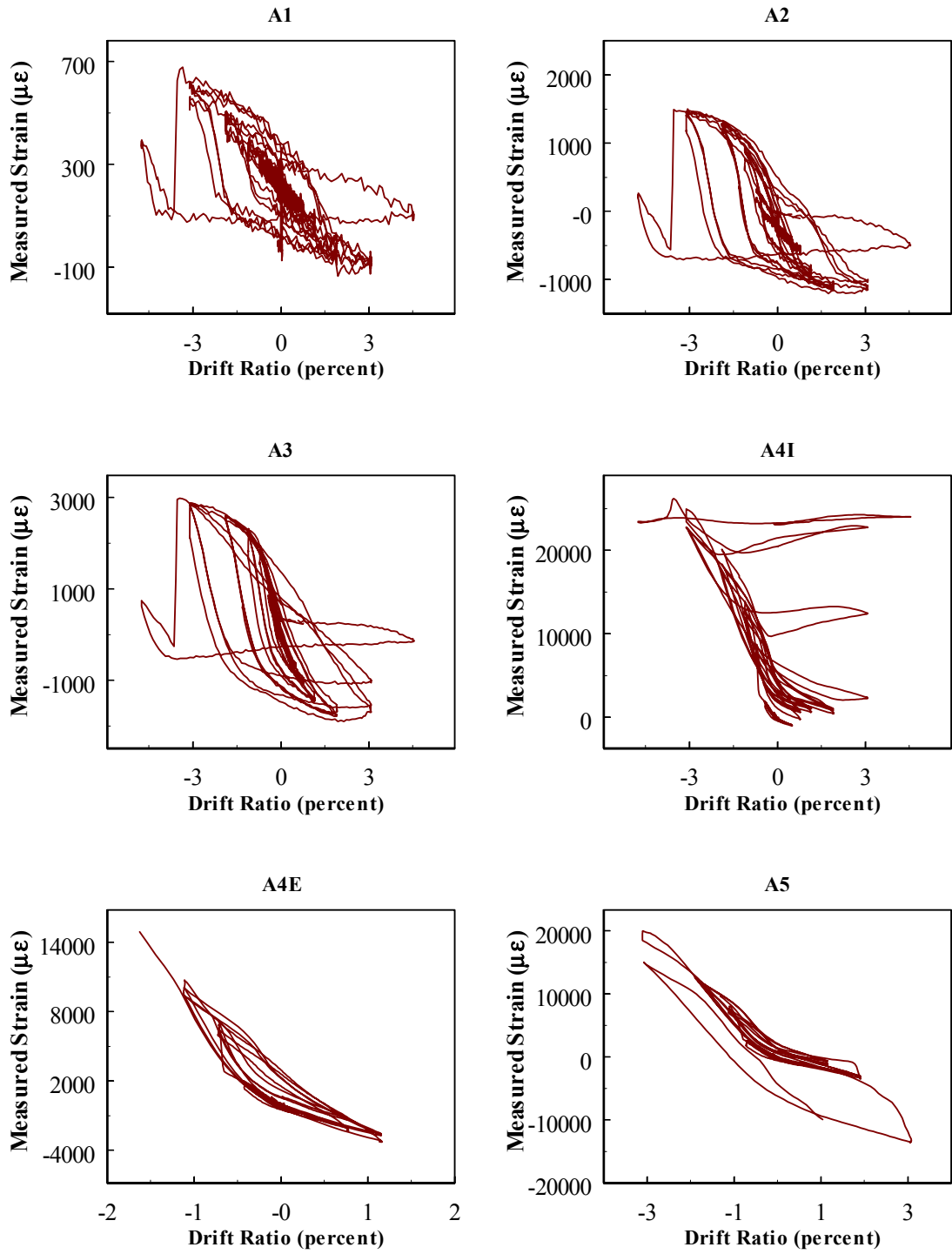


Fig. B.3 (cont.) Column S3 data

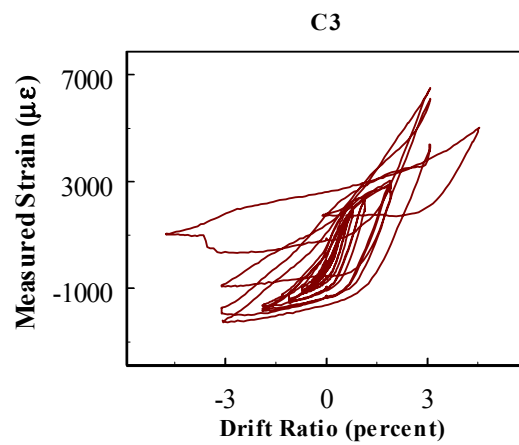
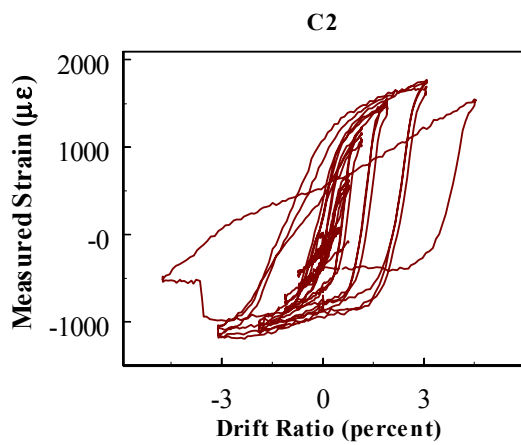
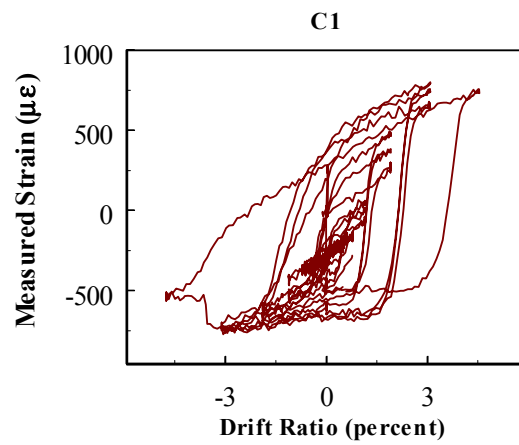
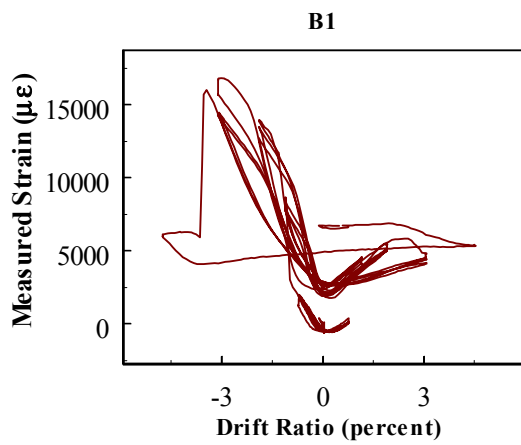
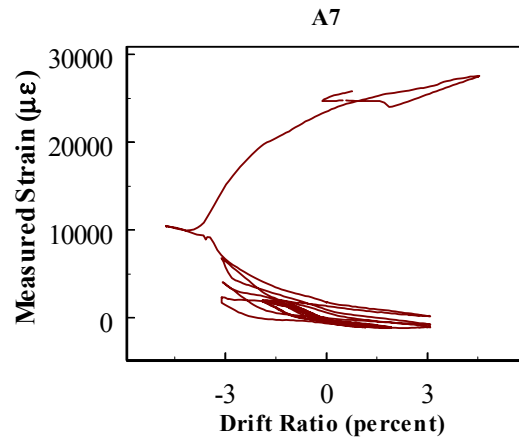
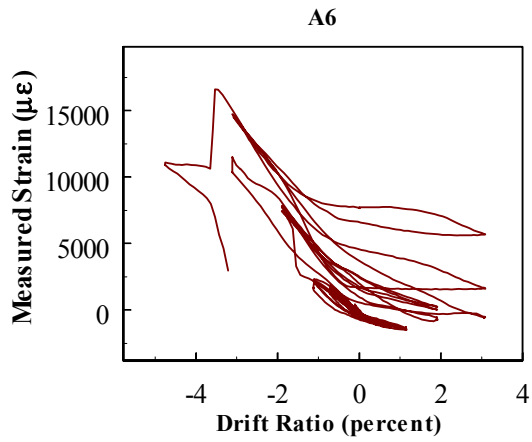


Fig. B.3 (cont.) Column S3 data

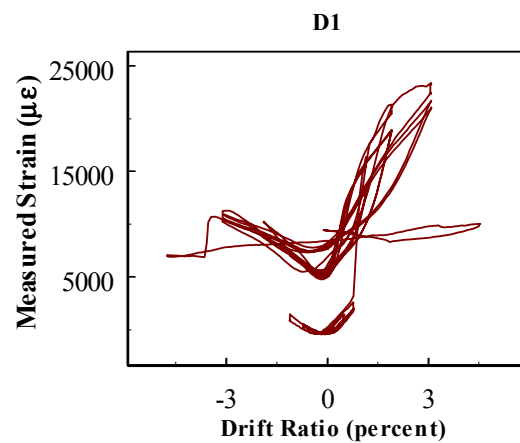
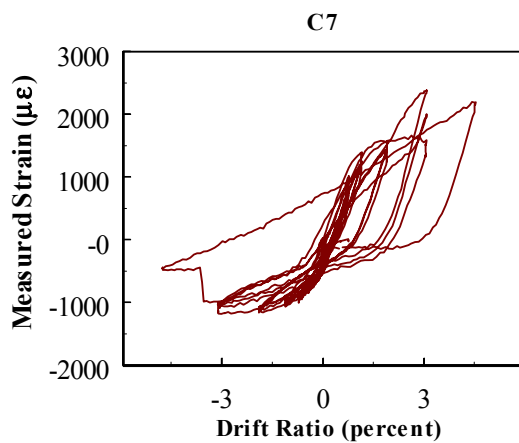
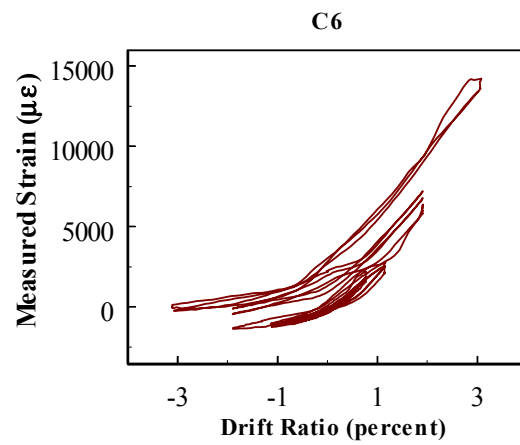
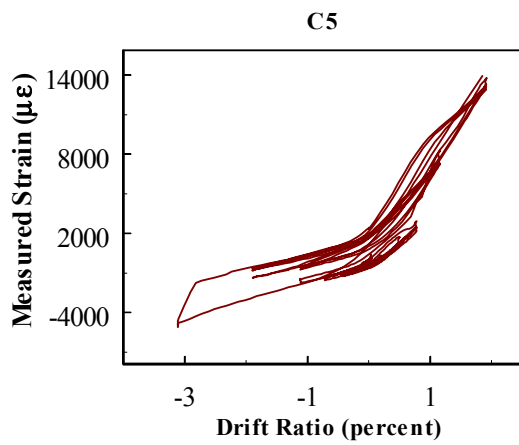
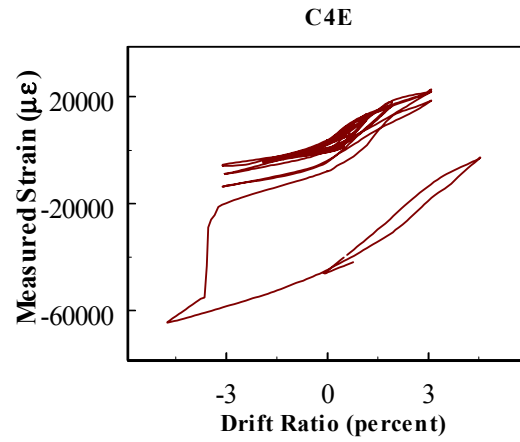
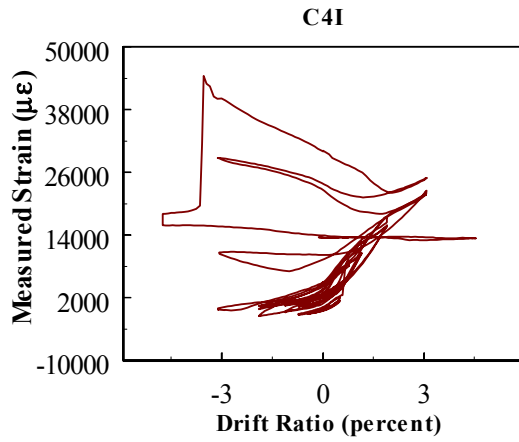


Fig. B.3 (cont.) Column S3 data

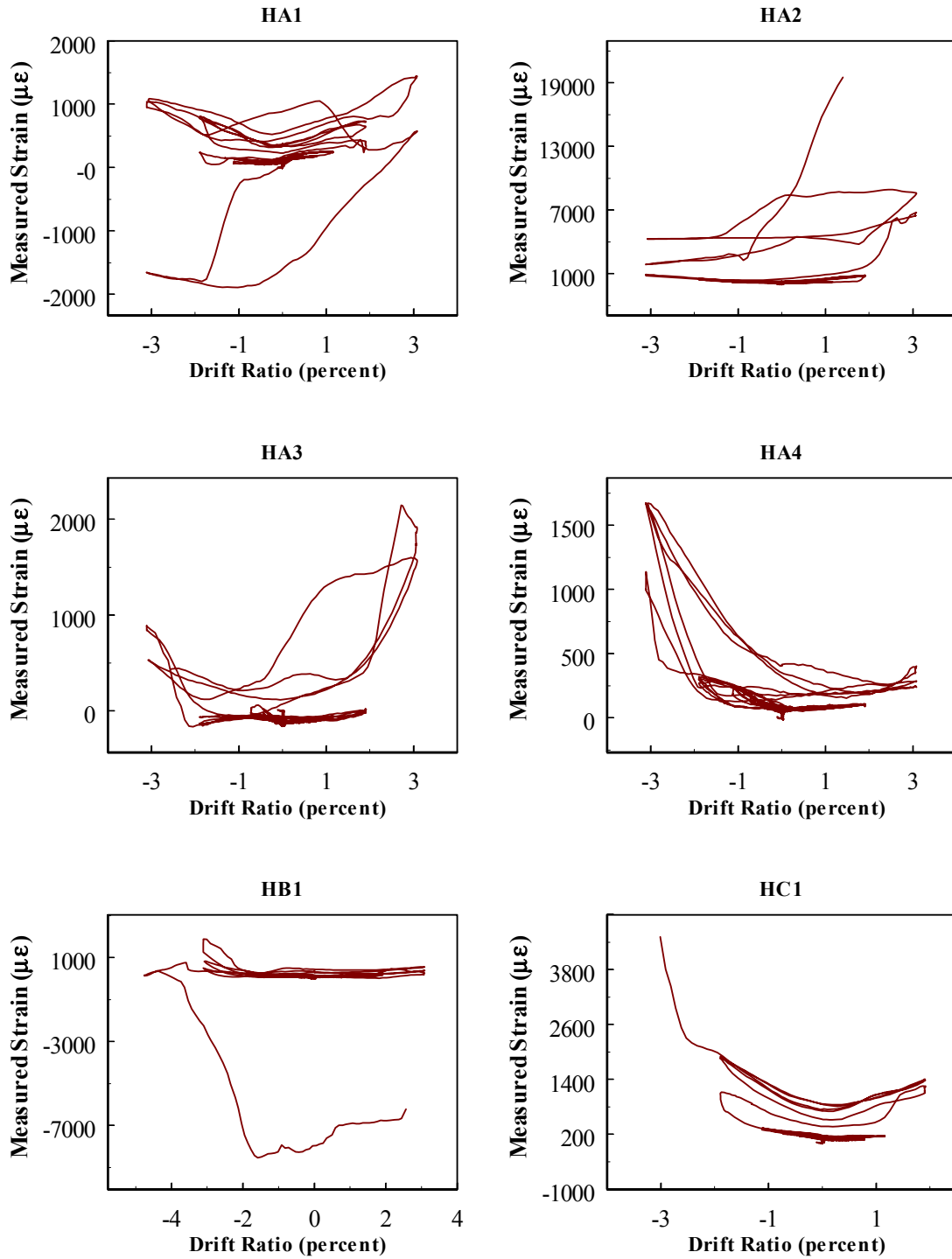


Fig. B.3 (cont.) Column S3 data

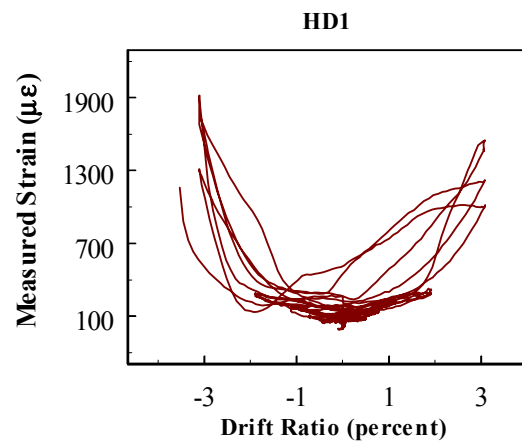
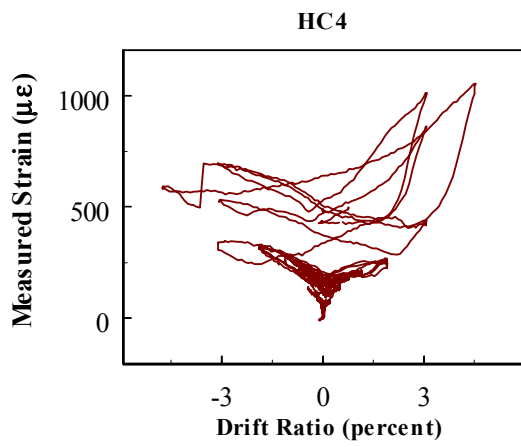
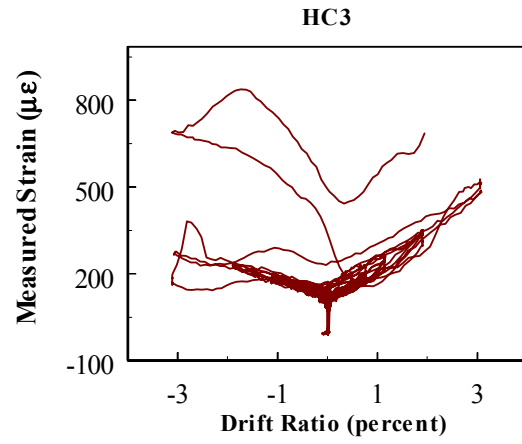
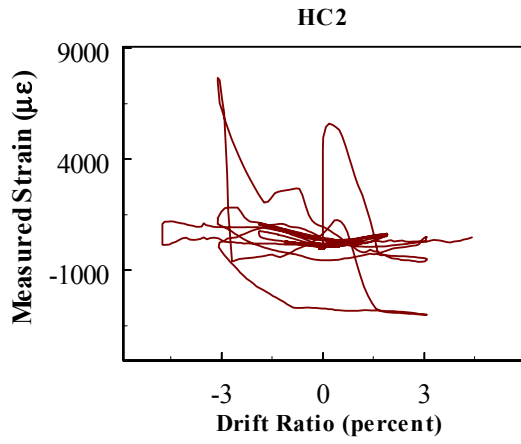


Fig. B.3 (cont.) Column S3 data

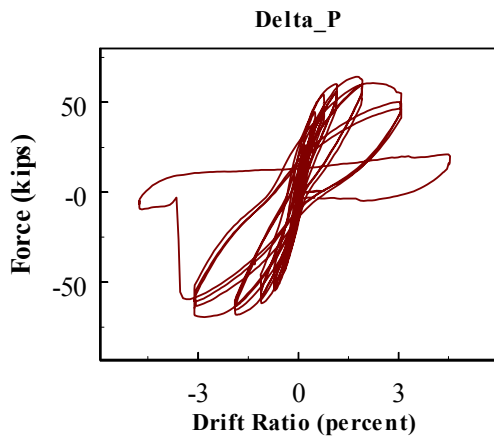
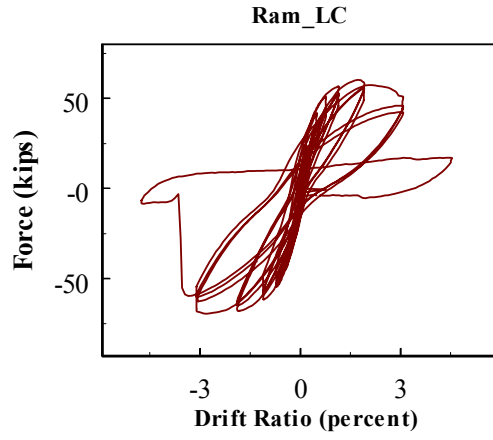
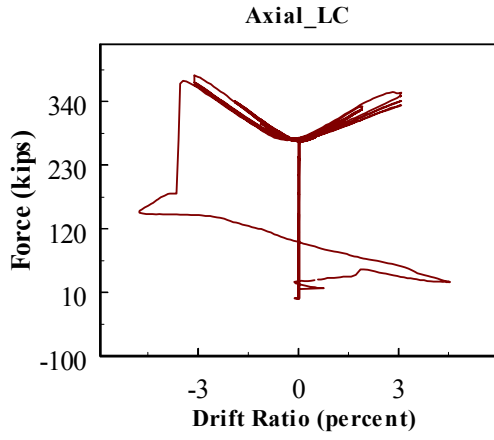


Fig. B.3 (cont.) Column S3 data

B.2 COLUMN C2

Column C2 was subjected to single cycles at half the cracking moment and $2\Delta_y$, followed by 10 cycles at $5\Delta_y$, 3 cycles at $8\Delta_y$, and finally 1 cycle at $10\Delta_y$.

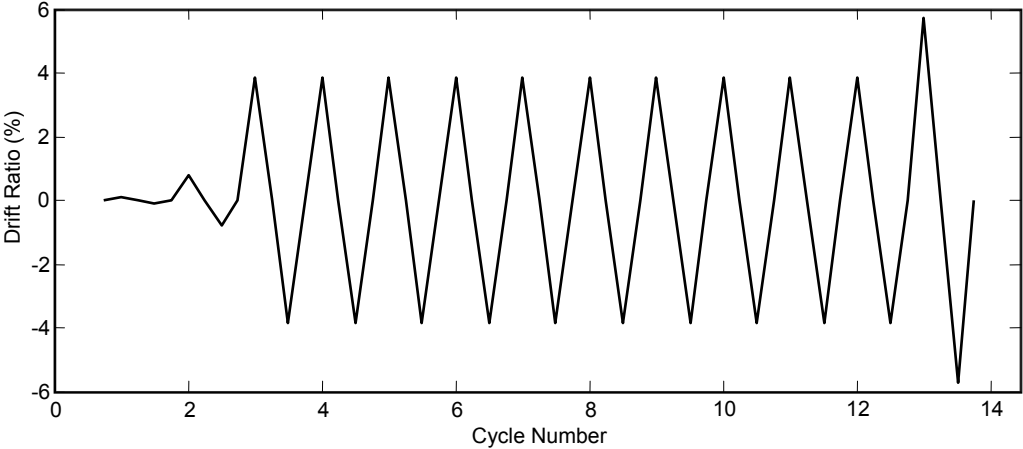


Fig. B.4 Displacement history for Column C2

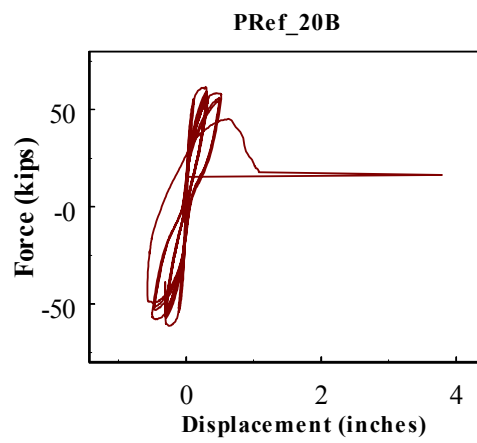
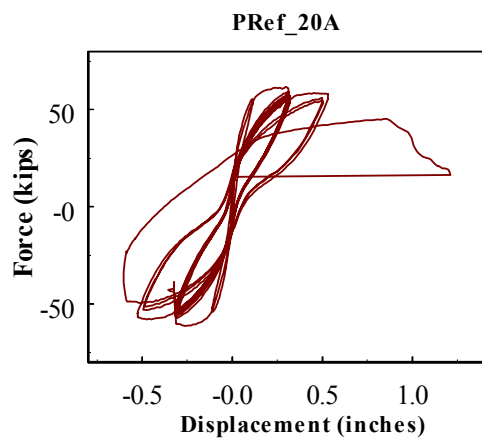
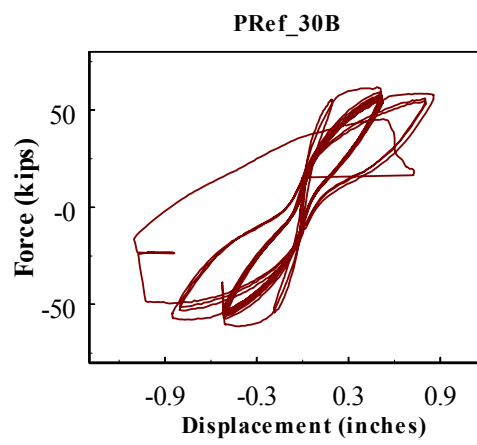
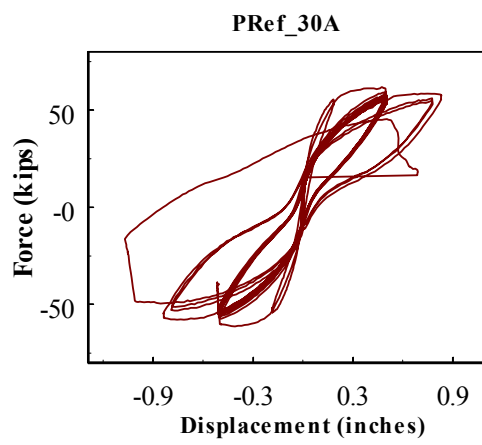
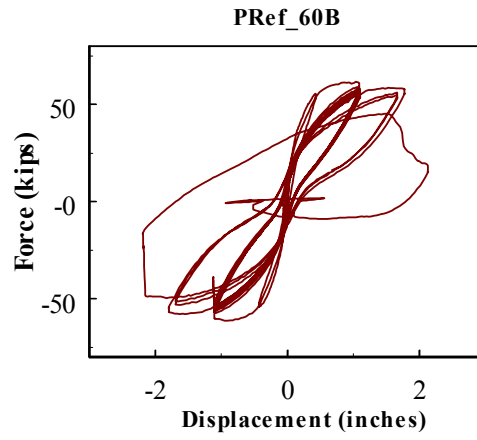
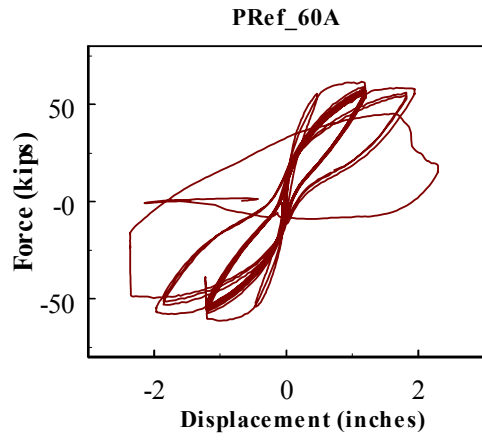


Fig. B.5 Column C2 data

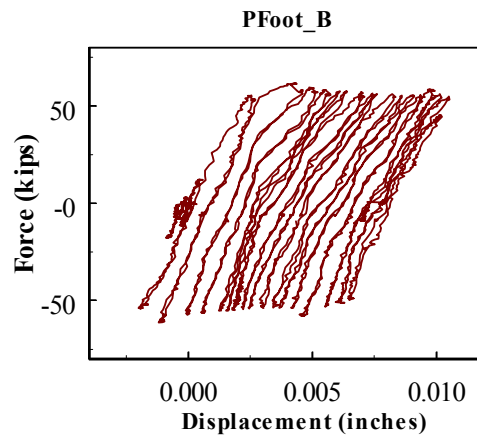
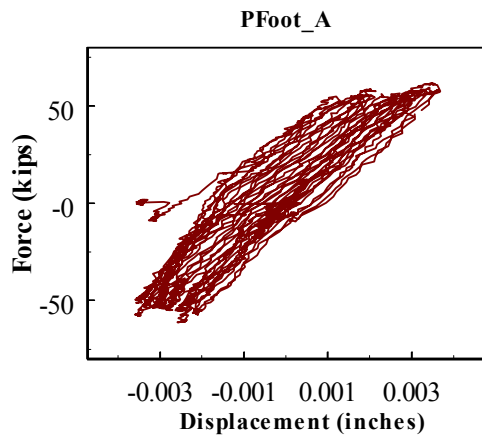
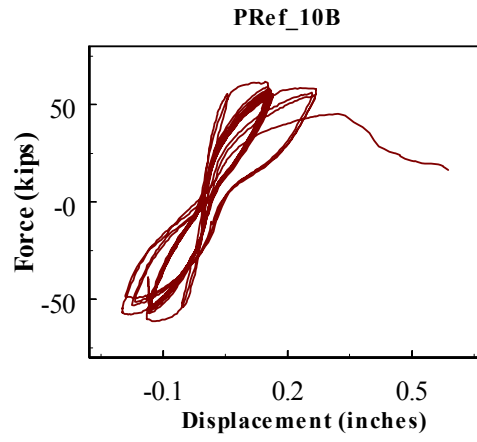
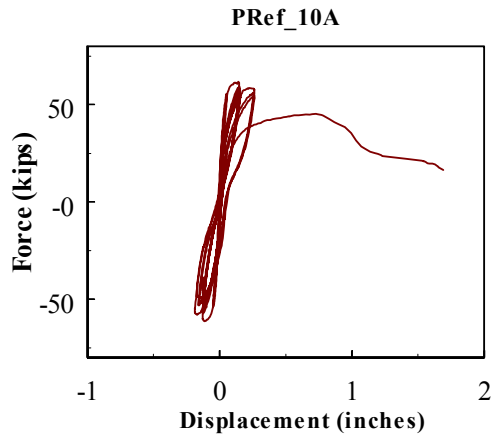


Fig B.5 (cont.) Column C2 data

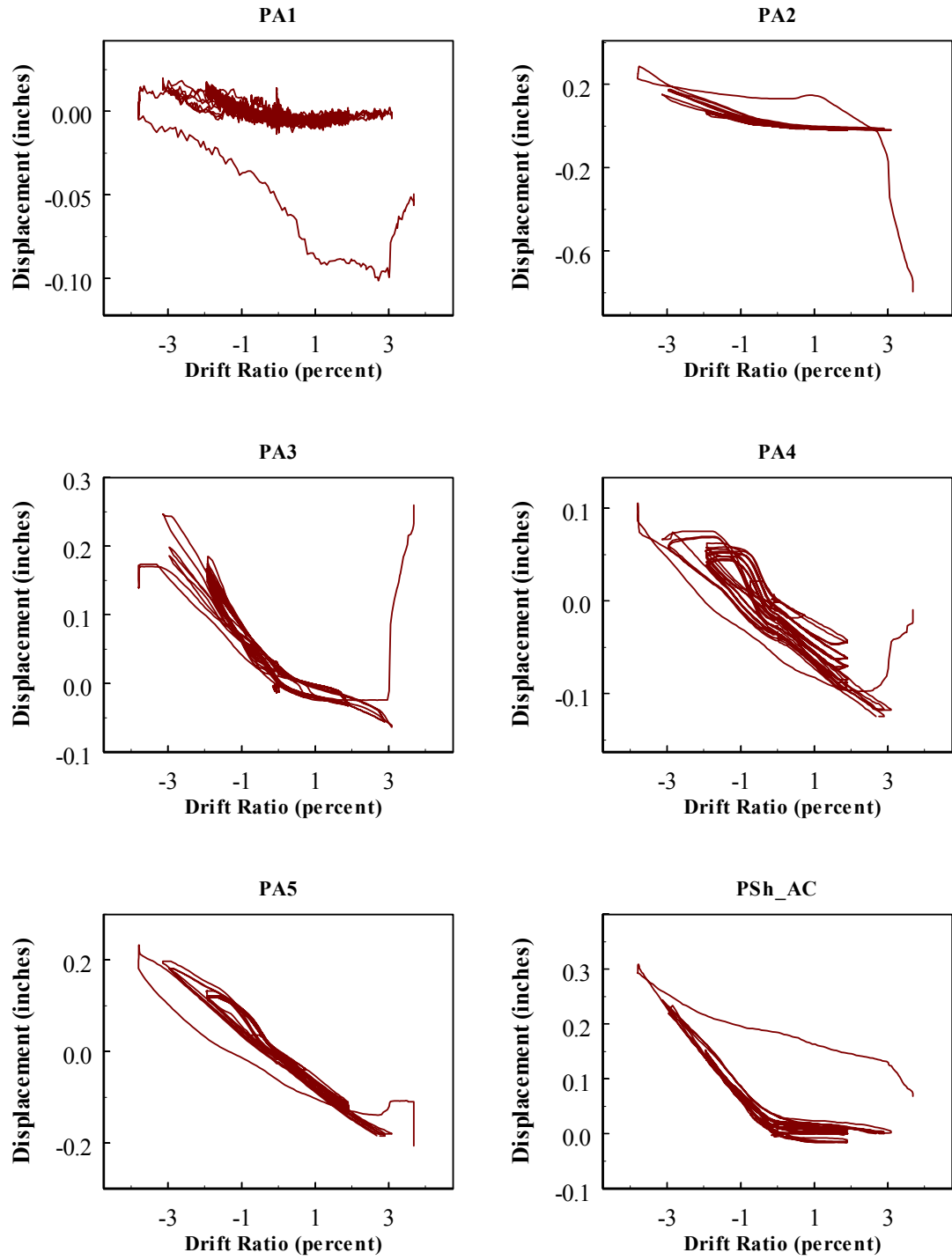


Fig B.5 (cont.) Column C2 data

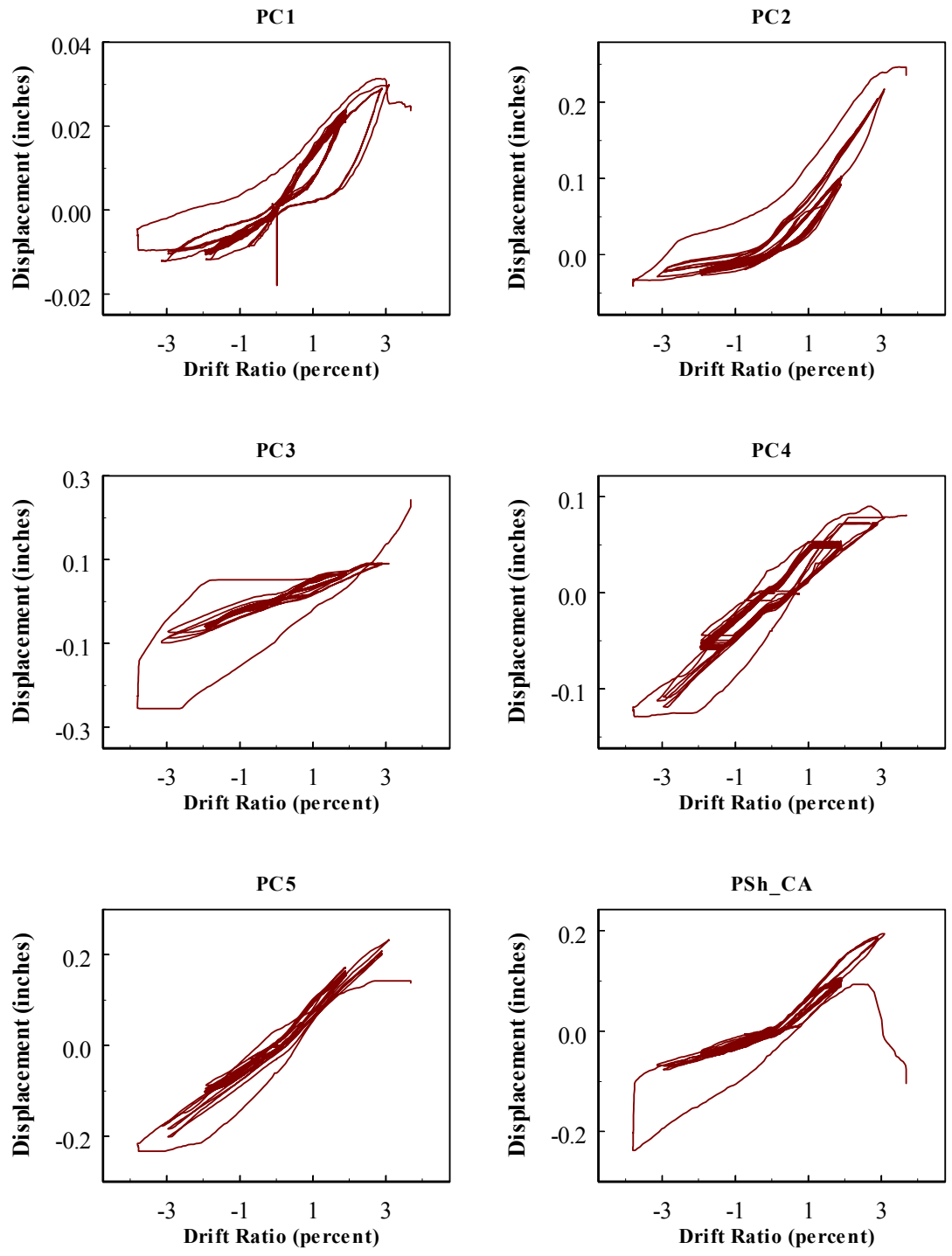


Fig. B.5 (cont.) Column C2 data

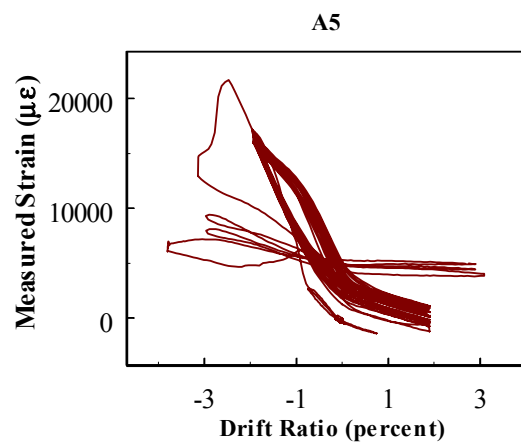
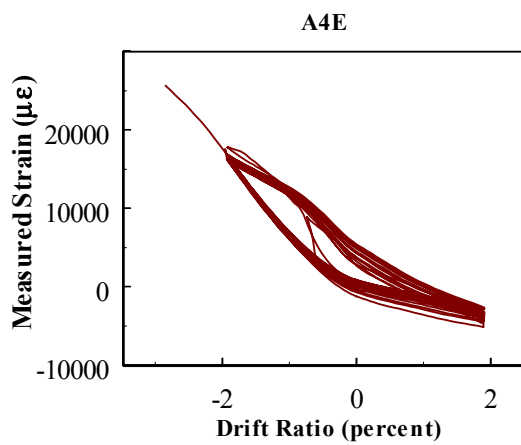
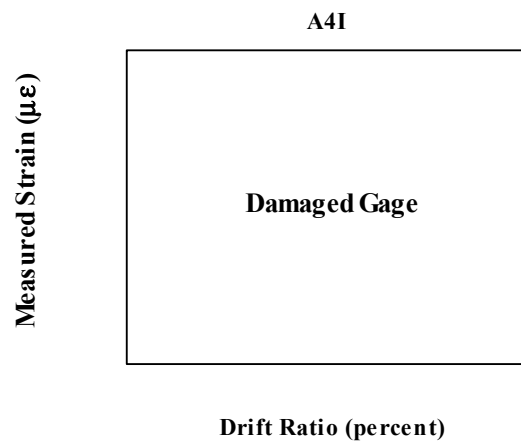
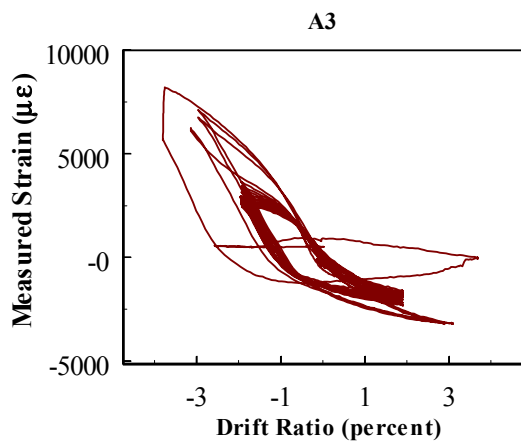
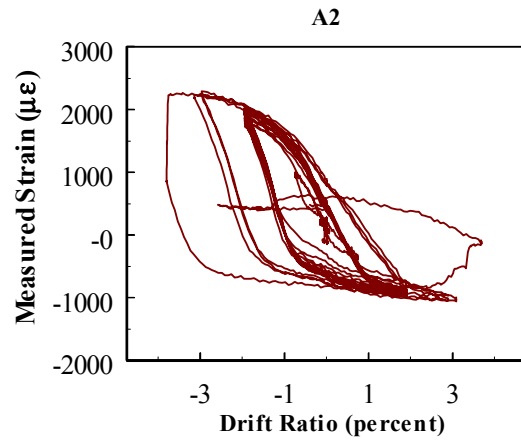
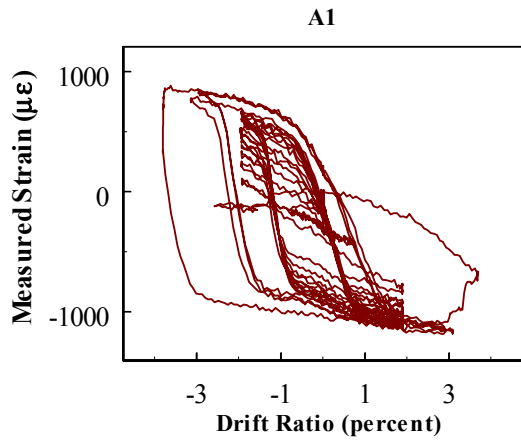


Fig. B.5 (cont.) Column C2 data

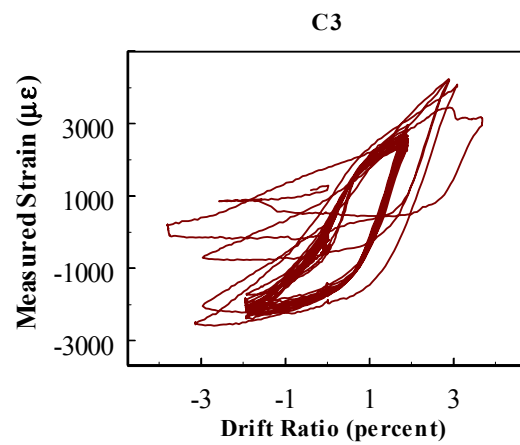
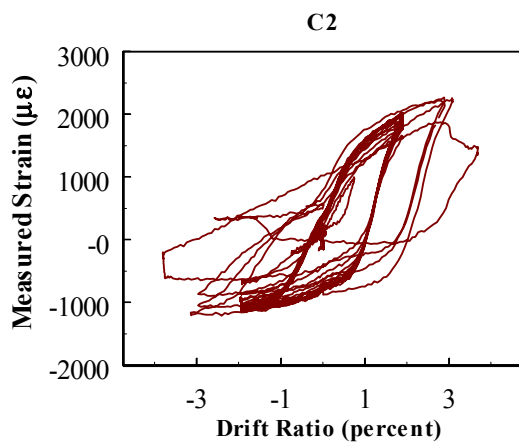
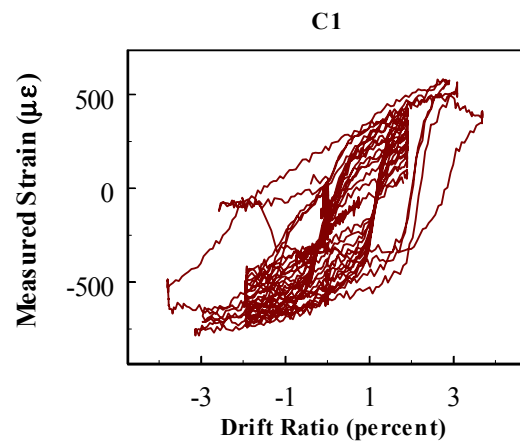
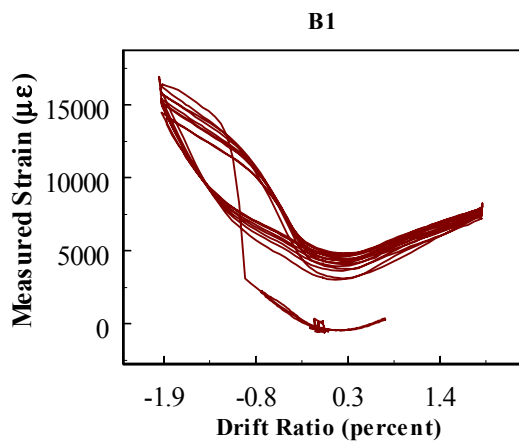
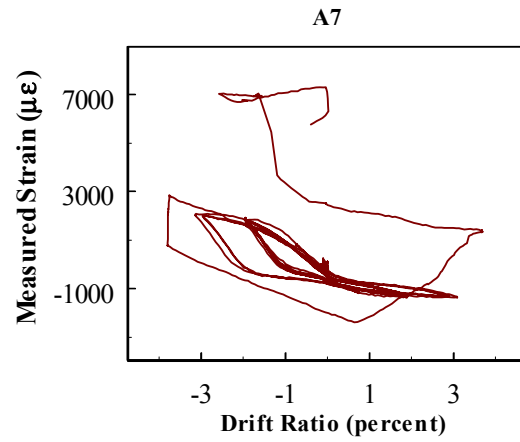
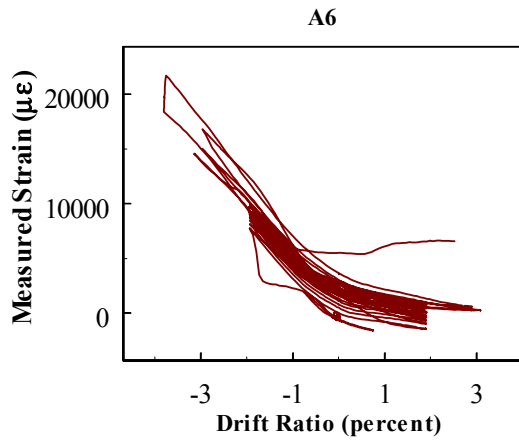


Fig. B.5 (cont.) Column C2 data

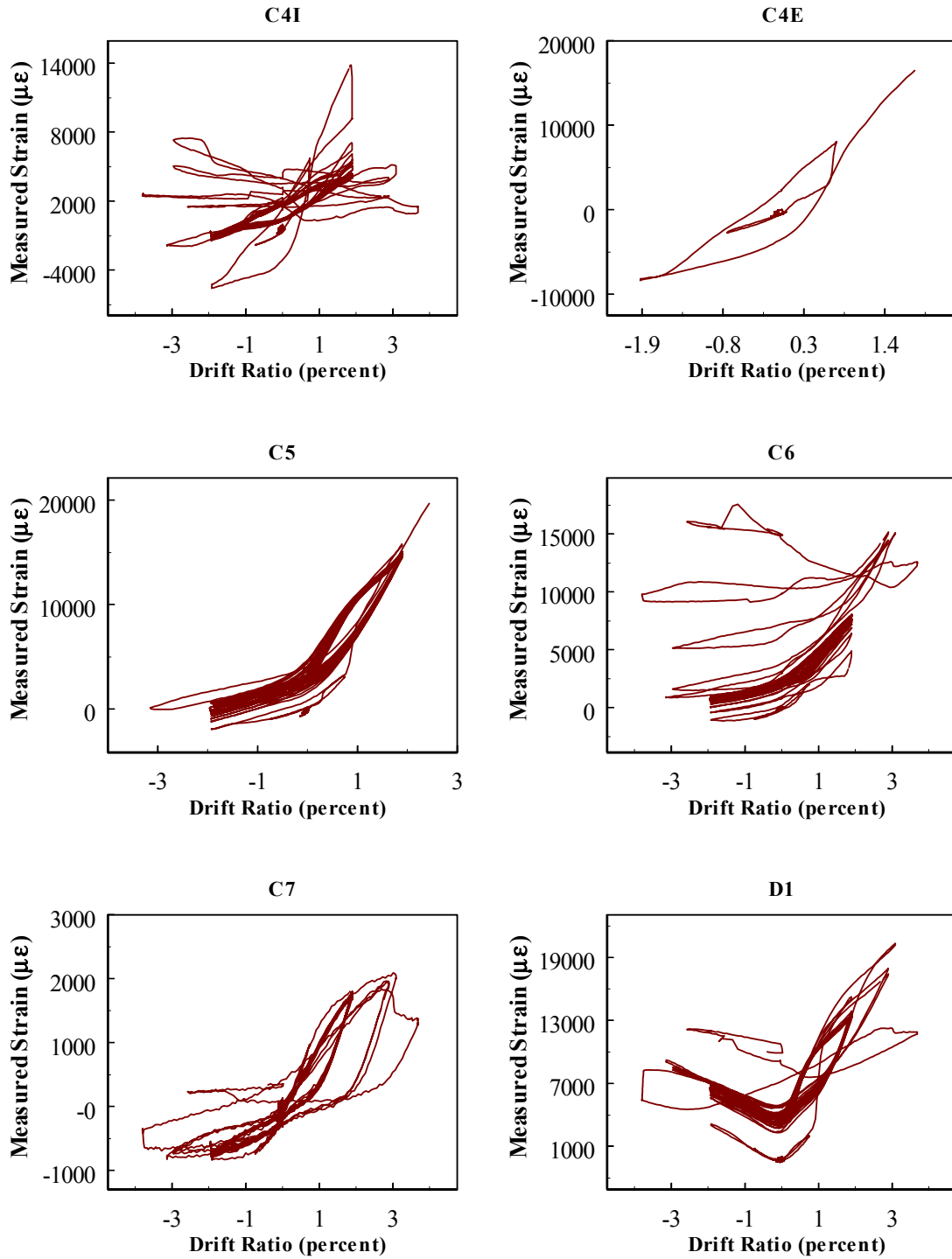


Fig. B.5 (cont.) Column C2 data

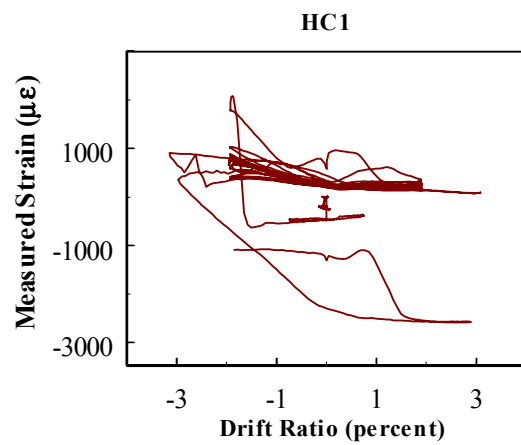
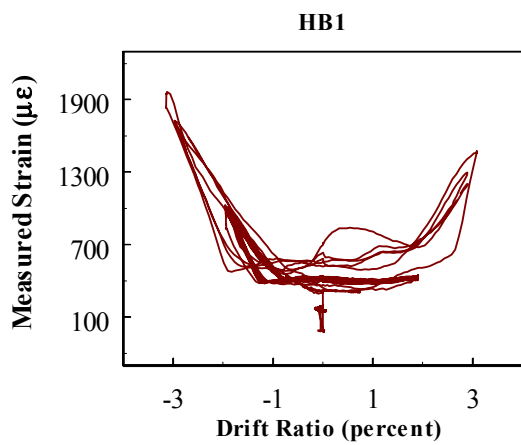
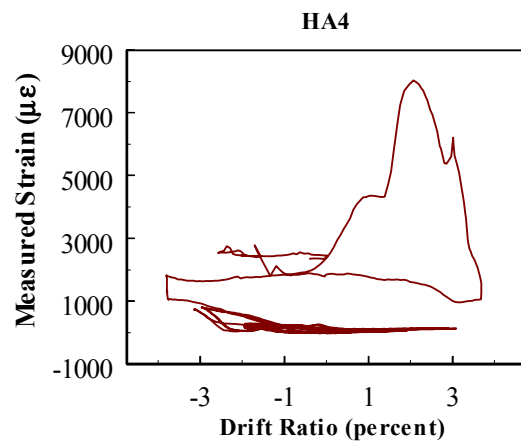
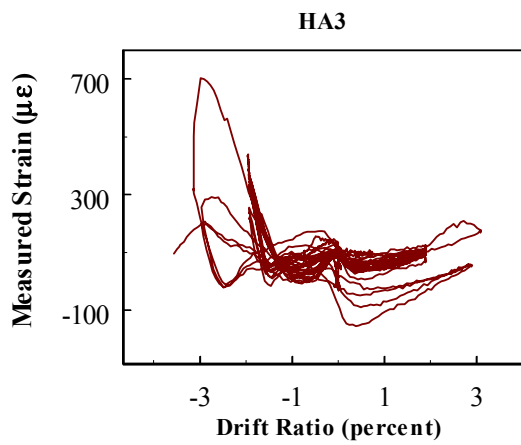
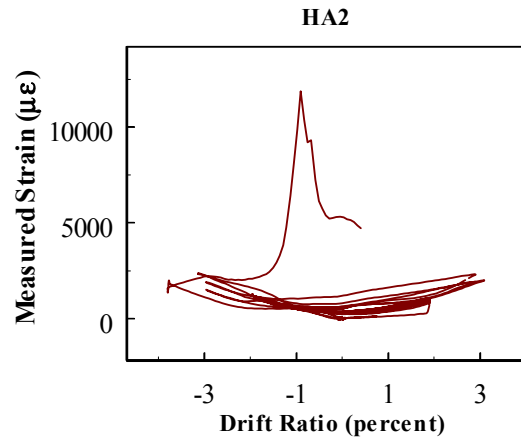
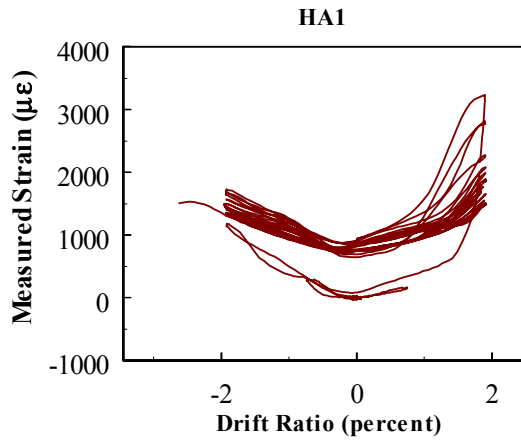


Fig. B.5 (cont.) Column C2 data

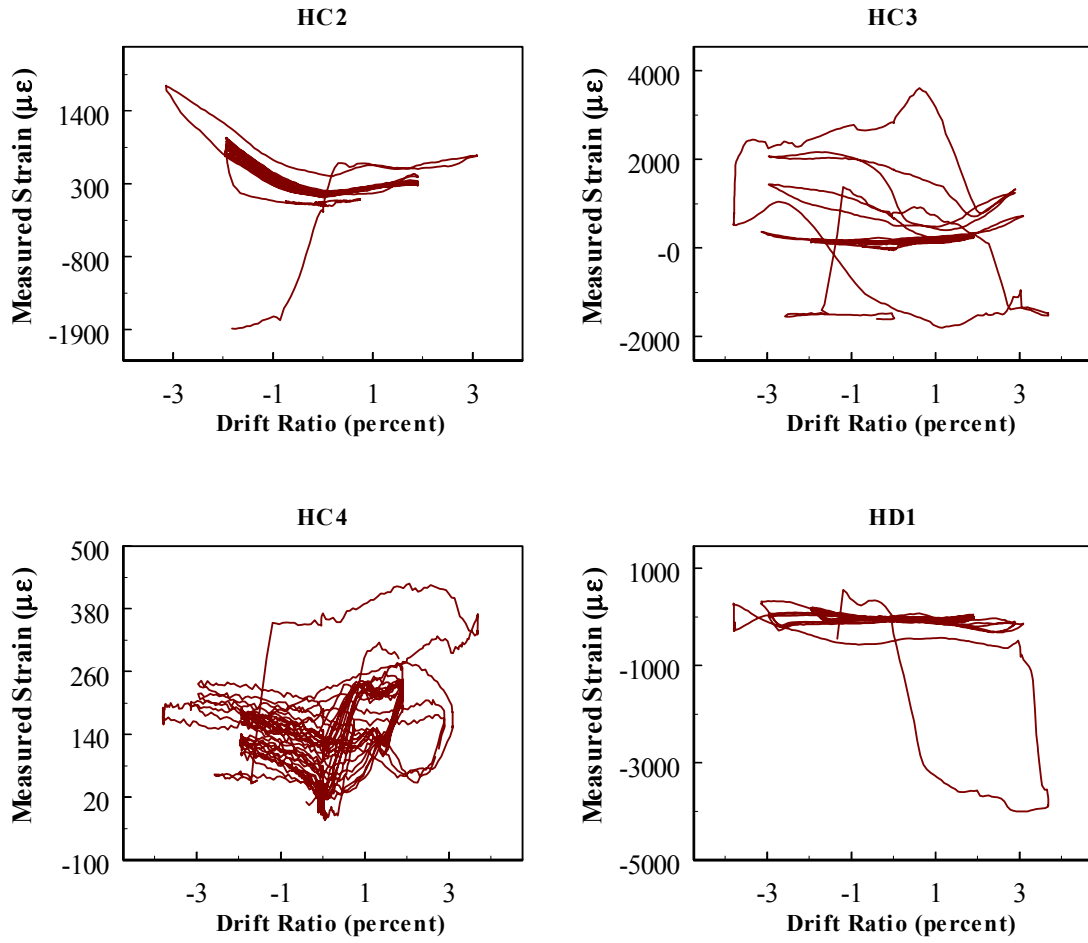


Fig. B.5 (cont.) Column C2 data

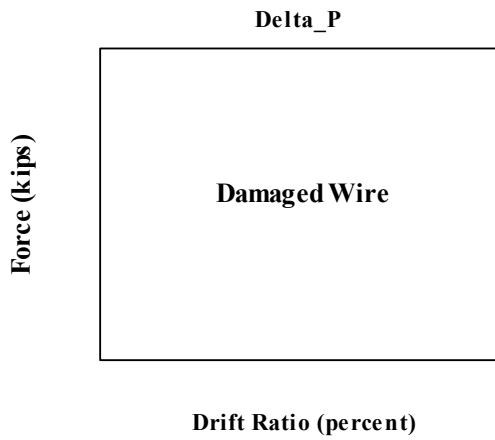
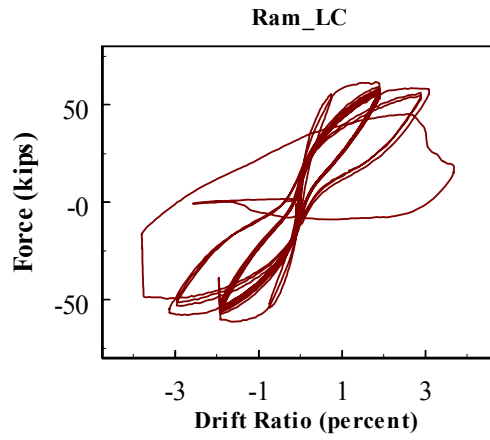
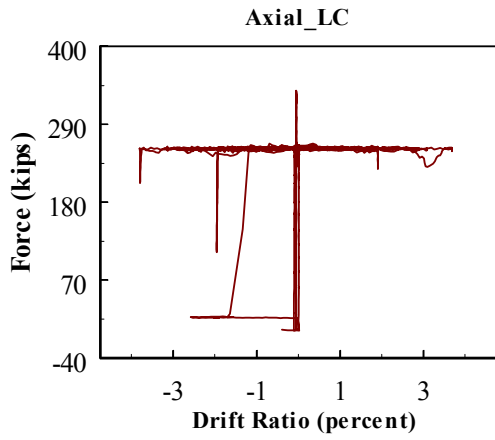


Fig. B.5 (cont.) Column C2 data

B.3 COLUMN C4

Column C4 was subjected to one cycle at half the calculated cracking moment and one cycle at $2\Delta_y$ before being subjected to 10 cycles at $10\Delta_y$, followed by one cycle at $15\Delta_y$. This is shown in Figure B.6, below.

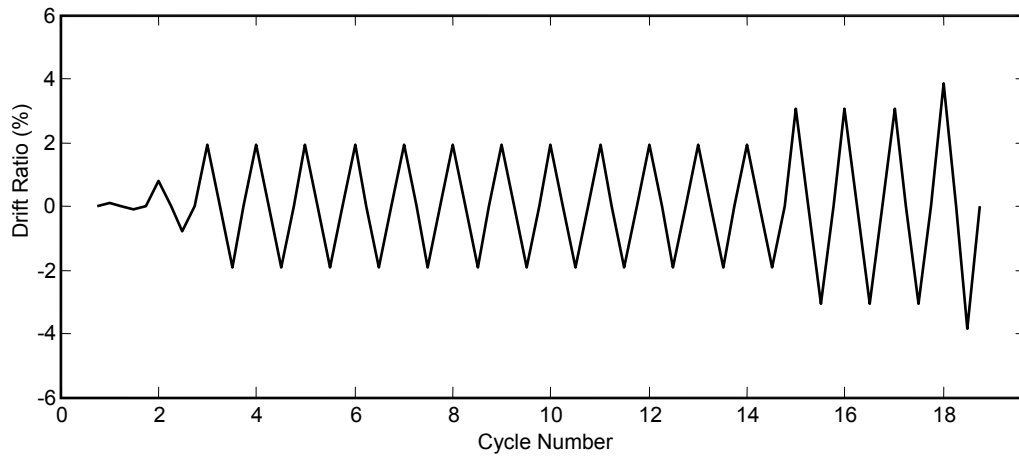


Fig. B.6 Displacement history for Column C4

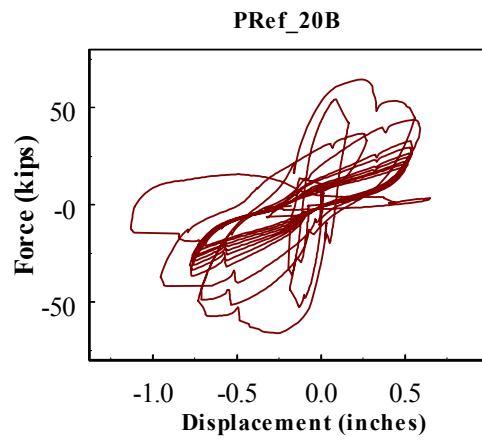
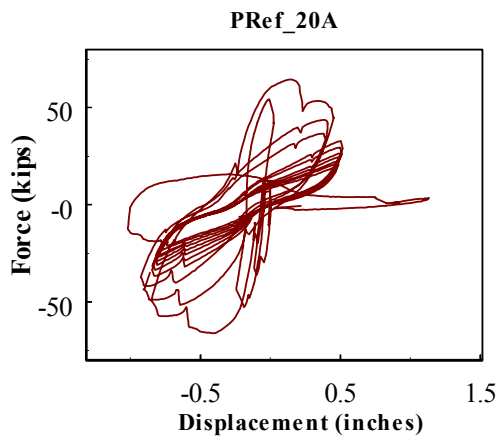
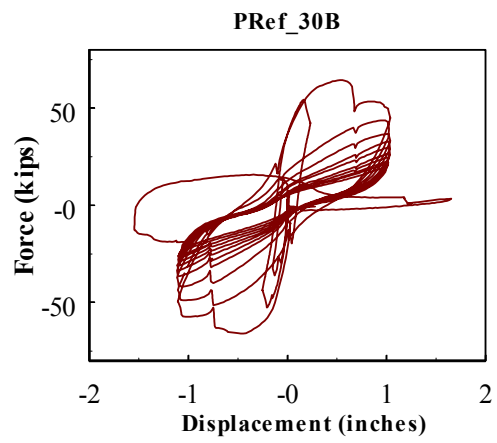
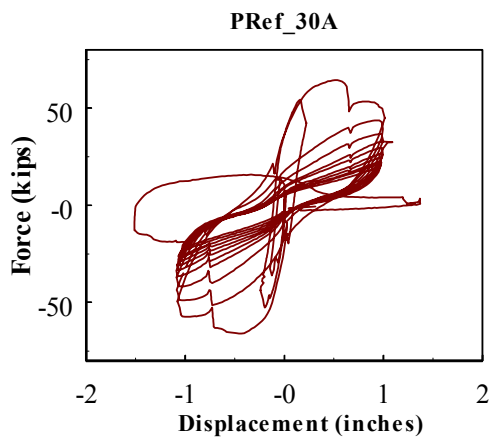
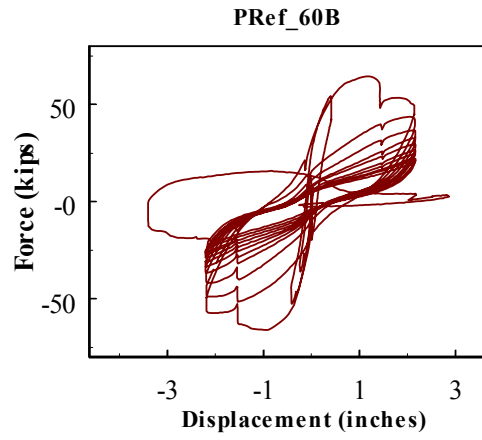
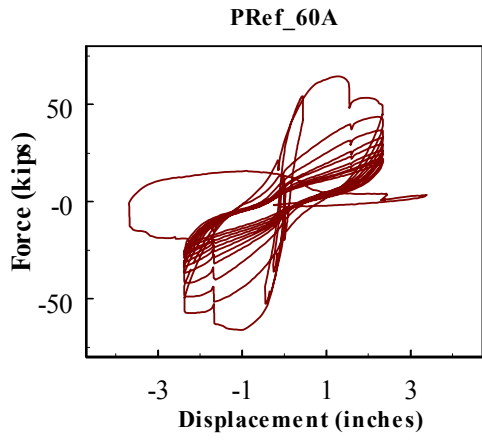


Fig. B.7 Column C4 data

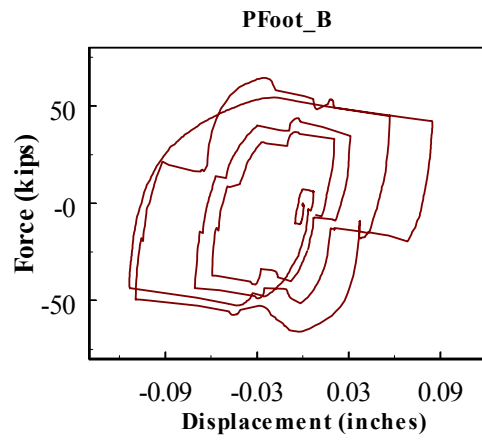
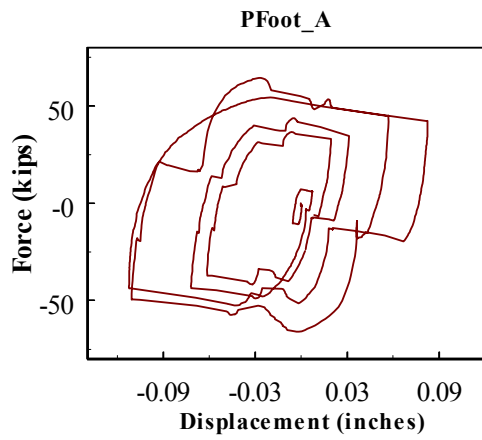
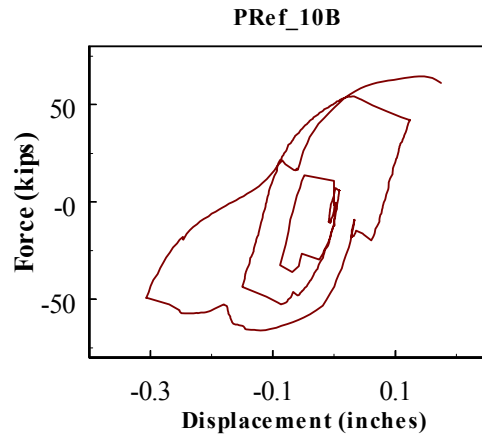
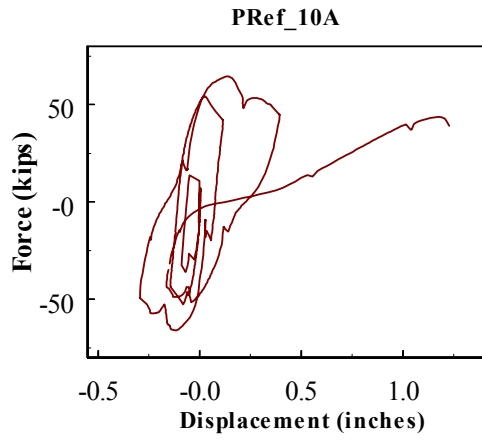


Fig. B.7 (cont.) Column C4 data

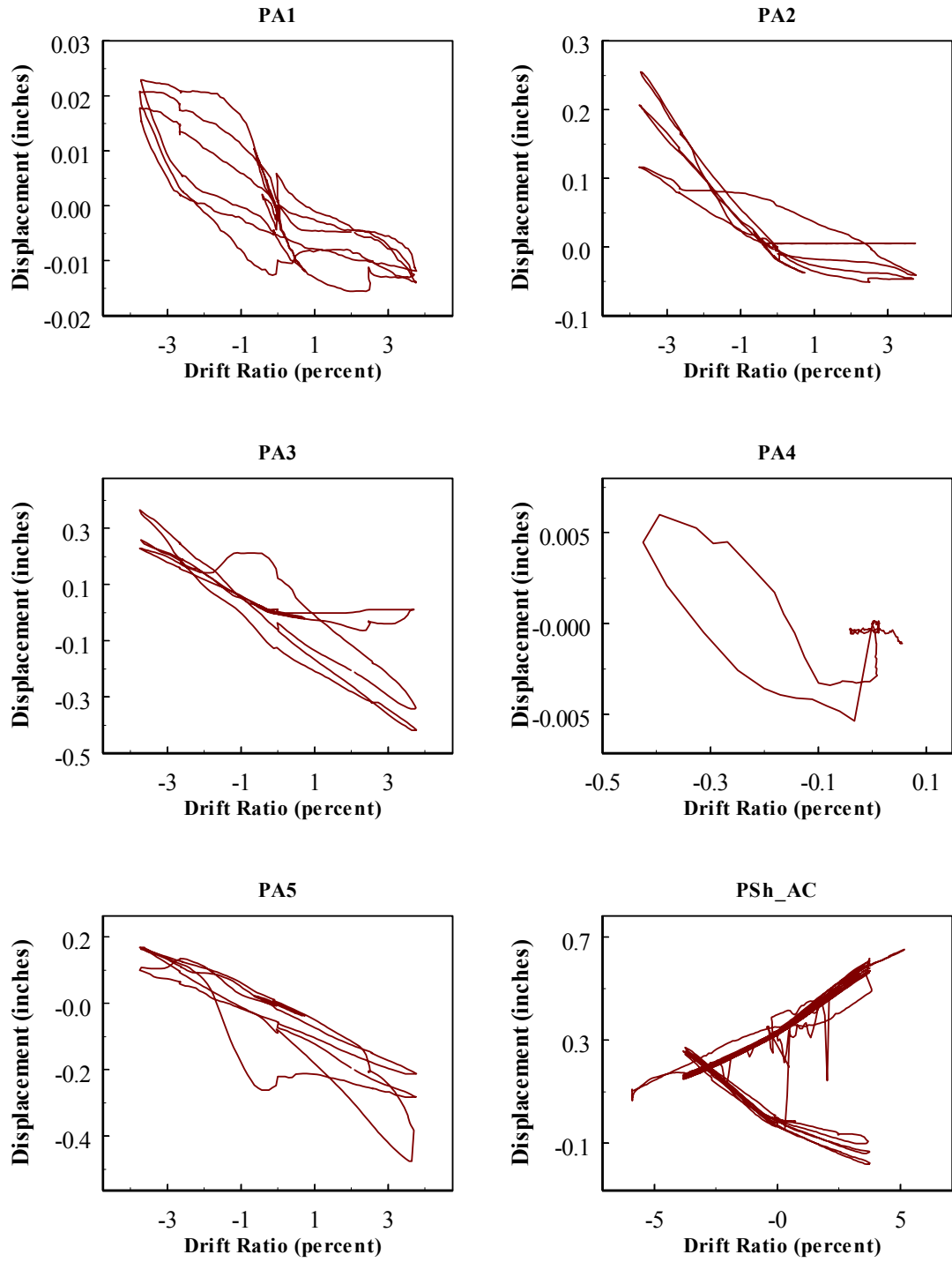


Fig. B.7 (cont.) Column C4 data

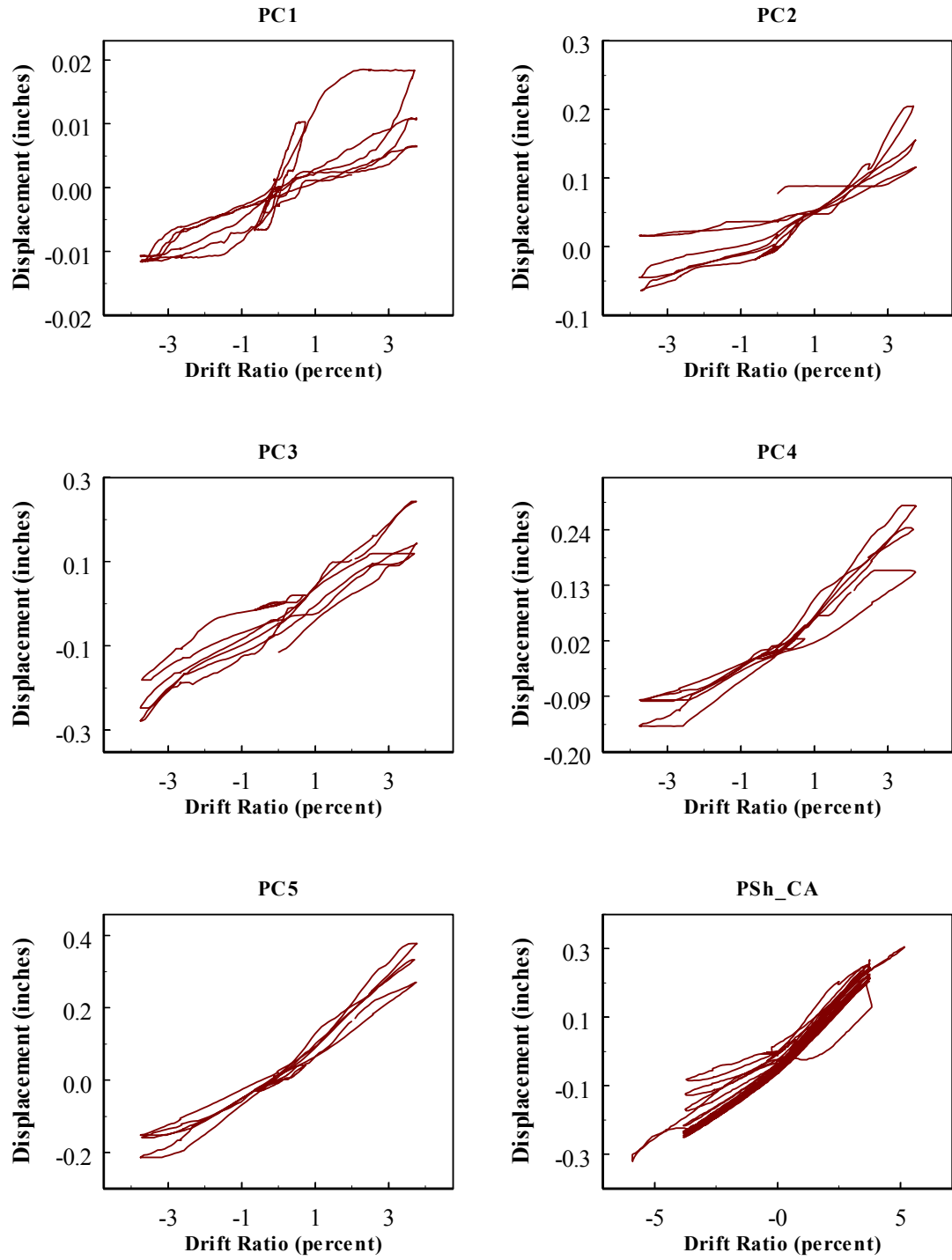


Fig. B.7 (cont.) Column C4 data

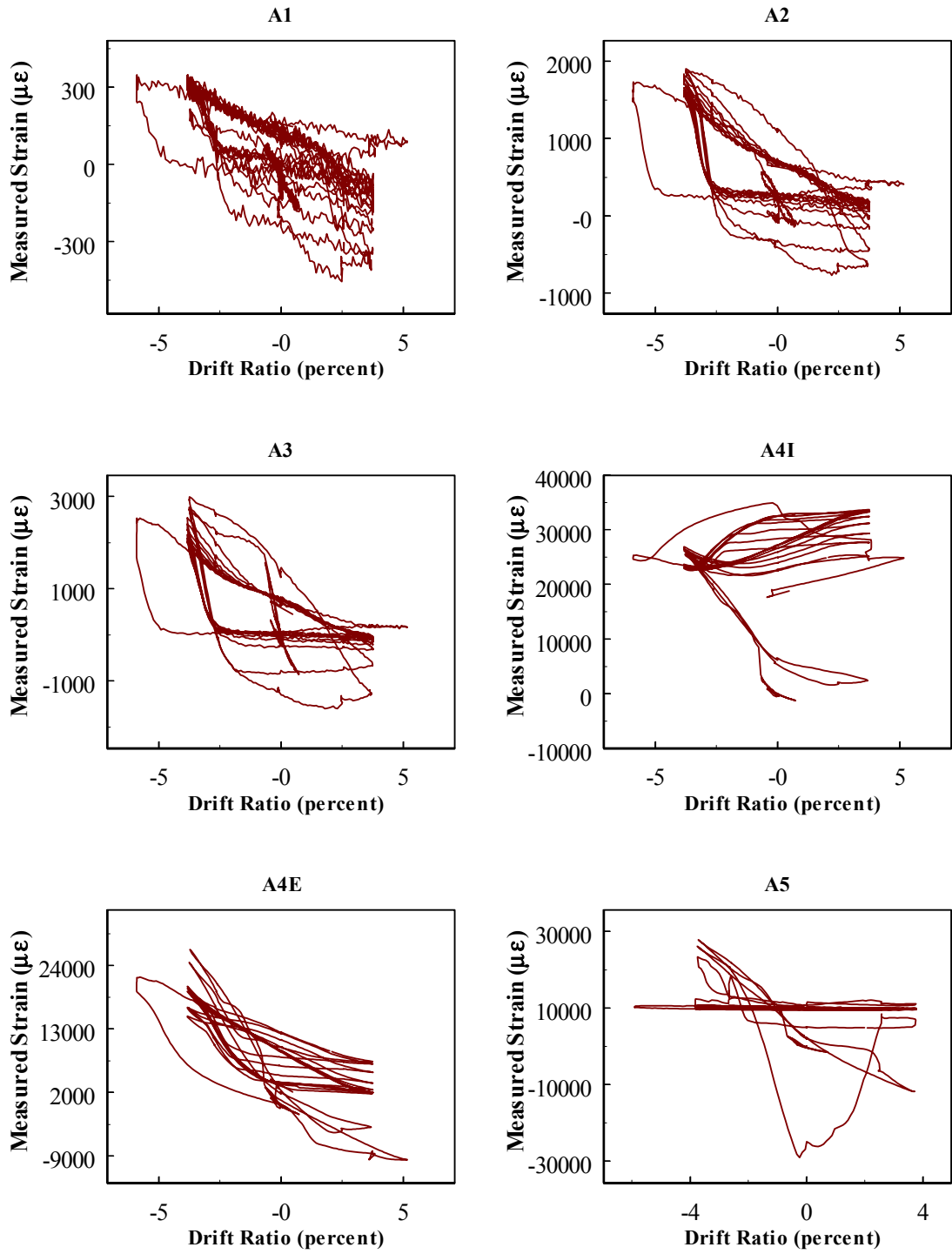


Fig. B.7 (cont.) Column C4 data

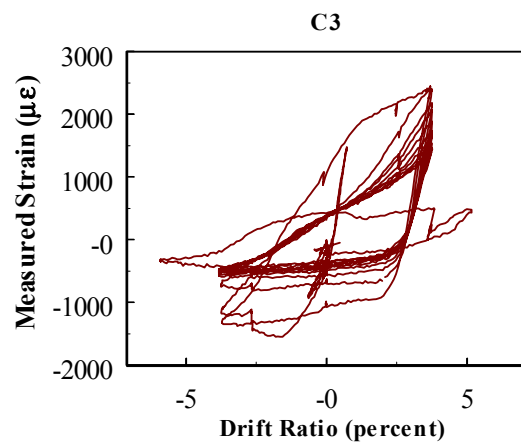
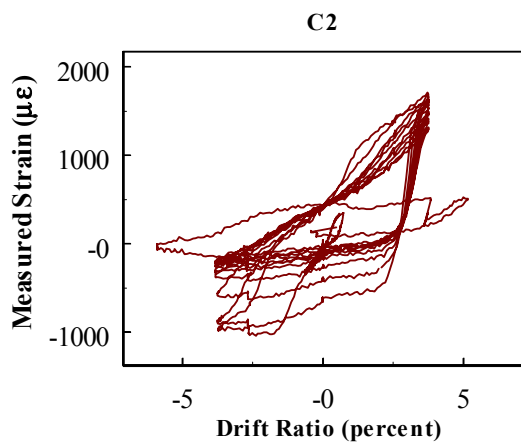
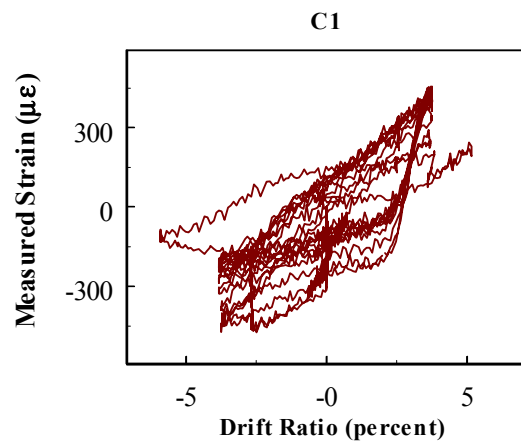
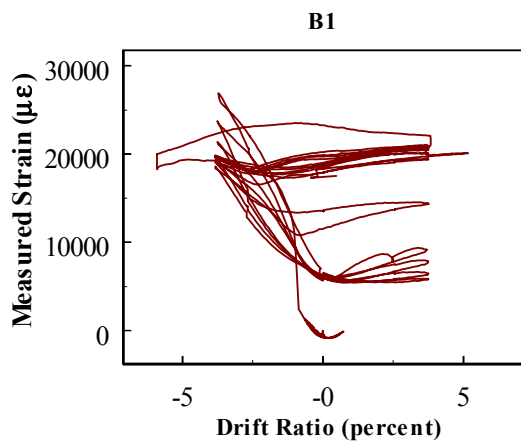
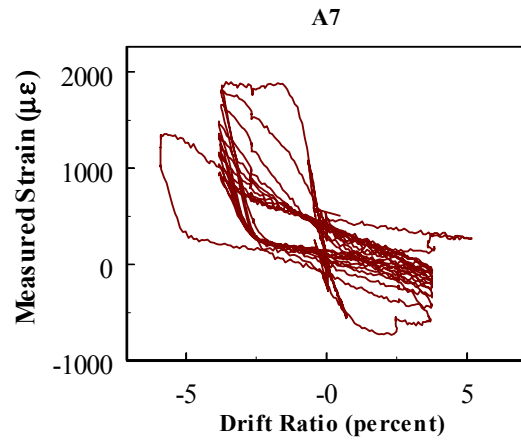
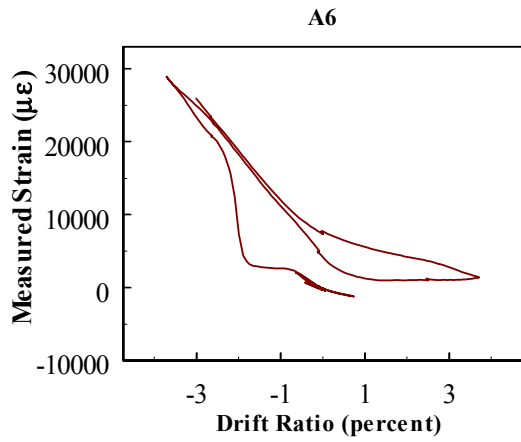


Fig. B.7 (cont.) Column C4 data

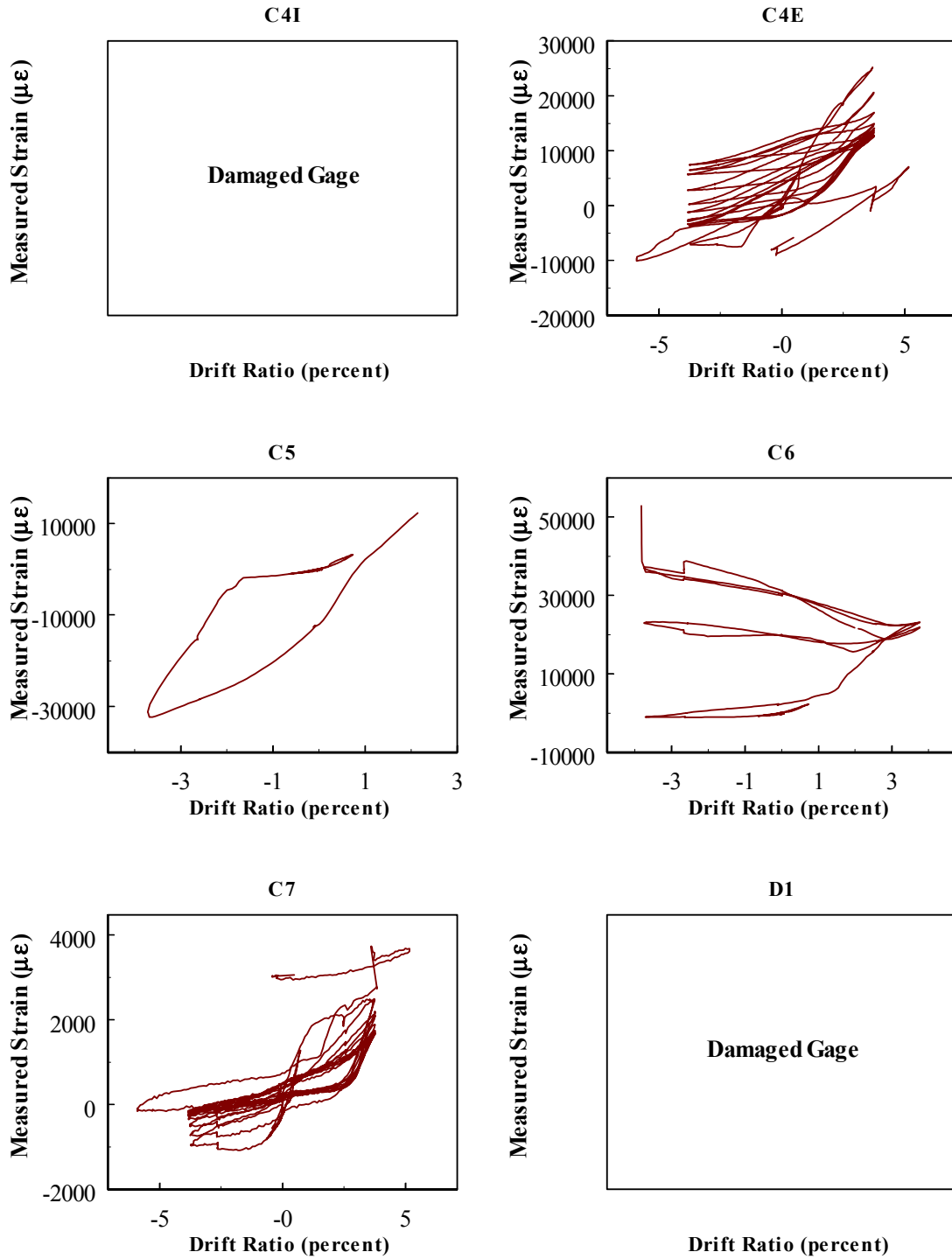


Fig. B.7 (cont.) Column C4 data

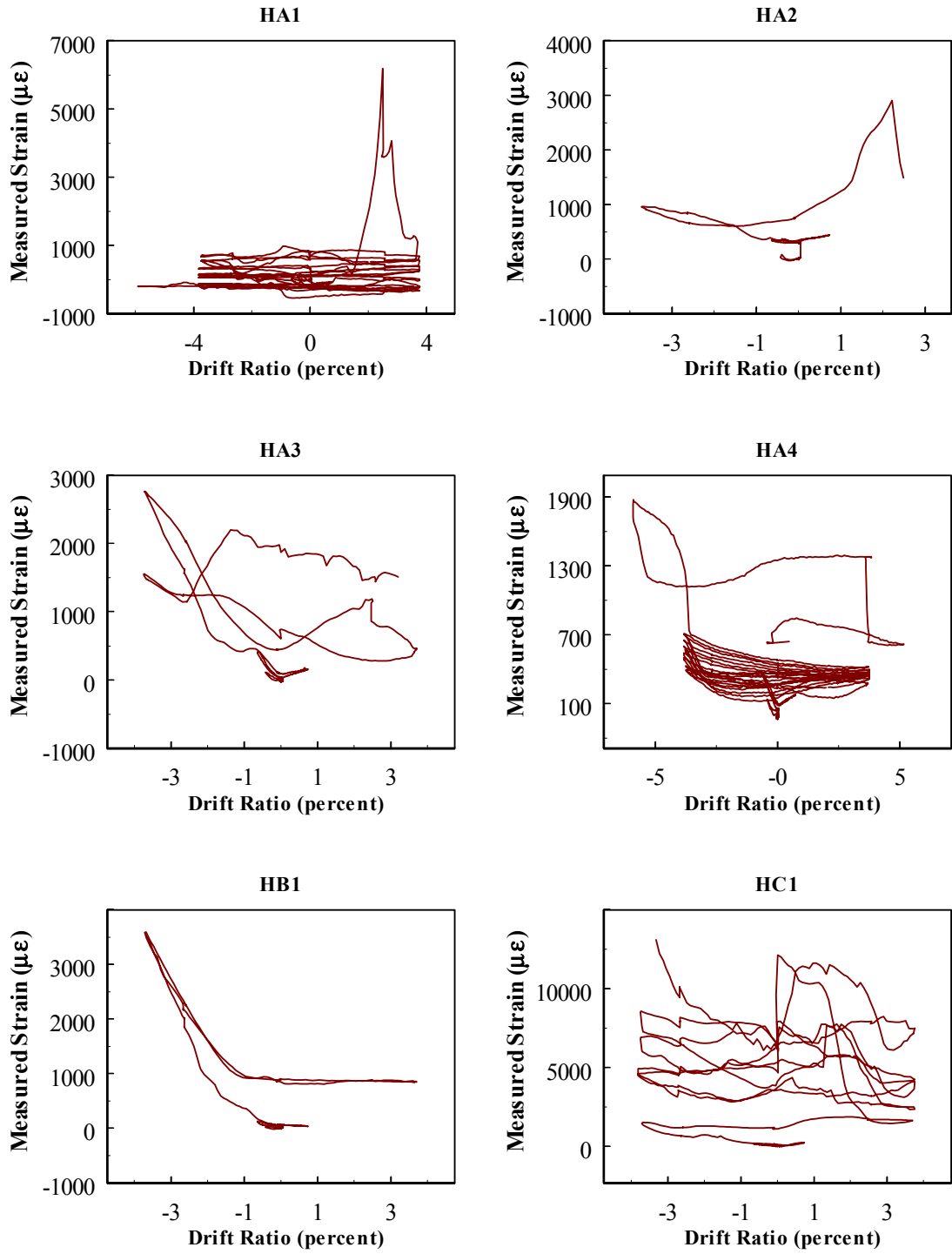


Fig. B.7 (cont.) Column C4 data

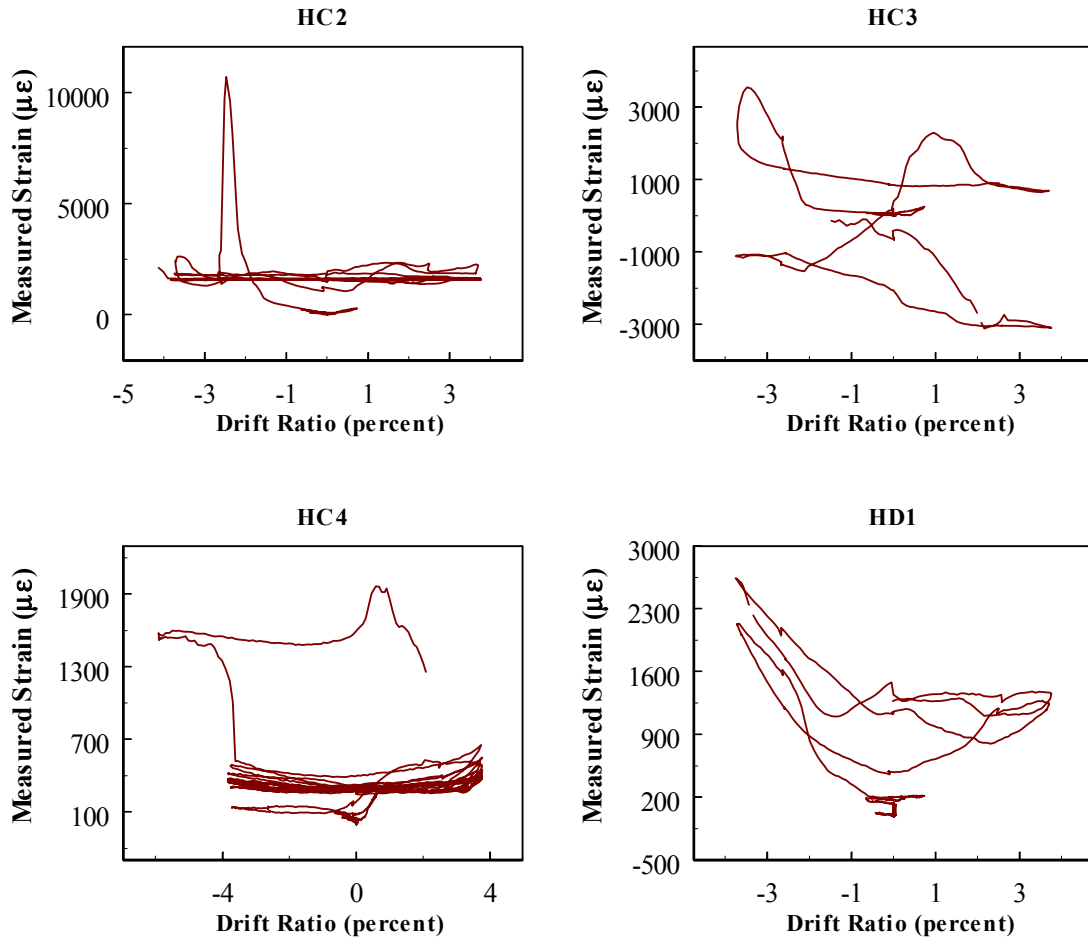


Fig. B.7 (cont.) Column C4 data

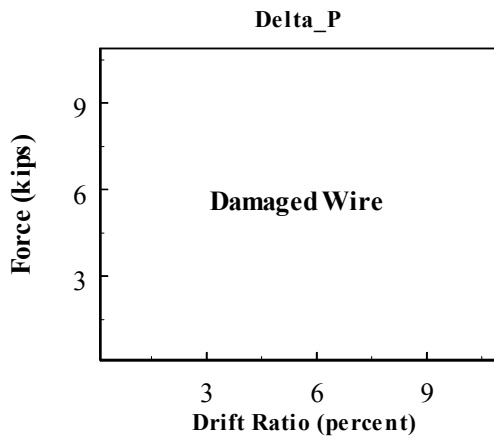
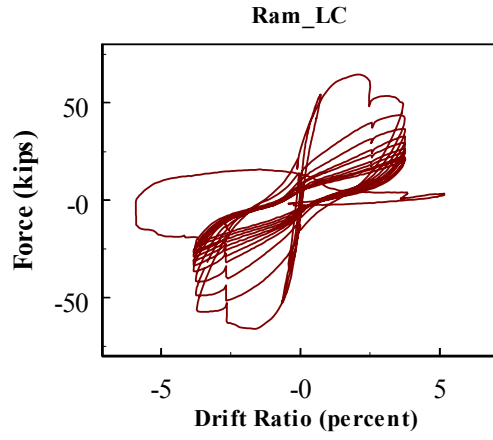
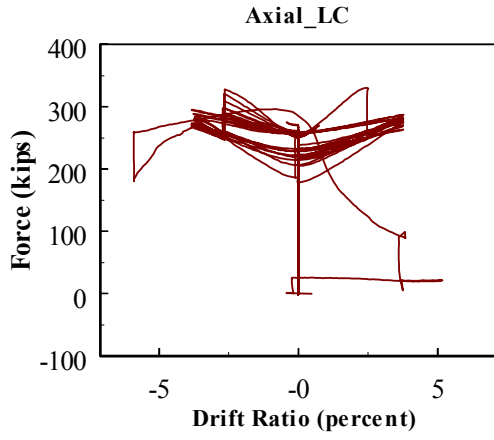


Fig. B.7 (cont.) Column C4 data

B.4 COLUMN C3R

Column C3R was subjected to preliminary cycles at half the cracking moment and $2\Delta_y$, followed by 10 cycles at $8\Delta_y$, and 5 cycles at $5\Delta_y$. Figure B.8 summarizes this displacement history.

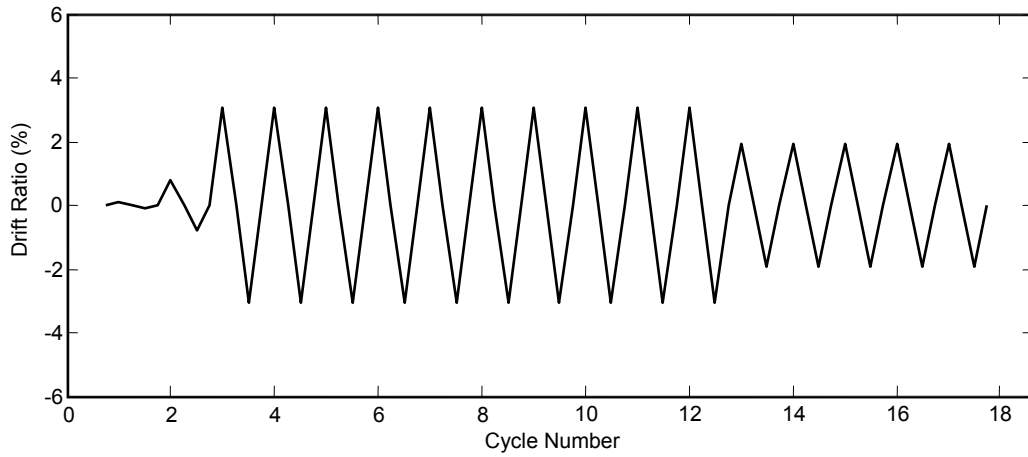


Fig. B.8 Displacement history for Column C3R

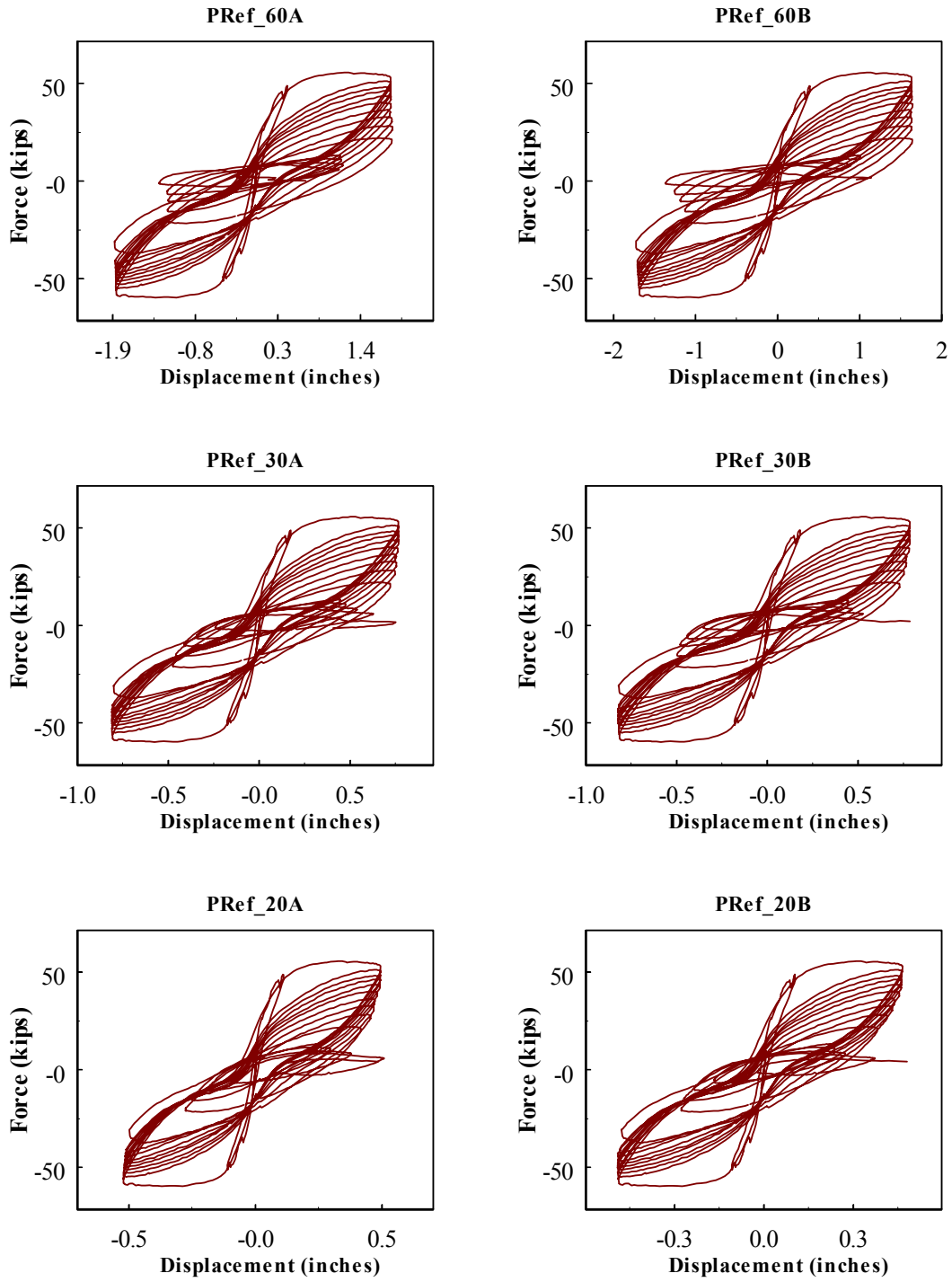


Fig. B.9 Column C3R data

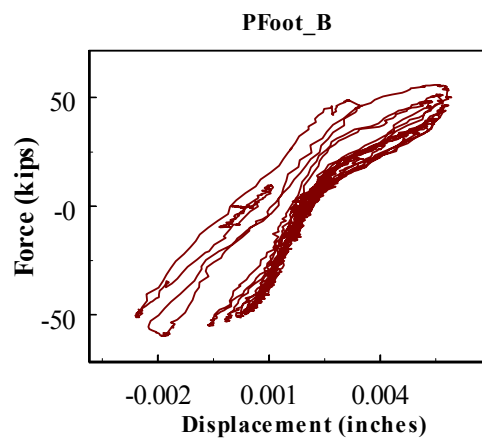
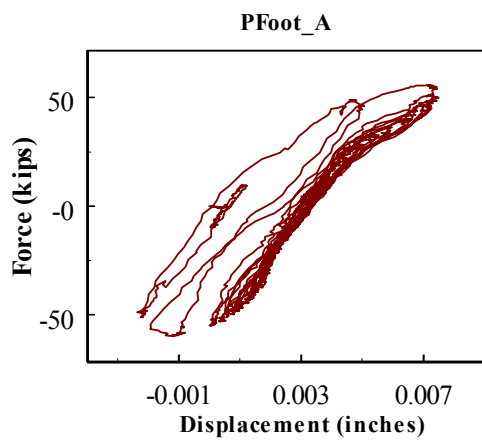
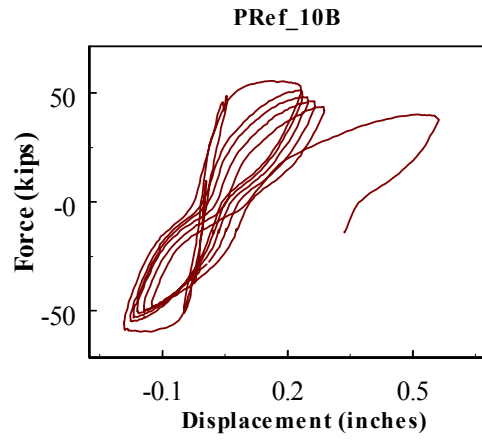
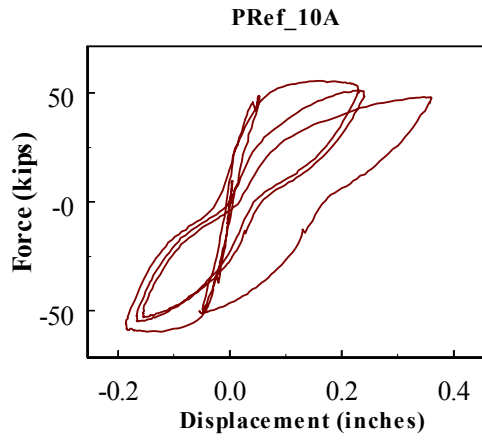


Fig. B.9 (cont.) Column C3R data

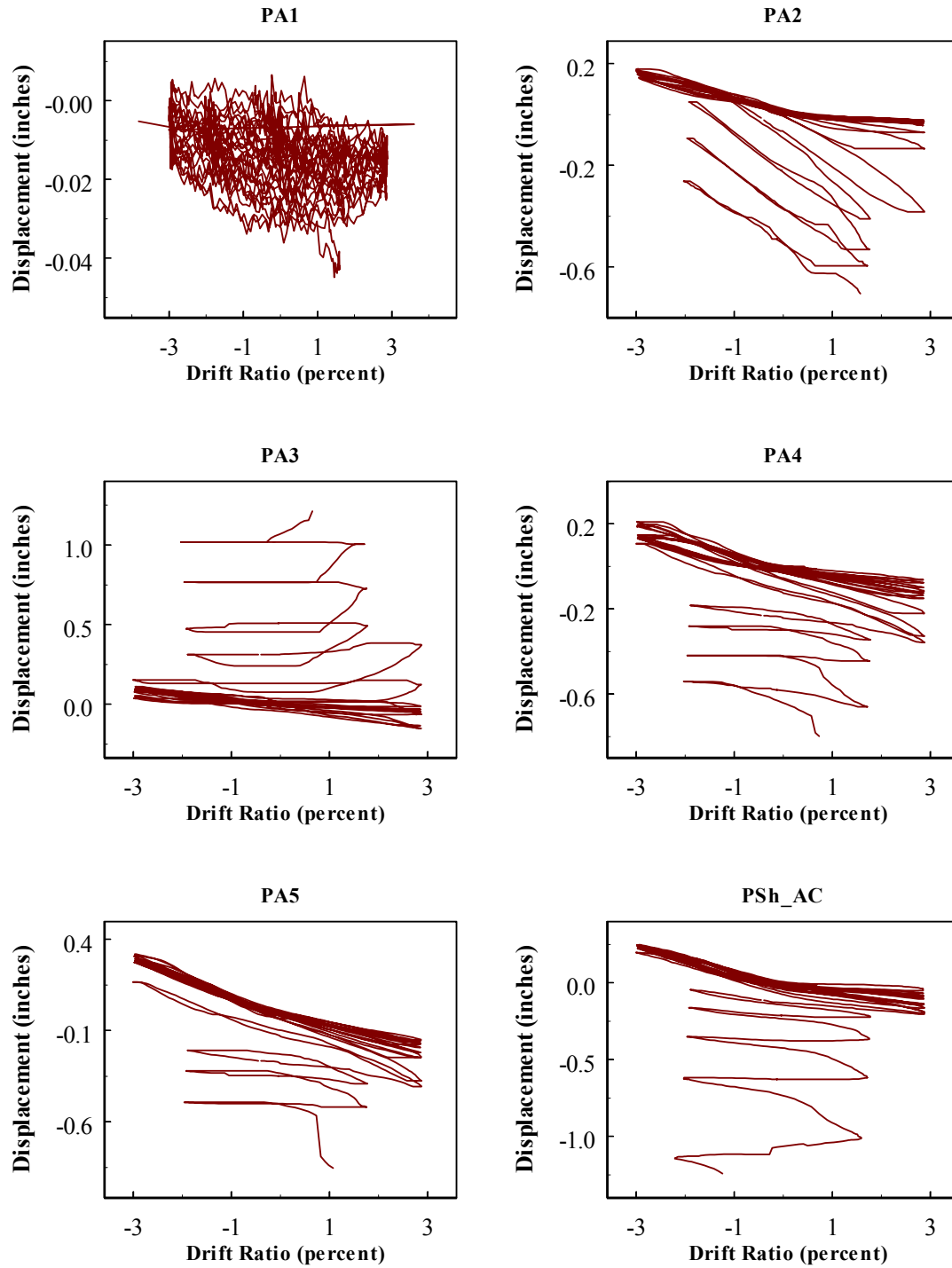


Fig. B.9 (cont.) Column C3R data

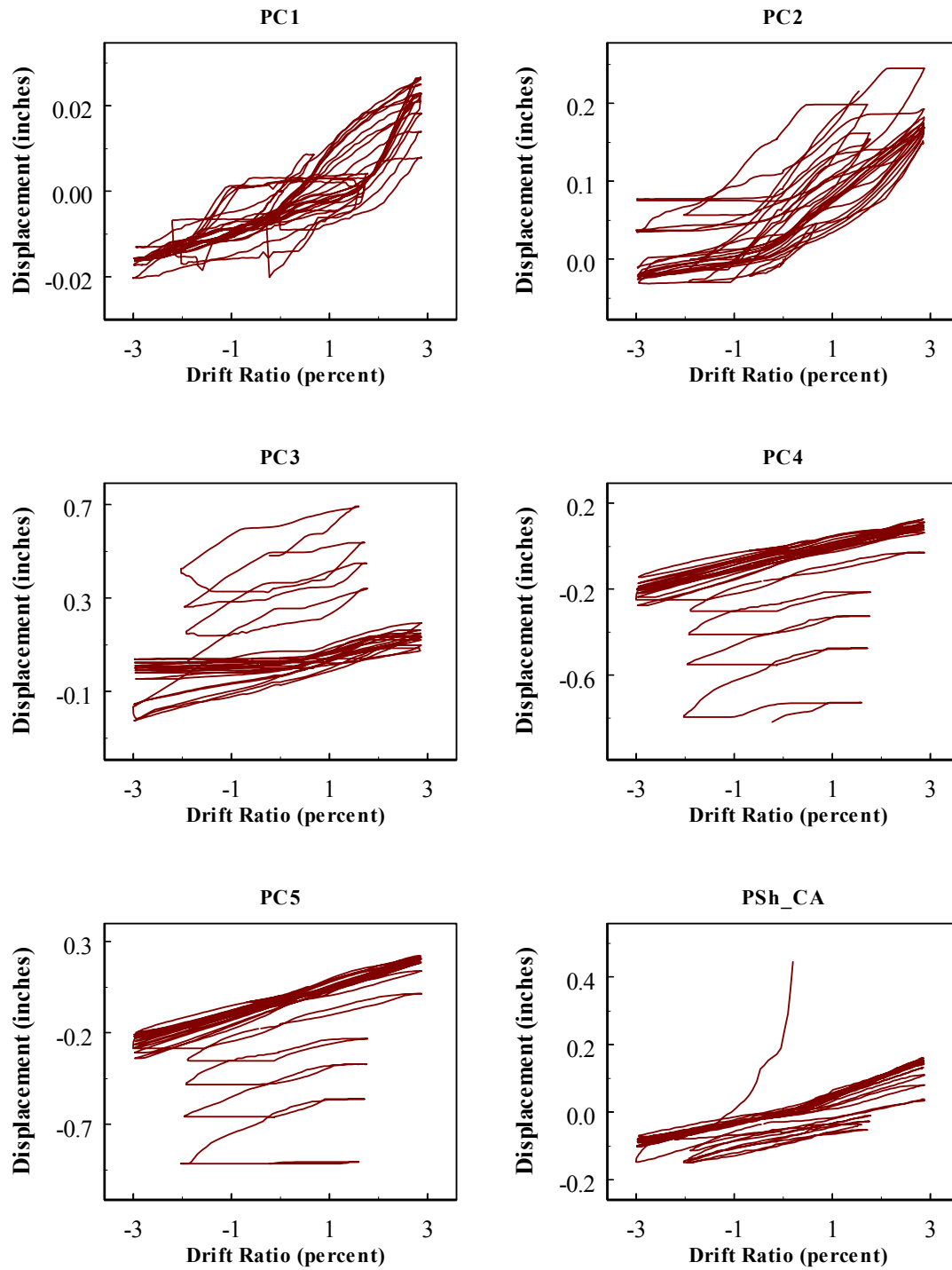


Fig. B.9 (cont.) Column C3R data

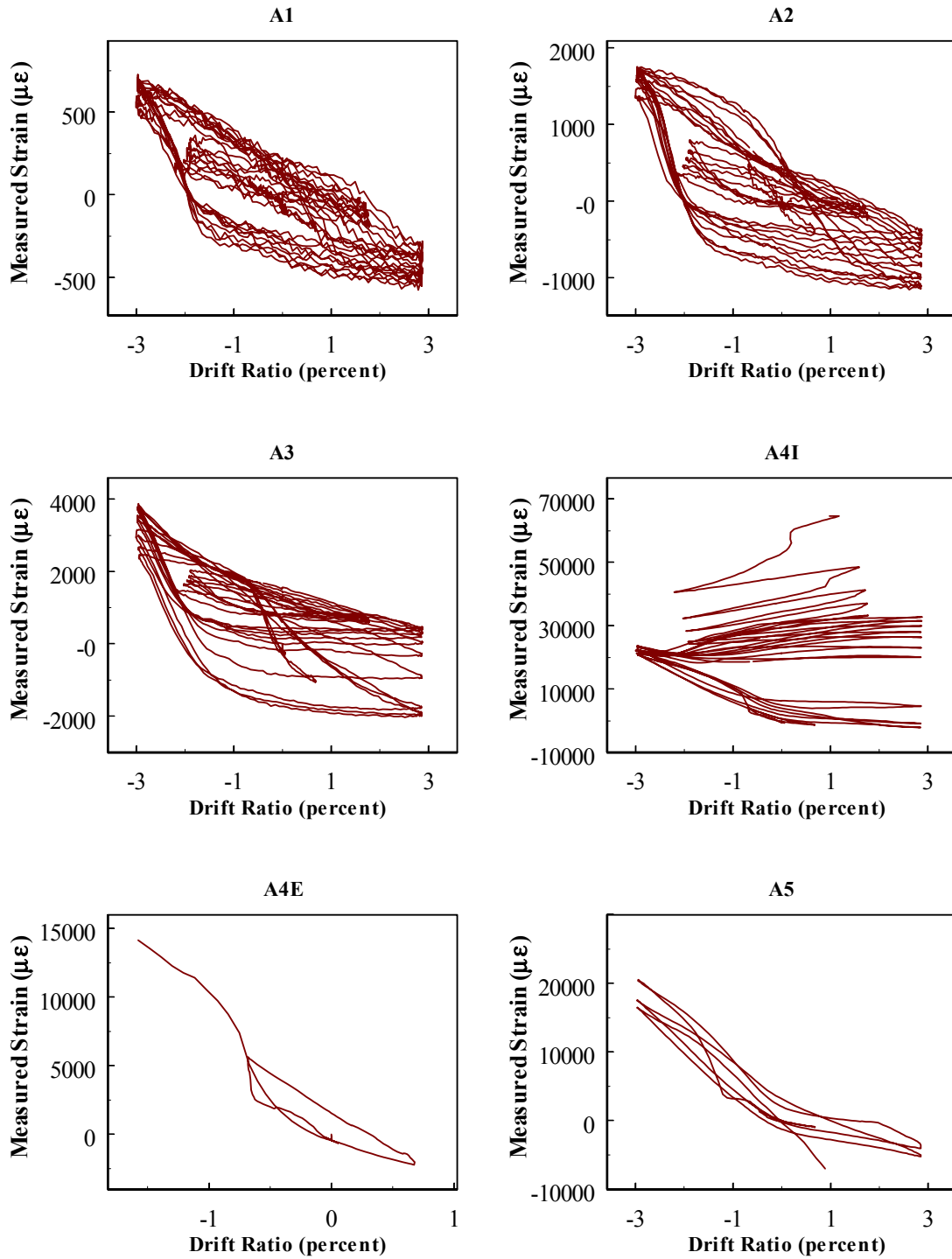


Fig. B.9 (cont.) Column C3R data

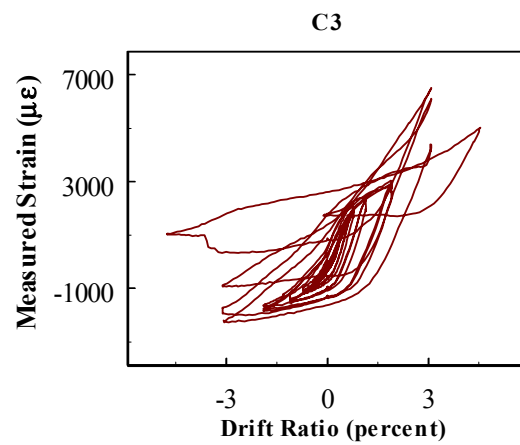
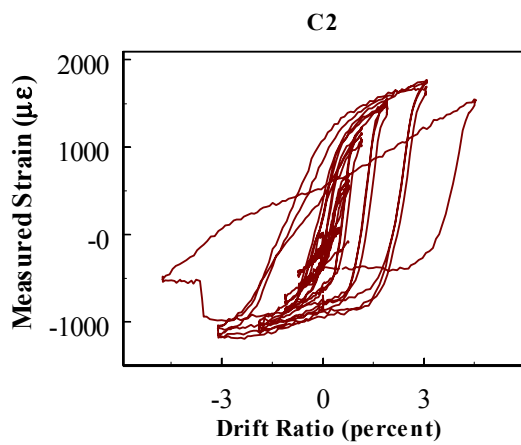
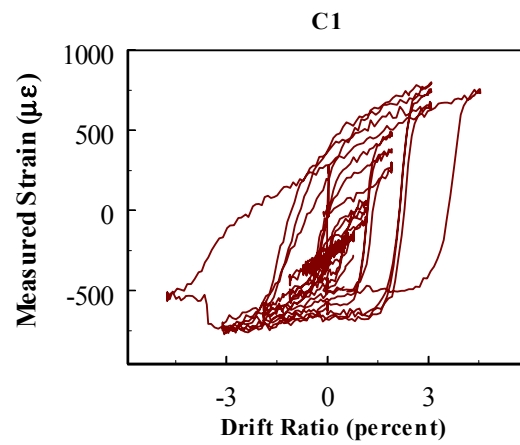
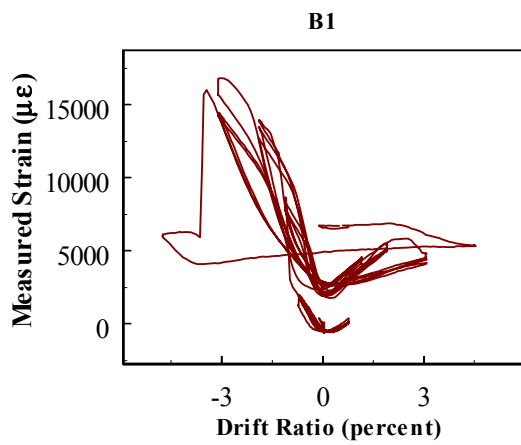
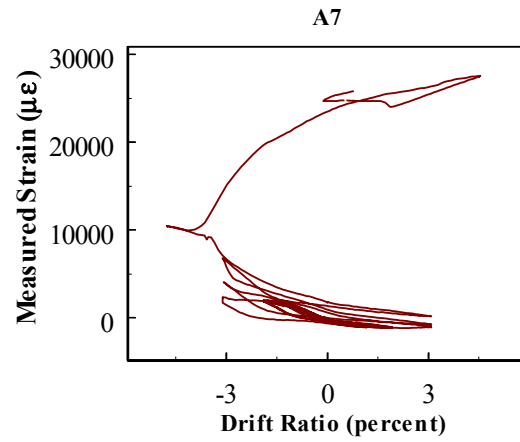
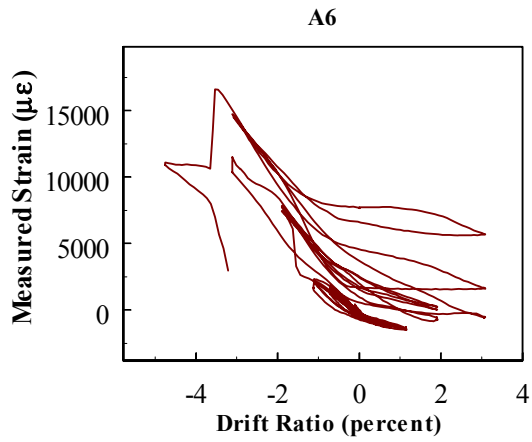


Fig. B.9 (cont.) Column C3R data

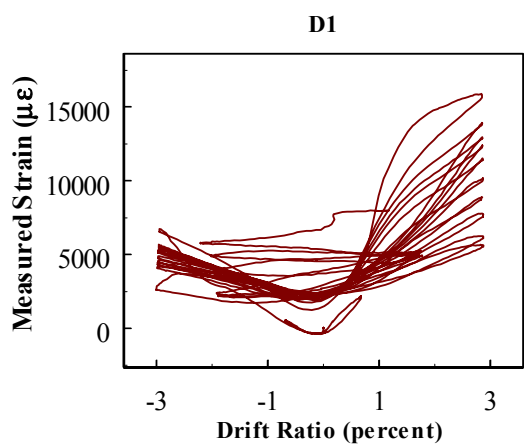
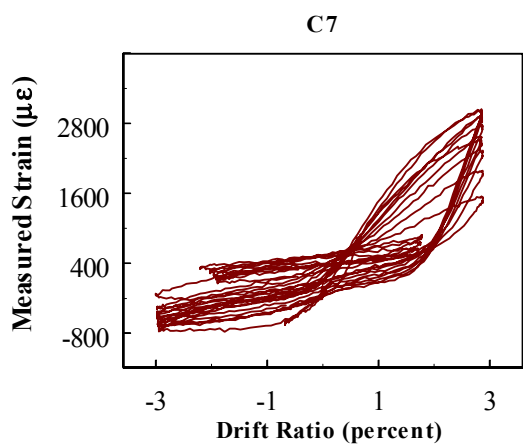
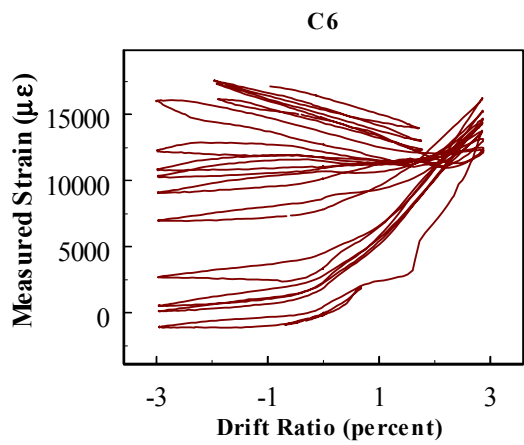
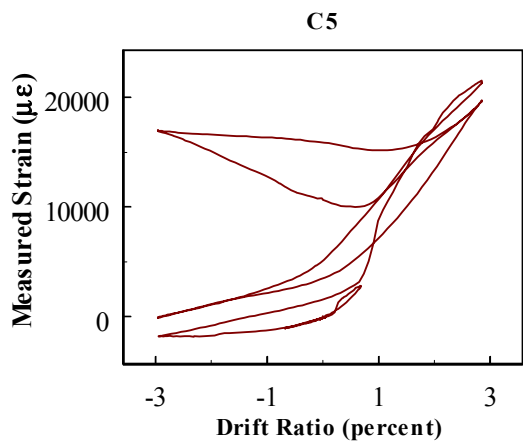
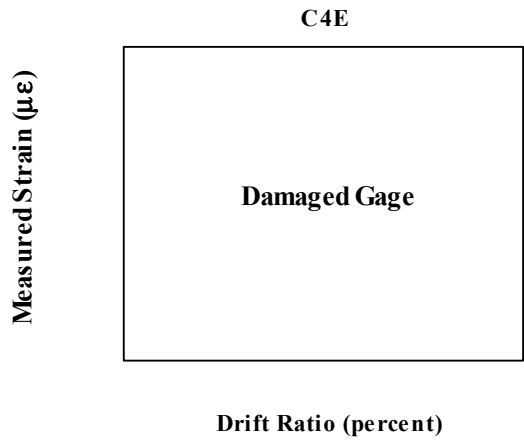
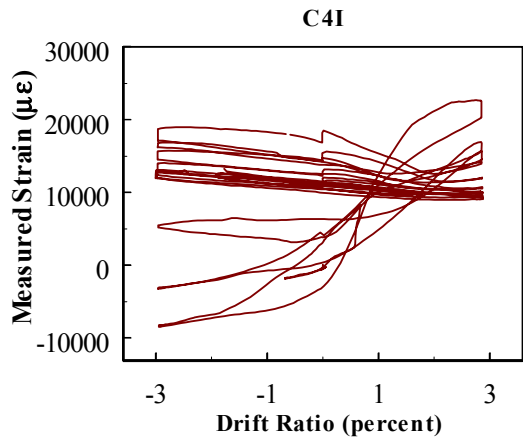


Fig. B.9 (cont.) Column C3R data

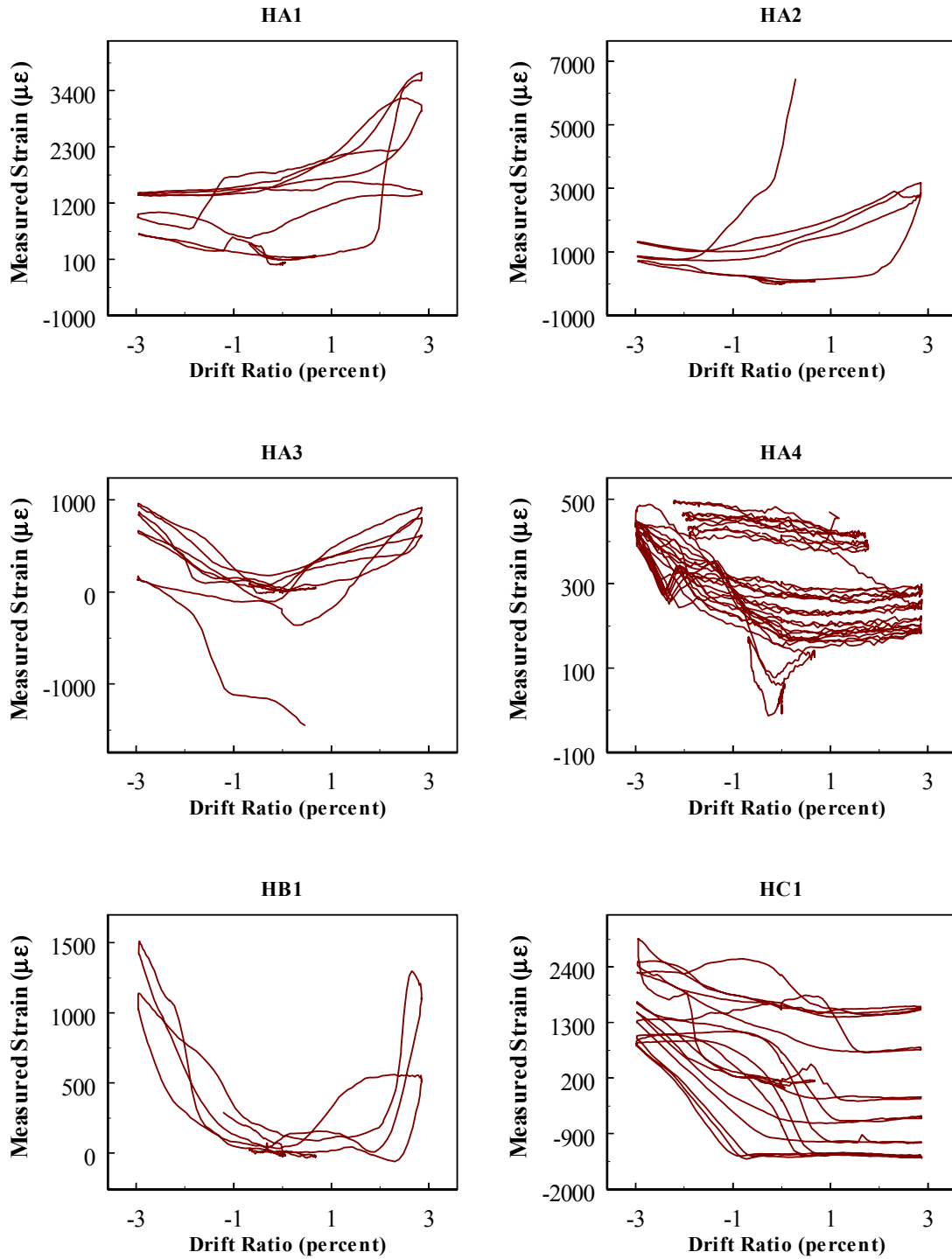


Fig. B.9 (cont.) Column C3R data

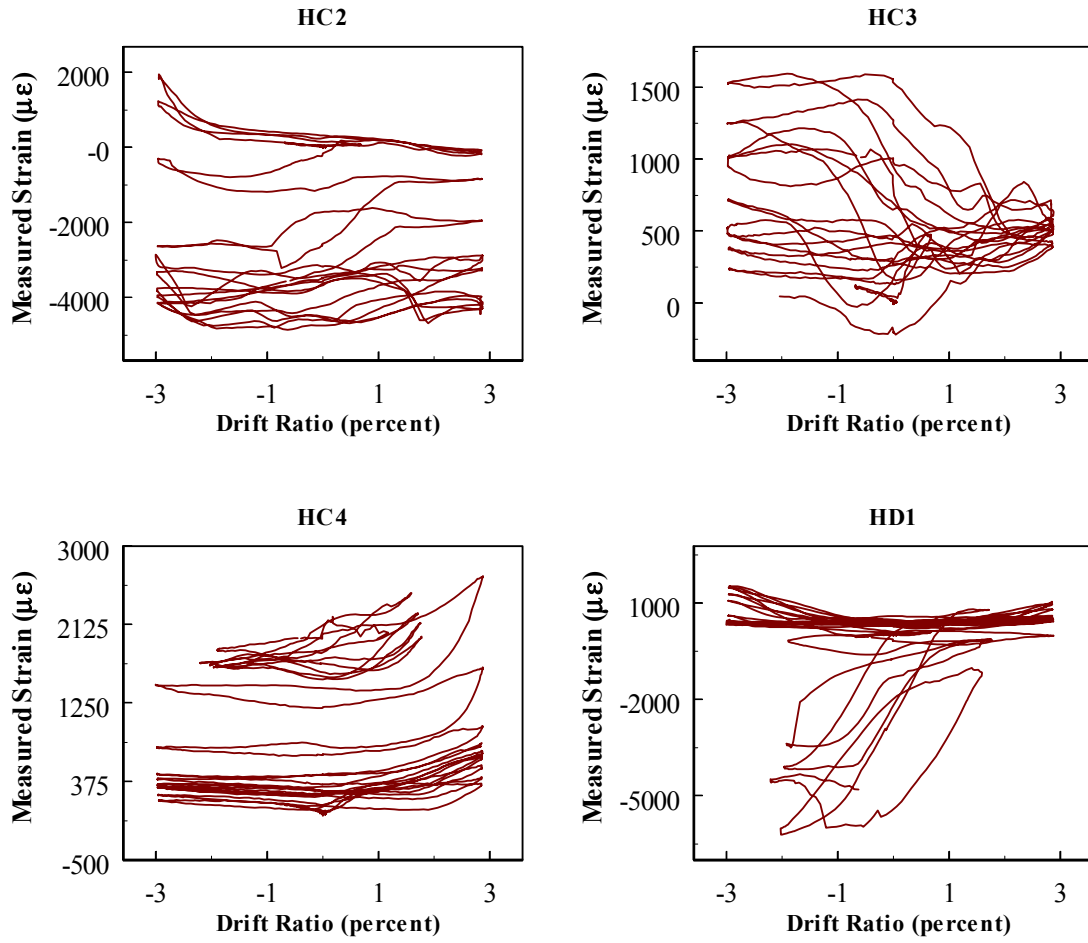


Fig. B.9 (cont.) Column C3R data

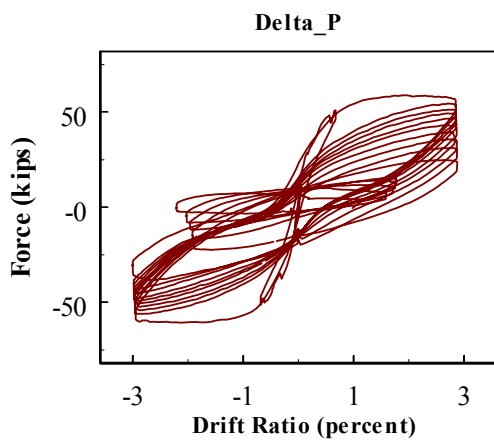
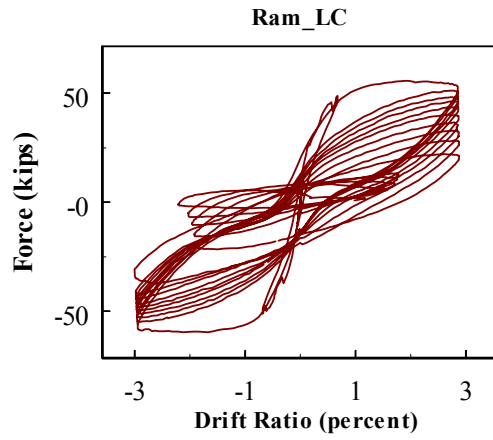
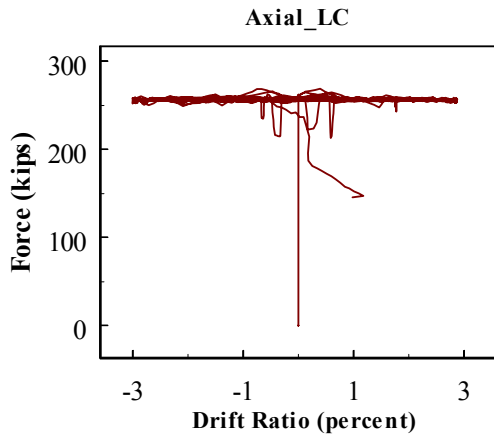


Fig. B.9 (cont.) Column C3R data

Appendix C: Instrument Histories (Columns S1 and S15)

This section contains all of the column data recorded during the testing program of the last two columns (Columns S1 and S15). The values output from the axial-load cell have been converted into the true axial load (i.e., the load cell reading has been multiplied by two). Data offset by a constant value (such as from rezeroing the data-acquisition system during testing) have been adjusted to the correct values. In addition, the following data points have been removed:

- Data points resulting from stray voltage spikes or potentiometer slip
- Data recorded after the failure of a given strain gage
- Data points after the loss of axial capacity

All of the channels included in this section are defined in Tables C.1 and C.2. In plotting the data, certain quantities need to be defined. All reference column and base slip data are plotted on the x-axis versus actuator force, with the channel data plotted on the x-axis and the force data plotted on the y-axis; the force data is simply the data from Ram_LC. The data for the axial load are plotted on the y-axis versus the displacement from the top potentiometer, which are plotted on the x-axis.

Table C.1 Load cell nomenclature

Channel	Description
Axial_LC	Axial-load cell, placed on one side of axial-load spreader beam
Ram_LC	Actuator load cell, attached between piston and front swivels

Table C.2 Translational potentiometer nomenclature

Channel	Description
PRef_60A	Reference column, 60-inch elevation, on Side B
PRef_60B	Reference column, 60-inch elevation, on Side D
PRef_30B	Reference column, 30-inch elevation, on Side D
PRef_20B	Reference column, 20-inch elevation, on Side D
PRef_10B	Reference column, 10-inch elevation, on Side D
PFoot_B	Base slip, on Side D

C.1 COLUMN S1

Column S1 was subjected to sets of one cycle at displacement levels corresponding to half the calculated cracking moment, the average of the calculated cracking moment, and the calculated yield moment, $1.25\Delta_y$, $2\Delta_y$, $3\Delta_y$, $5\Delta_y$, and $8\Delta_y$; the test concluded with one cycle at $12\Delta_y$. This displacement history is shown in Figure C.1 below.

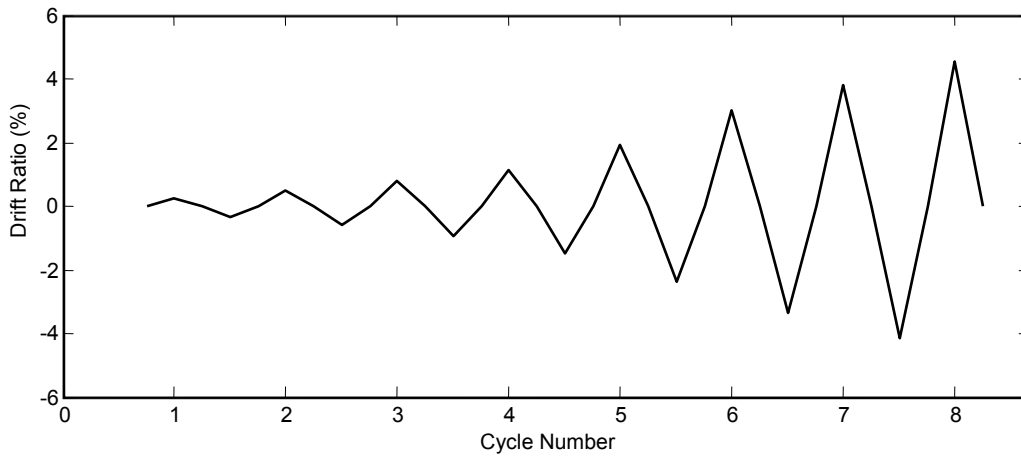


Fig. C.1 Displacement history for Column S1

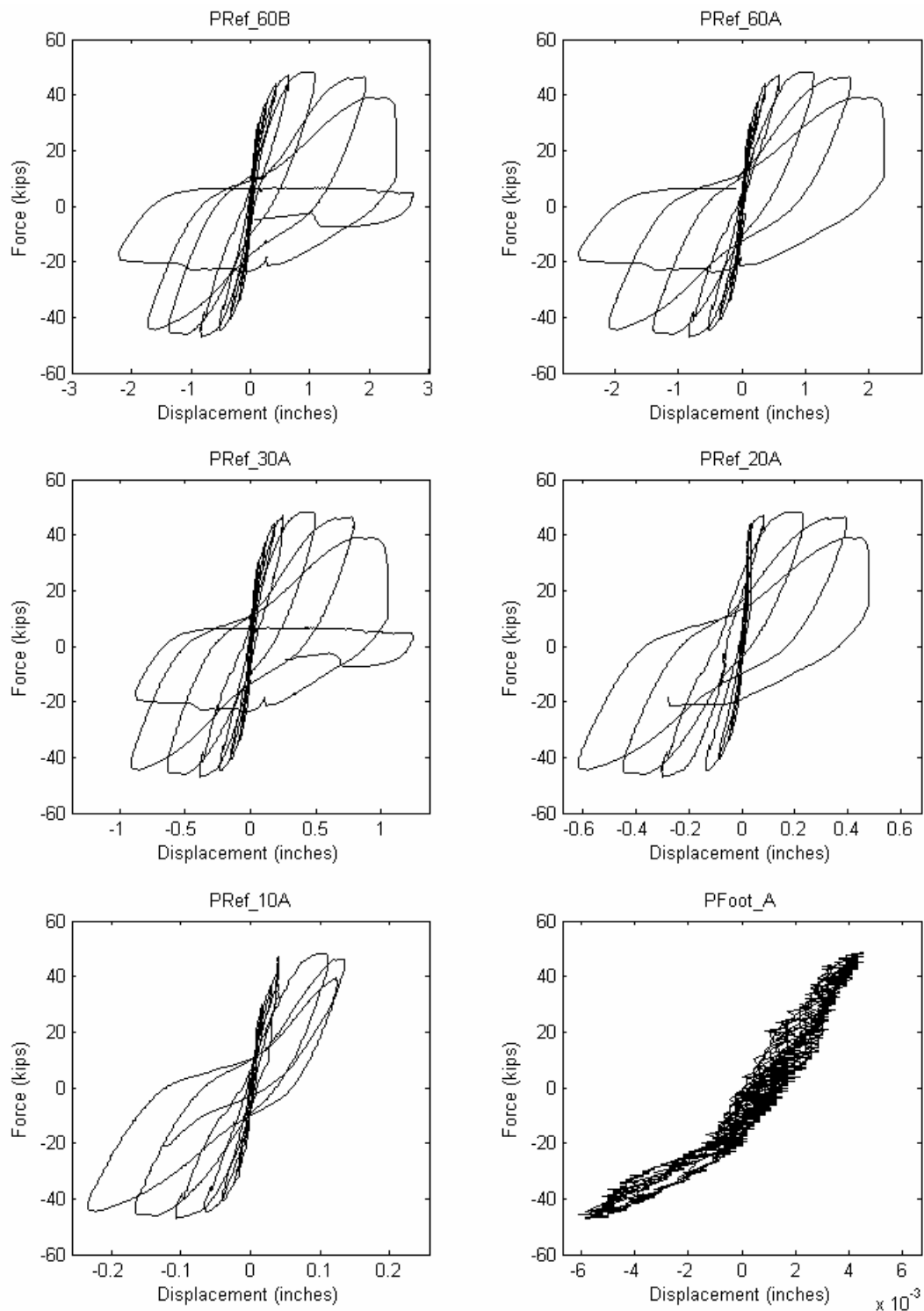


Fig. C.2 Column S1 data

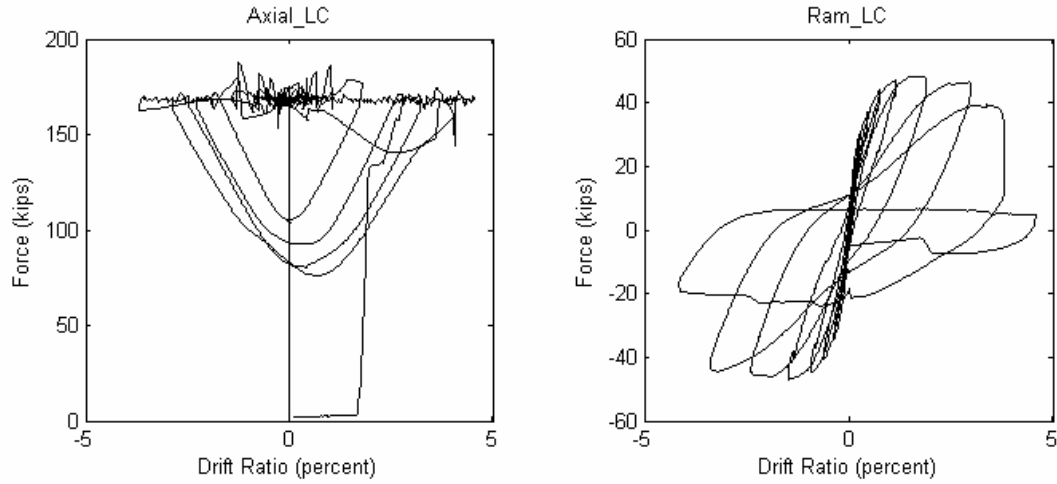


Fig C.2 (cont.) Column S1 data

C.2 COLUMN S15

Like Column S1, Column S15 was subjected to sets of 15 cycles at displacement levels corresponding to half the calculated cracking moment, the average of the calculated cracking moment and the calculated yield moment, $1.25\Delta_y$, $2\Delta_y$, $3\Delta_y$, $5\Delta_y$, and $8\Delta_y$; the test concluded with one cycle at $12\Delta_y$. This displacement history is shown in Figure C.3 below.

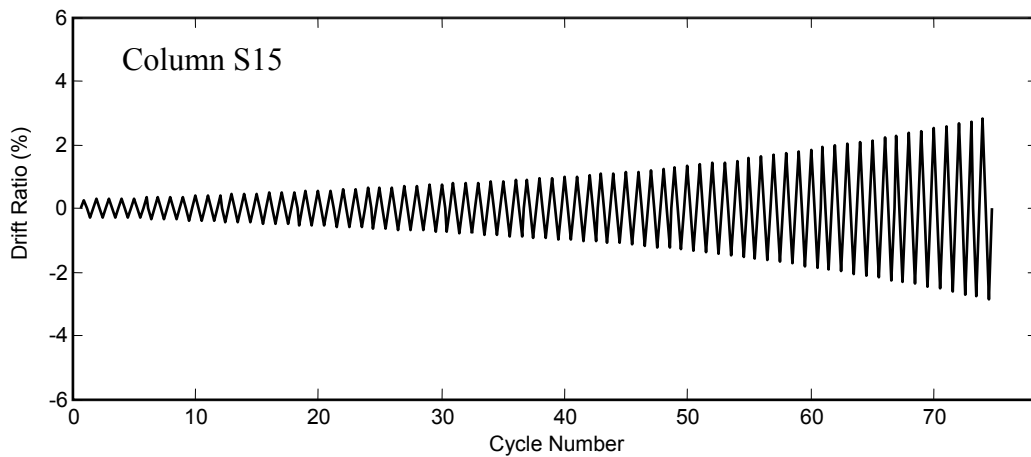


Fig. C.3 Displacement history for Column S15

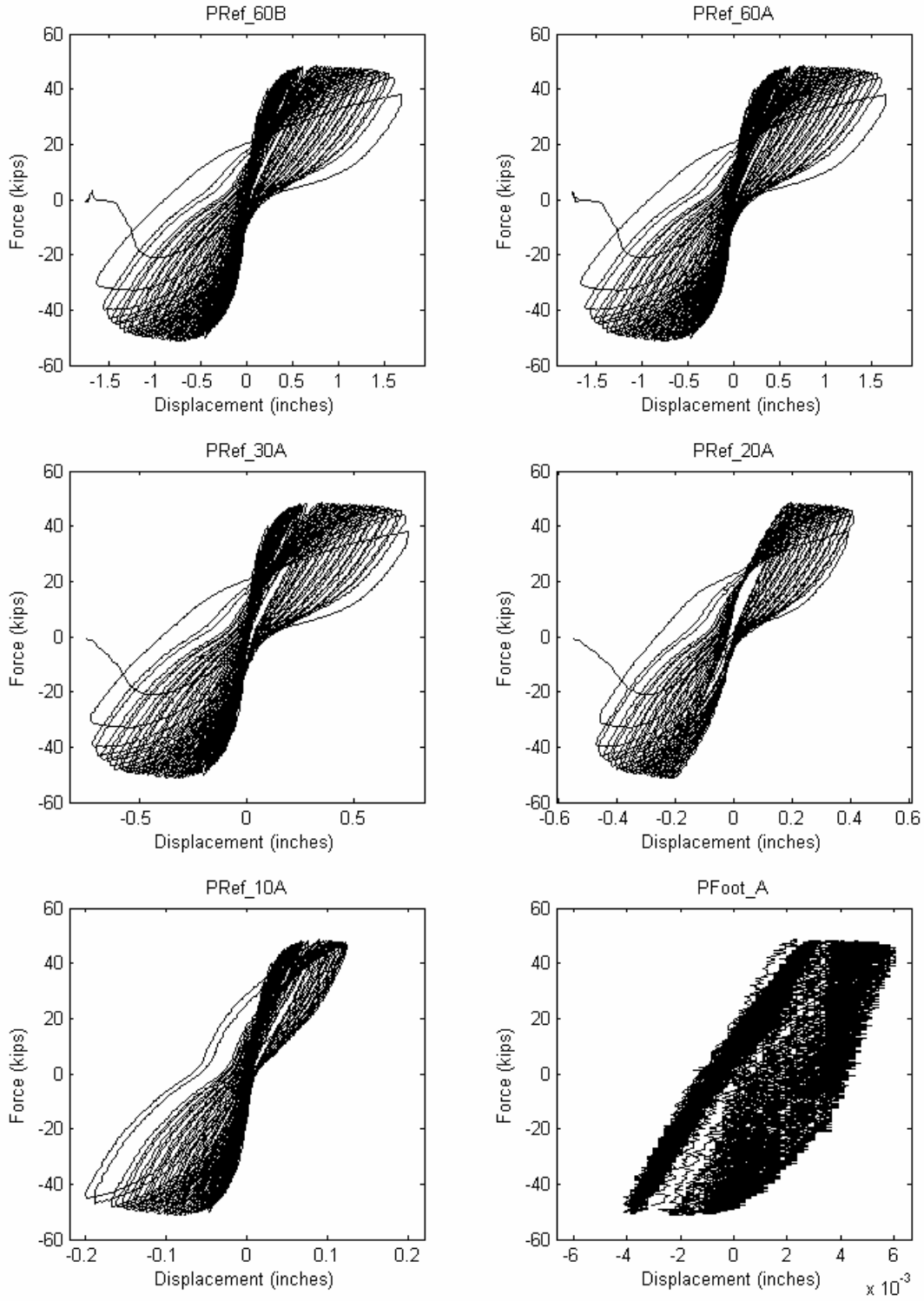


Fig. C.4 Column S15 data

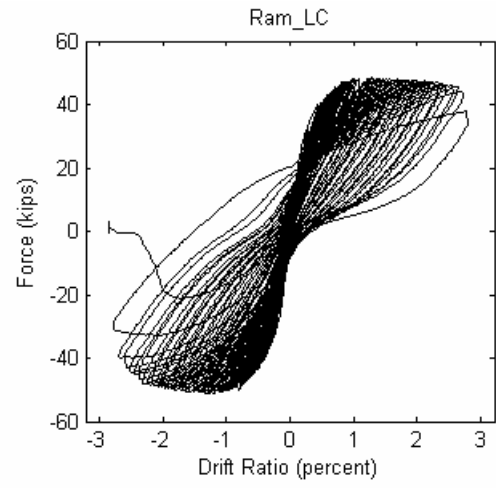
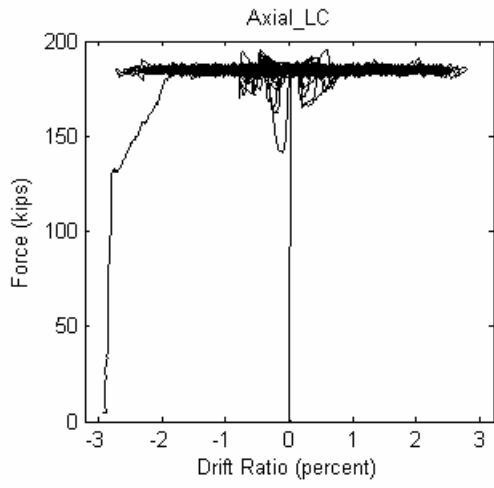


Fig C.4 (cont.) Column S15 data

Appendix D: Material Models

The models that will be covered in this section include the modified Burns-Seiss steel model (D.1), the Mander, Priestley, and Park confined concrete model (D.2), the Razvi-Saatcioglu concrete model (D.3), and the Lehman two-component anchorage slip model (D.4).

D.1 MODIFIED BURNS-SEISS STEEL MODEL

For a given steel strain, the steel stress f_s was modeled using a modified Burns and Seiss (1962) constitutive model, defined as follows:

for $\epsilon_s \leq \epsilon_y$,

$$f_s = \epsilon_s E_s \quad (D.1)$$

for $\epsilon_y \leq \epsilon_s \leq \epsilon_{sh}$,

$$f_s = f_y \quad (D.2)$$

for $\epsilon_{sh} \leq \epsilon_s \leq \epsilon_{su}$,

$$f_s = f_y \left[\frac{m(\epsilon_s - \epsilon_{sh}) + 2}{60(\epsilon_s - \epsilon_{sh}) + 2} + \frac{(\epsilon_s - \epsilon_{sh})(60 - m)}{2(30r + 1)^2} \right] \quad (D.3)$$

where ϵ_s , ϵ_y , ϵ_{sh} , and ϵ_{su} are the strain in the steel, the yield strain, the strain at which the steel begins to harden and the ultimate tensile strain of the steel, respectively. E_s is the elastic modulus of the steel, f_y is the yield stress of the steel, m is a dimensionless constant, and the term r can be defined by the equation

$$r = \epsilon_{su} - \epsilon_{sh} \quad (D.4)$$

Tension tests of the longitudinal reinforcement provided the material properties needed to calibrate the constitutive model (Table D.1). Given the material properties listed in Table D.1, the stress-strain curve for the longitudinal reinforcement is seen in Figure D.1.

Table D.1 Properties of longitudinal steel

Property	Measured Value
ϵ_y	0.00235
ϵ_{sh}	0.0095
ϵ_u	0.080
f_y	68.2 ksi
f_u	105 ksi

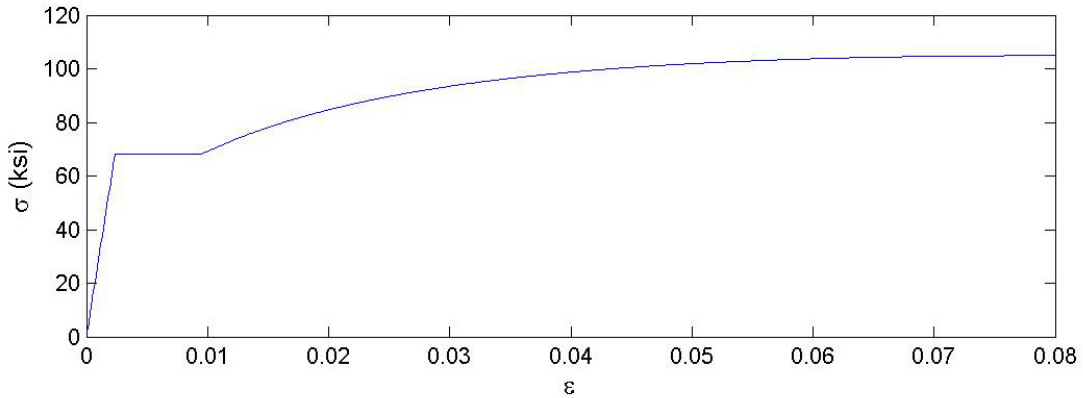


Fig. D.1 Burns-Seiss constitutive model for (a) Columns S3, C2, C4, and C3R and (b) Columns S1 and S15

D.2 MANDER, PRIESTLEY, AND PARK (1988) CONCRETE MODEL

The Mander, Priestley, and Park concrete model was developed for both confined and unconfined concrete. For confined concrete, the relationship between the concrete stress (f_c) and the concrete strain (ϵ_c) is given by:

$$f_c = \frac{f'_{cc}\chi\gamma}{\gamma - 1 + \chi^\gamma} \quad (D.5)$$

where f'_{cc} is the peak confined stress in the concrete, χ is the ratio of the concrete strain (ϵ_c) to the concrete strain at the peak confined stress, and γ is the ratio of the elastic modulus of the concrete (E_c) to the difference between the elastic modulus of the concrete and the secant modulus of the concrete (E_{sec}).

For unconfined concrete, the value of f_c is given by

$$f_c = \begin{cases} \frac{f'_{co}\chi\gamma}{\gamma-1+\chi^\gamma} & \varepsilon_c \leq 2\varepsilon_{co} \\ \left(\varepsilon_c - \varepsilon_{sp}\right) \frac{f_{2,peak}}{2\varepsilon_{co} - \varepsilon_{sp}} & 2\varepsilon_{co} \leq \varepsilon_c \leq \varepsilon_{sp} \\ 0 & \varepsilon_c > \varepsilon_{sp} \end{cases} \quad (D.6)$$

where $\varepsilon_{co} = 0.002$, $\varepsilon_{sp} = 0.006$, f'_{co} is the peak unconfined stress in the concrete and $f_{2,peak}$ is the unconfined concrete stress at $2\varepsilon_{co}$. The equations presented above provide the fundamental equations for this concrete model; for further details, refer to Mookerjee (1999), and Mander, Priestley, and Park (1988).

D.3 RAZVI AND SAATCIOGLU (1999) CONCRETE MODEL

For unconfined concrete, the value of the concrete stress, f_c , for a given concrete strain ε_c , is given by:

$$f_c = \begin{cases} \left(f'_{cc} \left(\frac{\varepsilon_c}{\varepsilon_{01}} \right)^{r_{co}} \right) / \left(r - 1 + \left(\frac{\varepsilon_c}{\varepsilon_{01}} \right)^{r_{co}} \right) & \varepsilon_c \leq \varepsilon_{01} \\ f'_{cc} \left(\frac{0.15(\varepsilon_c - \varepsilon_{01})}{(\varepsilon_{01} - \varepsilon_{085})} + 1 \right) & \varepsilon_c > \varepsilon_{01} \end{cases} \quad (D.7)$$

where f'_{co} = the peak unconfined stress in the concrete,

$$f'_{co} = 0.85f'_c \quad (D.8)$$

ε_{01} = the strain corresponding to the peak stress in the unconfined concrete,

$$\varepsilon_{01} = 0.0028 - 0.0008k_3 \quad (D.9)$$

$$k_3 = 40/f'_{co} \leq 1 \quad (D.10)$$

ε_{085} = the strain corresponding 85% of the peak stress of the unconfined concrete on the descending branch,

$$\varepsilon_{085} = \varepsilon_{01} + 0.0018k_3^2 \quad (D.11)$$

r_{co} = the ratio of the elastic modulus of the unconfined concrete (E_{co}) to the difference between the elastic modulus of the unconfined concrete and the secant modulus of the unconfined concrete ($E_{sec,co}$)

$$r_{co} = \frac{E_{co}}{E_{co} - E_{sec,co}} \quad (D.12)$$

$$E_{sec,co} = f'_{co} / \varepsilon_{01} \quad (D.13)$$

$$E_{co} = E_c > E_{sec,co} \quad (D.14)$$

For the unconfined concrete, this model assumes a linear decrease in ε_{01} after reaching the peak strength (Eq. D.9). The paper is ambiguous about whether this decrease continues until the strength reaches zero, or if there is some residual strength. Using recommendations by Saatcioglu (2000), the analyses reported in this thesis were performed assuming that after the unconfined concrete reaches its peak stress, the strength of the unconfined concrete decreases linearly to zero.

For confined concrete, the value of the concrete stress, f_c , for a given concrete strain ε_c , is given by:

$$f_c = \begin{cases} \left(f'_{cc} \left(\frac{\varepsilon_c}{\varepsilon_1} \right) r_{cc} \right) / \left(r - 1 + \left(\frac{\varepsilon_c}{\varepsilon_1} \right)^\gamma \right) & \varepsilon_c \leq \varepsilon_1 \\ f'_{cc} \left(\frac{0.15(\varepsilon_c - \varepsilon_1)}{(\varepsilon_1 - \varepsilon_{85})} + 1 \right) & \varepsilon_1 \leq \varepsilon_c \leq \varepsilon_{20} \\ 0.2f'_{cc} & \varepsilon_c > \varepsilon_{20} \end{cases} \quad (D.15)$$

where f'_{cc} = the peak confined stress in the concrete,

$$f'_{cc} = f'_{co} + k_1 f_{le} \quad (D.16)$$

$$k_1 = 6.7(f_{le})^{-0.17} \quad (D.17)$$

$$f_{le} = k_2 f_l \quad (D.18)$$

$$k_2 = 0.15 \sqrt{\left(\frac{b_c}{s}\right)\left(\frac{b_c}{s_l}\right)} \leq 1.0 \quad (\text{D.19})$$

$$f_l = \frac{2A_s f_s}{b_c s} \quad (\text{D.20})$$

$$f_s = E_s \left[0.0025 + 0.04 \left(\frac{k_2 \rho_c}{f'_{co}} \right)^{\frac{1}{3}} \right] \leq f_{yt} \quad (\text{D.21})$$

$$\rho_c = \frac{2A_s}{b_c s} \quad (\text{D.22})$$

ε_1 = the strain corresponding to the peak stress in the confined concrete

$$\varepsilon_1 = \varepsilon_{01} (1 + 5k_3 K) \quad (\text{D.23})$$

$$K = \frac{k_1 f_{le}}{f'_{co}} \quad (\text{D.24})$$

ε_{85} = the strain corresponding 85% of the peak stress of the confined concrete on the descending branch

$$\varepsilon_{85} = 260k_3 \rho_c \varepsilon_1 [1 + 0.5k_2(k_4 - 1)] + \varepsilon_{085} \quad (\text{D.25})$$

$$k_4 = \frac{f_{yt}}{500} \geq 1.0 \quad (\text{D.26})$$

ε_{20} = the strain corresponding 20% of the peak stress of the confined concrete on the descending branch

$$\varepsilon_{20} = \frac{1}{3} (16\varepsilon_{85} - 13\varepsilon_1) \quad (\text{D.27})$$

r_{cc} = the ratio of the elastic modulus of the confined concrete (E_{cc}) to the difference between the elastic modulus of the confined concrete and the secant modulus of the confined concrete ($E_{sec,cc}$)

$$r_{cc} = \frac{E_{cc}}{E_{cc} - E_{sec,cc}} \quad (D.28)$$

$$E_{sec,cc} = f'_{cc} / \epsilon_1 \quad (D.29)$$

$$E_{cc} = E_c > E_{sec,cc} \quad (D.30)$$

In the equations above, A_s is the area of one leg of transverse reinforcement; s is the spacing of the transverse reinforcement; s_l is the spacing of the longitudinal reinforcement; b_c is the core dimension measured center-to-center of the hoop; and f'_c is the compressive strength of the concrete, obtained from a standard cylinder test.

D.4 LEHMAN TWO-COMPONENT BOND STRESS MODEL CALIBRATION

A two component bond stress model proposed by Lehman (1998) was implemented to calculate the slip displacement, as seen in Figure D.2.

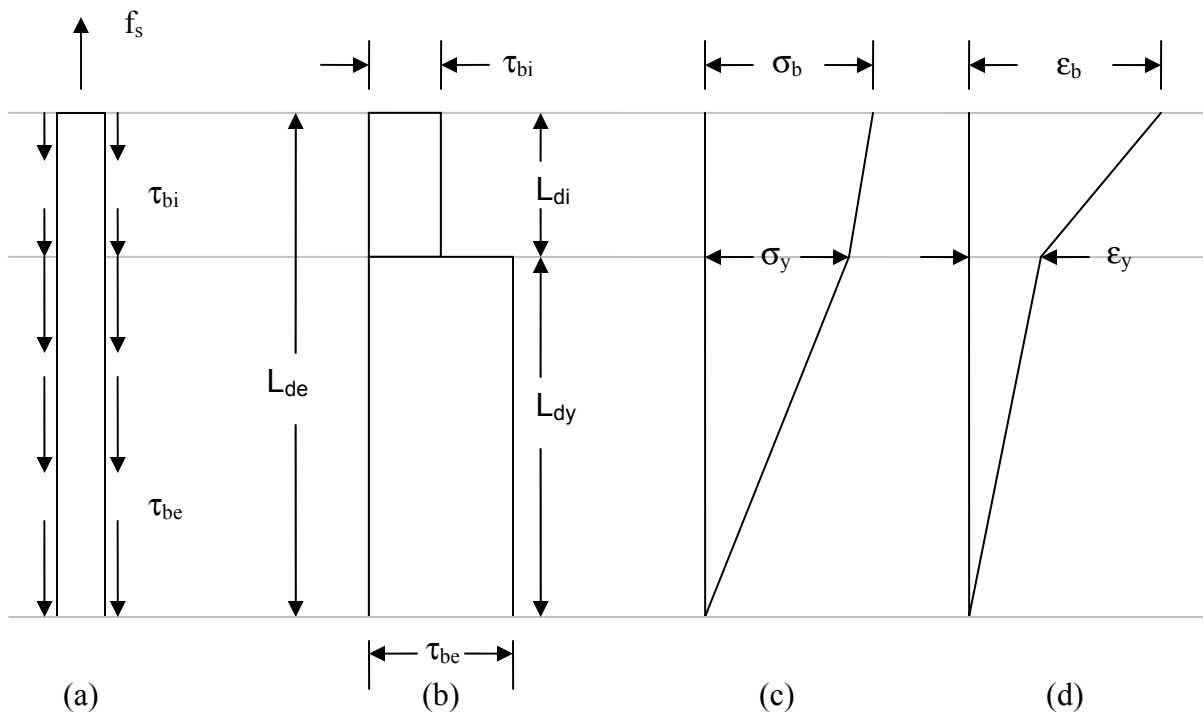


Fig. D.2 Two-component bond stress model

Figure D.2(a) shows the free body diagram of the longitudinal reinforcement below the base of the column. Figure D.2(b) shows the two component bond stress model that was used to characterize the bond stress along the bar presented in Figure D.2(a). Figure D.2(c) shows the reduction in the axial stress in the bar due to the bond stress, and Figure D.2(d) shows the corresponding strain diagram for a bilinear stress-strain model.

The total bond development length, L_{dt} , is composed of inelastic and elastic parts. The inelastic development length, L_{di} , is defined as the length of the bar below the base of the column that is inelastic, and can be determined by the equation

$$L_{di} = \frac{(\sigma_b - \sigma_y)d_b}{4\tau_{bi}} \quad (D.31)$$

where σ_b is the stress at the base of the column, σ_y is the yield stress of the longitudinal reinforcement, d_b is the longitudinal bar diameter, and τ_{bi} is the inelastic bond stress. The elastic development length can be described by the equation

$$L_{de} = \frac{\sigma_y d_b}{4\tau_{be}} \quad (D.32)$$

where τ_{be} is the elastic bond stress.

For this investigation, both the bilinear and Burn-Seiss stress-strain models were considered. The stress-strain curves for each of these models are shown in Figure D.3.

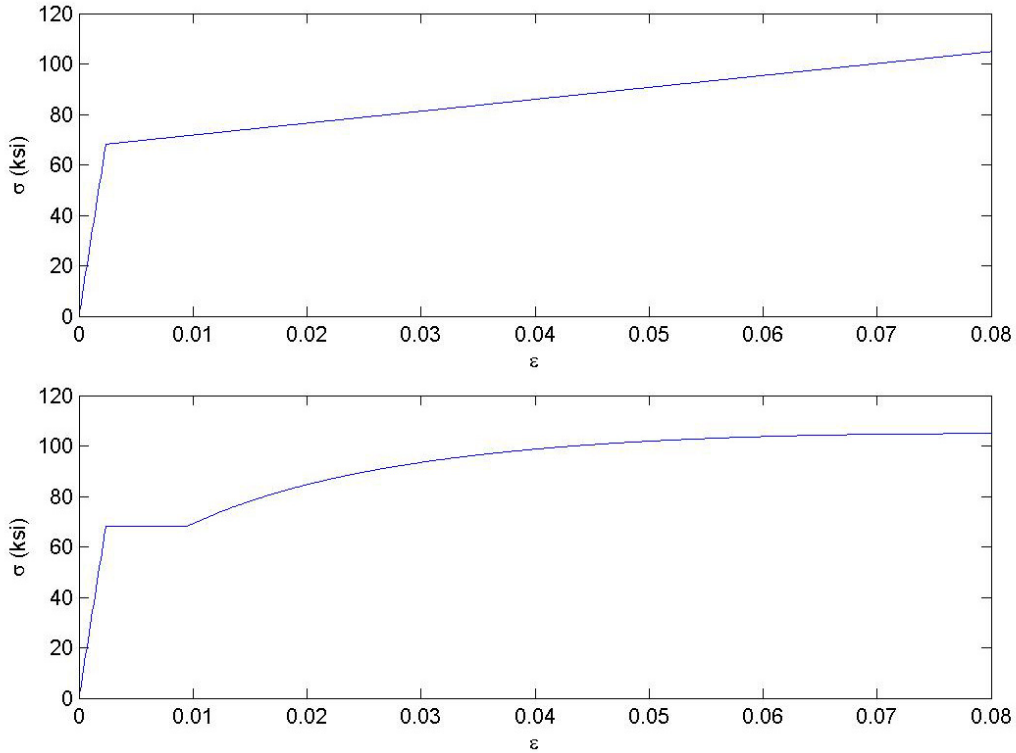


Fig. D.3 Stress-strain relationship for (a) bilinear model and (b) Burns-Seiss model

Each of the models in Figure D.3 were developed using data from tension tests performed on the longitudinal reinforcement. For this reason, each model has the same yield and ultimate components of force and displacement.

The elastic and inelastic bond stresses, τ_{be} and τ_{bi} , were assumed to be proportional to the concrete compressive strength, given by the equations

$$\tau_{bi} = a\sqrt{f'_c} \quad (D.33)$$

$$\tau_{be} = b\sqrt{f'_c} \quad (D.34)$$

where a and b are the inelastic and elastic bond stress coefficients, respectively. The ratio between the bond stresses is therefore equal to the ratio b/a . By keeping the ratio of b/a constant throughout the life of the column, the value of the elastic bond stress coefficient, b , can be optimized by minimizing the differences between a calculated and a measured parameter at each level of displacement. The two parameters that were minimized were the differences between the measured and calculated slip displacements and the measured and calculated strains, as defined in Equations D.35 and D.36.

$$\min \quad error = \sqrt{\frac{\sum_{i=1}^{\#ofcolumns} (\delta_{s,calc} - \delta_{s,meas})^2}{\sum_{i=1}^{\#ofcolumns} (\delta_{s,meas})^2}} \quad (D.35)$$

$$s.t. \quad b > 0$$

$$\min \quad error = \sqrt{\frac{\sum_{i=1}^{\#ofcolumns} \sum_{j=1}^{\#ofgauges} (\epsilon_{s,calc} - \epsilon_{s,meas})^2}{\sum_{i=1}^{\#ofcolumns} \sum_{j=1}^{\#ofgauges} (\epsilon_{s,meas})^2}} \quad (D.36)$$

$$s.t. \quad b > 0$$

In Equation D.35, δ_s is the displacement of the reinforcement at the base of the column due to slip between the reinforcement and the concrete, defined by the equation:

$$\delta_b = \frac{1}{2} [(\epsilon_b + \epsilon_y)L_{di} + \epsilon_y L_{de}] \quad (D.37)$$

Equation D.37 assumes that the sum of the elastic and inelastic development lengths does not exceed the maximum embedment length. This assumption was checked throughout the calibration.

Equation D.35 was minimized to determine the optimal elastic bond stress coefficient at various multiples of the column's yield displacement. For each of these multiples of the initial yield displacement, the optimal for three ratios of b/a was solved. The optimal elastic bond stress coefficient as a function of the level of displacement and the ratio of b/a is displayed in Figure D.4.

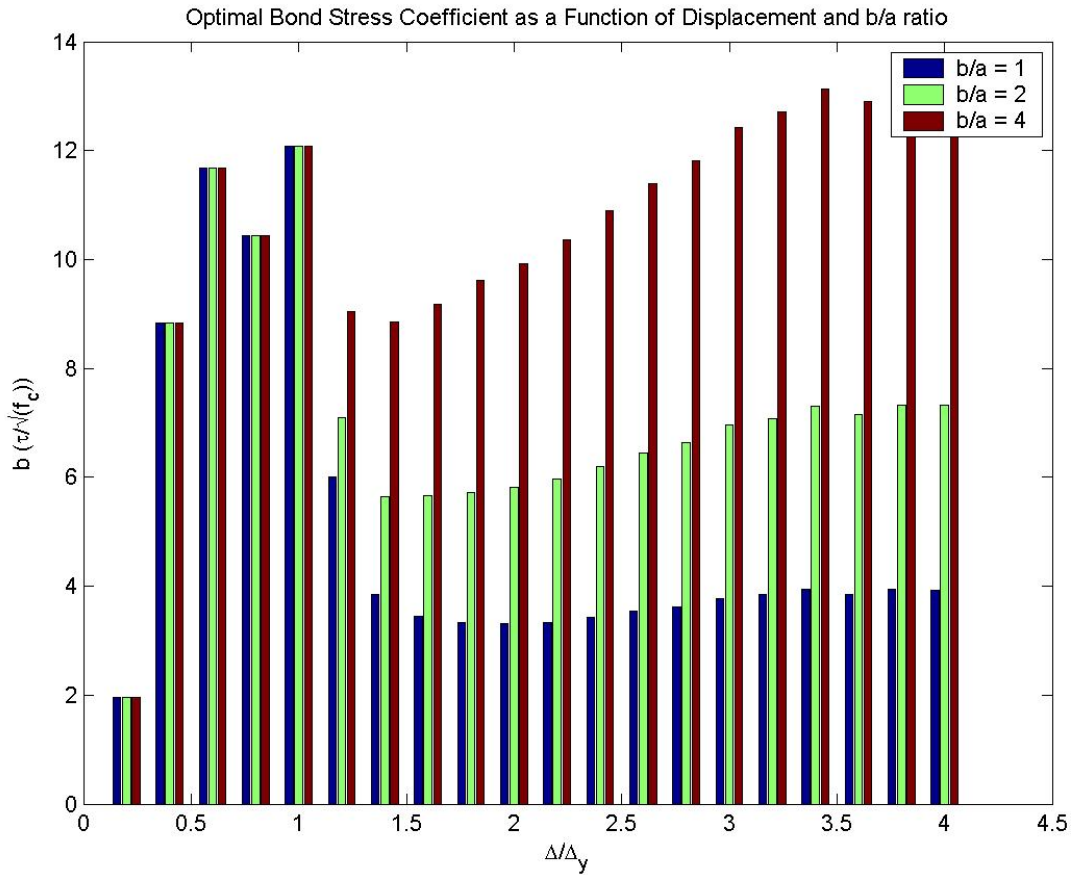


Fig. D.4 Optimal bond stress coefficient for each level of displacement

The optimal bond stress coefficients are the same for all three b/a ratios that were tested up to the point of yield because prior to yield, the inelastic bond stress, τ_{bi} , does not exist. As seen in Figure D.4, the bond stress increases until the column has reached its yield displacement due to an increase in bond demand without a reduction in capacity. After the yield displacement, the bond capacity drops down and rises again due to increased bond demand further down in the footing.

Figure D.4 displays the optimal elastic bond stress at each level of displacement. If a constant bond stress is assumed throughout the life of the column, the optimal bond stress for the entire displacement history can be determined by minimizing the error between the measured and calculated values of the displacements or the strains, given by the equations:

$$\min_{b > 0} \text{error} = \sqrt{\frac{\sum_{k=1}^{\#ofdisps} \sum_{i=1}^{\#ofcolumns} (\delta_{s(k,i),calc} - \delta_{s(k,i),meas})^2}{\sum_{k=1}^{\#ofdisps} \sum_{i=1}^{\#ofcolumns} (\delta_{s(k,i),meas})^2}} \quad (D.38)$$

s.t. $b > 0$

$$\min_{b > 0} \text{error} = \sqrt{\frac{\sum_{k=1}^{\#ofdisps} \sum_{i=1}^{\#ofcolumns} \sum_{j=1}^{\#ofgauges} (\epsilon_{s(k,i,j),calc} - \epsilon_{s(k,i,j),meas})^2}{\sum_{k=1}^{\#ofdisps} \sum_{i=1}^{\#ofcolumns} \sum_{j=1}^{\#ofgauges} (\epsilon_{s(k,i,j),meas})^2}} \quad (D.39)$$

s.t. $b > 0$

The optimal bond stress will vary slightly depending on which definition of error is used. The error as a function of bond stress for the optimization of Equation D.38 is seen in Figure D.5.

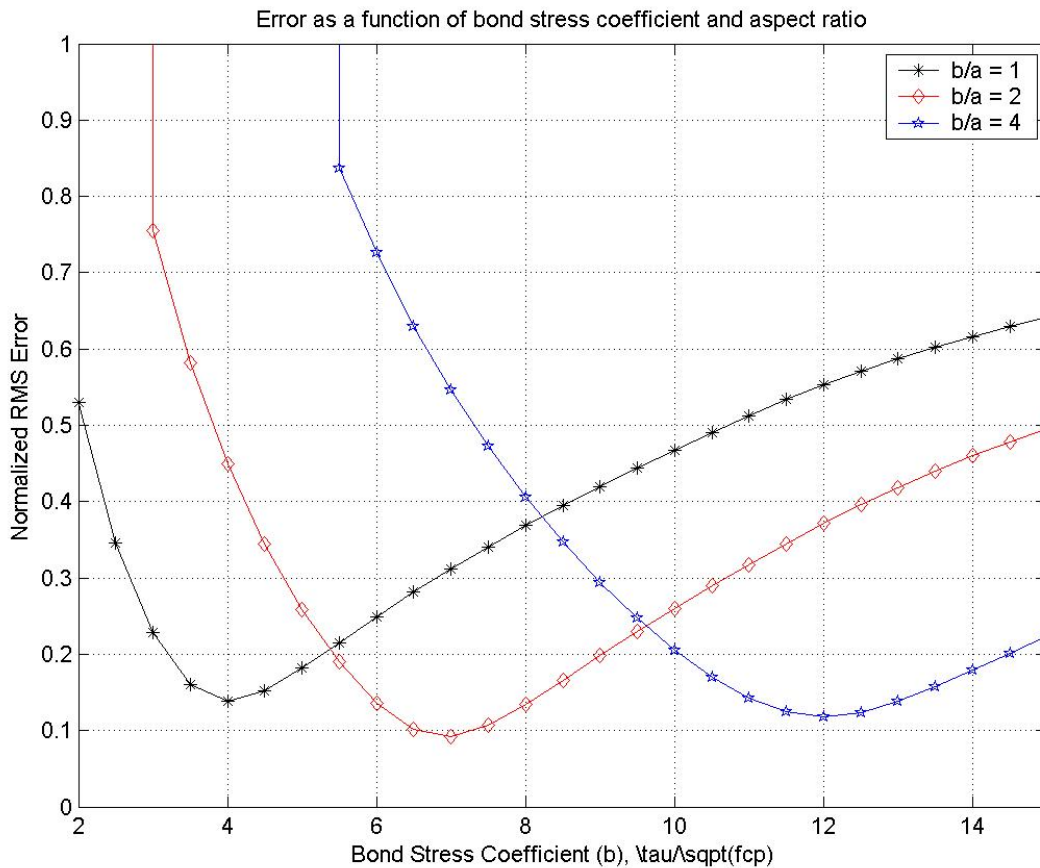


Fig. D.5 Error as a function of bond stress coefficient, b , for three ratios of b/a

As seen from Figure D.5, the optimal solutions for the three ratios of b/a are

$$b_{optimal} = \begin{cases} 4 & b/a = 1 & error = 0.14 \\ 7 & b/a = 2 & error = 0.09 \\ 10 & b/a = 4 & error = 0.12 \end{cases} \quad (D.40)$$

Using Equation D.39 to define the error, the optimal elastic bond stress coefficient, b, is

$$b_{optimal} = \begin{cases} 9 & b/a = 1 & error = 0.25 \\ 10 & b/a = 2 & error = 0.21 \\ 14 & b/a = 4 & error = 0.21 \end{cases} \quad (D.41)$$

Because the definition of the error is somewhat arbitrary, each of these optimal solutions can be used to explain the slip displacement of the column. However, because there is consistently less error with the solutions that involve minimizing the difference between the calculated and measured slip displacements, this is the definition of error that will be used for further analyses. As seen from Figure D.5, the least amount of error occurs when $b/a = 2$, and $b = 7$.

The reduction in the bond stress from the assumed $\tau_{be} = 12\sqrt{f'_c}$ to $\tau_{be} = 7\sqrt{f'_c}$ is attributed to the effect of waterproofing on the longitudinal reinforcement to protect the strain gages. Because Columns S1 and S15 did not have strain gages, a bond stress of $\tau_{be} = 12\sqrt{f'_c}$ was used for these columns.

Appendix E: Calibrated Park-Ang Damage Model

Using the Park-Ang damage model, there was a poor correlation between the effect of cycling and damage accumulation for the six columns. This was due to the model's sensitivity to small changes in the yield displacement. Because of this sensitivity, the calibrated Park-Ang damage model predicted that for most damage states, cycling increased the maximum column displacement at that damage state, which is contrary to what the Park-Ang damage model allows (Park and Ang 1985). The calibrated Park-Ang damage model for the nine damage states presented in Chapter 5 are shown in Figures E.1–E.9.

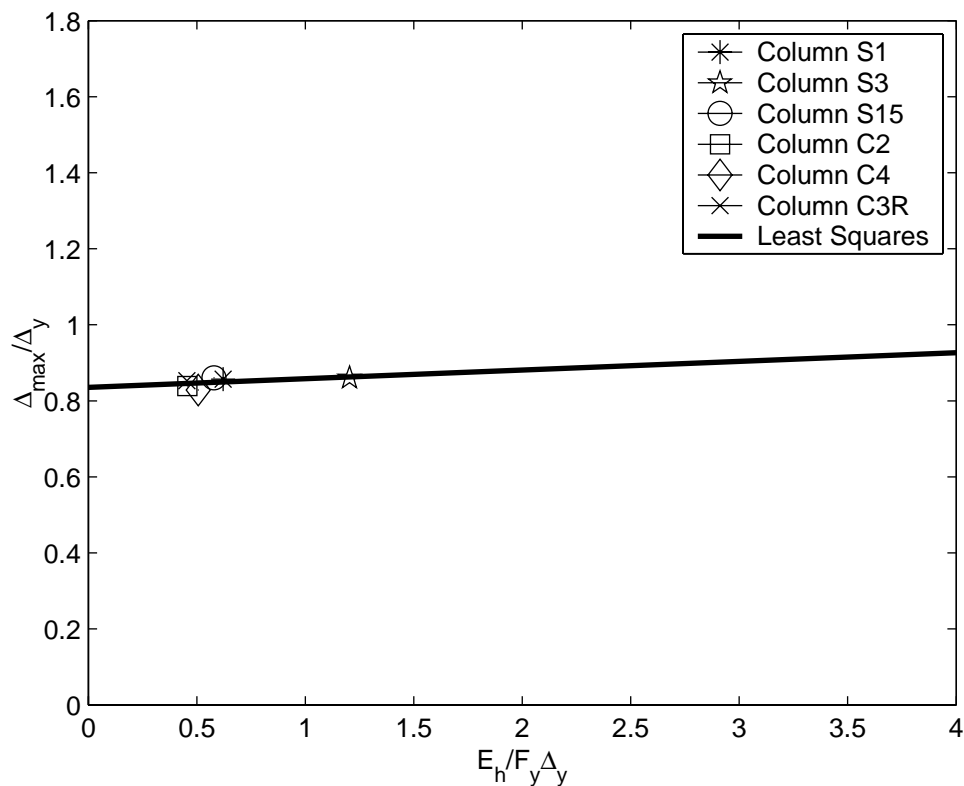


Fig. E.1 Park-Ang damage model for first yield of longitudinal reinforcement

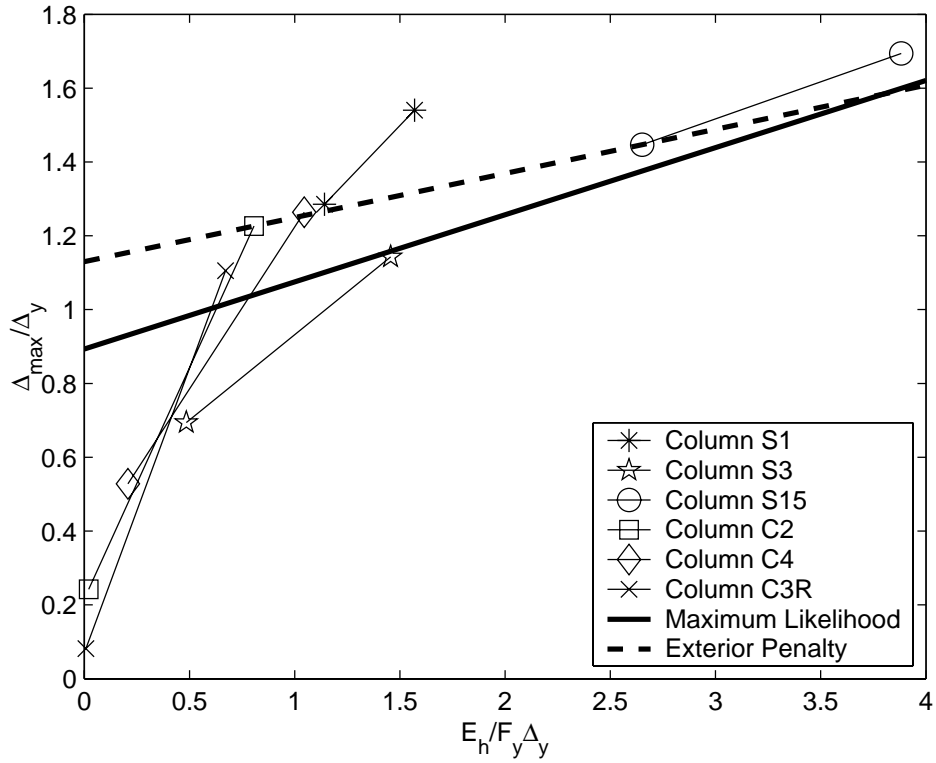


Fig. E.2 Park-Ang damage model for significant flexural cracking

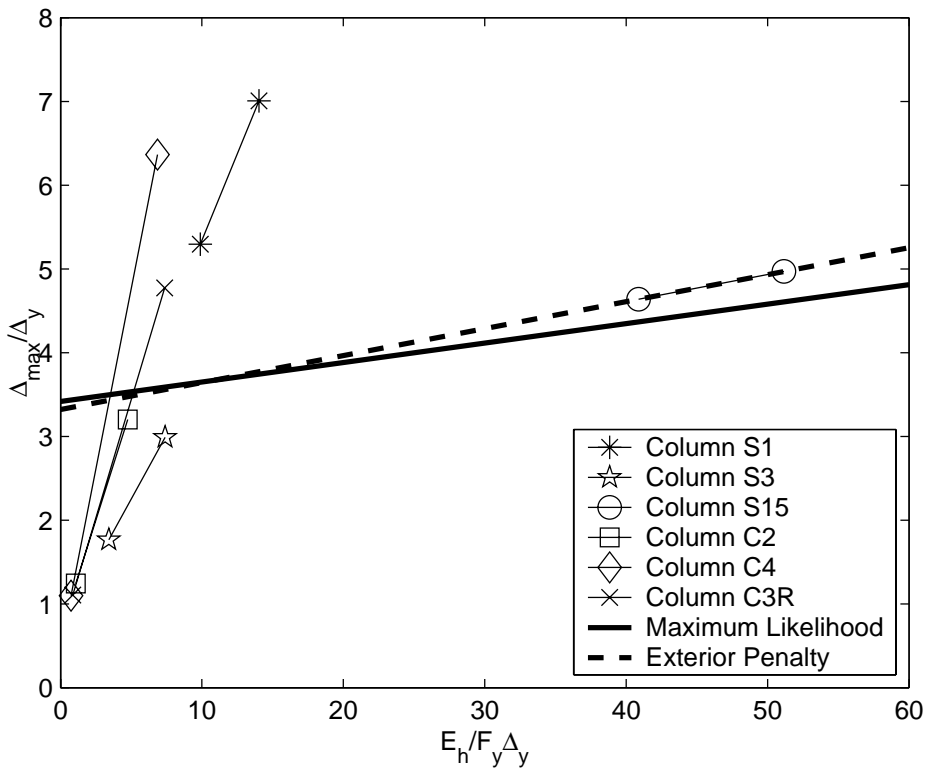


Fig. E.3 Park-Ang damage model for first significant spalling

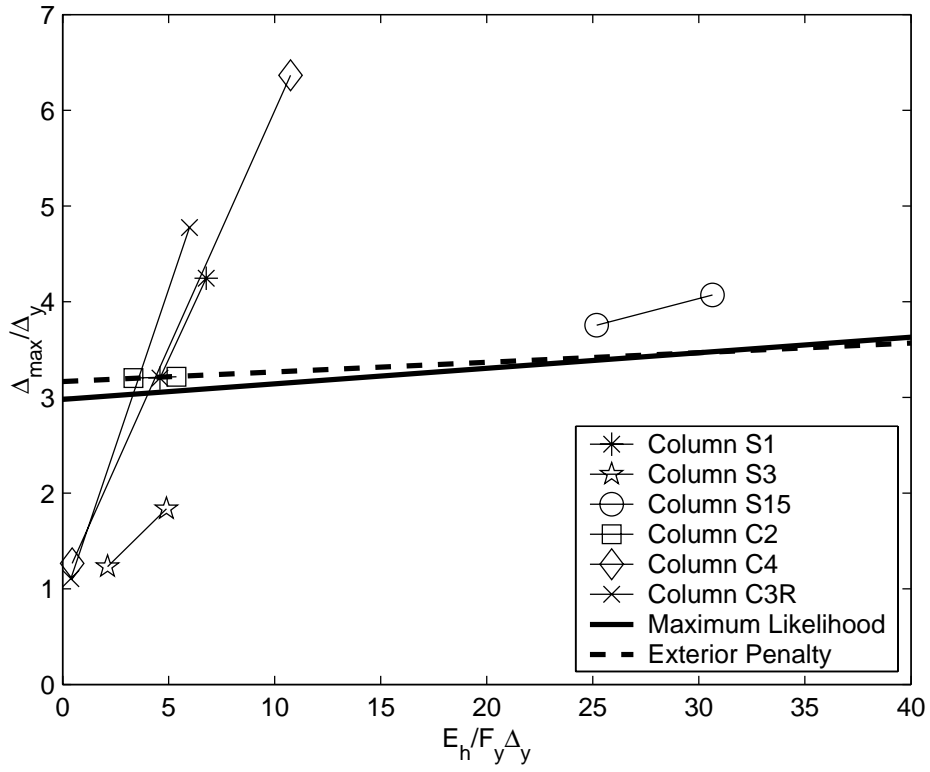


Fig. E.4 Park-Ang damage model for residual cracking

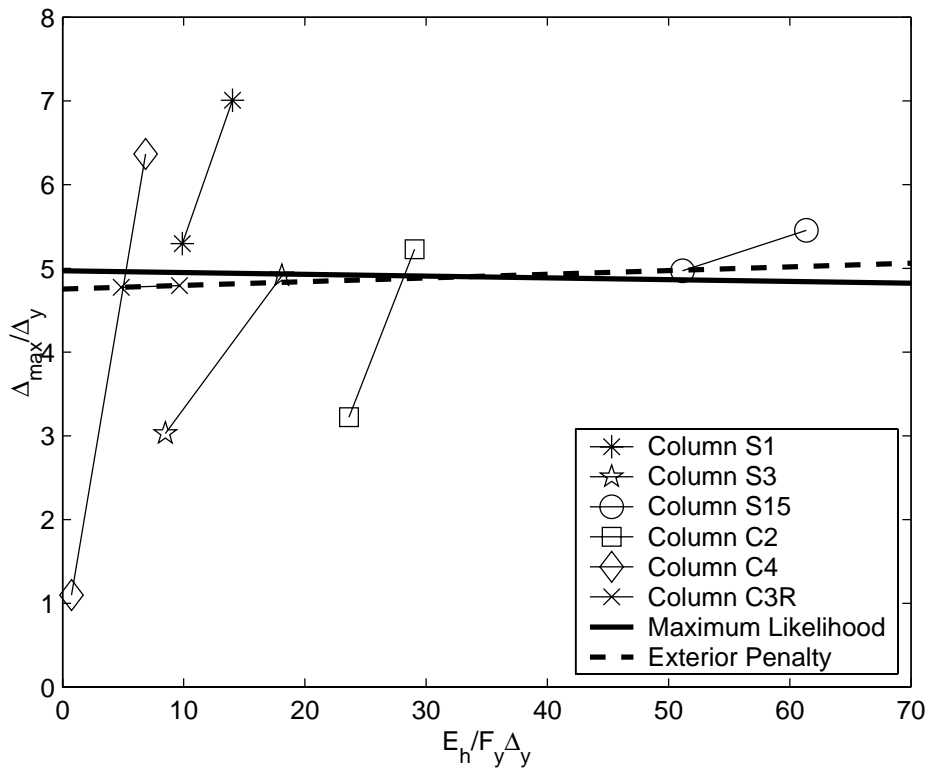


Fig. E.5 Park-Ang damage model for bar buckling

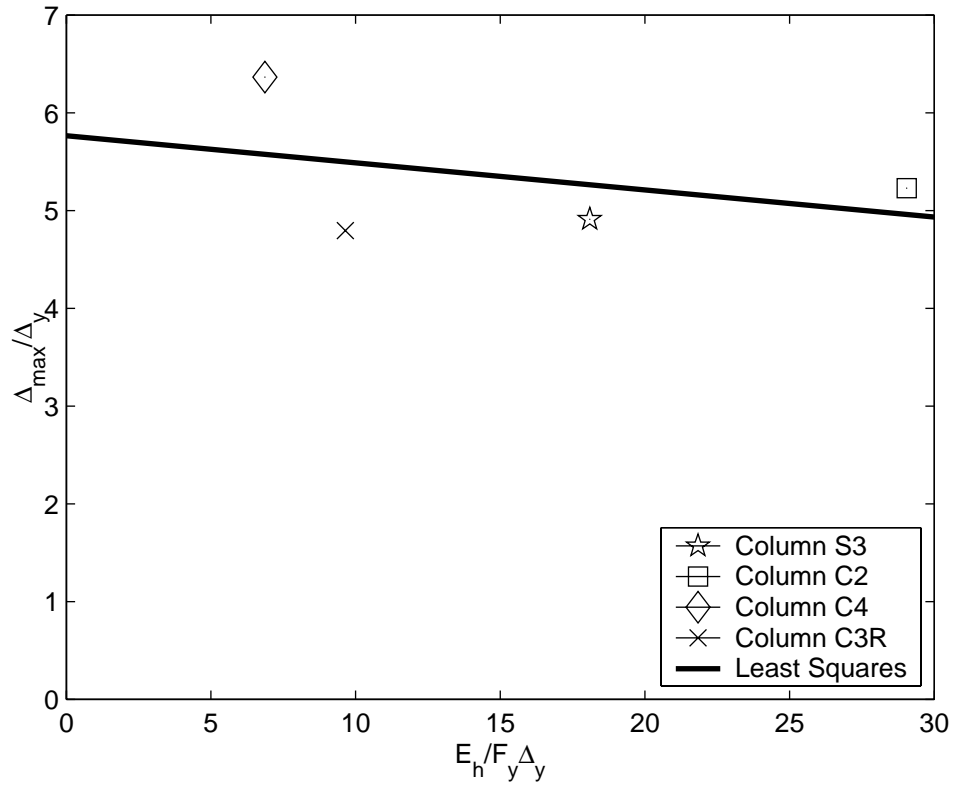


Fig. E.6 Park-Ang damage model for hoop fracture

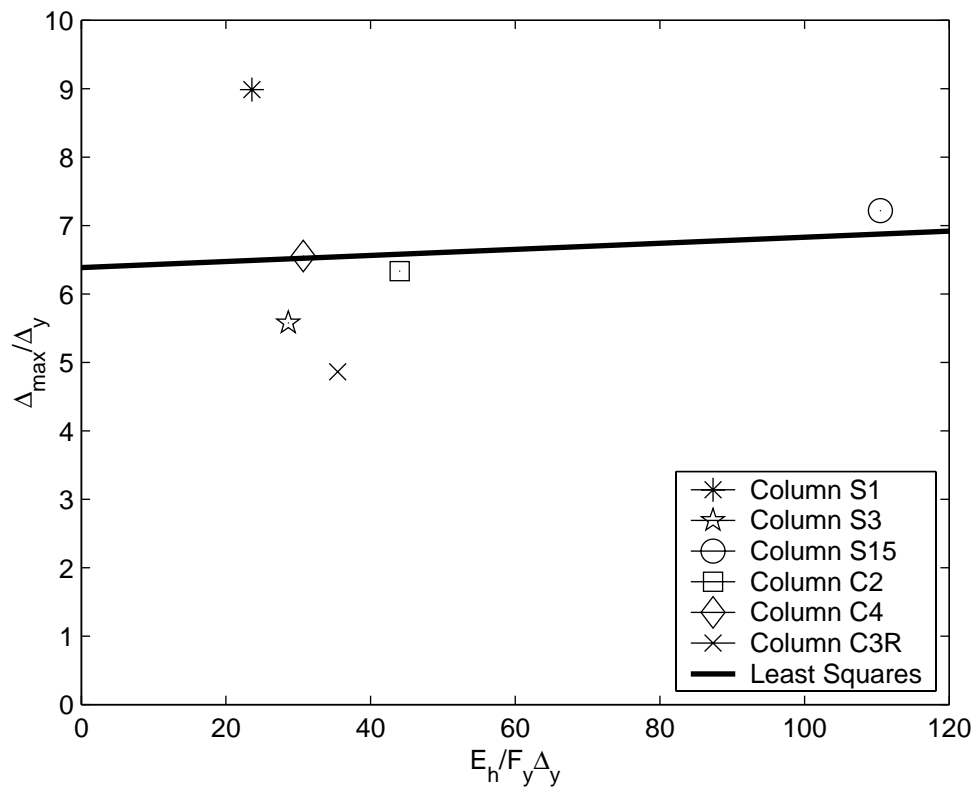


Fig. E.7 Park-Ang damage model for 20% loss of lateral load

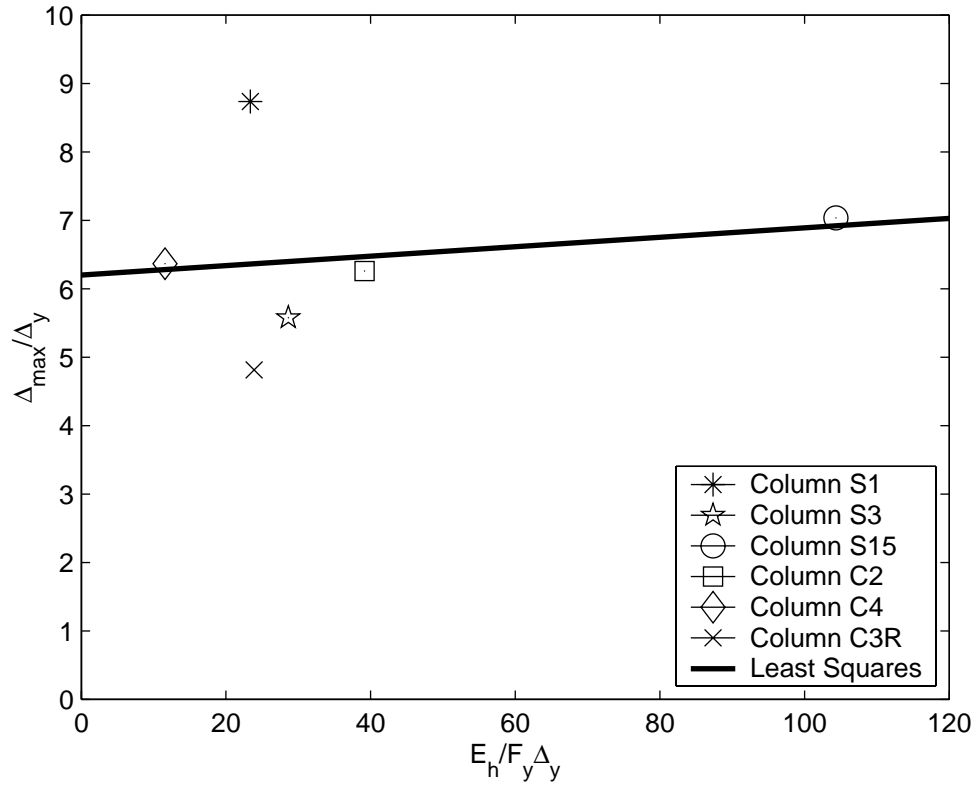


Fig. E.8 Park-Ang damage model for 50% loss of lateral load

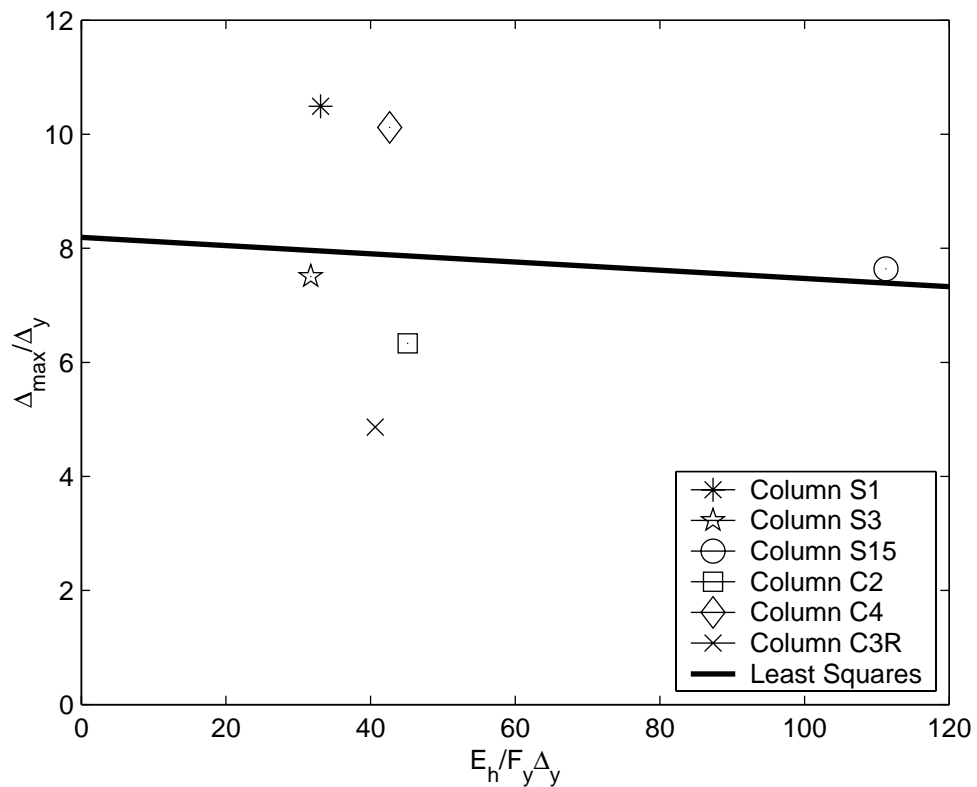


Fig. E.9 Park-Ang damage model for loss of axial load

The effect of cycling on each damage state is summarized in Table E.1. The parameters for the calibrated model using the three calibration methods are shown in Chapter 6.

Table E.1 Effect of cycling on the maximum displacement at each damage state using the Park-Ang damage model

Damage State	Effect of Cycling
First Yield of Longitudinal Reinforcement	Increases
Significant Flexural Cracking	Increases
Significant Spalling	Increases
Residual Cracking	Increases
Bar Buckling	Insignificant
Hoop Fracture	Decreases
20% Loss of Lateral Load	Increases
50% Loss of Lateral Load	Increases
Loss of Axial Load	Insignificant

As shown in Table E.1, the only damage state for which cycling decreases the maximum displacement is hoop fracture. This same result was predicted when using the other two damage models in Chapter 6, because hoop fracture was only calibrated using Columns S3, C2, C4, and C3R. Columns S1 and S15 did not experience hoop fracture; therefore the difference in the yield displacements does not effect this damage state.

PEER REPORTS

PEER reports are available from the National Information Service for Earthquake Engineering (NISEE). To order PEER reports, please contact the Pacific Earthquake Engineering Research Center, 1301 South 46th Street, Richmond, California 94804-4698. Tel.: (510) 231-9468; Fax: (510) 231-9 461.

- PEER 2005/12** *PEER Testbed Study on a Laboratory Building: Exercising Seismic Performance Assessment.* Mary C. Comerio, editor. November 2005.
- PEER 2005/11** *Van Nuys Hotel Building Testbed Report: Exercising Seismic Performance Assessment.* Helmut Krawinkler, editor. October 2005.
- PEER 2005/10** *First NEES/E-Defense Workshop on Collapse Simulation of Reinforced Concrete Building Structures.* September 2005.
- PEER 2005/08** *Damage Accumulation in Lightly Confined Reinforced Concrete Bridge Columns.* R. Tyler Ranf, Jared M. Nelson, Zach Price, Marc O. Eberhard, and John F. Stanton. April 2006.
- PEER 2005/07** *Experimental and Analytical Studies on the Seismic Response of Freestanding and Anchored Laboratory Equipment.* Dimitrios Konstantinidis and Nicos Makris. January 2005.
- PEER 2005/06** *Global Collapse of Frame Structures under Seismic Excitations.* Luis F. Ibarra and Helmut Krawinkler. September 2005.
- PEER 2005/04** *Numerical Modeling of the Nonlinear Cyclic Response of Shallow Foundations.* Chad Harden, Tara Hutchinson, Geoffrey R. Martin, and Bruce L. Kutter. August 2005.
- PEER 2005/03** *A Taxonomy of Building Components for Performance-Based Earthquake Engineering.* Keith A. Porter. September 2005.
- PEER 2005/02** *Fragility Basis for California Highway Overpass Bridge Seismic Decision Making.* Kevin R. Mackie and Bozidar Stojadinovic. June 2005.
- PEER 2005/01** *Empirical Characterization of Site Conditions on Strong Ground Motion.* Jonathan P. Stewart, Yoojoong Choi, and Robert W. Graves. June 2005.
- PEER 2004/09** *Electrical Substation Equipment Interaction: Experimental Rigid Conductor Studies.* Christopher Stearns and André Filiatrault. February 2005.
- PEER 2004/08** *Seismic Qualification and Fragility Testing of Line Break 550-kV Disconnect Switches.* Shakhzod M. Takhirov, Gregory L. Fenves, and Eric Fujisaki. January 2005.
- PEER 2004/07** *Ground Motions for Earthquake Simulator Qualification of Electrical Substation Equipment.* Shakhzod M. Takhirov, Gregory L. Fenves, Eric Fujisaki, and Don Clyde. January 2005.
- PEER 2004/06** *Performance-Based Regulation and Regulatory Regimes.* Peter J. May and Chris Koski. September 2004.
- PEER 2004/05** *Performance-Based Seismic Design Concepts and Implementation: Proceedings of an International Workshop.* Peter Fajfar and Helmut Krawinkler, editors. September 2004.
- PEER 2004/04** *Seismic Performance of an Instrumented Tilt-up Wall Building.* James C. Anderson and Vitelmo V. Bertero. July 2004.
- PEER 2004/03** *Evaluation and Application of Concrete Tilt-up Assessment Methodologies.* Timothy Graf and James O. Malley. October 2004.
- PEER 2004/02** *Analytical Investigations of New Methods for Reducing Residual Displacements of Reinforced Concrete Bridge Columns.* Junichi Sakai and Stephen A. Mahin. August 2004.
- PEER 2004/01** *Seismic Performance of Masonry Buildings and Design Implications.* Kerri Anne Taeko Tokoro, James C. Anderson, and Vitelmo V. Bertero. February 2004.
- PEER 2003/18** *Performance Models for Flexural Damage in Reinforced Concrete Columns.* Michael Berry and Marc Eberhard. August 2003.
- PEER 2003/17** *Predicting Earthquake Damage in Older Reinforced Concrete Beam-Column Joints.* Catherine Pagni and Laura Lowes. October 2004.

- PEER 2003/16** *Seismic Demands for Performance-Based Design of Bridges.* Kevin Mackie and Božidar Stojadinovic. August 2003.
- PEER 2003/15** *Seismic Demands for Nondeteriorating Frame Structures and Their Dependence on Ground Motions.* Ricardo Antonio Medina and Helmut Krawinkler. May 2004.
- PEER 2003/14** *Finite Element Reliability and Sensitivity Methods for Performance-Based Earthquake Engineering.* Terje Haukaas and Armen Der Kiureghian. April 2004.
- PEER 2003/13** *Effects of Connection Hysteretic Degradation on the Seismic Behavior of Steel Moment-Resisting Frames.* Janise E. Rodgers and Stephen A. Mahin. March 2004.
- PEER 2003/12** *Implementation Manual for the Seismic Protection of Laboratory Contents: Format and Case Studies.* William T. Holmes and Mary C. Comerio. October 2003.
- PEER 2003/11** *Fifth U.S.-Japan Workshop on Performance-Based Earthquake Engineering Methodology for Reinforced Concrete Building Structures.* February 2004.
- PEER 2003/10** *A Beam-Column Joint Model for Simulating the Earthquake Response of Reinforced Concrete Frames.* Laura N. Lowes, Nilanjan Mitra, and Arash Altoontash. February 2004.
- PEER 2003/09** *Sequencing Repairs after an Earthquake: An Economic Approach.* Marco Casari and Simon J. Wilkie. April 2004.
- PEER 2003/08** *A Technical Framework for Probability-Based Demand and Capacity Factor Design (DCFD) Seismic Formats.* Fatemeh Jalayer and C. Allin Cornell. November 2003.
- PEER 2003/07** *Uncertainty Specification and Propagation for Loss Estimation Using FOSM Methods.* Jack W. Baker and C. Allin Cornell. September 2003.
- PEER 2003/06** *Performance of Circular Reinforced Concrete Bridge Columns under Bidirectional Earthquake Loading.* Mahmoud M. Hachem, Stephen A. Mahin, and Jack P. Moehle. February 2003.
- PEER 2003/05** *Response Assessment for Building-Specific Loss Estimation.* Eduardo Miranda and Shahram Taghavi. September 2003.
- PEER 2003/04** *Experimental Assessment of Columns with Short Lap Splices Subjected to Cyclic Loads.* Murat Melek, John W. Wallace, and Joel Conte. April 2003.
- PEER 2003/03** *Probabilistic Response Assessment for Building-Specific Loss Estimation.* Eduardo Miranda and Hesameddin Aslani. September 2003.
- PEER 2003/02** *Software Framework for Collaborative Development of Nonlinear Dynamic Analysis Program.* Jun Peng and Kincho H. Law. September 2003.
- PEER 2003/01** *Shake Table Tests and Analytical Studies on the Gravity Load Collapse of Reinforced Concrete Frames.* Kenneth John Elwood and Jack P. Moehle. November 2003.
- PEER 2002/24** *Performance of Beam to Column Bridge Joints Subjected to a Large Velocity Pulse.* Natalie Gibson, André Filiatrault, and Scott A. Ashford. April 2002.
- PEER 2002/23** *Effects of Large Velocity Pulses on Reinforced Concrete Bridge Columns.* Greg L. Orozco and Scott A. Ashford. April 2002.
- PEER 2002/22** *Characterization of Large Velocity Pulses for Laboratory Testing.* Kenneth E. Cox and Scott A. Ashford. April 2002.
- PEER 2002/21** *Fourth U.S.-Japan Workshop on Performance-Based Earthquake Engineering Methodology for Reinforced Concrete Building Structures.* December 2002.
- PEER 2002/20** *Barriers to Adoption and Implementation of PBEE Innovations.* Peter J. May. August 2002.
- PEER 2002/19** *Economic-Engineered Integrated Models for Earthquakes: Socioeconomic Impacts.* Peter Gordon, James E. Moore II, and Harry W. Richardson. July 2002.
- PEER 2002/18** *Assessment of Reinforced Concrete Building Exterior Joints with Substandard Details.* Chris P. Pantelides, Jon Hansen, Justin Nadauld, and Lawrence D. Reaveley. May 2002.
- PEER 2002/17** *Structural Characterization and Seismic Response Analysis of a Highway Overcrossing Equipped with Elastomeric Bearings and Fluid Dampers: A Case Study.* Nicos Makris and Jian Zhang. November 2002.
- PEER 2002/16** *Estimation of Uncertainty in Geotechnical Properties for Performance-Based Earthquake Engineering.* Allen L. Jones, Steven L. Kramer, and Pedro Arduino. December 2002.

- PEER 2002/15** *Seismic Behavior of Bridge Columns Subjected to Various Loading Patterns.* Asadollah Esmaeily-Gh. and Yan Xiao. December 2002.
- PEER 2002/14** *Inelastic Seismic Response of Extended Pile Shaft Supported Bridge Structures.* T.C. Hutchinson, R.W. Boulanger, Y.H. Chai, and I.M. Idriss. December 2002.
- PEER 2002/13** *Probabilistic Models and Fragility Estimates for Bridge Components and Systems.* Paolo Gardoni, Armen Der Kiureghian, and Khalid M. Mosalam. June 2002.
- PEER 2002/12** *Effects of Fault Dip and Slip Rake on Near-Source Ground Motions: Why Chi-Chi Was a Relatively Mild M7.6 Earthquake.* Brad T. Aagaard, John F. Hall, and Thomas H. Heaton. December 2002.
- PEER 2002/11** *Analytical and Experimental Study of Fiber-Reinforced Strip Isolators.* James M. Kelly and Shakhzod M. Takhirov. September 2002.
- PEER 2002/10** *Centrifuge Modeling of Settlement and Lateral Spreading with Comparisons to Numerical Analyses.* Sivapalan Gajan and Bruce L. Kutter. January 2003.
- PEER 2002/09** *Documentation and Analysis of Field Case Histories of Seismic Compression during the 1994 Northridge, California, Earthquake.* Jonathan P. Stewart, Patrick M. Smith, Daniel H. Whang, and Jonathan D. Bray. October 2002.
- PEER 2002/08** *Component Testing, Stability Analysis and Characterization of Buckling-Restrained Unbonded Braces™.* Cameron Black, Nicos Makris, and Ian Aiken. September 2002.
- PEER 2002/07** *Seismic Performance of Pile-Wharf Connections.* Charles W. Roeder, Robert Graff, Jennifer Soderstrom, and Jun Han Yoo. December 2001.
- PEER 2002/06** *The Use of Benefit-Cost Analysis for Evaluation of Performance-Based Earthquake Engineering Decisions.* Richard O. Zerbe and Anthony Falit-Baiamonte. September 2001.
- PEER 2002/05** *Guidelines, Specifications, and Seismic Performance Characterization of Nonstructural Building Components and Equipment.* André Filiatrault, Constantin Christopoulos, and Christopher Stearns. September 2001.
- PEER 2002/04** *Consortium of Organizations for Strong-Motion Observation Systems and the Pacific Earthquake Engineering Research Center Lifelines Program: Invited Workshop on Archiving and Web Dissemination of Geotechnical Data, 4–5 October 2001.* September 2002.
- PEER 2002/03** *Investigation of Sensitivity of Building Loss Estimates to Major Uncertain Variables for the Van Nuys Testbed.* Keith A. Porter, James L. Beck, and Rustem V. Shaikhutdinov. August 2002.
- PEER 2002/02** *The Third U.S.-Japan Workshop on Performance-Based Earthquake Engineering Methodology for Reinforced Concrete Building Structures.* July 2002.
- PEER 2002/01** *Nonstructural Loss Estimation: The UC Berkeley Case Study.* Mary C. Comerio and John C. Stallmeyer. December 2001.
- PEER 2001/16** *Statistics of SDF-System Estimate of Roof Displacement for Pushover Analysis of Buildings.* Anil K. Chopra, Rakesh K. Goel, and Chatpan Chintanapakdee. December 2001.
- PEER 2001/15** *Damage to Bridges during the 2001 Nisqually Earthquake.* R. Tyler Ranf, Marc O. Eberhard, and Michael P. Berry. November 2001.
- PEER 2001/14** *Rocking Response of Equipment Anchored to a Base Foundation.* Nicos Makris and Cameron J. Black. September 2001.
- PEER 2001/13** *Modeling Soil Liquefaction Hazards for Performance-Based Earthquake Engineering.* Steven L. Kramer and Ahmed-W. Elgamal. February 2001.
- PEER 2001/12** *Development of Geotechnical Capabilities in OpenSees.* Boris Jeremić. September 2001.
- PEER 2001/11** *Analytical and Experimental Study of Fiber-Reinforced Elastomeric Isolators.* James M. Kelly and Shakhzod M. Takhirov. September 2001.
- PEER 2001/10** *Amplification Factors for Spectral Acceleration in Active Regions.* Jonathan P. Stewart, Andrew H. Liu, Yoojoong Choi, and Mehmet B. Baturay. December 2001.
- PEER 2001/09** *Ground Motion Evaluation Procedures for Performance-Based Design.* Jonathan P. Stewart, Shyh-Jeng Chiou, Jonathan D. Bray, Robert W. Graves, Paul G. Somerville, and Norman A. Abrahamson. September 2001.
- PEER 2001/08** *Experimental and Computational Evaluation of Reinforced Concrete Bridge Beam-Column Connections for Seismic Performance.* Clay J. Naito, Jack P. Moehle, and Khalid M. Mosalam. November 2001.

- PEER 2001/07** *The Rocking Spectrum and the Shortcomings of Design Guidelines.* Nicos Makris and Dimitrios Konstantinidis. August 2001.
- PEER 2001/06** *Development of an Electrical Substation Equipment Performance Database for Evaluation of Equipment Fragilities.* Thalia Agnanos. April 1999.
- PEER 2001/05** *Stiffness Analysis of Fiber-Reinforced Elastomeric Isolators.* Hsiang-Chuan Tsai and James M. Kelly. May 2001.
- PEER 2001/04** *Organizational and Societal Considerations for Performance-Based Earthquake Engineering.* Peter J. May. April 2001.
- PEER 2001/03** *A Modal Pushover Analysis Procedure to Estimate Seismic Demands for Buildings: Theory and Preliminary Evaluation.* Anil K. Chopra and Rakesh K. Goel. January 2001.
- PEER 2001/02** *Seismic Response Analysis of Highway Overcrossings Including Soil-Structure Interaction.* Jian Zhang and Nicos Makris. March 2001.
- PEER 2001/01** *Experimental Study of Large Seismic Steel Beam-to-Column Connections.* Egor P. Popov and Shakhzod M. Takhirov. November 2000.
- PEER 2000/10** *The Second U.S.-Japan Workshop on Performance-Based Earthquake Engineering Methodology for Reinforced Concrete Building Structures.* March 2000.
- PEER 2000/09** *Structural Engineering Reconnaissance of the August 17, 1999 Earthquake: Kocaeli (Izmit), Turkey.* Halil Sezen, Kenneth J. Elwood, Andrew S. Whittaker, Khalid Mosalam, John J. Wallace, and John F. Stanton. December 2000.
- PEER 2000/08** *Behavior of Reinforced Concrete Bridge Columns Having Varying Aspect Ratios and Varying Lengths of Confinement.* Anthony J. Calderone, Dawn E. Lehman, and Jack P. Moehle. January 2001.
- PEER 2000/07** *Cover-Plate and Flange-Plate Reinforced Steel Moment-Resisting Connections.* Taejin Kim, Andrew S. Whittaker, Amir S. Gilani, Vitelmo V. Bertero, and Shakhzod M. Takhirov. September 2000.
- PEER 2000/06** *Seismic Evaluation and Analysis of 230-kV Disconnect Switches.* Amir S. J. Gilani, Andrew S. Whittaker, Gregory L. Fenves, Chun-Hao Chen, Henry Ho, and Eric Fujisaki. July 2000.
- PEER 2000/05** *Performance-Based Evaluation of Exterior Reinforced Concrete Building Joints for Seismic Excitation.* Chandra Clyde, Chris P. Pantelides, and Lawrence D. Reaveley. July 2000.
- PEER 2000/04** *An Evaluation of Seismic Energy Demand: An Attenuation Approach.* Chung-Che Chou and Chia-Ming Uang. July 1999.
- PEER 2000/03** *Framing Earthquake Retrofitting Decisions: The Case of Hillside Homes in Los Angeles.* Detlof von Winterfeldt, Nels Roselund, and Alicia Kitsuse. March 2000.
- PEER 2000/02** *U.S.-Japan Workshop on the Effects of Near-Field Earthquake Shaking.* Andrew Whittaker, ed. July 2000.
- PEER 2000/01** *Further Studies on Seismic Interaction in Interconnected Electrical Substation Equipment.* Armen Der Kiureghian, Kee-Jeung Hong, and Jerome L. Sackman. November 1999.
- PEER 1999/14** *Seismic Evaluation and Retrofit of 230-kV Porcelain Transformer Bushings.* Amir S. Gilani, Andrew S. Whittaker, Gregory L. Fenves, and Eric Fujisaki. December 1999.
- PEER 1999/13** *Building Vulnerability Studies: Modeling and Evaluation of Tilt-up and Steel Reinforced Concrete Buildings.* John W. Wallace, Jonathan P. Stewart, and Andrew S. Whittaker, editors. December 1999.
- PEER 1999/12** *Rehabilitation of Nonductile RC Frame Building Using Encasement Plates and Energy-Dissipating Devices.* Mehrdad Sasani, Vitelmo V. Bertero, James C. Anderson. December 1999.
- PEER 1999/11** *Performance Evaluation Database for Concrete Bridge Components and Systems under Simulated Seismic Loads.* Yael D. Hose and Frieder Seible. November 1999.
- PEER 1999/10** *U.S.-Japan Workshop on Performance-Based Earthquake Engineering Methodology for Reinforced Concrete Building Structures.* December 1999.
- PEER 1999/09** *Performance Improvement of Long Period Building Structures Subjected to Severe Pulse-Type Ground Motions.* James C. Anderson, Vitelmo V. Bertero, and Raul Bertero. October 1999.
- PEER 1999/08** *Envelopes for Seismic Response Vectors.* Charles Menun and Armen Der Kiureghian. July 1999.

- PEER 1999/07** *Documentation of Strengths and Weaknesses of Current Computer Analysis Methods for Seismic Performance of Reinforced Concrete Members.* William F. Cofer. November 1999.
- PEER 1999/06** *Rocking Response and Overturning of Anchored Equipment under Seismic Excitations.* Nicos Makris and Jian Zhang. November 1999.
- PEER 1999/05** *Seismic Evaluation of 550 kV Porcelain Transformer Bushings.* Amir S. Gilani, Andrew S. Whittaker, Gregory L. Fenves, and Eric Fujisaki. October 1999.
- PEER 1999/04** *Adoption and Enforcement of Earthquake Risk-Reduction Measures.* Peter J. May, Raymond J. Burby, T. Jens Feeley, and Robert Wood.
- PEER 1999/03** *Task 3 Characterization of Site Response General Site Categories.* Adrian Rodriguez-Marek, Jonathan D. Bray, and Norman Abrahamson. February 1999.
- PEER 1999/02** *Capacity-Demand-Diagram Methods for Estimating Seismic Deformation of Inelastic Structures: SDF Systems.* Anil K. Chopra and Rakesh Goel. April 1999.
- PEER 1999/01** *Interaction in Interconnected Electrical Substation Equipment Subjected to Earthquake Ground Motions.* Armen Der Kiureghian, Jerome L. Sackman, and Kee-Jeung Hong. February 1999.
- PEER 1998/08** *Behavior and Failure Analysis of a Multiple-Frame Highway Bridge in the 1994 Northridge Earthquake.* Gregory L. Fenves and Michael Ellery. December 1998.
- PEER 1998/07** *Empirical Evaluation of Inertial Soil-Structure Interaction Effects.* Jonathan P. Stewart, Raymond B. Seed, and Gregory L. Fenves. November 1998.
- PEER 1998/06** *Effect of Damping Mechanisms on the Response of Seismic Isolated Structures.* Nicos Makris and Shih-Po Chang. November 1998.
- PEER 1998/05** *Rocking Response and Overturning of Equipment under Horizontal Pulse-Type Motions.* Nicos Makris and Yiannis Roussos. October 1998.
- PEER 1998/04** *Pacific Earthquake Engineering Research Invitational Workshop Proceedings, May 14–15, 1998: Defining the Links between Planning, Policy Analysis, Economics and Earthquake Engineering.* Mary Comerio and Peter Gordon. September 1998.
- PEER 1998/03** *Repair/Upgrade Procedures for Welded Beam to Column Connections.* James C. Anderson and Xiaojing Duan. May 1998.
- PEER 1998/02** *Seismic Evaluation of 196 kV Porcelain Transformer Bushings.* Amir S. Gilani, Juan W. Chavez, Gregory L. Fenves, and Andrew S. Whittaker. May 1998.
- PEER 1998/01** *Seismic Performance of Well-Confined Concrete Bridge Columns.* Dawn E. Lehman and Jack P. Moehle. December 2000.